



Universitat Autònoma de Barcelona

**ADVERTIMENT.** L'accés als continguts d'aquesta tesi queda condicionat a l'acceptació de les condicions d'ús establertes per la següent llicència Creative Commons:  [http://cat.creativecommons.org/?page\\_id=184](http://cat.creativecommons.org/?page_id=184)

**ADVERTENCIA.** El acceso a los contenidos de esta tesis queda condicionado a la aceptación de las condiciones de uso establecidas por la siguiente licencia Creative Commons:  <http://es.creativecommons.org/blog/licencias/>

**WARNING.** The access to the contents of this doctoral thesis it is limited to the acceptance of the use conditions set by the following Creative Commons license:  <https://creativecommons.org/licenses/?lang=en>

# Enhancing the High-temperature Chiral Magnetic State in $\text{YBaCuFeO}_5$

**Xiaodong Zhang**

Thesis submitted for the degree of Doctor of Philosophy

PhD programme in Materials Science

Supervisors: Prof. José Luis García-Muñoz

Dr. Javier Herrero Martín



Crystallography of Magnetic and Electronic Oxides and Surfaces

Institut de Ciència de Materials de Barcelona

Universitat Autònoma de Barcelona

May 2022



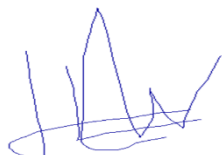
Prof. José Luis García-Muñoz and Dr. Javier Herrero Martín

CERTIFY

that the work reported in the present by Xiaodong Zhang, entitled “Enhancing the High-temperature Chiral Magnetic State in YBaCuFeO<sub>5</sub>”, has been done at the group of “Crystallography of magnetic and electronic oxides and surfaces (CMEOS)” in the Institut de Ciència de Materials de Barcelona (ICMAB-CSIC). This work constitutes the Doctoral Thesis Memory submitted by the interested person to the Facultat de Ciències de la Universitat Autònoma de Barcelona to apply for the degree of Material Science.

Bellaterra, May 10<sup>th</sup>, 2022

Signature:



Prof. José Luis García-Muñoz

Research professor at the Institut de Ciència de Materials de Barcelona (ICMAB-CSIC)

Signature:



Dr. Javier Herrero Martín

Beamline Scientist at the ALBA Synchrotron Light Source in Barcelona





Zeal without knowledge is like  
expedition in the dark.

Sir Isaac Newton



# Abstract

Magnetolectric multiferroic materials, where magnetic order induces ferroelectricity are attracting high interest because of the importance of controlling magnetism by electric fields and vice versa. Spiral (cycloidal) magnetolectric (spin-driven) multiferroics are an ideal platform for the pursuit of strong magnetolectric coupling because spin and ferroelectric orders are coupled “by construction”. Most of the chiral (spiral) magnetolectric multiferroics investigated in recent years are geometrically frustrated magnets, where the presence of frustrated spin networks produces low spiral transition temperatures  $T_S$  (typically  $T_S < 50$  K). This critically limits their potential uses in spintronic and low-power magnetolectric devices. Exceptionally, the layered perovskite  $YBaCuFeO_5$  have been reported to display cycloidal magnetic order at unexpectedly high temperatures. This motivating exception is considered one of the most promising spin-driven multiferroic candidates at high-temperature.

The doctoral Thesis presented here has explored and investigated different strategies to tune and optimize the high-temperature chiral magnetic properties in the  $YBaBB'O_5$  family of this layered perovskite, structurally simple in appearance but complex due to the decisive presence of cation disorder. The strategy is based on modifying both structural and physical elements (such as the magnetic or the spin-orbit couplings, the magnetic moments or the single-ion magnetic anisotropy) through cationic substitutions at the divalent Cu (B) and trivalent Fe (B') sites. Many compounds of the families  $YBa(Cu,B)FeO_5$  (B: Co and Mg) and  $YBaCu(Fe,B')O_5$  (B': Cr and Mn) were prepared as polycrystalline or single crystal samples. They were thoroughly investigated combining magnetometry, X-ray spectroscopies, synchrotron X-ray and neutron diffraction.

Summarizing, (i) we demonstrated an alternative way for increasing Fe/Cu disorder (that controls the level of frustration and  $T_S$ ) not based on the cooling rate. (ii) The T-x magnetic phase diagrams for these B and B' site substitutions were built up. (iii) A huge increase in the stability of the spiral order ( $T_S$ ) was obtained with divalent Co and Mg dopings preserving a linear  $T_S$ - $q_S$  relationship for the spiral modulation. (iv) A triple point was achieved with a maximum spiral transition temperature  $T_S \approx 360$  K, well above RT, describing how to increase the spiral stability by acting on the  $Cu^{2+}$  J-T splitting. (v) We studied in detail magnetic phase competition (phase separation) and magnetic anisotropy as a function of temperature and doping in all these families. The spiral orientation may critically determine the ferroelectric and magnetolectric behavior in these systems. We showed how to induce a systematic reorientation of the spin rotation plane in the spiral phase by doping. Changing from a more helical ( $\mathbf{k} // \mathbf{Q}$ ) into a more cycloidal ( $\mathbf{k} \perp \mathbf{Q}$ ) spin order, and proving that for selected dopings the most cycloidal spiral found is as well the most thermally stable.



## Acknowledgments

I have to admit that the doctoral thesis is a great deal of work and it took me long time to finish it. Despite the tough process, the result is cheerful. It makes me gratified and complete. As everyone's feeling, time always flies. It has been four years that I stay in Barcelona - a "dream city" full of beautiful scenery, friendly people, artistic atmosphere. Thanks to the city Barcelona in which many happy moments and exciting experience that I left here.

The "dream journey" started four years ago, when I stepped on the flight directly to Barcelona with my companions, the first 12 hours flight that I had ever took. To be honest, to study abroad for a doctoral degree was a quick decision that I did not have sufficient time to prepare for it. Before this decision, I had never thought that someday I would study abroad, speaking a different language, working with foreigners and living in an exotic city. I think my grandfather is the person who helped me to make the decision. He is an ordinary man in my village but with great wisdom and experience. I always keep in my memory that when I was a child, he often told me stories about his childhood and youth. In the newly established China in 1950s, the economy is very backward, so was my grandfather's family. He had to climb over two mountains and walk miles every day to his primary school and only take two potatoes as his lunch. My grandfather grew up in this background. Despite the tough life, he never gave up learning from society. Bad times always make a capable man. So, I knew from my childhood that my grandfather was the first person to install a voltage transformer in my village and from then my village had electricity. He used to be a carpenter for a long time. He had been many cities in China. He had taken a five-day-train to Heilongjiang province, the northernmost province in China, for business, and the tiredness made him a two-day rest in a shabby hotel for saving money. He had been a southern city in China and his friend entertained him with snake meat and rice, and so forth. Many old stories sound interesting, but of educational significance. The old stories and rich experience from my grandfather are like a seed that rooted in my heart from then.

I always regard my grandfather as role model and hope to be a person like him. His spirit of living hard but working diligently in defiance of difficulty has always encouraged me. To study and to experience are progressively developed as kind of my sense of worth. Therefore, once I learned that one can study abroad through national scholarship program, why not had a try to obtain a chance to see a much bigger world

to experience a different culture, to know the native customs, to make friends with different cultural background. So far, I had travelled to about 40 cities in China and about 10 countries over the world. I suppose that more places and cities over the world are waiting for me to discover. Great appreciation to my grandfather for lighting me on my way ahead and giving me courage.

For the doctoral Thesis presented here, I would like to express my sincere gratitude to those who have contributed to this work and those who have helped and supported me greatly during the whole process.

Firstly, I would like to thank Prof. José Luis García-Muñoz, my research supervisor. Four years ago, I was accepted by him as a group member and started my research work on a novel and fabulous project. During my stay in the institute, I received plenty of assistance on whether it is the fundamental or experimental knowledge on crystallography, magnetism, x-ray diffraction and condensed matter physics from José Luis, I always remember our countless times face-to-face meetings in his office. Thanks to him for introducing me to the large experimental facilities such as the synchrotron diffraction facility ALBA and the neutron diffraction facility Institute Laue Langevin (ILL), which opens the portal for me to the research of material utilizing these state-of-the-art technologies. Furthermore, what he has delivered to me is not only the expertized academic knowledge, but also his ardently love and conscientious attitude towards academic work. Many times when we discuss something, he was just very excited and with great joy, which left deep impressions on me. And I also very often noticed that he had lunch so late and was busy finishing his work. In addition, I am especially grateful for the kind help, patient guidance and revision throughout the production of my doctoral thesis. In a word, it was a huge privilege and honour to conduct this exciting research work under his guidance.

I would like to thank Dr. Javier Herrero Martín, my other supervisor. I remembered that many times he performed XAS experiment on my samples until very late night. He taught me the data analysis, software using and he also recommended me lots of related books and research papers to read. Thanks again for his regular discussion and patient guidance to me on the XAS experiment and the enormous effort he has paid on this thesis.

I also would like to give my appreciation to my colleague Arnau Romaguera Camps. We have always been the only two group members in my group for a long time, we learn and work together, discuss together, perform countless experiments in the

ALBA and ILL together, we have built closed friendship during our four year's collaboration. We have many unforgettable "experiment nights" in ILL, and every time he sighed humorously: life is hard. And we also have many enjoyable moments when we climb the mountains, swimming in the sea and have dinner at Chinese restaurants. Thanks to him again for the four year's companionship.

I also thank my new group member Ruyong Li who has helped me on the refinements of synchrotron and neutron diffraction data and some administration works. I wish you can enjoy your study and life in Spain.

Within this line of research, collaborative efforts from other colleagues should be emphasized also, which are essential for the completion of the thesis project. I gained numerous inspiring interactions and exchange of ideas with them. In particular, a sincere thank you:

To Oscar Fabelo, the local contact in the ILL. He helped me a lot on the neutron diffraction experiment in the beamline D1B, D2B, D20, D9 and Orient Express station. He explained me well the principles of neutron scattering and taught me how to measure samples with the complexed furnaces and computer systems.

To Francois Fauth, the local contact in the ALBA. He offered me a great deal of assistance on the synchrotron diffraction experiment in the BL-04 MSPD beamline. Thanks to him for the great effort made on the measurements of my samples and kind discussions within us.

To the scientific and technical staff of ICMAB for their support and willingness to help. Special thanks to Anna Crespi, Xavier Campos and Joan Esquiús for the XRD technical support; to Bernat Bozzo and Ferran Vallés, for their four years help on the magnetization measurements of my samples; to Roberta Ceravola for the thermal analysis of my samples and Anna Esther for the electron microscopy service.

I am obliged to the personnel, the library, IT department and maintenance services at ICMAB for providing a comfortable and cheerful working environment. I also would like to express my sincere gratitude to Dr. Eva Pellicer Vilá and Dr. Roger Bofill Arasa, the UAB material science doctoral program coordinators, for their support and kind availability.

Apart from the work, I also thank my many other good friends in life, with special mention to Zheng Ma, Hailin Wang, Pengmei Yu, Yunwei Sheng, Songbai Zhang, Hao Li, Jinhui Hu, Minghua Kong, Huan Tan, Fei Yang, Lei Zhao, Saúl Estantia, Mengdi Qian and Adrian Crespo, for making my everyday life brighter and fill it with so much



joy. I also would like to thank my landlord, an old couple, for giving help on the repair of household appliances time after time; to my Spanish teacher for introducing me plenty of Spanish customs and culture. All people I met in Spain is friendly and enthusiasm to me, their smile, cheerful and outgoing character have left me deep impression.

I would like to acknowledge the China Scholarship Council (CSC) for the financial support for my stay in Spain. This research work has received financial support from the Spanish Ministerio de Ciencia, Innovacion y Universidades (MINECO), through Projects No. MAT2015-68760-C2-2 and RTI2018-098537-B-C21, cofounded by ERDF from EU, and “Severo Ochoa” Programme for centres of Excellence in R&D (FUNFUTURE (CEX2019-000917-S)). I also acknowledge ALBA, ILL and D1B-CRG (MINECO) for provision of beam time.

Last but not the least, my deepest gratitude always goes to my family, for their incredible support, their sacrifice during these years. My family is forever a warm harbour to me. It is their love that raised me up from a primary school student to a Doctor, the first Doctor in my big family. I hope I have made you all proud.

# Contents

<b>Chapter 1</b> Introduction and motivation: towards high- $T_S$ cycloidal multiferroics .....	1
1.1 A brief history of magnetoelectric materials .....	1
1.2 Why are multiferroics interesting?.....	3
1.3 Classification of multiferroics.....	4
1.4 Fundamental physics concepts.....	6
1.4.1 Magnetic order .....	6
1.4.2 Dzyaloshinskii-Moriya interaction .....	8
1.4.3 Spin-driven ferroelectricity .....	9
1.5 Introduction on YBaCuFeO <sub>5</sub> .....	11
1.5.1 Crystal structure .....	11
1.5.2 Magnetic properties .....	13
1.6 Scope and objectives.....	18
<b>Chapter 2</b> Sample synthesis and experimental techniques .....	21
2.1 Introduction.....	21
2.2 Synthesis and growth: polycrystalline and single crystal samples .....	22
2.2.1 Polycrystalline sample synthesis.....	22
2.2.2 Single crystal growth .....	23
2.3 Magnetic physical property characterization .....	25
2.4 Structural and magnetic characterization: diffraction .....	27
2.4.1 Laboratory x-ray diffraction.....	27
2.4.2 Synchrotron X-ray powder diffraction and instrumentation.....	29
2.4.3 Neutron diffraction and instrumentation.....	32
2.4.4 Rietveld method .....	40
2.5 Synchrotron X-ray spectroscopy.....	43
<b>Chapter 3</b> CrIII doping – a cationic substitution YBaCuFeO <sub>5</sub> is not eager to admit..	49
3.1 Introduction.....	49

3.2 Sample synthesis .....	50
3.3 Laboratory x-ray diffraction.....	51
3.4 Magnetization .....	52
3.5 X-ray absorption spectroscopy .....	53
3.6 Synchrotron x-ray powder diffraction analysis.....	56
3.7 Summary and conclusions .....	60
<b>Chapter 4</b> Boosting spin-orbit coupling in Mn-doped YBaCuFeO <sub>5</sub> .....	63
4.1 Introduction.....	63
4.2 Sample synthesis .....	65
Part I: Samples prepared by a cooling rate of 300 K/h .....	69
4.3 Phase composition and structural evolution .....	69
4.3.1 X-ray phase analysis .....	69
4.3.2 Structural evolution.....	72
4.4 Neutron powder diffraction analysis.....	78
4.4.1 Magnetic transitions.....	78
4.4.2 Temperature dependence.....	81
4.4.3 Easy axis and magnetic plane inclination .....	85
Part II: Samples prepared with different cooling methods or atmosphere.....	93
4.5 Magnetization measurement .....	93
4.6 X-ray absorption spectroscopy .....	94
4.7 Neutron powder diffraction analysis.....	101
4.7.1 Oxygen stoichiometry determination.....	101
4.7.2 Structural characterization .....	105
4.7.3 Temperature dependence.....	107
4.8 Summary and conclusions .....	114
<b>Chapter 5</b> New strategy to rise the spiral temperature in YBaCuFeO <sub>5</sub> by Cu/Co substitution.....	117
5.1 Introduction.....	117

5.2 Sample synthesis and basic characterization .....	120
5.3 X-ray absorption spectroscopy .....	123
5.4 Synchrotron x-ray powder diffraction.....	125
5.5 Neutron powder diffraction.....	131
5.5.1 Temperature dependence: new insight on the phase evolution.....	132
5.5.2 Magnetic phase diagrams: huge increase of $T_s$ by Co substitution ..	141
5.5.3 Impact of Co doping on the easy axis and magnetic anisotropy.....	146
5.6 Summary and conclusions .....	156
<b>Chapter 6</b> Characteristics of the spiral magnetic phase in Mg-doped YBaCuFeO <sub>5</sub> .	161
6.1 Introduction.....	161
6.2 Sample synthesis.....	163
6.2.1 Laboratory x-ray characterization.....	164
6.2.2 Magnetic characterization.....	165
6.3 Synchrotron x-ray powder diffraction.....	167
6.4 Neutron powder diffraction.....	176
6.4.1 Temperature dependence: largest $q_0$ and quality spiral phase observed for a quenched sample .....	177
6.4.2 Magnetic phase diagrams: influence of Mg and the chemical disorder .....	183
6.4.3 Influence of Mg doping on the easy axis and inclination of the magnetic spiral plane .....	186
6.5 Summary and conclusions .....	191
<b>Chapter 7</b> Fabrication and characterization of the single crystal YBaCuFe <sub>0.95</sub> Mn <sub>0.05</sub> O <sub>5</sub> .....	195
7.1 Introduction.....	195
7.2 Growth of the Mn-doped YBCFO single crystal by the TSFZ method.....	197
7.2.1 Rod preparation.....	197
7.2.2 Single crystal growth .....	198

7.3 Characterization and discussion.....	199
7.3.1 Structural characterization .....	199
7.3.2 Magnetic characterization and neutron magnetic diffraction .....	204
7.4 Summary and conclusions .....	214
<b>Chapter 8</b> Conclusions and outlook.....	217
8.1 Conclusions.....	217
8.2 Outlook and future work.....	220
<b>Publications</b> .....	223
<b>Bibliography</b> .....	225

## List of acronyms

AFM	Antiferromagnetic
CM	Commensurate
DAS	Data acquisition system
DC	Direct current
DM	Dzyaloshinskii-Moriya
FC	Field cooling
FM	Ferromagnetic
FWHM	Full-width at half-maximum
FY	Fluorescence yield
FZ	Floating zone
GKA	Goodenough-Kanamori-Anderson
HRTEM	High resolution transmission electron microscopy
HS	High spin
ICDD	International Center for Diffraction Data
ICM	Incommensurate
ILL	Institute Laue-Langevin
J-T	Jahn-Teller
LN	Liquid nitrogen
MAD	Multi analyzer detection
ME	Magnetoelectric
MSPD	Material science and powder diffraction
NN	Nearest-neighbor
NPD	Neutron powder diffraction
Oe	Extra-oxygen (symbol)
PPMS	Physical Properties Measurement System

PSD	Position sensitive detector
RT	Room temperature
SDD	Si-drift diode
SG	Space group
SQUID	Superconducting Quantum Interference Device
SXRD	Synchrotron X-ray diffraction
SXRPD	Synchrotron X-ray powder diffraction
TEM	Transmission electron microscopy
TEY	Total-electron yield
TM	Transition metal
TSFZ	Traveling solvent floating zone
VSM	Vibrating Sample Magnetometer
XAS	X-ray absorption spectroscopy
XRD	X-ray diffraction
YBCFO	YBaCuFeO <sub>5</sub>

# Chapter 1

## Introduction and motivation: towards high- $T_S$ cycloidal multiferroics

### 1.1 A brief history of magnetoelectric materials

In the most general definition, the magnetoelectric (ME) effect denominates the coupling between the electric and the magnetic fields in matter. A systematic progression of contributions to the ME effect is obtained from the expansion of the free energy of a material, i.e.

$$F(\vec{E}, \vec{H}) = F_0 - P_i^S E_i - M_i^S H_i - \frac{1}{2} \epsilon_0 \epsilon_{ij} E_i E_j - \frac{1}{2} \mu_0 \mu_{ij} H_i H_j - \alpha_{ij} E_i H_j - \frac{1}{2} \beta_{ijk} E_i H_j H_k - \frac{1}{2} \gamma_{ijk} H_i E_j E_k - \dots \quad (1)$$

with  $\vec{E}$  and  $\vec{H}$  as the electric field and magnetic field, respectively. Differentiation leads to the polarization:

$$P_i(\vec{E}, \vec{H}) = -\frac{\partial F}{\partial E_i} \quad (2)$$

and to the magnetization:

$$M_i(\vec{E}, \vec{H}) = -\frac{\partial F}{\partial H_i} \quad (3)$$

where  $P_i^S$  and  $M_i^S$  denote the spontaneous polarization and magnetization, whereas  $\epsilon$  and  $\mu$  are the electric and magnetic susceptibilities. The tensor  $\alpha$  corresponds to the induction of polarization by a magnetic field or of magnetization by an electric field



which is designated as the ME effect. It is supplemented by a higher-order ME effect like those parametrized by the tensors  $\beta$  and  $\gamma$  [1].

There are two independent events that lead to the generation of the ME effect. First, in 1888 Röntgen discovered that a moving dielectric became magnetized when placed in an electric field, which was followed by the observation of the reverse effect—polarization of a moving dielectric in a magnetic field [2]. Second, in 1894, based on the lattice symmetry argument, Pierre Curie predicted the possibility of an intrinsic magnetoelectric effect in some crystals [3]. While the terminology “magnetoelectric effect” was defined by Debye in 1926 [4], the speculation remained inactive until 1960 when the first real magnetoelectric material  $\text{Cr}_2\text{O}_3$  was discovered [5], following Dzyaloshinskii’s generic prediction one year earlier [6].

In the whole twentieth century, studies on the ME physics and corresponding materials were slow. Reasons of this background were due to the lack of available ME materials, and the poor ME performance observed. In addition, the ME theories in early years were generally phenomenological, lacking the ingredients of the modern electronic theory based on quantum mechanics. An extensive research on the correlated electronic materials did not appear until the late 1980s [7], and the colossal magnetoresistive manganites in the 1990s [8], which paved a good foundation for the advanced ME research. In 1994, H. Schmid coined a new terminology in a proceeding publication: multiferroics, which denotes the coexistence of multiple ferroic orders in a single-phase material [9].

The long stagnation was finally folded up due to the two unexpected breakthroughs which were both discovered in 2003: the  $\text{BiFeO}_3$  thin films [10] and the orthorhombic  $\text{TbMnO}_3$  [11]. Although the strong magnetization of the reported  $\text{BiFeO}_3$  thin films was later found to be non-intrinsic [12], it was the first time that a single-phase ME material providing good multiferroic behavior with potential room temperature applications was obtained. The orthorhombic  $\text{TbMnO}_3$  displays only a weak polarization appearing only at low temperature ( $< 28$  K) [11]. Despite its poor performance regarding the

ferroelectric polarization and magnetism, it became a milestone due to the intrinsically strong ME coupling it offers. A few years later, another two interesting multiferroic materials were discovered: the orthorhombic  $\text{TbMn}_2\text{O}_5$  [13] and the hexagonal  $\text{HoMnO}_3$  [14], even these materials were reported either having a small polarization or presenting a low Néel (i.e. antiferromagnetic ordering) temperature. Since then, the interest on this exciting subject has enormously grown, with a huge number of novel materials and ME phenomena emerging. Many publications on the fundamental research and different multiferroic materials have promoted the progress of this discipline [15][16][17][18][19][20][21][22][23][24].

## 1.2 Why are multiferroics interesting?

Multiferroics, as firstly defined by H. Schmid in 1994 [9], are materials that exhibit more than one of the primary ferroic properties in a single phase. Schematically, we display below the main characteristics of four primary ferroic orders and their microscopic origins in Figure 1.1. These days the term is usually used to describe the ME multiferroic that are simultaneously ferromagnetic and ferroelectric [19] [20], as shown in the Figure 1.2. Sometimes the definition is expanded to cover a much broader spectrum of relevant materials and include non-primary order parameters, such as anti-ferromagnetism or ferrimagnetism.

Although the technological merits of ferromagnetism and ferroelectricity are quite different and mutually exclusive, attempts were made to combine them in the same phase of a material to enhance its functionalities. There are mainly two respects to explain why multiferroic materials are interesting: (i) The mutually control of ferromagnetic and ferroelectric state might prompt a flurry of novel functionalities for new generation ME devices. For example, the control of the magnetic properties by an electric field instead of a magnetic field is an advantage that multiferroic materials can provide, because the magnetic-field-generating electric current can be avoided, thus lead to energy-efficient, faster and smaller data-storage technologies; and (ii) the field

of multiferroics covers a broad variety of fundamental research areas, such as complex magnetism and ferroelectricity, oxide heterostructures and interfaces, spintronics and also seemingly remote subjects such as cosmology [25].

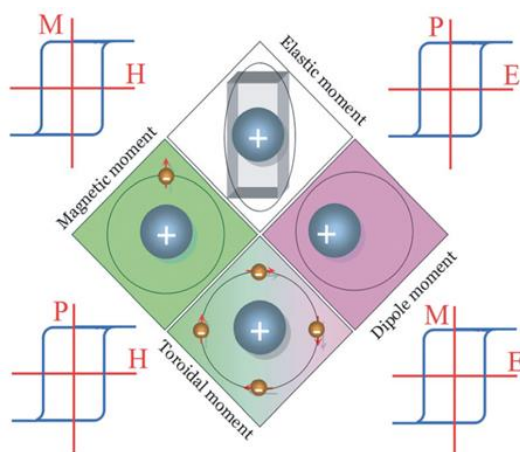


Figure 1.1. A schematic of four primary ferroic moments and their microscopic origins. In general, a magnetic moment, which breaks the time-reversal symmetry, originates from unpaired electrons and thus corresponding partially occupied orbitals (usually  $d$  or  $f$  orbitals); an electric dipole moment, which breaks the space-inversion symmetry, is a relative displacement of positive and negative charges; An elastic moment, which breaks neither the time-reversal symmetry nor the space-inversion symmetry, comes from lattice distortions. A toroidal moment, which breaks both the time-reversal and space-inversion symmetries, can be visualized as a toroidal arrangement of magnetic moments. Figure adapted from reference [19].

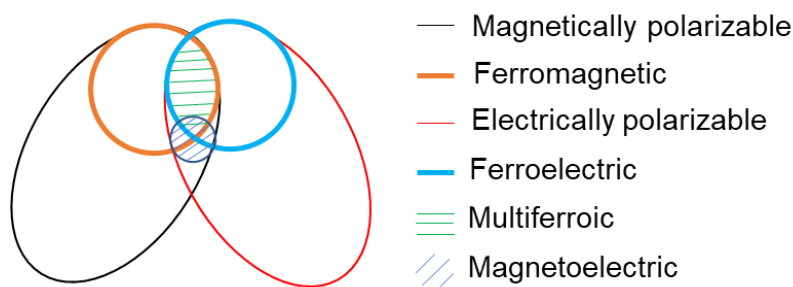


Figure 1.2. The relationship between multiferroic and ME materials. Ferromagnets (ferroelectrics) form a subset of magnetically (electrically) polarizable materials such as paramagnets and antiferromagnets (paraelectrics and antiferroelectrics). The intersection (green hatching) represents materials that are multiferroic.

### 1.3 Classification of multiferroics

In 2009, Khomskii released the issue of multiferroic classification. Regarding his

explanation, the multiferroics was classified into two categories [26], the type-I and type-II multiferroics. The type-II multiferroics would encompass all those magnetic ferroelectrics, where ferroelectricity gets induced by some specific magnetic orders, as evidenced in  $\text{TbMnO}_3$ . All the other multiferroics got classified as of type-I multiferroics, and in them ferroelectricity does not have magnetic origin, with  $\text{BiFeO}_3$  being an archetypical example.

Type-I and type-II multiferroics have their own advantages and disadvantages. The type-I multiferroics have an independent microscopic mechanism responsible for the magnetic and electric order [27][28][29]. As mentioned above, in  $\text{BiFeO}_3$  perovskite ( $\text{ABO}_3$ ) which has a highly polarizable electronic lone pair on Bi ion at the A site inducing ferroelectricity and a magnetic ion at the B site (Fe) responsible for the ferromagnetism. In addition, even this type of materials usually shows high magnetic and ferroelectric transition temperatures, and they exhibit relatively high electrical polarization, mutually exclusive mechanisms for multiferroicity indicate that the coupling of electric and magnetic orders is weak in type-I multiferroics.

On the other hand, in type-II multiferroics the ferroelectricity is induced by inner specific magnetic orders, their magnetic and ferroelectric transition temperatures are similar to each other. And this type of multiferroics displays significantly stronger coupling of the magnetic and electric order parameters than the type-I materials. However, the transition temperatures are low, normally below 100 K, and the induced polarization is poor. In the type-II multiferroic  $\text{TbMnO}_3$ , magnetic ordering appears at  $T_{N1} \approx 41$  K, at a lower temperature  $T_{N2} \approx 28$  K, the magnetic structure changes to the incommensurate and spontaneous polarization appears. The finite spontaneous polarization is observed to be  $P_c$  ( $P \parallel c$  axis)  $\approx 8 \times 10^{-4} \text{ C} \cdot \text{m}^{-2}$  at 10 K [26][30], rather small than the reported polarization of  $50 \sim 60 \mu\text{C} \cdot \text{cm}^{-2}$  in  $\text{BiFeO}_3$  thin film [31]. All these drawbacks have restricted the development and applications of type-II multiferroic.

## 1.4 Fundamental physics concepts

### 1.4.1 Magnetic order

In this section, we are providing a brief introduction on magnetic order, including its origin and different types.

Magnetism is a direct consequence of the quantum nature of materials based on the spins and Pauli's exclusion principle. The magnetic ordered state is the eigenvector of the Hamiltonian:

$$\mathcal{H} = \mathcal{H}_{Coulomb} + \mathcal{H}_{S-O} + \mathcal{H}_{CristalField} \quad (4)$$

where  $\mathcal{H}_{Coulomb}$  takes into account the Coulomb interaction between non-coupled electrons,  $\mathcal{H}_{S-O}$  refers to the spin-orbit interaction and  $\mathcal{H}_{CristalField}$  is the crystal-field interaction which introduces the effect of the crystalline structure in the magnetic order.

The total Hamiltonian,  $\mathcal{H}$ , can be simplified within the Heisenberg model, as a function of the spins as:

$$\mathcal{H} = -\sum_{ij} J_{ij} \mathbf{S}_i \cdot \mathbf{S}_j \quad (5)$$

where  $J_{ij}$  indicates the exchange constant between the two spins  $\mathbf{S}_i$  and  $\mathbf{S}_j$  (explicitly located at the atom positions):  $J_{ij} > 0$  refers to a ferromagnetic interaction which tends to align the two spins parallel;  $J_{ij} < 0$  indicates an antiferromagnetic interaction, which tends to align the two spins antiparallel. Below a certain temperature, those magnetic interactions may "freeze" the spins so that the materials become magnetically ordered.

The presence of unpaired electrons is one of the necessary conditions for the magnetic order in material. Whereas at high enough temperature the order will be destroyed by the thermal fluctuations. In the paramagnetic state the response of the randomly fluctuating magnetic moments to an external field, namely, the magnetic susceptibility  $\chi$ , follows the Curie-Weiss law:

$$\chi = \frac{C}{T - \Theta_P} \quad (6)$$

where  $C$  represents the Curie constant and  $\Theta_P$  is the paramagnetic temperature. The

latter is directly related to the exchange interactions.

Below we will give an oversimplified introduction on the main types of different magnetic orders and their principle features.

**Ferromagnetism:** The exchange interaction between neighboring spins is positive and, as a result, the magnetic moments have a parallel alignment below the Curie temperature,  $T_C$ . Therefore, there is spontaneous magnetization in the ordered state, even in the absence of any external magnetic field. The magnetic susceptibility diverges at  $T=T_C \sim \Theta_P$ , where the spontaneous magnetization emerges.

**Ferrimagnetism:** The exchange interaction is negative, and thus we find an antiparallel magnetic moments alignment. However, not all of them have the same magnitude. One possibility is that the material exhibits an antiparallel alignment of non-equivalent neighboring moments below  $T_C$ . The second one is that two different ferromagnetic sublattices interpenetrate each other in an antiparallel way, the different magnetic moments not cancelling each other, which results in a non-zero, net magnetization.

**Antiferromagnetism:** If the sublattices in a ferrimagnet have equal moments, the material is an antiferromagnet. Therefore, the total magnetization is canceled out and no spontaneous magnetization arises in the material when it is below the Néel temperature,  $T_N$ . The magnetic susceptibility has a maximum at  $T=T_N$ .

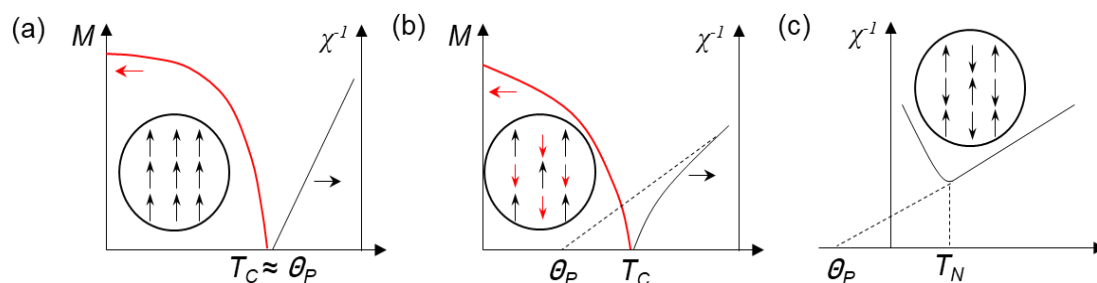


Figure 1.3. Schematic graphs showing the temperature dependence of magnetization  $M$ , and the inverse of magnetic susceptibility  $\chi^{-1}$ , for (a) ferromagnetism, (b) ferrimagnetism and (c) antiferromagnetism.

In addition to the three basic types of magnetic orders described above, there are many others such as amplitude modulated structures, proper-screw, cycloidal structures, conical structures...as we will show in section 1.4.3. Here we should point out the difference between the proper-screw and the cycloidal structures because they will be discussed along this Thesis. The main difference between them lies in the relation between the rotation plane of the spins and the direction of the propagation vector  $\mathbf{k}$ : in a cycloidal structure, the propagation vector  $\mathbf{k}$  is within the rotation plane, whereas in a screw structure they are perpendicular to each other. Because these exotic structures do not show any spontaneous magnetization and the magnetic susceptibility has a similar temperature dependence property, so materials with these structures are very often considered as antiferromagnets.

#### **1.4.2 Dzyaloshinskii-Moriya interaction**

After the discovery of the giant ME response in TbMnO<sub>3</sub> by Kimura and coworkers [11], the spin-driven ferroelectricity has become a central issue of the research field of correlated electron systems. Common to all the spin-driven ferroelectricity is the breaking of space inversion by magnetic order. From the microscopic of view, several types of origins were theoretically proposed and intensive experimental studies have confirmed that these mechanisms really induce the electric polarization. In 1958, Dzyaloshinskii proposed a thermodynamic theory to explain the weak ferromagnetism observed in Cr<sub>2</sub>O<sub>3</sub> [32]. This was the first time to postulate an asymmetrical exchange interaction which was subsequently elaborated as a consequence of the spin-orbit coupling by Moriya using quantum theory in 1960 [33]. It was later coined as the Dzyaloshinskii-Moriya (DM) interaction, as it is known today. The microscopic origin of this interaction is the relativistic correction to the exchanges in the presence of the spin-orbit coupling. The DM interaction plays a crucial role not only in the physics of multiferroics (mainly the so-called type-II multiferroics), but also in many subfields of magnetism.

The DM interaction is an antisymmetric, anisotropic exchange coupling between two spins on lattice bonds  $i$  and  $j$  with no inversion center [34]. For spins  $\mathbf{S}_i$  and  $\mathbf{S}_j$ , a new term in the Hamiltonian is then given by

$$H_{DM} = \mathbf{D}_{ij} \cdot (\mathbf{S}_i \times \mathbf{S}_j) \quad (7)$$

where  $\mathbf{D}_{ij}$  is the coefficient of the DM interaction between the two spins  $\mathbf{S}_i$  and  $\mathbf{S}_j$ . The effect of the DM interaction is often to offer a small canting of the spins in an antiferromagnetic structure, resulting in a non collinear order that produces weak ferromagnetism. An example are  $\text{R}_2\text{CuO}_4$  cuprates [35]. Generally, in DM weak ferromagnets the non-collinear order is not at the origin, but it is a consequence of the structural distortion.

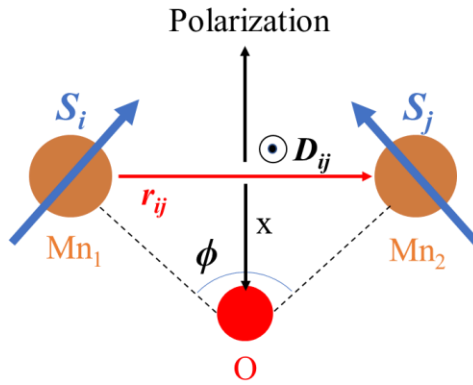


Figure 1.4. Electric polarization as induced by the displacement of the oxygen atoms due to the DM interaction. The direction of the DM vector coefficient  $\mathbf{D}_{ij}$  is perpendicular to the plane.

### 1.4.3 Spin-driven ferroelectricity

Various types of spin order can have a potential to break the inversion symmetry and produce a spontaneous polarization. This has been valid for both collinear and non-collinear forms of magnetic order, when they are arranged in some specific lattice geometry. Some types of non-collinear cases are illustrated in Figure 1.5. When the spins on the adjacent atomic sites are mutually canted, as Figure 1.4, the horizontal mirror-plane symmetry is lost, resulting in the possible generation of a polarization along the vertical direction [37][38][39][40]. Recently, it has also been shown



theoretically [37] that the overlap of the electron wave function between the two atomic sites with canted spins generates a genuine electric polarization via the spin-orbit interaction.

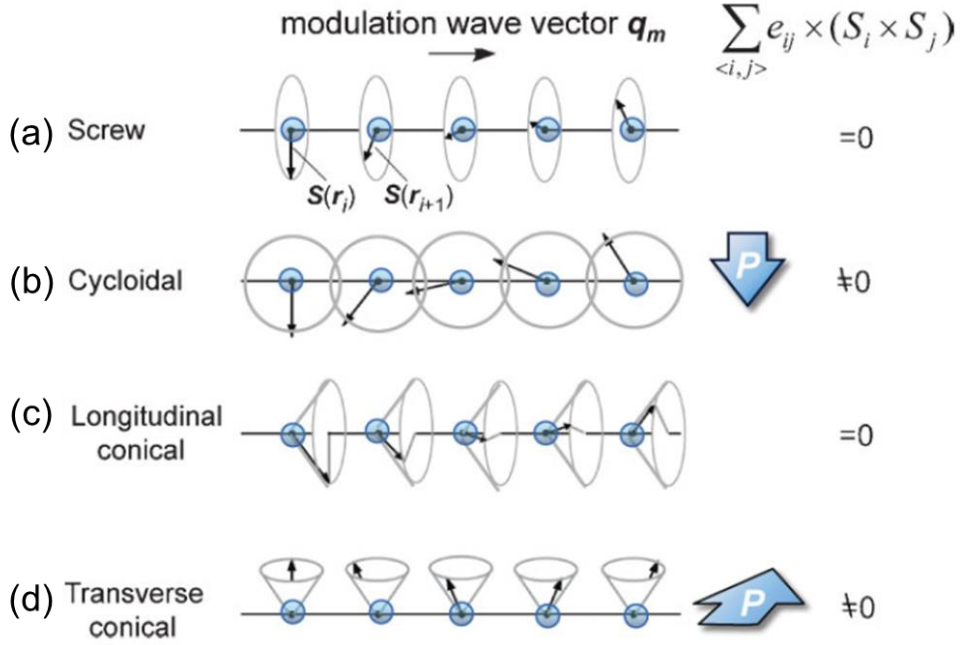


Figure 1.5. Schematic illustrations of types of spiral magnetic structures on (a) proper-screw, (b) cycloidal, (c) longitudinal-conical and (d) transverse-conical magnetic structure. Figure adapted from ref. [36].

When the spins form a transverse-spiral (cycloidal) modulation along a specific crystallographic direction [Figure 1.5(b)], every nearest-neighbor spin pair produces a unidirectional local polarization and hence the macroscopic polarization should be generated. The direction of the polarization can be expressed with equation (8):

$$\mathbf{P} = a \sum_{i,j} \mathbf{e}_{i,j} \times (\mathbf{S}_i \times \mathbf{S}_j) \quad (8)$$

Here,  $\mathbf{e}_{i,j}$  is the unit vector connecting the neighboring spins  $\mathbf{S}_i$  and  $\mathbf{S}_j$ , and  $a$  is a constant determined by the spin-orbit and spin-exchange interactions. The sign of  $P$  depends on a clock-wise or counter-clock-wise rotation of the spins propagating along the spiral axis. In this class of spiral-spin multiferroics governed by the DM mechanism, the spontaneous polarization can be easily controlled by an external magnetic field along a specific direction [30][41].

## 1.5 Introduction on YBaCuFeO<sub>5</sub>

So far, the discovery of materials with strongly coupled magnetic and ferroelectric orders has attracted a great deal of interest regarding the potential applications in the ME devices for information storage. As we have referred to previously, for many such type-II multiferroics, the spontaneous appearance of the electric polarization is associated to the onset of incommensurate (ICM) magnetic order [16][42][37]. As a result, this is often the signature of competing magnetic interactions and characterized by the low ordering temperatures (typically <100 K). The layered double perovskite YBaCuFeO<sub>5</sub> (YBCFO) with a structure AA'BB'O<sub>5</sub> is an exception to this phenomenon, since it displays a magnetism-driven ferroelectricity below an unexpectedly high temperature ( $T < T_{N2} \sim 230$  K) [21] and its characteristic magnetic spiral state can be stabilized within a long temperature range. This makes it one of the best candidates to switchable, magnetism-driven ferroelectricity at zero field and room temperature. This material was firstly synthesized in 1988 [43], but it has received much less attention because of the difficulties in fabricating it as a single-crystal or in thin film forms. Nowadays, the material has been extensively studied and its characteristics have been reported [44][45][46][47] by different groups over the world.

### 1.5.1 Crystal structure

The schematic representation of the layered crystal structure of the YBCFO perovskite is depicted in Figure 1.6. The A/A'-site is occupied by equal amounts of Y<sup>3+</sup> and Ba<sup>2+</sup> that order in planes perpendicular to the *c* axis due to their very different ionic radii [48]. The B/B'-site accommodates Fe<sup>3+</sup> and Cu<sup>2+</sup> ions. The basic structure of YBCFO can be described as [CuFeO<sub>9</sub>] bipyramids of corner-sharing Cu<sup>2+</sup>O<sub>5</sub> and Fe<sup>3+</sup>O<sub>5</sub> square pyramids. Y<sup>3+</sup> layers separate the [CuFeO<sub>9</sub>] bipyramids and accommodate the oxygen vacancies. Finally, the ordered array of Ba<sup>2+</sup> ions are located within the bilayer spacing. In addition, it has been confirmed that the material prefers to adopt the space

group (SG)  $P4mm$  with split Fe/Cu distribution within each square pyramid, which is able to give best reliability factors as compared with the SG  $P4/mmm$  [44]. Perfect Fe/Cu order in the bipyramids is a particular case of this scenario. The structure, therefore, is non-centrosymmetric and the mirror plane containing the  $Y^{3+}$  ions is lost.

In contrast to  $Y^{3+}$  and  $Ba^{2+}$  ions, due to the small difference of the  $Fe^{3+}$  and  $Cu^{2+}$  ionic radii (0.58 Å for  $Fe^{3+}$  and 0.65 Å for  $Cu^{2+}$ , both in V coordination) [48], the occupation of the Fe/Cu atoms in bipyramids (or the occupation of Fe/Cu in upper and lower pyramids in respect to a unit cell) is strongly dependent on the different preparation methods. As shown in the Figure 1.7, when the Cu/Fe chemical disorder is increased in YBCFO samples by adopting different cooling rates after the last annealing, the spiral ordering temperature increases by ~150 K up to 300 K [45]. The Fe/Cu occupation plays a significant role in respect to the magnetic frustration, magnetic interactions and the magnetic ordering temperatures, as we will discuss in the following chapters.

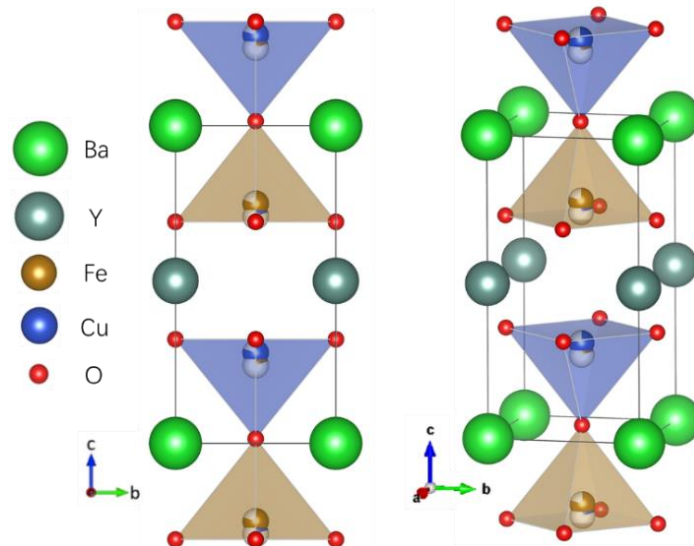


Figure 1.6. The crystal structure of  $YBaCuFeO_5$ . The color of the pyramids corresponds to the color of the dominant cation in it.

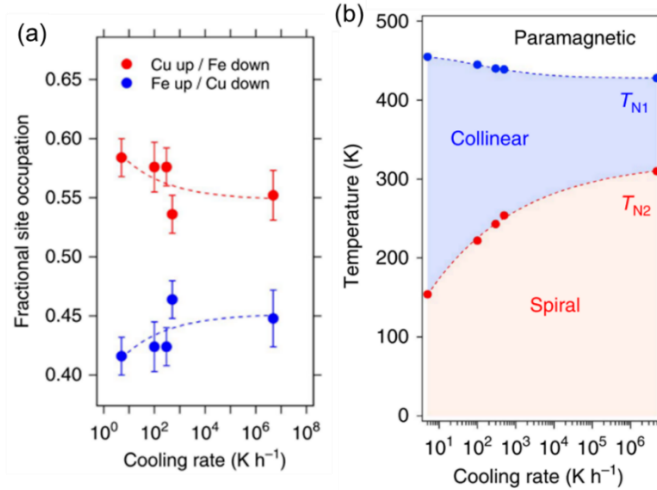


Figure 1.7. (a) Cu/Fe chemical occupation of the split B-sites in the pyramids for YBCFO samples obtained by adopting different cooling approaches after the last annealing. (b) Magnetic phase diagram showing the stability range of the collinear and spiral phases with the cooling rate. Dashed lines are guides for the eye. Figures adapted from reference [45].

## 1.5.2 Magnetic properties

**Neutron diffraction, spontaneous polarization and phase diagram:** Figure 1.8(a) shows the temperature dependent neutron powder diffraction (NPD) patterns of YBCFO around the main magnetic reflections  $(1/2 \ 1/2 \ 1/2)$  and  $(1/2 \ 1/2 \ 3/2)$ , as collected on the DMC diffractometer at the Swiss Neutron Source SINQ of the Paul Scherrer Institute (Villigen, Switzerland) with  $\lambda=2.45 \text{ \AA}$ . Upon cooling from 500 K two phase transitions are clearly observable and can be determined at the two onset temperatures  $T_{N1}$  ( $\sim 430 \text{ K}$ ) and  $T_{N2}$  ( $\sim 200 \text{ K}$ ). Have a look at the main magnetic reflection in the left, the new Bragg reflection below  $T_{N1}$  can be characterized by the propagation vector  $\mathbf{k}_1 = (1/2, 1/2, 1/2)$  and the satellites appear below  $T_{N2}$  can be indexed with the propagation vector  $\mathbf{k}_2 = (1/2, 1/2, 1/2 \pm q)$ .

The integrated intensities corresponding to the commensurate (CM) and ICM magnetic reflections as a function of temperature are plotted in Figure 1.8(b). As we can see, below  $T_{N2}$ , the CM magnetic reflection quickly weakens down to the background level. Instead, the ICM magnetic satellites start growing. At 1.5 K, the CM peak is still visible, but its intensity is much lower than that of the ICM satellites. A

similar behavior is observed for all the CM and ICM reflections [Fig. 1.8(a)]. It is worth noting that such behavior contrasts with previous works, where the ICM satellites were either absent or much less intense than the CM reflections at all temperatures [49]. This gets illustrated in Fig. 1.8(c), where the  $(1/2\ 1/2\ 1/2)$  CM magnetic reflection and the satellites around it as measured at 1.5 K are shown for one of our YBCFO samples (described in following chapters) and for a sample prepared using the method reported in reference [43].

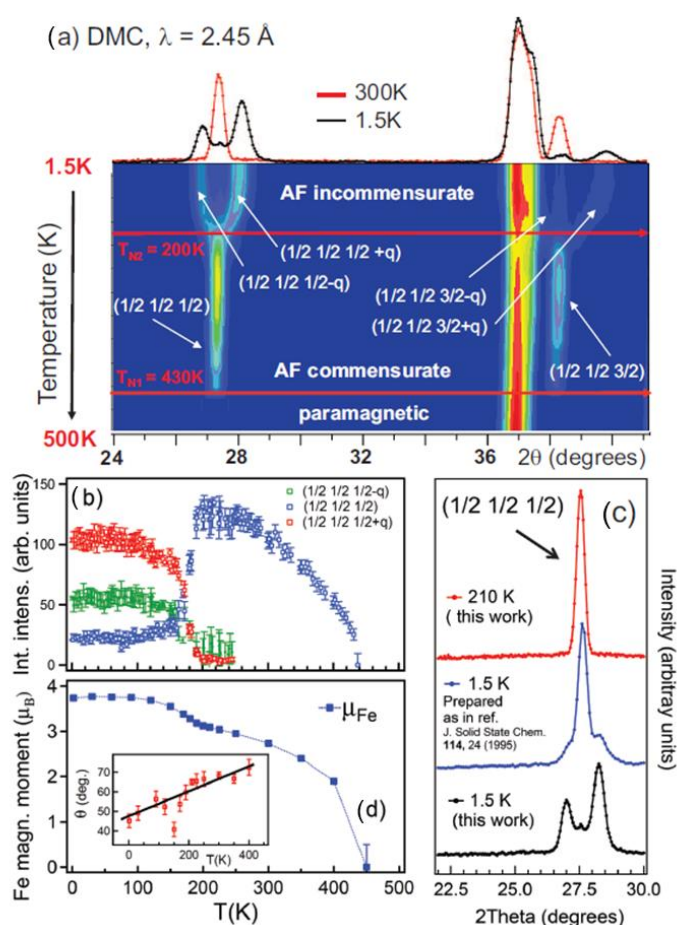


Figure 1.8. (a) Contour plot showing the temperature dependence of the NPD patterns for YBaCuFeO<sub>5</sub> measured in the diffractometer DMC ( $\lambda=2.45 \text{ \AA}$ ). The patterns collected at 300 K and 1.5 K are shown separately. (b) Temperature dependence of the integrated intensity of the magnetic reflections  $(1/2\ 1/2\ 1/2)$  and its incommensurate satellites  $(1/2\ 1/2\ 1/2\pm q)$ . (c) Portion of the NPD patterns showing these reflections for YBCFO sample (210 K and 1.5 K) and a sample prepared according to the reference [49]. (d) The evolution of the Fe<sup>3+</sup> magnetic moment as a function of temperature. Inset: angle  $\theta$  between the magnetic moment direction ( $T_{N1} < T < T_{N2}$ ) and the spiral plane ( $T < T_{N2}$ ) with the c axis. Figure adapted from reference [44].

The evolution of the Fe<sup>3+</sup> magnetic moment is shown in Fig. 1.8(d). Its value at 1.5 K is 3.74 (2)  $\mu_B$ , which is about 1/3 lower than expected for a free-ion, considering spin-only moments. Such reduction may be related to the Fe/Cu chemical disorder. The inset in the figure shows a decreasing evolution of  $\theta$  with lowering temperature, whereas we have confirmed in this Thesis (as shown in the following chapters) that the  $\theta$  value practically remains constant in the CM and ICM phases, respectively.

Below  $T_{N2}$ , the ICM modulation parameter  $q$  appears and increases continuously with decreasing temperature until nearly saturating at base temperature, as shown in Figure 1.9. As we can see, the onset of the ICM magnetic order coincides with a sharp anomaly in the – also shown – magnetic susceptibility and with the appearance of a net electric polarization  $P$ , indicating a direct relation between the two phenomena. In reference [38] the authors reported a  $P$  value of about 0.64  $\mu\text{C}/\text{cm}^2$ , close but larger than that found by Kundys *et al* ( $\sim 0.4 \mu\text{C}/\text{cm}^2$ ) [21].

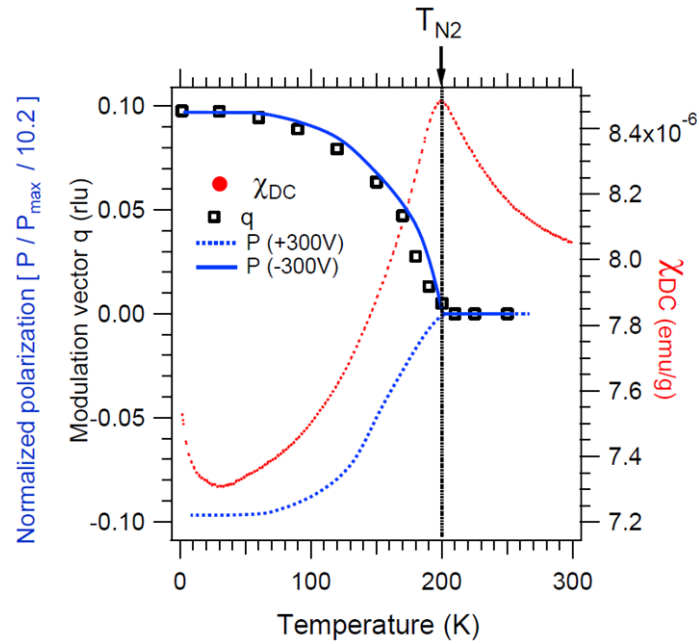


Figure 1.9. Red dots: DC magnetic susceptibility of YBCFO measured at 1T by heating after cooling in zero field. Black open squares: incommensurate modulation vector  $q$  (reciprocal lattice units). Blue dotted and continuous lines: normalized electric polarization measured by applying an electric field of  $\pm 300$  V. In order to use the same axis as  $q$ , the polarization values have been normalized to their saturation value (0.64  $\mu\text{C}/\text{cm}^2$ ) and further divided by a constant value of  $\sim 10.2$ . Figure adapted from reference [44].

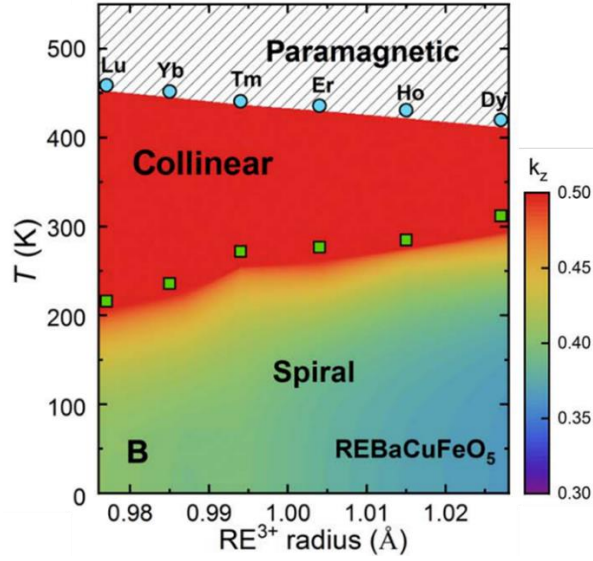


Figure 1.10. Magnetic phase diagram showing the evolution of  $T_{\text{collinear}}$  and  $T_{\text{spiral}}$  replacing the A-site  $\text{Y}^{3+}$  by rare-earth cation in the YBCFO compound. Figure adapted from reference [46].

A recent work carried out by T. Shang *et al* investigated the A-site substitution of  $\text{Y}^{3+}$  by different rare-earth cations for the YBCFO. The corresponding magnetic phase diagram showing the evolution of magnetic ordering temperatures for collinear and spiral phase for this family is demonstrated in the Figure 1.10. This phase diagram shows an increasing spiral ordering temperature as increasing the rare-earth radius, tuning this parameter from  $\sim 220$  K to  $\sim 310$  K, above room temperature. This is due to the progressive modification of the distance between the bipyramids layers using the rare-earths with increasing cationic size, resulting in an interior tuning of the magnetic frustration. For this thesis, the A-site cation has been fixed as  $\text{Y}^{3+}$ , this is because on one hand, the ionic size of this cation is very similar with  $\text{Dy}^{3+}$ , more importantly, the  $\text{Y}^{3+}$  is a non-magnetic ion, thus avoiding complicated magnetic interactions in the YBCFO system.

**Magnetic structures:** The magnetic structure of YBCFO in polycrystalline form was described by M. Morin, A. Scaramucci *et al.* using the representation analysis [44], demonstrated in the Figure 1.11. According to their analysis, two magnetic structures, with the best agreement to the neutron diffraction data, has been found for the magnetic moment arrangements compatible with the SG  $P4mm$ . For the CM phase ( $T_{\text{N}2} < T <$



$T_{N1}$ ), the best agreement corresponds to the collinear magnetic structure illustrating in Figure 1.11(a). In the **ab** plane, spins are antiferromagnetically (AFM) coupled, while the magnetic moment distribution along **c** alternates, in the unit cell, two spins across the Y layer and oxygen vacancies are antiferromagnetic (AFM) coupled, whereas it is a ferromagnetic (FM) coupling in the bipyramid units.

In case of the ICM phase ( $T < T_{N2}$ ), the magnetic moments would arrange in a circular spiral configuration, with the AFM coupling within the unit cell being preserved, but where the FM coupling inside the bipyramids gets lost, leading to the formation of a spiral structure with an incommensurability parameter  $q$  along **c**. This also indicates that the FM coupling in bipyramids is more sensitive to the external thermal changes as compared with the AFM coupling across the Y layers. The corresponding magnetic structure at low temperature is shown in Figure 1.11(b).

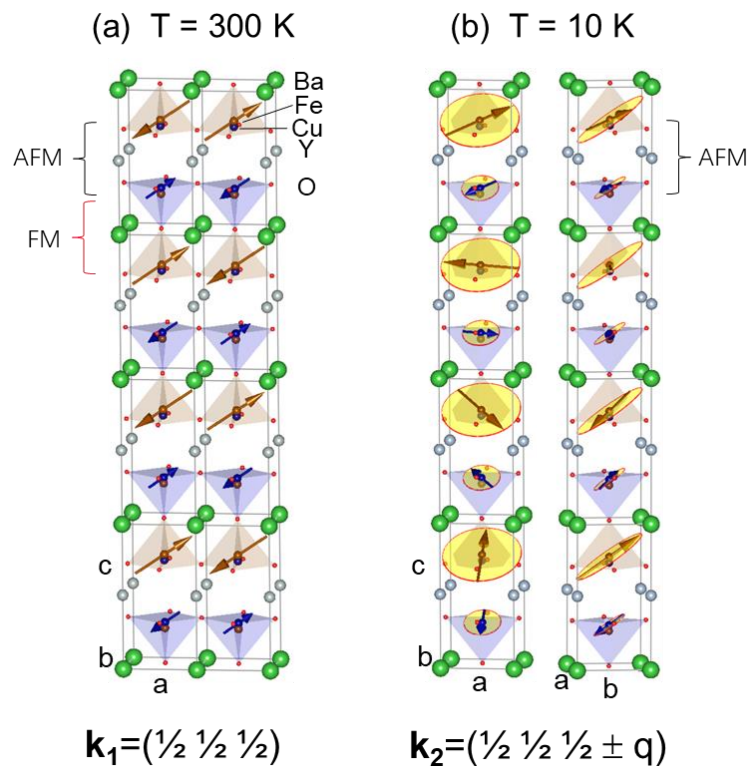


Figure 1.11. Magnetic structures of YBaCuFeO<sub>5</sub> correspond to the two magnetic phases. (a) Collinear magnetic structure at  $T = 300 \text{ K}$ . (b) Circular spiral magnetic structure at  $T = 10 \text{ K}$  in two views. The  $\mathbf{k}_1$  and  $\mathbf{k}_2$  are propagation vectors correspond to each phase. The color of pyramid is associated to the color of the dominant metal in it.



## 1.6 Scope and objectives

As we have described previously, in the crystal structure of the layered perovskite YBCFO, the two cations of  $Y^{3+}$  and  $Ba^{2+}$  are accommodated in A/A'-site, and they are ordered due to their very different ionic radii. Meanwhile, the B/B'-site occupying  $Fe^{3+}$  and  $Cu^{2+}$  cations feature a very particular kind of correlated disorder, leading to a preparation-dependent averaged Fe/Cu occupation of the atomic positions inside the bipyramids. In general, this thesis focuses on the sample preparation and characterization of the B/B'-site under chemical substitution of YBCFO, in polycrystalline and single-crystal forms. We have employed Cr, Mn and Co transition metals, and alkaline-earth Mg, with the aim of performing isovalent partial substitutions at the Fe and Cu sites. State-of-the-art characterization techniques such as the synchrotron x-ray diffraction (SXRD) and neutron diffraction were employed, which allowed a thorough and detailed fruitful investigation on all the synthesized samples.

The main objective of this thesis is to investigate the effect of chemical substitution over the magnetic properties of the layered perovskite YBCFO. This material can be viewed as a fascinating reference of a magnetic lattice without geometric frustration where competing nearest-neighbor (NN) interactions can stabilize a ferroelectric spiral phase up to high temperatures. The chemical substitution of magnetic and non-magnetic metals introduced in the crystal structure of YBCFO thus provides a possibility to upgrade the ME effect of this material, including the tunability of its spiral ordering temperature, the stabilization of the spiral phase and the potential ferroelectric response, by modifying the magnetic interactions and the generation of internal magnetic frustration. In addition, such a study also promotes the development of our knowledge on its fundamental physics, of particularly importance for a better understanding of the origin of multiferroicity and of the strongly correlated electron systems domain, in general.

Based on the above introduction, this Thesis work has been distributed in the following chapters: the chemical substitution of the trivalent Fe site by Cr and Mn is

presented in the Chapter 3 and Chapter 4; the chemical substitution of divalent Cu by Co and Mg is introduced in the Chapter 5 and Chapter 6; and the Chapter 7 gets dedicated to a 5%-Mn doped YBCFO single crystal.



# **Chapter 2**

## **Sample synthesis and experimental techniques**

### **2.1 Introduction**

This chapter provides a brief introduction and overview of the various experimental methods and techniques used to synthesize and characterize the samples presented in this work. A brief description of the main instruments used in the experimental characterization in different large facilities is also offered. On one hand, we introduce here in detail the preparation process of all the studied samples in different forms: polycrystalline and single crystal. Samples presented in this thesis were prepared in our group Crystallography of magnetic and electronic oxides and surfaces (CMEOS) at the Institut de Ciència de Materials de Barcelona (ICMAB-CSIC). On the other hand, for sample characterization, the conventional X-ray diffraction and magnetic macroscopic physical property measurements were carried out in the X-ray Diffraction Lab and Low Temperature and Magnetometry Service Lab, respectively, at the ICMAB. Synchrotron X-ray powder diffraction (SXRPD) experiments were performed on the BL04-MSPD beamline of the ALBA Synchrotron Light Facility using a MYTHEN position sensitive detector (PSD). In addition, all soft X-ray Absorption Spectroscopy

(XAS) measurements were performed also in ALBA on the BL29-BOREAS beamline. All the neutron diffraction measurements in powder and single crystal form were conducted at the Institute Laue-Langevin (ILL) in Grenoble, France. Depending on different purposes and sample forms, different instruments were utilized, including D1B, D2B and D20 for powder samples, D9, Orient Express and Cyclops for single crystal samples. Details of various corresponding methodologies will be also presented in this chapter.

## **2.2 Synthesis and growth: polycrystalline and single crystal samples**

### **2.2.1 Polycrystalline sample synthesis**

Most of the samples studied in this thesis were synthesized by solid-state reaction method. Solid-state reaction is the most conventional method to prepare perovskite-oxide materials. The synthesis is produced due to the ionic diffusion between reactants assisted by thermal energy. So, in general it is a slow process, and high temperatures and long annealing processes are required for this reaction method. Furthermore, another important parameter during the heat treatment is the use of appropriate atmospheres to control the oxygen content. In particular, the properties of some samples strongly depend on the oxygen content. For instance, in the annealing process an inert gas such as Argon can be used to preserve the oxidation state of elements and prevent oxidation to a higher oxidation state, and an oxygen atmosphere can be used to encourage the formation of high-oxidation states; on the contrary, a hydrogen atmosphere can be used to produce a low oxidation state [50].

In general, the process involves several procedures to achieve the final quality samples. Firstly, weighing and mixing the required high purity precursors according to the stoichiometric amounts; then grind and press the initial mixture powder into pellets form; finally anneal the pellets in a tubular furnace with specific warm up and cooling rates and dwell temperature. In order to achieve homogenous single-phase materials,

intermediate grindings and annealing processes could be applied until quality samples are obtained. The specific procedures and annealing processes followed for particular compositions of different samples will be presented in the corresponding chapters.

The main procedures for polycrystalline sample preparation are presented below as a flow chart.

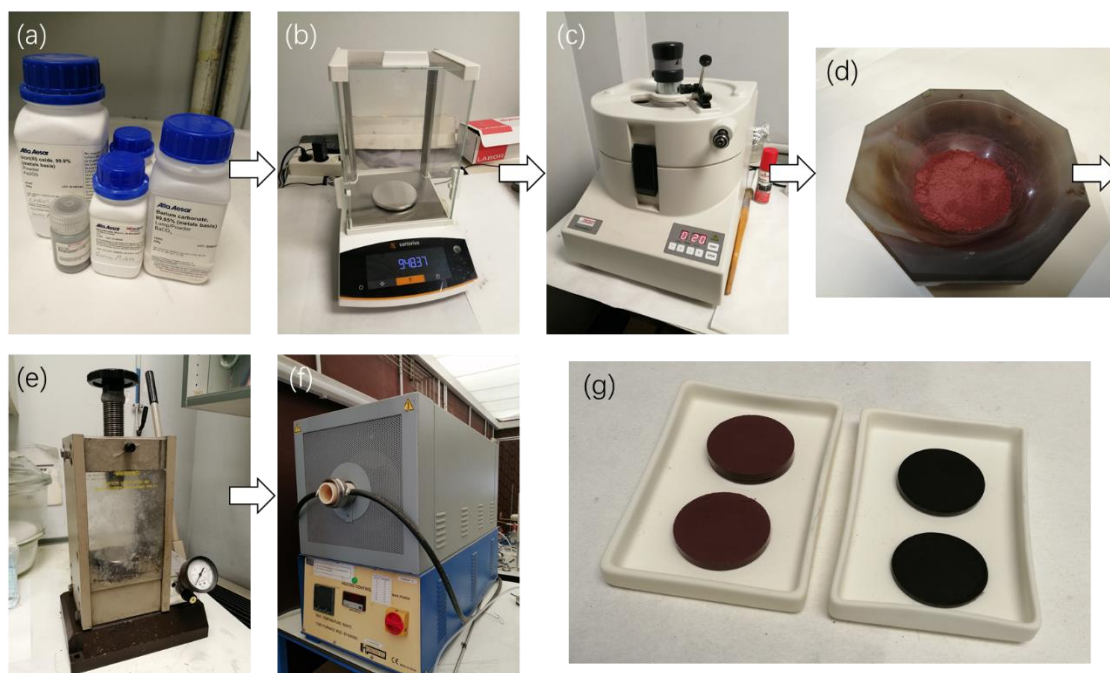


Figure 2.1. Sequential procedures showing the solid-state reaction method. The selected precursors are weighed, mixed, grinded, pelleted and eventually sintered in a tubular furnace. Figure (g) shows the pressed pellets before (left) and after annealing (black).

### 2.2.2 Single crystal growth

The crystals studied in this thesis have been grown using a Four-Mirror Optical Floating Zone Furnace (model: FZ-T-P1200\_H-I-S-PC from Crystal System Corporation) at the Single Crystal Growth Lab of the CMEOS group in ICMAB-CSIC. The idea of the optical floating zone (FZ) is presented in Figure 2.2. Two ceramic rods are mounted in such a way that their tips meet at the focal point of the ellipsoidal mirrors. Halogen lamps of appropriate power sit at the other focal points of these mirrors. Any crystal growth process performed by the optical FZ starts by melting the tips of

polycrystalline rods, bringing them together and establishing a liquid in the so-called FZ (movable area irradiated by the light) initially between the bottom (seed) rod and a top (feed) rod. After the melting zone is created the mirrors start moving upwards, the liquid zone cools and the material eventually crystallizes on the seed rod. During growth the rods rotate in opposite directions with experimentally established rates. The rate of rotation is important as it is responsible for mixing of material, for the shape of the crystallization front (solid-liquid interface), and for the defects resulting from it [51][52].

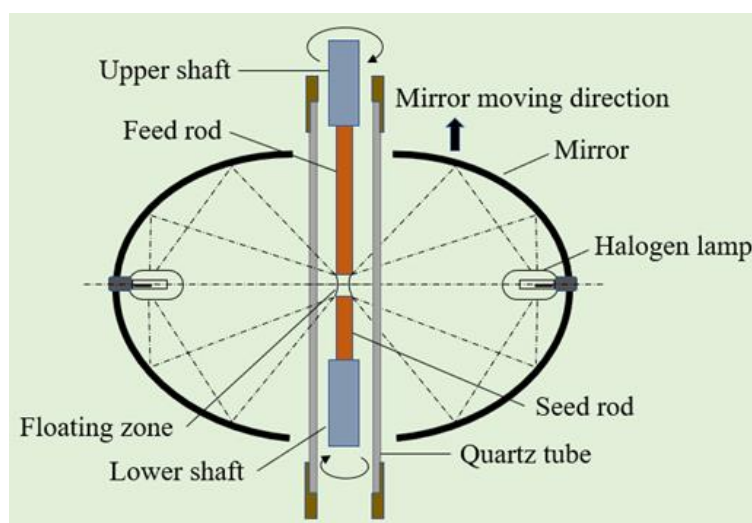


Figure 2.2. Schematic configuration of the mirror optical floating zone furnace.

The lines illustrated above is a normal procedure to grow a single crystal, actually in our case, to grow an incongruent material, a modified traveling solvent floating zone (TSFZ) technique [53][54][55] was used. Initially we prepared polycrystalline samples in the form of cylindrical bars with a size of 5 mm in diameter and 100 mm in length (see Figure 2.3) by solid-state reaction. In addition, a small chip-like solvent rod consists of CuO with 2 wt% B<sub>2</sub>O<sub>3</sub> was prepared also [53]. A cut piece of bar or another crystal can be used as the seed rod and the rest of the bar is used as the feed rod. The two bars should be mounted and aligned very well in order to stabilize the melted zone. Then the chip-like solvent rod should be put on the top of the seed rod. The FZ will be created by melting the solvent rod firstly. Additional details on the thermal treatment of

the cylindrical bars and other details about the growth method are given in Chapter 7. Eventually, we install a quartz tube to protect the set of bars from external environment and moreover, it allows to attain the required gas atmosphere and necessary gas pressure depending on crystal growth requirements.

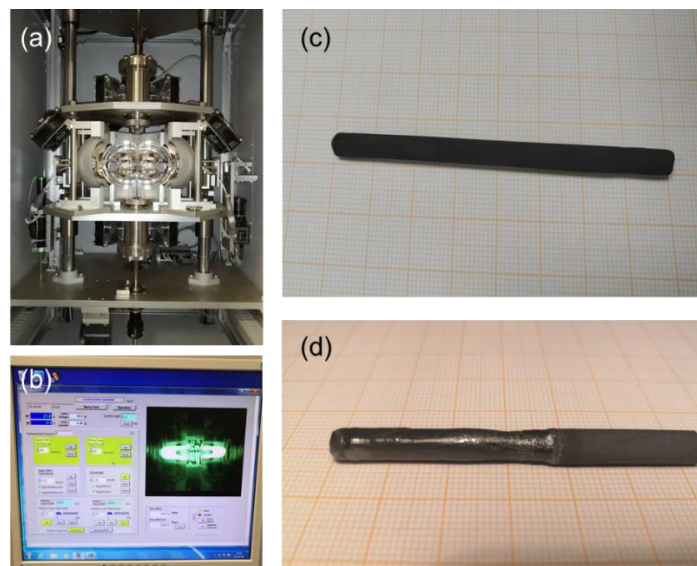


Figure 2.3. Pictures illustrating the growth of a single crystal using the modified traveling solvent floating zone (TSFZ) technique: (a) the four-mirror platform equipped with halogen lamps inside the furnace; (b) the computer controlling system during the growth process; (c) the polycrystalline sintered bar-shape sample used as feed rod or seed rod; (d) the as-grown single crystal sample, the background square grid side length is 1 cm.

### 2.3 Magnetic physical property characterization

The magnetic physical property characterization of bulk samples and single crystals studied in this work were carried out on the Superconducting Quantum Interference Device (SQUID, Quantum Design Inc) and the Vibrating Sample Magnetometer (VSM) in a Physical Properties Measurement System (PPMS, Quantum Design Inc). Both instruments belong to the Low Temperature and Magnetometry Service of the ICMAB, and the measurements were done with the support of the service technician.

The SQUID is a highly sensitive instrument nowadays used for magnetic measurements providing the magnetic susceptibility as a function of temperature or



magnetic field. The device is based on the Josephson effect [56] via a Josephson junction in which a current flow across two weakly coupled superconductors (set of coils), separated by a very thin insulating barrier. When a sample is placed inside the SQUID and moved along the vertical axis of the superconducting coils a current-voltage is created. This is a consequence of the changes associated to the magnetic flux which is proportional to the magnetic moment of the sample. Using a sensor, the magnetic flux can be directly determined from the output voltage.

The VSM-based magnetometers provide a fast and precise method for the determination of the direct current (DC) magnetization of a material. A specially built sample holder that contains a heater allows to extend the working temperature up to 1000 K. Thus, this device provides magnetic characterization of the samples above and below room temperature. It has a temperature range from 2 K to 300 K for normal measurements, and from 300 K to 1000 K an oven sample holder is used. In this technique, a magnetic sample is mounted on the sample holder and placed between the electromagnet poles, typically oriented horizontally. During measurement, the sample is subjected to a constant vibration vertically at a fixed frequency  $\omega$ . An emf is generated via Faraday's law of induction as the magnetized sample moves through the pickup coils. Signal processing using a lock-in amplifier enables high signal-to-noise ratios to be obtained [57][58].



Figure 2.4. The (a) SQUID and (b) PPMS magnetometer located at the Low Temperature and Magnetometry Service Lab in ICMAB.

## 2.4 Structural and magnetic characterization: diffraction

The polycrystalline samples were initially characterized by the X-ray diffraction (XRD) technique using a Siemens D-5000 diffractometer [ $\lambda$  (Cu  $K_\alpha$ )=1.541840 Å] located at the X-ray Diffraction Lab in ICMAB-CSIC. Furthermore, most of the diffraction measurements were carried out by means of synchrotron X-ray diffraction and neutron diffraction in large scientific facilities such as the ALBA Synchrotron Light Source in Spain and the ILL in Grenoble, France.

### 2.4.1 Laboratory x-ray diffraction

The polycrystalline powder XRD is a rapid analytical technique primarily used for phase identification of a material and can provide information on unit cell dimensions. In 1912, Max von Laue discovered that crystalline substances act as three-dimensional gratings for X-ray wavelengths similar to the spacing of planes in a crystal lattice [59]. X-ray diffraction is nowadays a common technique for the study of crystal structures and atomic spacing.

XRD is based on a constructive interference of diffracted X-ray waves by the crystalline lattice. These x-ray photons are generated by a cathode ray tube, filtered to produce monochromatic radiation, collimated to concentrate, and directed toward the sample. The interaction of the incident x-rays with the sample produces constructive interference (and a diffracted x-ray photos) when conditions satisfy the Bragg's Law:

$$n\lambda=2d \sin \theta \quad (\text{Eq. 2.1})$$

where  $d$  is the spacing between the lattice planes ( $hkl$ ),  $\theta$  is the angle of the diffracted wave respect to the incident X-rays,  $n$  is the order of diffraction and  $\lambda$  is the wavelength of the incident X-ray beam.

This law relates the wavelength of electromagnetic radiation to the diffraction angle and the lattice spacing in a crystalline sample. These diffracted X-rays are then detected, processed and counted. By scanning the sample through a range of  $2\theta$  angles,

all possible diffraction directions of the lattice should be attained due to the random orientation of the powdered material. The conversion of the diffraction peaks to  $d$ -spacings allows the identification of the compound because each crystalline compound has a set of unique  $d$ -spacings. Typically, this is achieved by comparison of  $d$ -spacings with standard reference patterns which released by the International Center for Diffraction Data (ICDD) (<https://www.icdd.com/>).

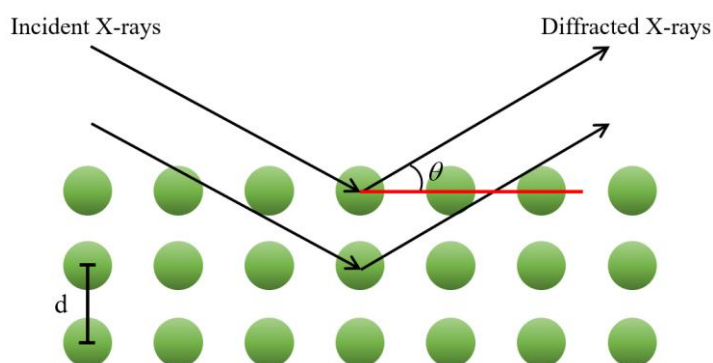


Figure 2.5. Schematic illustration of Bragg's law in X-ray diffraction. The layers of green dots form lattice planes,  $d$  being the spacing between them.

For theoretically understanding the scattering of X-rays with matter, we should recall some fundamental concepts and theories. The process essentially occurs by means of two modes: (i) some photons of the incident beam are deflected without a loss of energy, they constitute the Thomson scattering with exactly the same wavelength as the incident radiation; (ii) other photons are scattered with a small loss of energy, they constitute the Compton radiation with wavelengths slightly greater than that of the incident radiation. Both processes are simultaneously present and they are precisely described by modern quantum mechanics.

For a free material particle with electric charge  $e$  and mass  $m$ , when it interacts with incident beam, i.e. the X-rays, the beam will be scattered and the intensity of the scattered beam  $I_e$  in distance  $r$  is:

$$I_e = I_0 \left( \frac{e^2}{mc^2 r} \right)^2 \frac{1 + \cos^2 2\theta}{2} \quad (\text{Eq. 2.2})$$

where  $I_0$  is the intensity of the incident beam,  $c$  is the velocity of the electromagnetic

radiation ( $3 \times 10^5 \text{ km s}^{-1}$ ), and  $2\theta$  is the angle between the incident and scattered beams.

For a single atom, the electrons in it can be described as an electron cloud with a certain distribution. An atomic electron can be represented by its distribution function  $\rho(\mathbf{r}) = |\phi(\mathbf{r})|^2$ , where  $\phi(\mathbf{r})$  is the wave function which satisfies the Schrödinger equation. If each electron can be considered independent of the others, then the total distribution function of electrons is  $\rho_a(\mathbf{r}) = \sum_{j=1}^Z \rho_j(\mathbf{r})$ , where  $Z$  is the total electron number in atom. Then the Fourier transform of  $\rho_a(\mathbf{r})$  is called the atomic scattering factor which describes the ability of atoms to coherently scattering x-rays, which we here denote by  $f_a$ :

$$f_a(\mathbf{s}) = \sum_{j=1}^Z \int_v \rho_j(\mathbf{r}) e^{i2\pi\mathbf{s}\cdot\mathbf{r}} d\mathbf{r} \quad (\text{Eq. 2.3})$$

where  $\mathbf{s}$  is the scattering vector defined as  $\mathbf{s} = \lambda^{-1}(\mathbf{S}-\mathbf{S}_\theta)$ , i.e. as a function of the initial and final wave vector, respectively. The modulus of  $\mathbf{s}$  can be also defined as  $2\sin\theta/\lambda$ .

In a real crystalline structure constituted by a number of  $N$  atoms in the unit cell, the structure factor can be derived from (Eq. 2.3):

$$F(\mathbf{s}) = \sum_{j=1}^N f_j(\mathbf{s}) e^{i2\pi\mathbf{s}\cdot\mathbf{r}_j} \quad (\text{Eq. 2.4})$$

where  $f_j(\mathbf{s})$  is the atomic factor for the  $j^{\text{th}}$  atom in the unit cell,  $\mathbf{r}_j$  is the position ( $x_j, y_j, z_j$ ) of the atom  $j$ .

Finally, the diffracted intensity is described as:

$$I_N(\mathbf{s}) = |F(\mathbf{s})|^2 \quad (\text{Eq. 2.5})$$

### 2.4.2 Synchrotron X-ray powder diffraction and instrumentation

When a relativistic electron moves on a curved path at nearly the speed of light, it emits electromagnetic radiation. This radiation was theoretically predicated and studied by Lienard, Wiechert and Schott in around 1900, and this electromagnetic radiation has been called synchrotron radiation since around 1947 [60].

As a kind of circular particle accelerator, synchrotron can accelerate charged particles from low energy to high energy or keep the particles circulating on the circular

orbit at a constant energy for hours and days, which is referred to as storage ring. The electron storage ring is the core part of synchrotron light source. Relativistic electrons, circulating in the storage ring, generate synchrotron radiation when passing through three on-path major source components: the bending magnet, wiggler, and undulator magnets. This synchrotron radiation is extremely intense over a broad range of wavelengths from infrared through the visible and ultraviolet range, to the soft and hard X-ray part of the electromagnetic spectrum. Bending magnet radiation has broad spectrum and good photon flux; wiggler radiation provides higher photon energies and more photon flux; and undulator provides brighter radiation with smaller spot size and partial coherence.

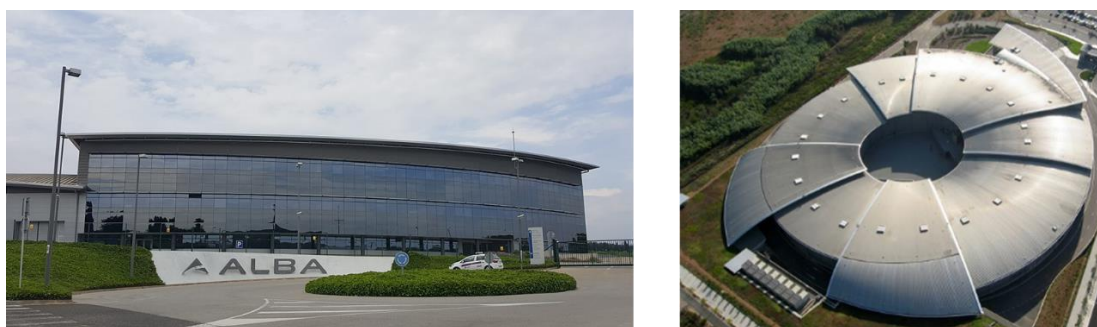


Figure 2.6. The ALBA Synchrotron Light Source Facility located in Barcelona, Spain.

The main characteristics that make distinctive the synchrotron radiation are [61]:

- (i) High brilliance: many orders of magnitude more than with conventional X-ray produced in X-ray tubes;
- (ii) Broad spectrum: the electromagnetic spectrum (white radiation) covers from radio-frequency to hard X-ray regions. Available to select the wavelength required for specific experiments;
- (iii) High level of polarized beam: the radiation emitted by the electrons is linearly polarized in the orbital plane of the electrons, but it is elliptical outside the orbital plane;
- (iv) High collimation: the photon beam is highly collimated due to small angular divergence;

- (v) Pulsed light emission: the pulse durations at or below one nanosecond, or a billionth of a second;
- (vi) High stability.

The SXRPD is a powerful technique for the structural characterization of materials due to the extraordinary features of synchrotron radiation. The exceptional properties of the synchrotron radiation applied to powder diffraction have major advantages over laboratory X-rays:

- (i) High photon wavelength resolution ( $\Delta\lambda/\lambda$  better than  $2 \times 10^{-4}$ );
- (ii) Very high signal/noise and signal/background ratios;
- (iii) Ultrafast data acquisition;
- (iv) Tunable photon energy to use very short wavelengths, which allows collecting data at very high  $Q$  and at the same time to reduce the absorption by heavy elements;
- (v) High angular (FWHM) resolution;
- (vi) Very high counting statistics in a few seconds.

As previously commented, a great part of the structural analysis of the samples in this thesis has been done using the synchrotron diffraction data that were collected in the ALBA Synchrotron Light Facility. Here we provide a brief introduction on the beamline.

**BL04\_MSPD:** The **M**aterials **S**cience and **P**owder **D**iffraction beamline BL04-MSPD is devoted to high angular resolution powder diffraction, high pressure powder diffraction using Diamond Anvil Cells and Micro powder Diffraction at high energy.

The beamline operates between 8 and 50 keV (wiggler). This range adequately covers the desirable energy for almost any kind of powder diffraction experiments in transmission geometry. The high energy part makes possible total scattering experiments and high-pressure diffraction using Diamond Anvil Cells. The easily tunable energy allows selecting the most adequate conditions for powder diffraction in transmission geometry: optimizing absorption and avoiding atomic absorption edges.

To accommodate the various experimental techniques, the BL04\_MSPD beamline has two experimental end stations, one devoted to high angular resolution powder diffraction and the second one dedicated to high pressure and micro diffraction experiments.

The Powder Diffraction end station consists of a heavy duty 3 circles diffractometer manufactured by Huber (Germany). The outer and middle circles support respectively the high angular resolution Multi Analyzer Detection (MAD) setup and the high-throughput Position Sensitive Detector (PSD) MYTHEN. The inner circle is equipped with an Eulerian Cradle (512.1 model from Huber) on which all sample environments are mounted. An ALBA-designed 4-capillaries holder can be used with either a cryostream or a hot blower [62].

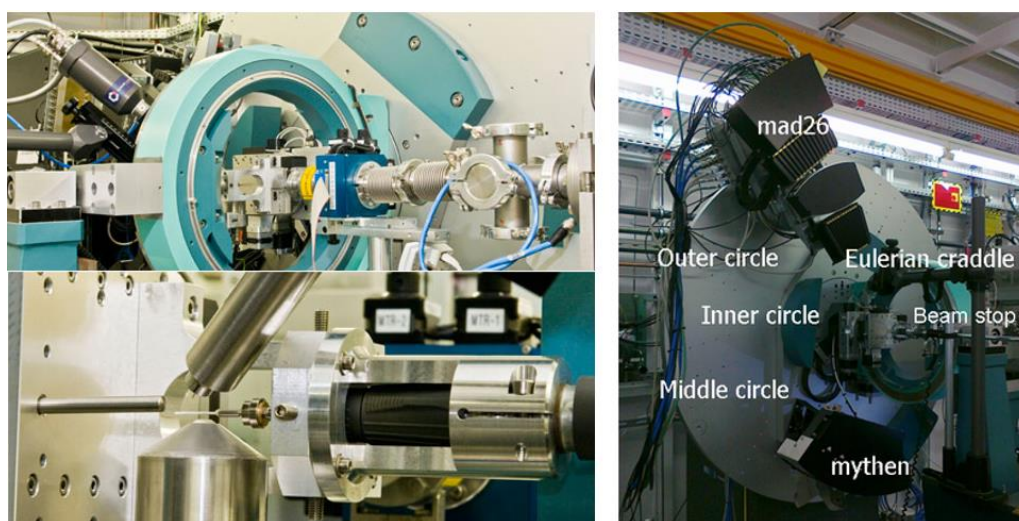


Figure 2.7. The beamline BL04\_MSPD powder diffraction endstation setup. Figures are adapted from the website of ALBA (<https://www.cells.es/en/beamlines/bl04-mspd>).

### 2.4.3 Neutron diffraction and instrumentation

Neutron diffraction is another key technique employed to characterize the materials investigated in this work. Diffraction is indeed the main interaction mechanism between neutrons and crystalline matter. However, unlike X-rays which primarily interact with the electron cloud surrounding atomic nucleus, the neutron-atom interaction comprises that with the nucleus and the interaction of the magnetic

momentum associated to the spin of the neutron with the magnetic momentum of the atom. This latter effect is most relevant in atoms with incompletely occupied outer electron shells (for instance, transition elements), and therefore it provides plenty of information on the magnetic properties of matter [63]. In fact, up to now, neutron diffraction is a unique tool to study magnetic structure, although some other techniques such as Resonant X-ray Magnetic Scattering provides details of these structures [64][65][66].

In the case of neutrons, it is proved that magnetic scattering is only sensitive to the perpendicular direction of the magnetic moment to the scattering vector [67]. So, for a magnetic phase  $F_h^2$  gets calculated using the general formula of Halpern and Johnson [68]:

$$F_h^2 = |\mathbf{F}_\perp(\mathbf{s})|^2 = |\mathbf{F}_m(\mathbf{s})|^2 - (\mathbf{e} \cdot \mathbf{F}_m(\mathbf{s}))^2 \quad (\text{Eq. 2.6})$$

where  $\mathbf{F}_m(\mathbf{s})$  is the magnetic structure factor,  $\mathbf{F}_\perp(\mathbf{s})$  is the projection of the magnetic structure factor along the perpendicular direction, and  $\mathbf{e}$  is the unit vector along the scattering vector  $\mathbf{s}$ . Here the scattering vector is written as  $\mathbf{s} = \mathbf{S} + \mathbf{k}$  where  $\mathbf{S}$  is a reciprocal lattice vector of the crystal structure and  $\mathbf{k}$  the propagation vector corresponding to the current magnetic reflection. The magnetic structure must have a distribution of magnetic moments that can be expanded as a Fourier series:

$$\mu_{l,j} = \sum_{\mathbf{k}} \mathbf{S}_{\mathbf{k},j} e^{-i2\pi\mathbf{k}\mathbf{R}_l} \quad (\text{Eq. 2.7})$$

In such a case the magnetic structure factor is given by:

$$F_m(\mathbf{s}) = p \sum_{j=1}^N f_j(\mathbf{s}) \mathbf{S}_{\mathbf{k},j} e^{i2\pi\mathbf{s}\mathbf{r}_j} \quad (\text{Eq. 2.8})$$

The sum is over all the atoms in the crystallographic cell. The constant  $p$  is 0.2695 and allows the conversion of the Fourier components of magnetic moments, given in Bohr magnetons  $\mu_B$  to scattering lengths units of  $10^{-12}\text{cm}$ .  $f_j(\mathbf{s})$  is the magnetic form factor and  $\mathbf{r}_j$  is the vector position of atom  $j$ , and  $\mathbf{S}_{\mathbf{k},j}$  is the Fourier component of the magnetic moment distribution.

The structural and magnetic properties of most of the compounds involved in this thesis were analyzed and characterized by neutron powder or single crystal diffraction



in the ILL in Grenoble, France. The instruments used in this work are briefly introduced in the following.

**D1B:** D1B (CRG) is a two-axis spectrometer dedicated to powder diffraction experiments requesting a high neutron flux. Highly demanded for real time experiments, and for very small samples because of its high efficiency PSD.

A great number of experiments performed on D1B concern the determination of magnetic structures. At small angles where magnetic peaks are expected, a high spatial resolution can be achieved, the FWHM reaches  $0.25^\circ$  at  $1.28 \text{ \AA}$  and  $0.3^\circ$  at  $2.52 \text{ \AA}$  (for a sample of 5 mm in diameter). D1B is equipped with a  $^3\text{He}/\text{CF}_4$  position sensitive detector composed of a system of multi electrodes with 1280 wires covering a  $2\theta$  range from  $0.8^\circ$  to  $128^\circ$ . Its specially designed cryostat is known for its low background crucial for some experiments with small intensity changes, the sample can be measured in the interval 1.5-300 K. A dedicated vanadium furnace achieving up to 1200 K is also available. A fast detection of phase transitions can be obtained by scanning temperature. A complete thermal variation of the diffraction patterns (1.5 - 300 K) can be achieved in few hours (3-5h).

**Table 2.1.** The characteristics of instrument D1B. Information available at the ILL website [69].

Monochromator		Detector	
Take-off angle $44.22^\circ$		3He multidetector containing 1280 cells	
Crystal	Pyrolytic graphite (002)	Angular range $2\theta$	$128^\circ$
Wavelength	$2.52 \text{ \AA}$	Radius of curvature	1.500m
Flux at sample/ $\text{n cm}^{-2}\text{s}^{-1}$	$7.9 \times 10^6$	Detector efficiency	86% at $\lambda=2.52 \text{ \AA}$

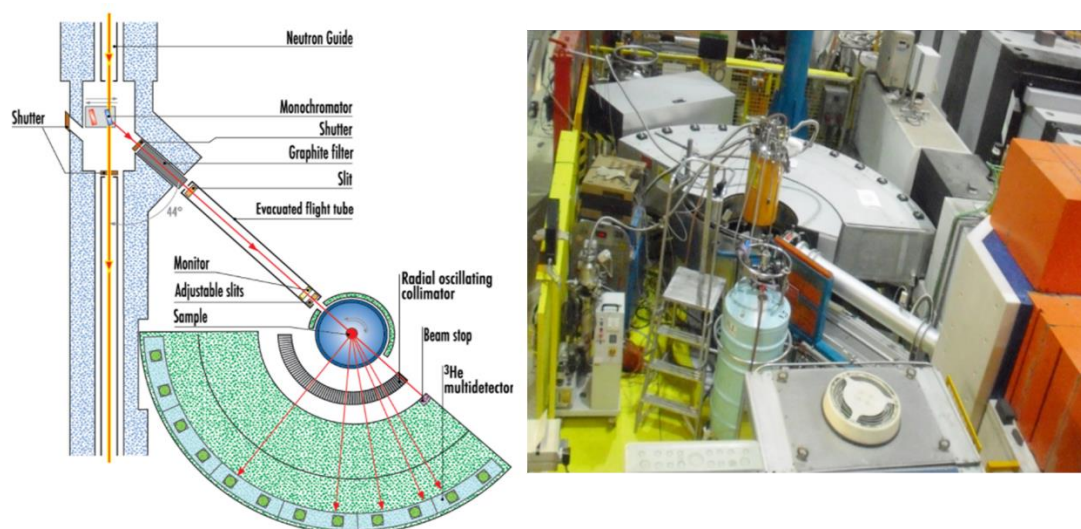


Figure 2.8. The D1B instrument layout and installation setup. Pictures are adapted from the website of Institut Laue Langevin [69].

**D20:** D20 is a very high intensity 2-axis diffractometer equipped with a large microstrip detector. Due to the extremely high neutron flux, it opens up new possibilities for real-time experiments on very small samples.

A pyrolytic graphite HOPG (002) monochromator in reflection position with fixed vertical focusing offers a wavelength of  $2.4 \text{ \AA}$  at a take-off angle of  $42^\circ$ . A variable vertical focusing Ge (113) monochromator gives increased resolution at higher take-off angles and several out of plane reflections are also accessible. The PSD housing of aluminium provides a detection zone about 4 m long by 0.15 m high. The major interests of the micro-strip detection system for the instrument D20 are the precise and perfectly stable geometry, resulting in a very homogeneous response and a very high stability, the possibility of achieving very high counting rates because of the small distance between the anode and cathode ( $170 \text{ }\mu\text{m}$ ), allowing a fast evacuation of the positive ions. The data acquisition system (DAS) has a parallel input for up to 1600 cells. The dead time between two successive diagrams is 160 ms in the conventional sequential data acquisition mode. This allows recording a series of short diagrams, typically a few seconds each, to observe irreversible kinetic phenomena.

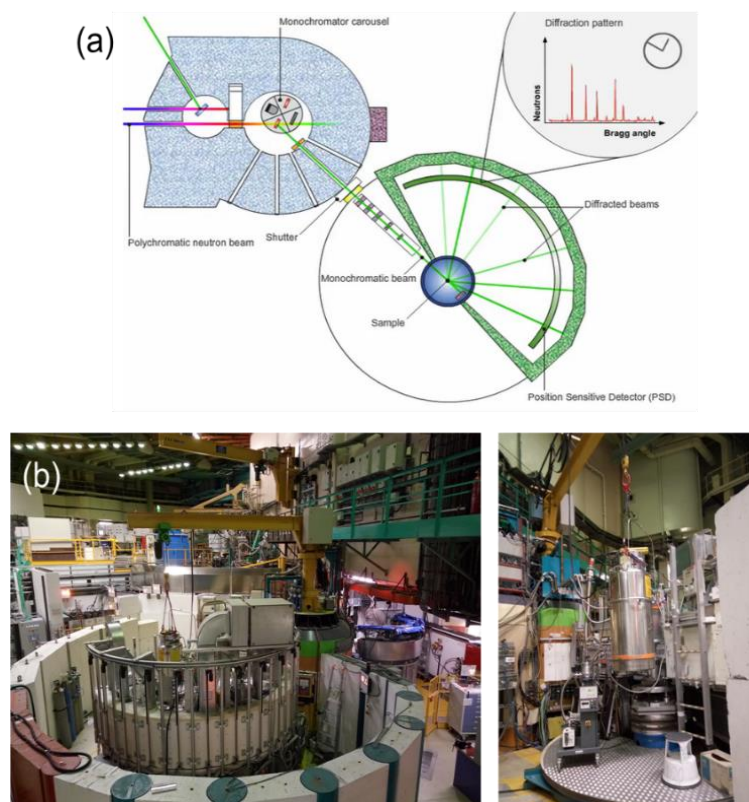


Figure 2.9. (a): The D20 instrument layout. The picture is taken from the website of the Institut Laue Langevin [69]; (b) The D20 diffractometer installation setup.

**D2B:** D2B is very high-resolution powder diffractometer designed to achieve the ultimate resolution, limited only by the powder particle size  $\Delta d/d \approx 5 \times 10^{-4}$ . It was built so that an alternative high flux option, but with much higher intensity, could be chosen at the touch of a button.

The diffractometer D2B is characterized by the very high take-off angle ( $135^\circ$ ) for the monochromator. A complete diffraction pattern is obtained after about 25 steps of  $0.05^\circ$  in  $2\theta$ , since the 128 detectors are spaced at  $1.25^\circ$  intervals. Such scans take typically 30 minutes and they are repeated to improve statistics. D2B was also designed for magnetism scientific cases in mind and to provide high resolution at very large d-spacings using wavelengths of between  $2.4 \text{ \AA}$  and  $6 \text{ \AA}$ . Wavelengths can easily be changed under computer control, since they are all obtained by a simple rotation within the  $\text{Ge}[hkl]$  plane. A large graphite filter can be switched in to provide a very clean beam at  $2.4 \text{ \AA}$ , and a cold Be-filter can be used for longer wavelengths.

**Table 2.2.** Characteristics of D2B instrument. Information available at the ILL website [69].

Monochromator		Sample environment	
Take-off angle	135°	cryostat	1.5 to 300 K
Germanium (hkl)	Wavelength $\lambda/\text{\AA}$	cryofurnace	1.5 to 525 K
557	1.051	furnace	200 to 1000 K
337	1.277	cryocooler	3.5 to 700 K
335	1.594 (optimum $\lambda$ )	Pressure cell	2 GPa and 4 to 300 K
Flux at sample $\lambda=1.594 \text{ \AA}$	$\text{\AA}10^6$ high resolution $\text{\AA}10^7$ high intensity	Dilution cryostat	50 to 4000 mk

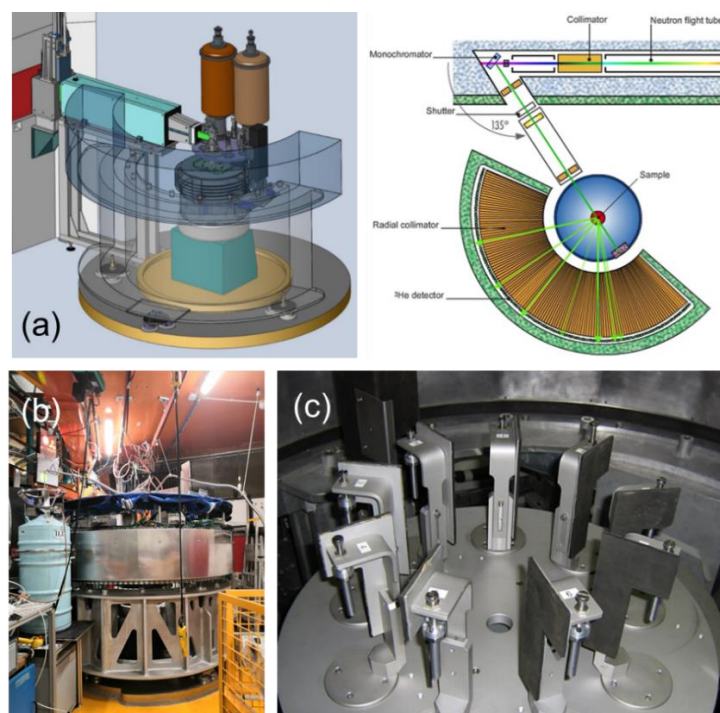


Figure 2.10. (a): The D2B instrument in visualization and top view layout. The pictures are taken from website of the Institut Laue Langevin [69]; (b) The D2B diffractometer installation setup; (c) the automated sample changer platform.

**D9:** D9 is a hot neutron Four-circle diffractometer, it is used for precise and accurate measurements of Bragg intensities up to very high momentum transfer. Its resolution allows routinely recording of extended data sets for the detailed study of atomic disorder and atomic thermal motions. The wavelength of neutrons is among the

shortest available at any reactor in the world. Therefore, the diffractometer is used in many research areas, the general applications being structural phase transitions, magnetic structures, atomic anharmonicity, hydrogen bonding and electron density studies, etc. and fundamentals in diffraction such as extinction effects, tests of the dynamical theory, resonant scattering and thermal diffuse scattering.

This instrument is placed on a Tanzboden floor allowing a continuous choice of wavelengths in the range 0.35-0.85 Å. In its standard “four-circle” geometry the sample holder sits on an Eulerian cradle with offset  $\chi$ -circle. A recent development also allows measurement in “normal beam” mode (lifting-counter geometry) (i.e. measurement with cryomagnet, orange cryostat, etc.). D9 is equipped with a small 2-D area detector which is particularly useful for rapid alignment and characterization of samples and for studies of satellites and twinning. It covers  $8 \times 8^\circ$  in  $32 \times 32$  pixels. Programs are available for intensity integration using this detector. Measurement of one Bragg reflection normally takes a few minutes, and recording of a full set of data takes a few days. If the crystal is studied as a function of temperature, pressure etc., the total measurement time is about a week.

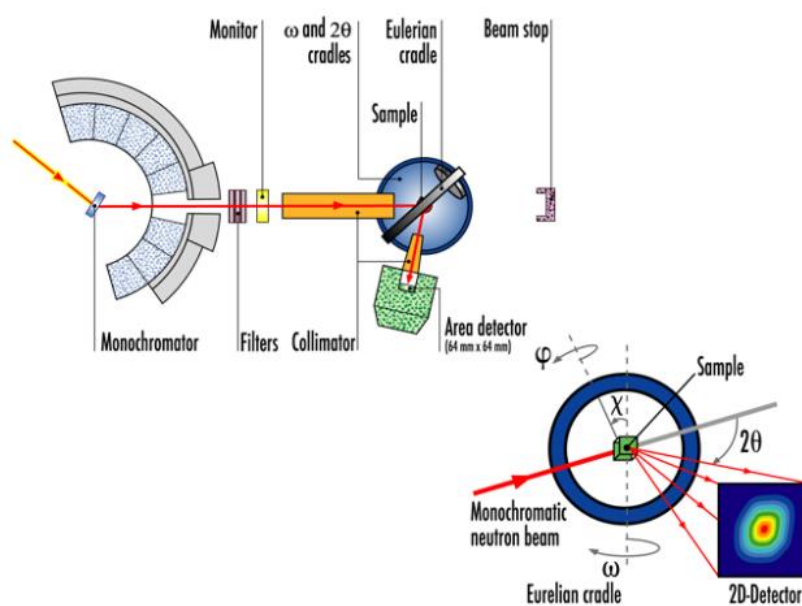


Figure 2.11. The D9 instrument layout and a schematic showing the four-circle geometry configuration. Figure adapted from ILL website [69].



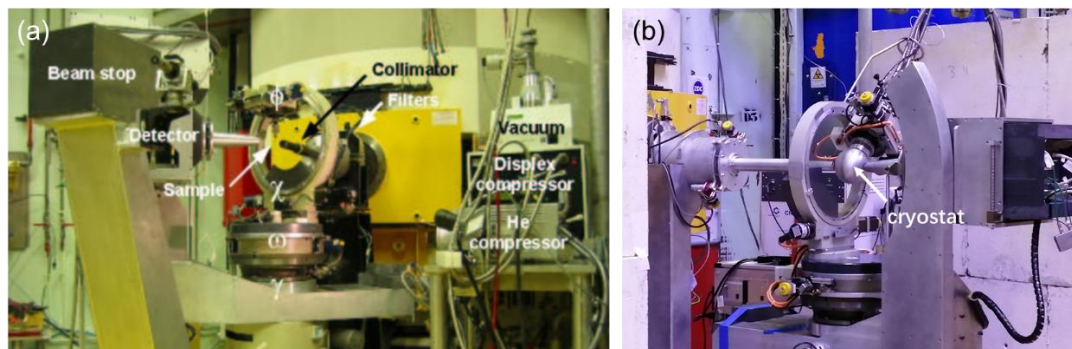


Figure 2.12. (a) D9 instrument with a standard sample holder mounted, and the main components are labeled; (b) another view of the D9 instrument, here integrating a cryostat.

The D9 monochromator is a Cu (220) single crystal working in transmission. It is surrounded by a lead protection ( $\gamma$ -radiation shield). The main polychromatic beam enters this shielding and strikes the monochromator. Non-diffracted neutrons are stopped by a combination of LiF absorber and polyethylene, placed after the monochromator. The take-off position with respect to the monochromator produces the different wavelengths.

**Table 2.3.** Some key specifications of D9 instrument. Information available at the ILL website [69].

Monochromator	Cu(2 2 0) in transmission geometry
Accessible wavelengths	0.3-0.9 Å ( $\lambda/2$ filters available)
Four-circle angle ranges	$5 < 2\theta < 120^\circ$ , $-34 < \omega < 48^\circ$ , $80 < \chi < 200^\circ$ , $-179 < \phi < 179^\circ$
Lifting counter angle range	$-12.5 < \nu < 25^\circ$
Detector resolution	$32 \times 32$ pixels
Detector pixel size	$2 \times 2$ mm <sup>2</sup>
Detector area	64mm <sup>2</sup>
Hot source-monochromator distance	10m (partly in vacuum)
Monochromator-sample distance	2.29m
Sample-detector distance	49cm
Visible size of hot source	15cm vertical, 5cm horizontal

### 2.4.4 Rietveld method

The Rietveld method is a technique described by Hugo Rietveld for use in the characterization of crystalline materials. This method was first implemented in 1967 [70] and reported in 1969 [71]. The X-ray and neutron diffraction of powder samples results in a pattern characterized by reflections (peaks in intensity) at certain positions. The Rietveld method uses a least squares approach to refine a theoretical profile until it matches the measured patterns. The introduction of this technique meant a significant step forward in the diffraction analysis of powder samples. Nowadays it is the most common procedure for neutron and X-rays powder diffraction data analysis. In this work, all diffraction data have been analyzed on the basis of the Rietveld method as implemented in the Fullprof suite program.

A powder diffraction pattern can be recorded in numerical form for a discrete set of scattering angles, times of flight or energies. We will refer to this scattering variable as  $T$ . Then, the experimental X-ray or neutron powder diffraction pattern is usually given as two arrays  $\{T_i, y_i\}_{i=1, \dots, n}$ . The profile can be modelled using the calculated counts  $y_{ci}$  at the  $i$ th step by summing the contribution from neighboring Bragg reflections plus the background:

$$y_{ci} = \sum_{\phi} S_{\phi} \sum_{\mathbf{h}} I_{\phi, \mathbf{h}} \Omega(T_i - T_{\phi, \mathbf{h}}) + b_i \quad (\text{Eq. 2.2})$$

The vector  $\mathbf{h}$  labels the Bragg reflections, the subscript  $\phi$  labels the phase and vary from 1 up to the number of phases existing in the model. In Fullprof the term phase means a same procedure for calculating the integrated intensities  $I_{\phi, \mathbf{h}}$ . This contains the usual meaning of a phase and the case of the magnetic contribution to scattering, which is treated as a different phase, coming from a single crystallographic phase in the sample. The general expression of the integrated intensity is:

$$I_{\phi, \mathbf{h}} = \{LAPCF^2\}_{\phi, \mathbf{h}} \quad (\text{Eq. 2.3})$$

For simplicity we drop the  $\phi$  index. We will refer to the whole arrays  $\{y_i\}$  and  $\{y_{ci}\}$  as  $y_{obs}$  and  $y_{calc}$  respectively. The meaning of the different terms appearing in (Eq. 2.2)

and (Eq. 2.3) is the following:  $S_\phi$  is the scale factor of the phase  $\phi$ ;  $L_h$  contains the Lorentz, polarization and multiplicity factors;  $F_h$  is the structure factor;  $A_h$  is the absorption correction;  $P_h$  is the preferred orientation function;  $\Omega$  is the reflection profile function that models both instrumental and sample effects;  $C_h$  includes special corrections (non linearity, efficiencies, special absorption corrections, extinction, etc. ) and  $b_i$  is the background intensity.

The Rietveld method consists of refining a crystal or magnetic structure by minimizing the weighted squared difference between the observed  $\{y_i\}_{i=1,\dots,n}$  and the calculated pattern  $\{y_{ci}\}_{i=1,\dots,n}$ . The function minimized in the Rietveld method is:

$$\chi^2 = \sum_{i=1}^n w_i \{y_i - y_{ci}\}^2 \quad (\text{Eq. 2.4})$$

with  $w_i = 1/\sigma_i^2$ , is the weight for each  $i$  experimental point, being  $\sigma_i$  is the standard deviation of the profile intensity  $y_i$  and  $\sigma_i^2$  the variance of the “observation”  $y_i$  [72][73].

The main parameters used for a good refinement between the experimental and the calculated pattern in the software can be separated into two principal groups:

- (1) Structural parameters: scale factor, temperature factors, occupation number and atomic positions for each atom;
- (2) Profile parameters: cell parameters, asymmetry, preferred orientation, background and the full width at half maximum (FWHM).

The calculated model should refine the position, shape and intensity for each peak from the diffraction pattern. For that, the following parameters are used:

- (1) Peak position: the correct position of each Bragg reflection can be refined by the cell parameters of each crystalline phase present in the specimen and the zero-shift error in the goniometer;
- (2) Peak intensity: the intensity of the peaks depends on the selected structural model for each crystalline phase, thus on the atomic positions;
- (3) Peak shape: this can be a more complexed feature for a good refinement. The complexity in a good refinement not only depends on the sample, but also on the instrumental features (radiation source, geometry, monochromator, slits sizes, etc.).



Accordingly, there are different choices of analytical peak-shape functions to refine a given pattern. For  $x = T - Th$ , being  $H$  the full-width at half-maximum (FWHM), we have several options:

$$\text{Gaussian: } \Omega(x) = G(x) = a_G \exp(-b_G x^2) \quad (\text{Eq. 2.5})$$

where:

$$a_G = \frac{2}{H} \sqrt{\frac{\ln 2}{\pi}} \quad b_G = \frac{4 \ln 2}{H^2}$$

$$\text{Lorentzian: } \Omega(x) = L(x) = \frac{a_L}{1+b_L x^2} \quad (\text{Eq. 2.6})$$

where:

$$a_L = \frac{2}{\pi H} \quad b_L = \frac{4}{H^2}$$

$$\text{pseudo-Voigt (pV): } \Omega(x) = pV(x) = \eta L'(x) + (1 - \eta)G'(x) \quad 0 \leq \eta \leq 1 \quad (\text{Eq. 2.7})$$

The  $pV(x)$  function is a linear combination of a Lorentzian ( $L'$ ) and a Gaussian ( $G'$ ) of the same FWHM, and thus there are two parameters characterising the peak shape:  $pV(x) = pV(x, \eta, H)$ .

The FWHM is usually considered to vary with scattering angle according to:

$$H_G = (U \tan^2 \theta + V \tan \theta + W)^{1/2} \quad (\text{Eq. 2.8})$$

For the Gaussian component, according to:

$$H_G = X \tan \theta + Y / \cos \theta \quad (\text{Eq. 2.9})$$

For the Lorentzian component.  $U, V, W$  and  $X, Y$  are variable parameters in the profile refinement.

The quality of the agreement between observed and calculated profiles are measured by a set of nowadays-conventional factors [7]:

Profile factor:

$$R_p = 100 \frac{\sum_{i=1}^n |y_i - y_{ci}|}{\sum_{i=1}^n y_i} \quad (\text{Eq. 2.10})$$

Weighted Profile factor:

$$R_{wp} = 100 \left[ \frac{\sum_{i=1}^n w_i |y_i - y_{ci}|}{\sum_{i=1}^n w_i y_i^2} \right]^{1/2} \quad (\text{Eq. 2.11})$$

Expected Weighted Profile factor:

$$R_{exp} = 100 \left[ \frac{n-p}{\sum_i w_i y_i^2} \right]^{1/2} \quad (\text{Eq. 2.12})$$

where  $n$  is the total number of points in the pattern minus total number of excluded points,  $p$  is the number of refined parameters and  $n-p$  is the number of degrees of freedom.

Reduced chi-square:

$$\chi^2 = \left[ \frac{R_{wp}}{R_{exp}} \right]^2 \quad (\text{Eq. 2.13})$$

Bragg factor:

$$R_B = 100 \frac{\sum_h |F_{obs,k} - F_{cal,h}|}{\sum_h |F_{obs,h}|} \quad (\text{Eq. 2.14})$$

Goodness of fit indicator:

$$S = \frac{R_{wp}}{R_{exp}} \quad (\text{Eq. 2.15})$$

## 2.5 Synchrotron X-ray spectroscopy

X-ray absorption spectroscopy (XAS) is a powerful technique for the investigation of the local electronic and atomic structure of solids, liquids or gases under varying external conditions like temperature or mechanical pressure, among others. If an assembly of atoms is exposed to x-rays, it will absorb some of the incoming photons. At a certain energy, depending on the atomic species present, a sharp rise in the absorption will be observed. This sharp rise in absorption is called an absorption edge. The energy of absorption edges in the different elements determined by the binding energy of electrons in atomic core levels. Exactly at the edge, the photon energy is equal to the binding energy, or more precisely, the edge identifies electronic transitions from a localized orbital to a low-lying empty state [74]. Thus, XAS provides us with valuable information on the partial density of unoccupied states in the ground state of the atoms.

In addition to the x-ray diffraction, x-ray absorption is the other main processes occurring when x-rays interact with matter. The attenuation of a monochromatic x-ray beam of intensity  $I_0$  passing through a uniform layer of material in thickness  $x$  is ruled

by the Lambert-Beer Law:

$$I(\Omega) = I_0(\Omega) \cdot e^{-\mu(\Omega)x} \quad (\text{Eq. 2.16})$$

where  $I$  is the transmitted beam intensity,  $\Omega$  is the specific wavelength or energy of the x-ray photons, and  $\mu$  is the mass-dependent absorption coefficient which incorporates the combined effects of all photoelectric and scattering processes.

Actually, the derivation of the absorption coefficient is in principle a complicated quantum mechanistic problem, but a number of key approximations allow to simplify the expression. First of all, the one-electron approximation should be invoked, which means that we consider only one photoelectron to be excited by each incoming photon, the other electrons being merely spectators. Then the absorption coefficient is proportional to the photoabsorption cross-section  $\sigma(E)$ , which is given by the Fermi Golden Rule stating that the probability per unit time ( $\Gamma_{i,f}$ ) to excite an electron from an initial state  $\Phi_i$  to a final state  $\Phi_f$ , with an energy density  $\rho(E_f)$  is:

$$\sigma(E)\alpha\Gamma_{i,f} = \frac{2\pi}{h^2} |\langle \Phi_f | H_{int} | \Phi_i \rangle|^2 \rho(E_f)(E - E_f - E_i) \quad (\text{Eq. 2.17})$$

Where  $H_{int}$  denotes the interaction operator reflecting a time-dependent perturbation of the Hamiltonian of the atom [74].

After the beam has passed the monochromator, its intensity ( $I_0$ ) is measured in an ionization chamber or by using a thin metallic foil or grid for absorbing some of the photons. The x-ray photons interact with the sample of interest and the transmitted intensity across it is measured with a second ionization chamber or a photodiode. This is the transmission mode for measuring x-ray absorption. Transmission XAS experiments are the standard for hard x-rays. An important limitation of transmission detection arises from the requirement for a homogeneous sample. Variations in the thickness or pinholes are reasons for the so-called thickness effect that can significantly affect the spectral shape by introducing nonlinear responses. In general, the combination of the short attenuation length with the thickness effect makes transmission experiments unsuitable for x-ray absorption below 1 keV. For the soft x-ray range, other detection modes are most often used. These are, the total-electron yield

(TEY) and fluorescence yield (FY). Both these detection modes are related to the decay channels (fluorescence or Auger decay) that may fill the electronic vacancy or core-hole in the excited atom. In the case of the photons created in the fluorescent decay excludes any surface effect. On the other hand, in the TEY mode, all the electrons that emerge from the sample surface are detected, regardless of their energy. Unlike FY, the interaction of electrons with matter is much larger than that of x-rays, which implies that most of the electrons that escape from the surface are originated close to it (the range lays from 3 to 10 nm).

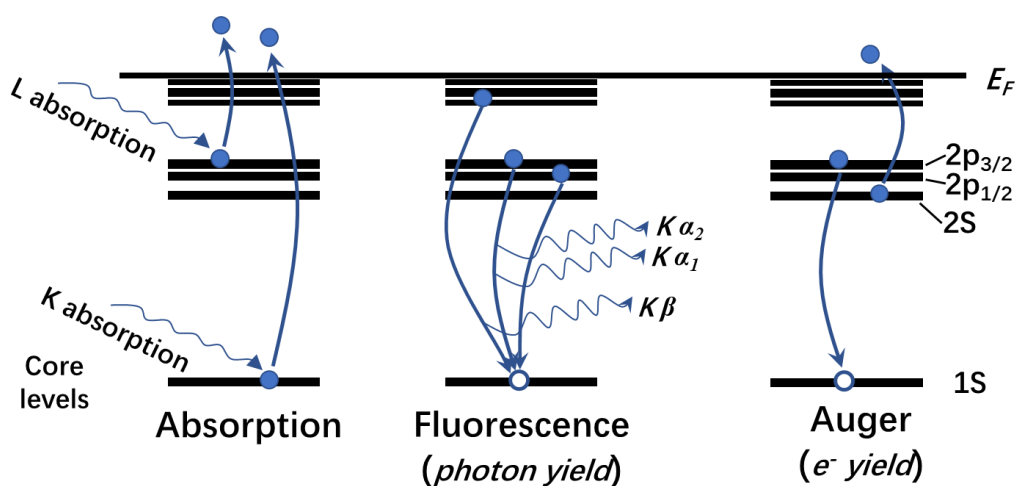


Figure 2.13. Schematic diagram of the absorption process and possible decay channels following it.

As commented previously, all XAS measurements presented in this work were performed in the BL<sub>29</sub>-BOREAS beamline at the ALBA Synchrotron Light Facility. In the following lines a brief introduction of this beamline is provided.

**BL<sub>29</sub>-BOREAS:** BL<sub>29</sub> is a soft X-ray beamline dedicated to polarization-dependent spectroscopic investigations of advanced materials of fundamental as well as applied interest. Experiments performed at BL<sub>29</sub> usually involve magnetic materials composed of 3d metals and rare earths, magnetic or superconducting oxides, semiconductors, Silicon and Carbon-based materials such as Graphene or organic molecules, ferro-electric, piezo-electric and multiferroic materials. The samples studied can be in bulk, thin film, multilayered, powder or nanostructured form. Experiments at

BL29 are generally relevant at a fundamental or applied level for novel micro- and nano-technology devices in fields like spintronics, photonics, sensors, actuators or information storage. The available wide instrumentation combined with the large photon energy range of the beamline and its full polarization control, permits that studies on other highly interesting materials such as polymers, 2D materials, topological insulators, novel superconductors, etc., can also be performed successfully.

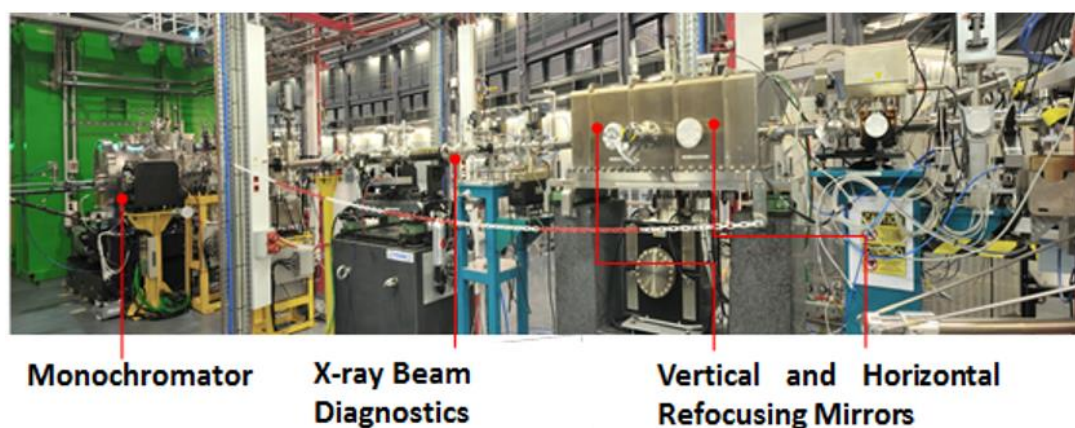


Figure 2.14. Some main optical components of BL\_29-BOREAS beamline. Figure adapted from ALBA website [75].

The BOREAS beamline advanced instrumentation and x-ray optical design make possible soft X-ray (magnetic) circular and linear dichroism (XMCD/XMLD) measurements and other related advanced characterization techniques such as resonant x-ray scattering or x-ray holography. A XAS absorption spectrum can be typically acquired in 2-3 min with high accuracy ( $\Delta E/E \sim 10^{-4}$ ) and repeatability (in the order of 20-30 meV).

The beamline is equipped with two state-of-art end-stations: (i) A high-field vector magnet (HECTOR) for soft x-ray absorption spectroscopy and dichroism techniques such as NEXAFS, XMCD or XMLD; and (ii) A UHV reflectometer (MARES) for scattering and reflection approaches including resonant soft x-ray reflectivity, resonant magnetic scattering GISAXS and x-ray holography [75].

In our case we focus on the HECTOR end-station, where all the experiments have been performed. This end-station consists of three orthogonal pairs of superconducting

coils that can produce magnetic fields of up to 6T along the beam direction (2T in any other direction). The system counts on three chambers for storage and sample preparation, all operating high-to-ultra-high vacuum conditions (UHV,  $P \leq 10^{-9}$  mbar) [75]: (i) the load-lock chamber; (ii) the buffer chamber; and (iii) the preparation chamber. The first one allows to introduce/change samples at ambient pressure and to reach a good vacuum in a few minutes. The buffer chamber is a transition chamber between the load-lock and the preparation chamber where UHV conditions are mandatory. Finally, the preparation chamber presents a complete range of sample preparation tools such as: a cleaver, a scraper, evaporators for metals and organic molecules, a heating stage or even, an ion sputtering gun.



Figure 2.15. HECTOR end station in BL\_29-BOREAS beamline at ALBA. Figure adapted from ALBA website [75].



# Chapter 3

## CrIII doping – a cationic substitution

### YBaCuFeO<sub>5</sub> is not eager to admit

#### 3.1 Introduction

There is presently a need for developing new strategies that are capable to optimise and upgrade the magnetic and magnetoelectric properties of high-temperature spiral oxides and potential ferroelectrics. One possible route is the chemical substitution. In this sense, we decided to introduce different transition metals at the B/B'-sites of the YBCFO structure which sit on the bipyramidal layers. We first aimed at exploring the properties when the trivalent B' cation  $\text{Fe}^{3+}$  is partially substituted by trivalent  $\text{Cr}^{3+}$  ions in the pyramids. Along this chapter we describe our efforts to synthesize, characterize and understand the effects produced by Cr introduction in the  $\text{YBaCuFe}_{1-x}\text{Cr}_x\text{O}_5$  solid solution.

We proposed this particular substitution of the trivalent B'-cation based on several motivations. One of the reasons is that, apart from being isovalent, the ionic radius of  $\text{Cr}^{3+}$  ( $\sim 0.615 \text{ \AA}$  in VI coordination) is very close to that of  $\text{Fe}^{3+}$  ( $\sim 0.645 \text{ \AA}$  in VI coordination) [48], which suggests that  $\text{Cr}^{3+}$  could easily penetrate into the YBCFO crystal lattice and substitute the position of  $\text{Fe}^{3+}$ . On the other hand, the presence of  $\text{Cr}^{3+}$  can have a strong impact over the competing superexchange terms in the system.



The Goodenough-Kanamori rules state that Fe<sup>3+</sup>-O-Cr<sup>3+</sup> superexchange interaction is ferromagnetic, in contrast to AFM Fe<sup>3+</sup>-O-Fe<sup>3+</sup> ones [76], which could modify the local canting of the frustrated spins and therefore the incommensurability factor of the spiral. Likewise, a change of sign is also expected in the only FM pair of the pristine compound (Fe<sup>3+</sup>-O-Cu<sup>2+</sup>) if some Fe sites are substituted by Cr ions. A priori, we cannot discard that reduced amounts of this substitution could favour a non-collinear order respect to the collinear high-temperature (1/2 1/2 1/2) magnetic phase. An interesting example in the literature can be seen in ref. [77]. Cr<sub>2</sub>O<sub>3</sub> and alpha-Fe<sub>2</sub>O<sub>3</sub> are crystallographically isomorphous, however both exhibit different AFM magnetic structures. The addition of Cr<sub>2</sub>O<sub>3</sub> in the solid solution xCr<sub>2</sub>O<sub>3</sub>-(1-x)Fe<sub>2</sub>O<sub>3</sub> generates a magnetic spiral phase (corn spiral) and the magnetic spiral components in this solid solution can be tuned varying the Cr fraction. In addition, the orientation of the spiral plane (and cone axis) can be modified as a function of Cr content, transforming the magnetic helix into a cycloid for 0.65 < x < 0.80 [77]. In the following sections we describe our efforts to investigate the influence over the successive magnetic phases of YBCFO when Cr<sup>3+</sup> is added to the position occupied by Fe<sup>3+</sup> in the structure (partial substitution of the trivalent B'-site in A<sup>+3</sup>A<sup>+2</sup>B<sup>+2</sup>B<sup>+3</sup>O<sub>5</sub>, A<sup>3+</sup>=Y, A<sup>2+</sup>=Ba, B<sup>2+</sup>=Cu and B<sup>3+</sup>=(Fe, Cr)).

### 3.2 Sample synthesis

Polycrystalline samples have been prepared following the conventional solid-state reaction route. After an optimization of the synthesis process of the undoped compound, the whole experimental procedures follow the steps listed below:

- i. High purity oxides of Y<sub>2</sub>O<sub>3</sub>, BaCO<sub>3</sub>, CuO, Fe<sub>2</sub>O<sub>3</sub> and Cr<sub>2</sub>O<sub>3</sub> were employed as precursors to prepare polycrystalline samples. Evaporation of the moisture of the precursor oxides BaCO<sub>3</sub>, CuO, Fe<sub>2</sub>O<sub>3</sub> and Cr<sub>2</sub>O<sub>3</sub> in a stove at 100 °C for 10 hours to avoid weighing errors. In case of Y<sub>2</sub>O<sub>3</sub>, a pre-annealing process was carried out at 900 °C for 10 hours in a furnace to promote the evaporation of possible carbonates.

- ii. Determination of the stoichiometric amounts of the precursor oxides required by the reaction; seven compositions of  $\text{YBaCuFe}_{1-x}\text{Cr}_x\text{O}_5$  samples with  $x=0, 0.01, 0.02, 0.03, 0.05, 0.10, 0.20$  were determined. Hereafter we denote the samples as Cr-0, Cr-1%, Cr-2%, Cr-3%, Cr-5%, Cr-10% and Cr-20%;
- iii. Weighing, mixing, and homogenization of different precursor oxides determined above, finally completely homogeneous fine powder was obtained;
- iv. Pressing of the above fine powder into pellets using a cylindrical mold under a pressure of 12 tons and hold for 20min (pellet size after pressing: 20mm in diameter and 5mm in thickness);
- v. Annealing of the pellets using a tubular furnace at 1100 °C for 50 hours in air atmosphere, with an initial positive temperature ramp of 300 °C/h and final negative ramp of 300 °C/h to cool the sample down to room temperature.
- vi. Checking of as prepared samples using laboratory x-ray powder diffraction to ensure good quality of samples.

### 3.3 Laboratory x-ray diffraction

First of all, we checked the prepared samples by laboratory x-ray diffraction within the scientific service of ICMAB. The XRD patterns were recorded using a Siemens D-5000 diffractometer and Cu  $K_\alpha$  radiation ( $\lambda=1.54 \text{ \AA}$ ). Some diffraction patterns for distinct compositions and their Rietveld refinement are shown in Figure 3.1. For Cr-1% and Cr-3%, samples are single-phase, without detectable impurities. For samples with Cr doping larger than 5% ( $x \geq 5\%$ ), secondary phases were observed (e.g. around  $2\theta \approx 30^\circ$ ), and by comparing patterns of Cr-5% and Cr-20% we found the impurity peaks increase with the Cr content. We have attempted to eliminate the impurity phases by increasing the annealing temperature and repeating annealing cycles in air, but all these approaches turned out to be fruitless.

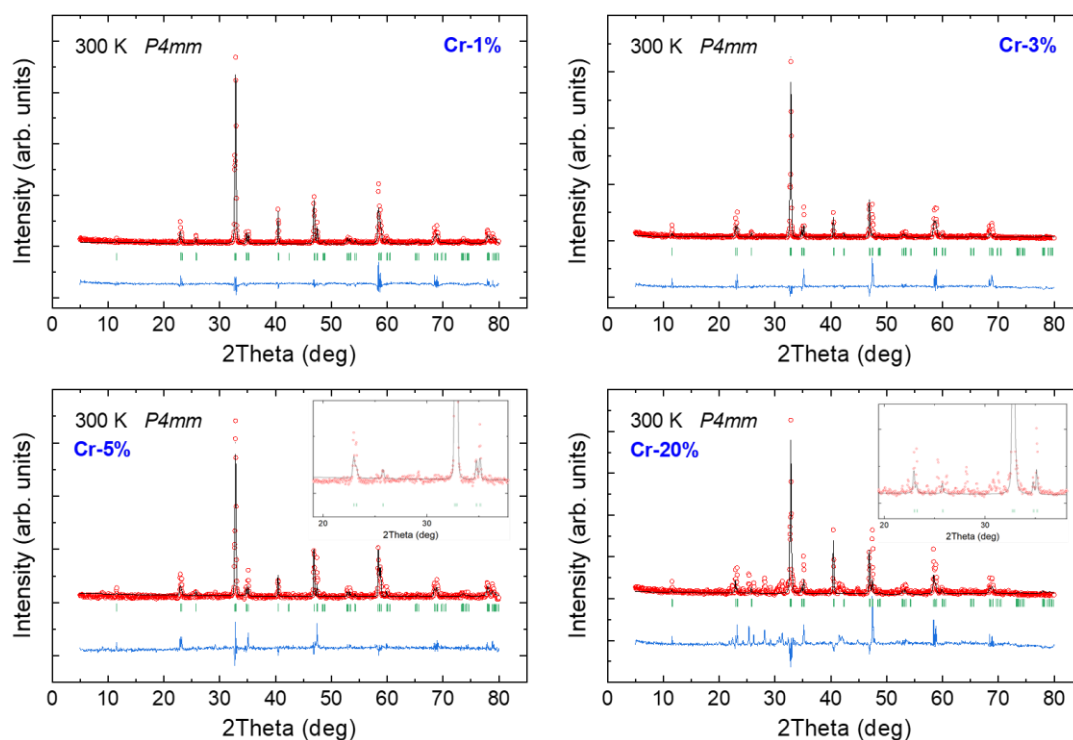


Figure 3.1. Rietveld refinement (black line) of laboratory x-ray diffraction patterns (red circles) of Cr-1%, Cr-3%, Cr-5% and Cr-20%. Green bars are the calculated Bragg positions and bottom line is the observed-calculated difference. Insets in Cr-5% and Cr-20%: detail of the refinement around  $2\theta \approx 30^\circ$  showing the non-indexed reflections (impurity phases).

### 3.4 Magnetization

The magnetization measurements were carried out using the Low Temperature and Magnetometry Service in ICMAB. The DC magnetization was measured in warming conditions up to 300 K using the SQUID for recording magnetic data below room-temperature (RT) under 2 kOe after field cooling (FC). In addition, the temperature dependence of the magnetization was recorded in the interval 300-650K using the VSM in the PPMS under the same magnetic field.

We performed magnetization measurements on some samples to check if there is any indication of the antiferromagnetic transition temperatures  $T_{N1}$  and  $T_{N2}$ . The susceptibility curves of these samples are shown in Figure 3.2. Two magnetic anomalies (peaked maxima) at  $T_{N1}$  and  $T_{N2}$  are clearly visible for the measured Cr doped samples. The two transition temperatures retain very similar values to the non-doped Cr-0 sample. These temperatures do not show any monotonous evolution with the increasing Cr

doping, even for the highest doping sample. This is not what we expected. The behaviour observed is probably related to the aforementioned presence of impurity phases as confirmed by laboratory x-ray diffraction. A more detailed investigation by other techniques should follow to fully understand these materials.

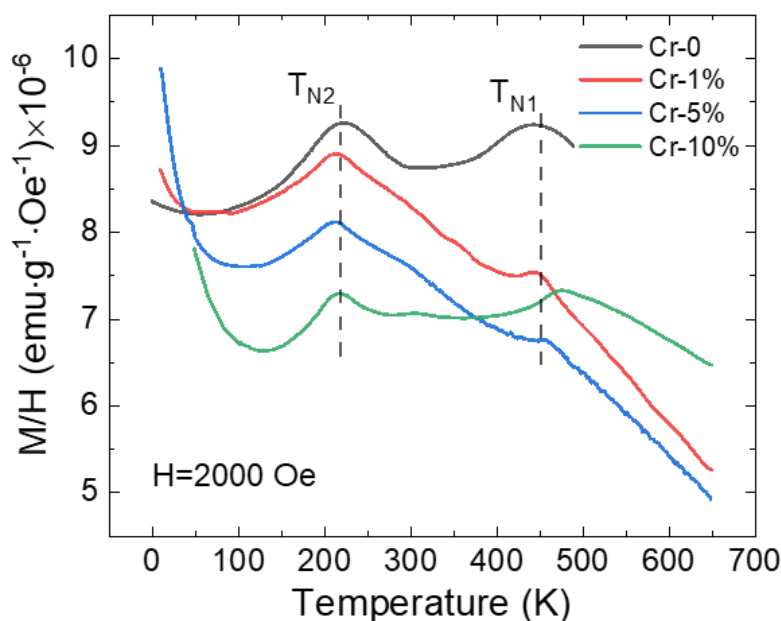


Figure 3.2. Magnetic susceptibility curves under 2 kOe magnetic field of four  $\text{YBaCuFe}_{1-x}\text{Cr}_x\text{O}_5$  ( $x=0, 0.01, 0.05, 0.10$ ) samples. The two transition temperatures observed at  $T_{N1}$  and  $T_{N2}$  correspond to the CM collinear and ICM magnetic phases, respectively. Curves are shifted by  $10^{-6} \text{ emu} \cdot \text{g}^{-1} \cdot \text{Oe}^{-1}$  for clarify.

### 3.5 X-ray absorption spectroscopy

As it has been mentioned in Chapter 2, XAS using synchrotron beams is a powerful technique for the investigation of the local electronic and atomic structure of solids. This is so because it is a measurement of the transition probability of core electrons into the lowest unoccupied states in the valence band, in an atomic selective manner. XAS measurements at the Cu, Fe and Cr  $L_{2,3}$  edges ( $2p \rightarrow 3d$  transitions) were performed in the HECTOR cryomagnet endstation at the BL29-BOREAS beamline of the ALBA Synchrotron Light Facility (Barcelona, Spain). Sintered pellets of  $\text{YBaCuFe}_{1-x}\text{Cr}_x\text{O}_5$  ( $x=0$  and  $0.05$ ) were stucked onto Al plates using a hard bicomponent

epoxy (Torrseal<sup>®</sup>) and diluted Ag paint. These plates were screwed into Cu sample holders while sandwiching In foil interfaces to optimize thermal conductivity. All data were recorded in TEY and partial FY detection modes. For the latter, a commercial Si-drift diode (SDD) built by Rayspec Ltd., UK was used. The main chamber of the cryomagnet was kept at approximately  $1 \times 10^{-10}$  mbar during measurements. The total incoming radiation flux was about  $5 \times 10^{11}$  photons/s with an energy resolution of  $\Delta E/E \sim 10^{-4}$ .

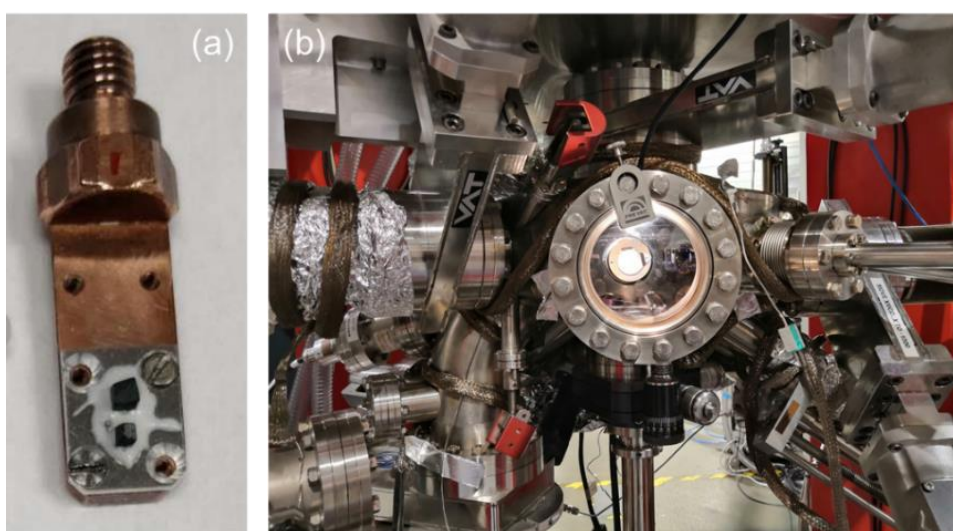


Figure 3.3. (a) Prepared sample holder for the XAS measurement, the sample pellets are stucked onto Al plates using a hard epoxy and diluted Ag paint; (b) the preparation chamber where the pellets get in-situ cut using a cleaver to ensure clean surfaces for the measurement.

Considering that there are quite scarce reports on the electronic state of transition metals in the YBCFO system, it is thus worth underlying that here we present the first study of this kind on materials of this family using XAS.

Figure 3.4 shows the XAS spectra of YBaCuFe<sub>1-x</sub>Cr<sub>x</sub>O<sub>5</sub> ( $x=0$  and  $0.05$ ) samples at 300 K across the Fe, Cu and Cr  $L_{2,3}$  edges. In general, one can observe that the spectra of Fe in both Cr-0 and Cr-5% samples appear in a very resilient high spin ( $S=5/2$ ) and trivalent state in this structure [81][82], and Cu looks like expected for a typical 3d9 configuration [83]. The spectra shown in Figure 3.4 (a) and (b) display all well-known fingerprints of Fe<sup>3+</sup> ( $3d: t_{2g}^3 e_g^2$ ) and Cu<sup>2+</sup> ( $3d: t_{2g}^6 e_g^3$ ) in oxide materials. However, if

we look at the experimental spectra in Figure 3.4 (c), the Cr  $L_{2,3}$  XAS spectrum from the Cr-5% sample exhibits an unexpected behavior, since it is strikingly similar to the also plotted  $\text{Cr}^{6+}$  reference [78]. Moreover, there is no trace of the typical  $\text{Cr}^{3+}$  and  $\text{Cr}^{2+}$  features [79][80] when the spectra is compared with those references. This suggests that all the trivalent Cr in the precursor  $\text{Cr}_2\text{O}_3$  has been oxidized to  $\text{Cr}^{6+}$ .

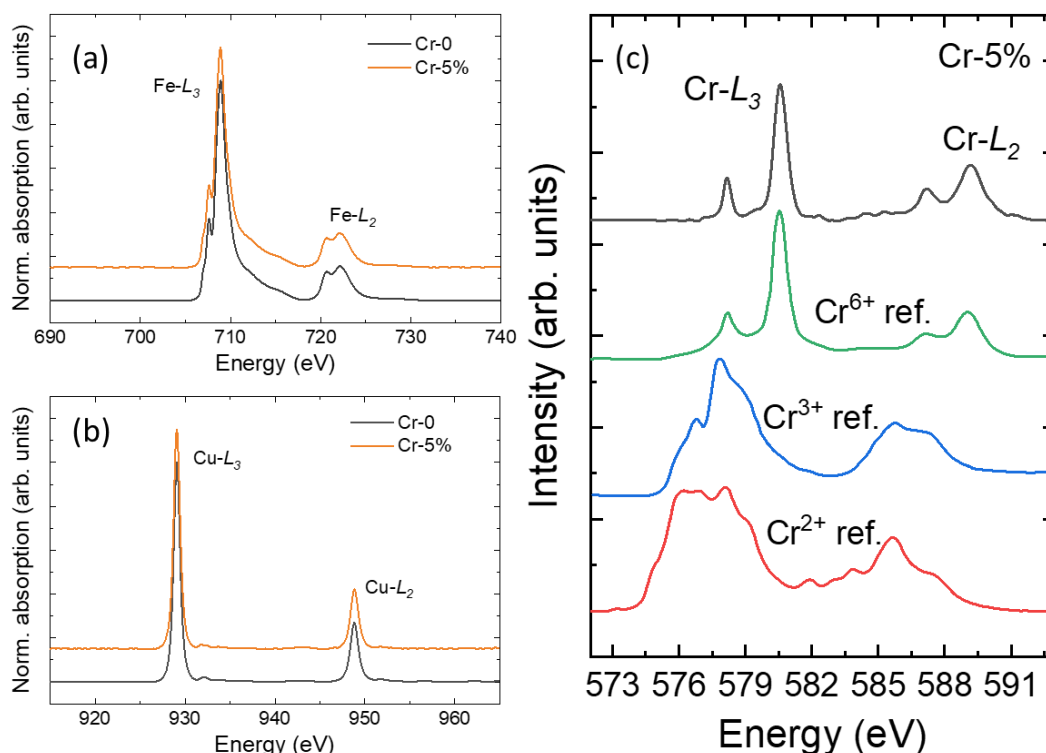


Figure 3.4. Experimental XAS spectra of  $\text{YBaCrFe}_{1-x}\text{Cr}_x\text{O}_5$  ( $x=0$  and  $0.05$ ) samples at (a) Fe, (b) Cu and (c) Cr  $L_{2,3}$  edges at 300 K. Regarding panel (c), the black curve is the experimental data of the studied sample, the green, blue and red curve are provided as XAS references of  $\text{Cr}^{6+}$  (Crocoite) [78],  $\text{Cr}^{3+}$  ( $\text{Cr}_2\text{O}_3$ ) [79][80] and  $\text{Cr}^{2+}$  ( $\text{CrO}$ ) [80], respectively.

A summarize to the XAS results on  $\text{YBaCuFe}_{1-x}\text{Cr}_x\text{O}_5$  ( $x=0$  and  $0.05$ ) samples, we found that the oxidation states of Fe and Cu metals were well preserved as  $\text{Fe}^{3+}$  and  $\text{Cu}^{2+}$ , whereas the oxidation state of Cr turns out to be more sensitive and easily oxidized under the sample preparation conditions presented above. Unexpectedly, we found evidence that Cr is only present in the sample as  $\text{Cr}^{6+}$ . Considering this high valence of Cr, it is necessary to distinguish between two possible distinct scenarios in these materials: (i) a high-valence chromium-based compound appeared as a secondary

phase; (ii) the high-valence Cr has managed to substitute Fe partially and accommodates in the Fe position as we expected (only as Cr<sup>6+</sup>). It is thus necessary to investigate and study in detail the phase composition of these materials.

### 3.6 Synchrotron x-ray powder diffraction analysis

In order to gain further insight on the secondary phases and their evolution with the Cr content, the SXPD experiment was carried out on YBaCuFe<sub>1-x</sub>Cr<sub>x</sub>O<sub>5</sub> samples at the BL04-MSPD beamline of the ALBA Synchrotron Light Facility (Barcelona, Spain) using the PSD MYTHEN. All the samples ( $x=0, 0.01, 0.02, 0.03, 0.05, 0.10, 0.20$ ) were measured at 300 K. The wavelength,  $\lambda=0.41338(4)$  Å, was determined by measuring a NIST standard silicon. The fine powder samples were loaded in borosilicate glass capillaries (diameter in 0.7 mm) and kept spinning during data acquisition. Figure 3.5 shows some prepared capillary samples and the powder diffraction setup in the beamline BL04-MSPD.

Figure 3.6 displays the refined synchrotron x-ray diffraction patterns of the seven compositions collected at 300 K. Patterns are similar for all compositions and the dominant phase is well described using the  $P4mm$  space group [44]. The powerful synchrotron x-ray diffraction enables us to detect phases which are present in relatively low fractions. By using the HighScore Plus code (Malvern Panalytical) program, three secondary phases were identified through search-and-match analysis of the extra reflections not corresponding to the main phase. We found that the three main impurity phases are the same in all compositions and they were identified as BaCrO<sub>4</sub>, Y<sub>2</sub>O<sub>3</sub> and Y<sub>2</sub>Cu<sub>2</sub>O<sub>5</sub>. The set of peaks from these impurities are shown in a selected angular range in the insets of Figure 3.6, associated to their corresponding secondary phases.

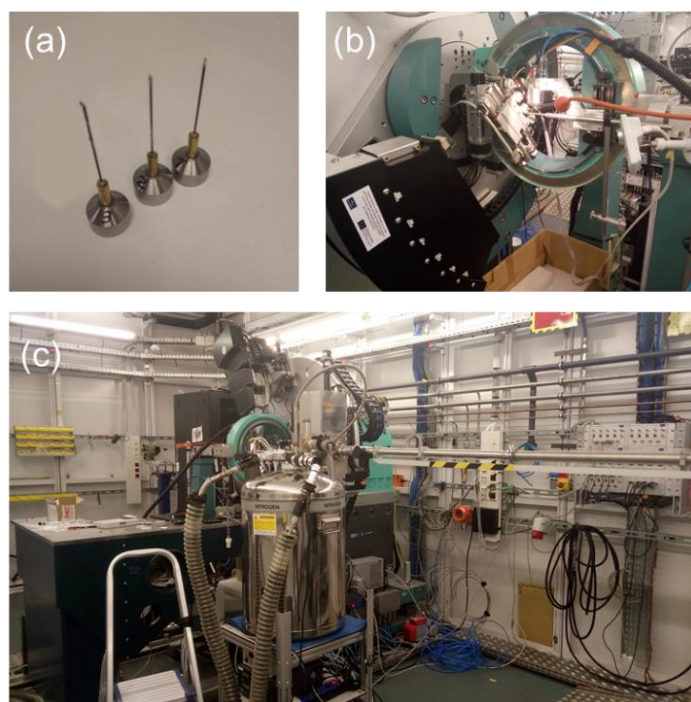


Figure 3.5. Pictures showing (a) some prepared samples in borosilica glass capillaries with a diameter of 0.7 mm; (b) the powder diffraction setup; (c) the high angular resolution powder diffraction experimental endstation (mspd@alba).

Then, the full patterns including secondary phases were refined. The mass fraction of the main and all secondary phases was carefully determined by applying the quantitative phase analysis using the Rietveld method and the results are displayed in the Table 3.1. The coefficients required for each phase in multi-phase Rietveld refinement to calculate the weight percentage of the phase are:

$$ATZ = Z M_W f^2 / t \quad (1)$$

Where  $Z$  is the number of formula units per cell, and  $M_W$  is the molecular weight. The  $f$  factor is used to transform the site multiplicities to their true values. For a stoichiometric phase  $f=1$  if these multiplicities are calculated by dividing the Wyckoff multiplicity  $m$  of the site by the general multiplicity  $M$  of the space group. Otherwise  $f=Occ \cdot M/m$ , where  $Occ$  is the occupation factor. The  $t$  is the Brindley coefficient that accounts for microabsorption effects. It is required for quantitative phase analysis only. When different phases have similar absorption coefficient, this factor is nearly 1 [73].



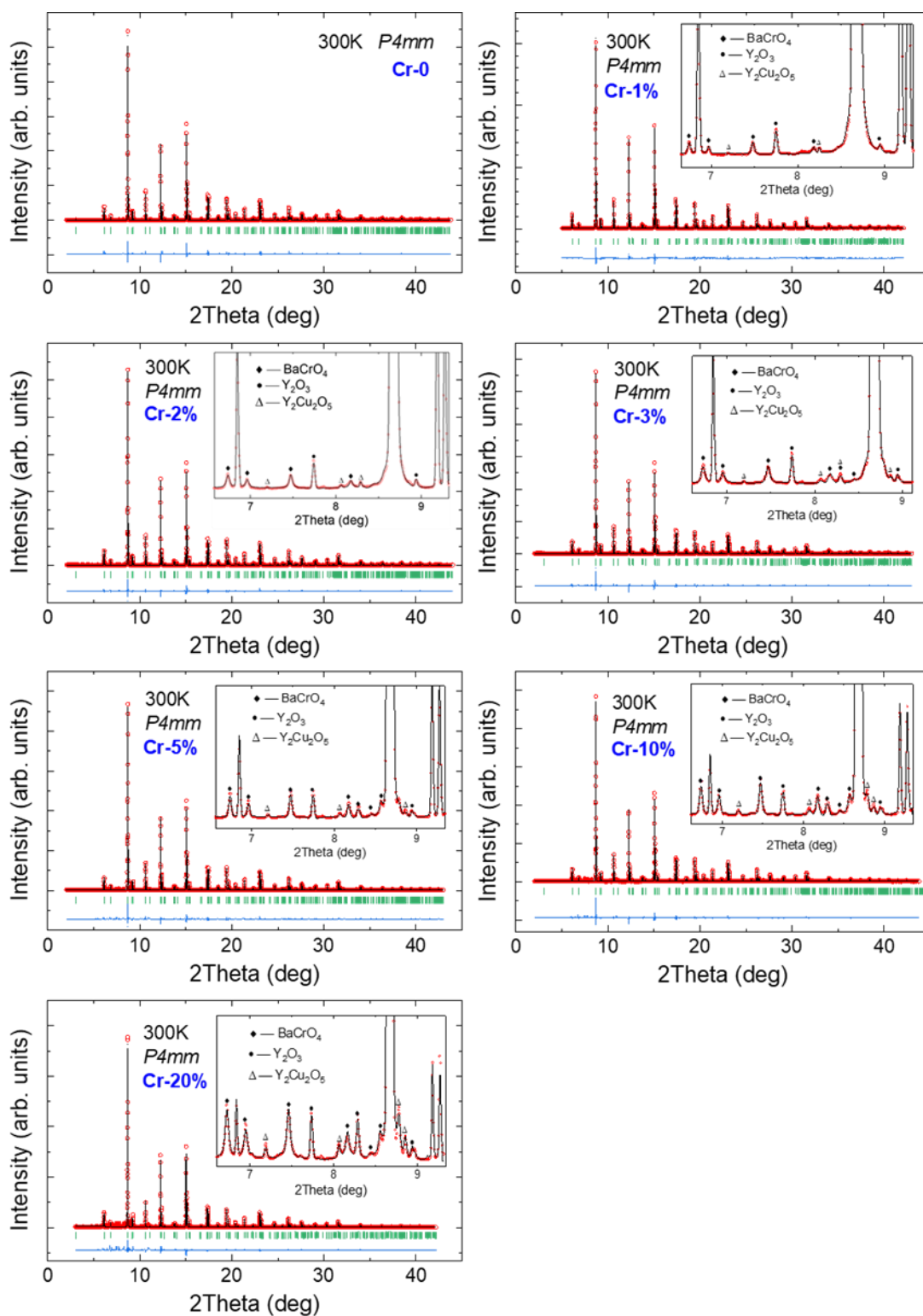


Figure 3.6. Rietveld refinement (black curve) of the synchrotron x-ray intensities (red circles) at 300 K of each composition. Bottom blue line is the observed-calculated difference, the row of green bar represents the calculated Bragg positions. Inset: Details of refined impurities at specific angles, impurities are the same in all compositions and they were identified as BaCrO<sub>4</sub>, Y<sub>2</sub>O<sub>3</sub> and Y<sub>2</sub>Cu<sub>2</sub>O<sub>5</sub>.

**Table 3.1.** Refined mass fraction of secondary phases obtained from the synchrotron x-ray diffraction data on  $\text{YBaCuFe}_{1-x}\text{Cr}_x\text{O}_5$  samples. The ratio  $n(\text{BaCrO}_4)/n(\text{pure})$  is defined as  $R_m$ .

Cr content x (%)	BaCrO <sub>4</sub> (wt%)	Y <sub>2</sub> O <sub>3</sub> (wt%)	Y <sub>2</sub> Cu <sub>2</sub> O <sub>5</sub> (wt%)	$R_m$
1	0.38 (4)	0.22 (4)	0.01 (1)	0.007
2	1.09 (6)	0.39 (5)	0.09 (6)	0.019
3	1.47 (6)	0.51 (3)	0.10 (1)	0.025
5	2.34 (6)	0.46 (6)	0.27 (2)	0.041
10	5.29 (12)	0.85 (9)	0.64 (3)	0.095
20	12.01 (17)	1.76 (9)	6.36 (15)	0.250

In general, the mass fraction of secondary phases increases systematically with the nominal Cr content  $x$ , being very significant in Cr-20% sample. More important is the fact that the fraction of the Cr precursor ( $\text{Cr}_2\text{O}_3$ ) we used for substituting  $\text{Fe}^{3+}$  site by  $\text{Cr}^{3+}$  in  $\text{YBaCuFeO}_5$  has reacted with  $\text{BaCO}_3$  and generated the  $\text{BaCrO}_4$ . The valence of Cr in this compound is  $\text{Cr}^{6+}$  which is in accordance with our findings by measuring XAS spectra. Furthermore, we calculated the ratio  $n(\text{BaCrO}_4)/n(\text{pure})$  (hereafter named as  $R_m = n(\text{BaCrO}_4)/n(\text{pure})$ ) that monitors the percentage of molar mass  $\text{BaCrO}_4$  per 1 mol of the nominal  $\text{YBaCuFe}_{1-x}\text{Cr}_x\text{O}_5$  phase. The results listed in the Table 3.1, imply that most of Cr element (70% in Cr-1% to 95% in Cr-10%) is in  $\text{BaCrO}_4$  form rather than incorporated in the YBCFO structure. Within errors we must conclude that the totality of Cr atoms has formed as  $\text{BaCrO}_4$  instead of substituting Fe sites or accommodate in the YBCFO structure. This conclusion is further confirmed by the tiny, almost negligible, variations in the lattice parameters and volume as a function of nominal Cr content  $x$  that is plotted in Figure 3.7. It is observed that both lattice parameters  $a$  and  $c$  present a decreasing tendency, but the magnitude of the change is very small (for  $\Delta a \sim 0.0007 \text{ \AA}$  and  $\Delta c \sim 0.003 \text{ \AA}$ ) in the sample with highest nominal Cr content in Cr-20%. Considering the respective ionic radius of  $\text{Fe}^{3+}$  and  $\text{Cr}^{3+}$ , if  $\text{Cr}^{3+}$  managed to substitute the site of Fe, the expected lattice change should be much more pronounced than the observed evolution. The tiny evolution shown in Figure 3.7

confirms that Cr atoms didn't enter the crystal lattice of YBCFO. The partial substitution of Fe<sup>3+</sup> site by Cr<sup>3+</sup> is confirmed to be difficult to achieve under the normal conditions described in section 3.2.

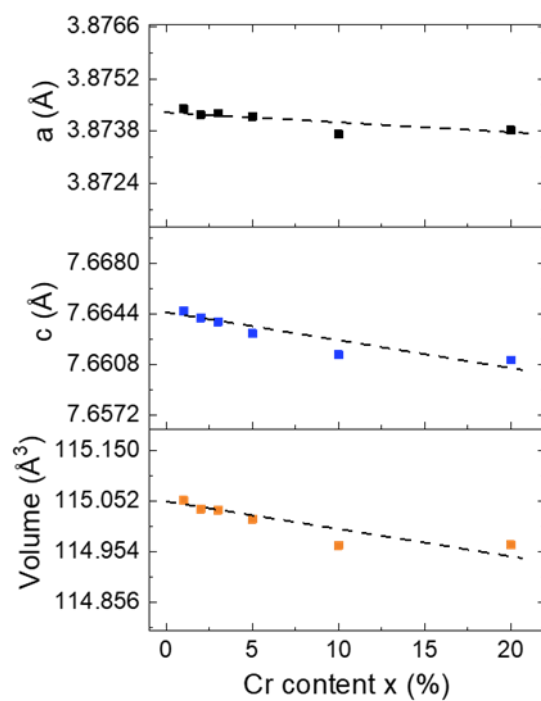


Figure 3.7. Evolution of cell parameters and volume of nominal YBaCuFe<sub>1-x</sub>Cr<sub>x</sub>O<sub>5</sub> samples from SXPD data at room temperature.

### 3.7 Summary and conclusions

In this chapter we have described our attempt to partially substitute of B'-site Fe<sup>3+</sup> ions by Cr<sup>3+</sup> in the promising candidate of multiferroic YBaCuFeO<sub>5</sub>. A series of nominal YBaCuFe<sub>1-x</sub>Cr<sub>x</sub>O<sub>5</sub> samples with x=0, 0.01, 0.02, 0.03, 0.05, 0.10 and 0.20 have been synthesized by conventional solid-state reaction method. Their study using a set of characterization techniques point to the same scenario, described below.

The laboratory XRD data shows that when the doping amount is higher than 5% (x≥0.05), the presence of secondary phases can be observed, and the amount of unwanted secondary phases progressively increase with the nominal Cr content x.

The XAS measurements enable us for the first time to study the electronic state of the transition metals in this material. The spectroscopic results indicate that the

oxidation states of Fe and Cu in Cr-0 and Cr-5% samples remain unchanged. They match perfectly well-known fingerprints of  $\text{Fe}^{3+}$  HS ( $3d: t_{2g}^3 e_g^2$ ) and  $\text{Cu}^{2+}$  ( $3d: t_{2g}^6 e_g^3$ ) expected electronic configurations in oxide materials with pyramidal coordination. On another hand, we have proved that all the Cr atoms were oxidized to  $\text{Cr}^{6+}$ , under the sample preparation route employed.

A detailed analysis of the SXRPD data has enabled us to detect the presence of secondary phases, which have been identified as  $\text{BaCrO}_4$ ,  $\text{Y}_2\text{O}_3$  and  $\text{Y}_2\text{Cu}_2\text{O}_5$ . The valence of Cr in  $\text{BaCrO}_4$  is coincident with that observed in XAS measurement at the Cr  $L_{2,3}$  edges which is definitely  $\text{Cr}^{6+}$ . The presence of  $\text{Cr}^{3+}$  is totally discarded. By applying the quantitative phase analysis method through Rietveld refinements, we determined the proportion of the coexisting phases in all the samples. The conclusion is that, the fraction of the  $\text{BaCrO}_4$  impurity increases progressively with the Cr doping  $x$ . Moreover, the  $R_m$  ratios confirm that, within errors, all Cr atoms get incorporated to the  $\text{BaCrO}_4$  impurity phase as  $\text{Cr}^{6+}$  rather than going to  $\text{YBaCuFeO}_5$  structure substituting isovalently the  $\text{Fe}^{3+}$  ions. This was also corroborated by the evolution of the magnetic properties studied by magnetometry. As a consequence, under our sample preparation conditions, Cr is easily oxidized to  $\text{Cr}^{6+}$  forming  $\text{BaCrO}_4$  instead of adopting a pyramidal  $\text{Cr}^{3+}\text{O}_5$  coordination.



# Chapter 4

## Boosting spin-orbit coupling in Mn-doped YBaCuFeO<sub>5</sub>

### 4.1 Introduction

Previous reports demonstrated that in the Y(Ba, Sr)CuFeO<sub>5</sub> system and R(Ba, Sr)CuFeO<sub>5</sub> oxides (R: rare-earth or Y), where the cationic substitution affects the A site of the perovskite, the interatomic distances between the magnetic transition metal atoms (TM) are modified with respect to YBCFO [46]. Of great importance are the changes in the distances parallel to  $c$  as they can tune the magnitude of the competing interactions in that direction [84][85]. A shrinkage in the height of the bipyramids ( $d_2$  distance, e.g. by partially substituting Ba<sup>2+</sup> by the smaller Sr<sup>2+</sup>) or an increase of the distance  $d_1$  between bipyramids (e.g. by substituting Y<sup>3+</sup> by a bigger trivalent rare-earth) produce the rise of the spiral transition temperature [46].

The principal theoretical model justifying the onset of the spiral phase in this YBCFO structure has been developed by Scaramucci *et al.* in refs. [84] and [85]. In a non-frustrated lattice of Heisenberg spins (perfect Cu/Fe order) with only nearest-neighbour (NN) interactions, chemical disorder and strong AFM Fe/Fe bonds in bipyramids are introduced as dilute impurity bonds that substitute weak FM Fe/Cu bonds and generate frustration within the bilayers. For sufficiently low dilution, the induced

frustration results in a local canting of the spins associated to the impurity bond. Thanks to the identical orientation of the impurity bonds (always parallel to the  $c$  axis) a magnetic spiral can be stabilized through long range coupling between the locally-canted spins. A continuous twist can be induced parallel to their direction (when all the impurity bonds point along to a single crystallographic direction), favoured in Bravais lattices where neighbouring impurities are closer in the plane than along the orientation of the impurity bonds. Essential ingredients for this mechanism are the sign and magnitude of the main NN exchange interactions (along the  $c$  axis and within the  $ab$  plane).

In the above model spin-orbit interactions play a key active role for determining the common plane of the NN spins along- $c$  that become coplanar [84]. Hence, spin-orbit coupling effects would be very relevant, the most important one likely being expressed in the form of Dzyaloshinskii–Moriya (DM) terms [22][23]. Considering the form of the DM terms and the magnetic wave vector parallel to  $c$ , a helical type arrangement of the spins parallel to the  $ab$  plane would not bring about any spontaneous polarization in YBCFO. This has been the cause alluded to explain the absence of ferroelectricity in the YBCFO single crystal studied in ref. [86]. In the work by Lai *et al.* the magnetic model refined from neutron diffraction patterns, collected using parts of the crystal crushed into powder form, shows a spiral with the rotation plane parallel to the  $ab$  plane (helix).

Inspired by the above presented theoretical works, we tried the chemical substitution of Fe<sup>3+</sup> by Mn<sup>3+</sup> ions in FeO<sub>5</sub> pyramids, which was expected to offer new possibilities for engineering the high-temperature magnetic response of this bipyramids-based YBCFO system. Along the lines of this chapter we present a selective investigation of Mn doped YBaCuFe<sub>1-x</sub>Mn<sub>x</sub>O<sub>5</sub> series samples. Thanks to the similarity of Mn<sup>3+</sup> and Fe<sup>3+</sup> ionic sizes (both  $\approx 0.58$  Å in pyramidal coordination [87]), the Mn<sup>3+</sup> ions were expected to enter the crystallographic lattice of YBCFO replacing the Fe<sup>3+</sup> at their sites. Thus, one may increase the spin-orbit coupling through the partial substitution of highly symmetric Fe<sup>3+</sup> ions (3d<sup>5</sup>, L=0, S=5/2) by less symmetric 3d<sup>4</sup> Mn<sup>3+</sup> ions (L=2, S=2). According to the antisymmetric DM interaction, this isovalent

chemical substitution could favour the generation of spontaneous polarization.

This chapter is divided into two parts. Part I mainly contributes to the investigation of  $\text{YBaCuFe}_{1-x}\text{Mn}_x\text{O}_5$  series samples synthesized in air using a controlled cooling rate of 300 K/h. Part II studies this series of samples further, including the investigation of cationic oxidation states, the influence of different cooling methods [cooling by submersion into room temperature (RT) water or liquid nitrogen (LN)] on the structural and magnetic properties and that of the use of different atmospheres (e.g. argon) during sample preparation. Proper comparisons between these samples are also presented.

## 4.2 Sample synthesis

Polycrystalline samples have been synthesized by the conventional solid-state reaction method. After an optimization of the synthesis process of the undoped compound, the sample preparation consists of the following procedures:

- (i) High purity oxides of  $\text{Y}_2\text{O}_3$ ,  $\text{BaCO}_3$ ,  $\text{CuO}$ ,  $\text{Fe}_2\text{O}_3$  and  $\text{Mn}_2\text{O}_3/\text{MnO}$  were employed to be precursors to prepare polycrystalline samples. The evaporation of the moisture of the precursor oxides  $\text{BaCO}_3$ ,  $\text{CuO}$ ,  $\text{Fe}_2\text{O}_3$  and  $\text{Mn}_2\text{O}_3/\text{MnO}$  took place in a stove at 100 °C for 10 hours to avoid weighing errors. In the case of  $\text{Y}_2\text{O}_3$ , a pre-annealing process was carried out at 900 °C for 10 hours in a furnace to promote the evaporation of possible carbonates;
- (ii) Determination of the stoichiometric amounts of the precursor oxides as required by the reaction;
- (iii) Weighing, mixing, and homogenization of the different precursor oxides to obtain a homogeneous fine powder;
- (iv) Pressing of the above fine powder into pellets using a cylindrical mold under a 12 tons pressure and hold for 20min (pellets size after pressing: 20mm in diameter and 5mm in thickness);
- (v) Annealing of the pellets using a tubular furnace at 1100 °C for 50 hours in air atmosphere, with an initial positive temperature ramp of 300 °C/h and a final



negative ramp of 300 °C/h to cool the sample down to RT. Small pieces of each sample were kept solid for their use in magnetization and XAS measurements, the rest were pulverized into powder and subsequently used in x-ray diffraction and neutron diffraction.

- (vi) Checking of as prepared samples using laboratory x-ray powder diffraction and magnetization to ensure good quality of samples.

**Mn substituting Cu:** We prepared polycrystalline samples of the YBaCu<sub>1-x</sub>Mn<sub>x</sub>FeO<sub>5</sub> series with  $x = 0.10$  and  $0.20$  using MnO as precursor in order to partially substitute Cu<sup>2+</sup> site by Mn<sup>2+</sup>. The Rietveld refinement of laboratory x-ray diffraction data confirmed that there are secondary phases in our samples. Then we tried to eliminate the secondary phases by repeating annealing cycles and increasing the annealing temperature in air, and using a reducing gas (a mixture with 5% hydrogen and 95% nitrogen, by volume fraction) as the chosen atmosphere during the annealing process. However, despite all these efforts we did not succeed in obtaining a good

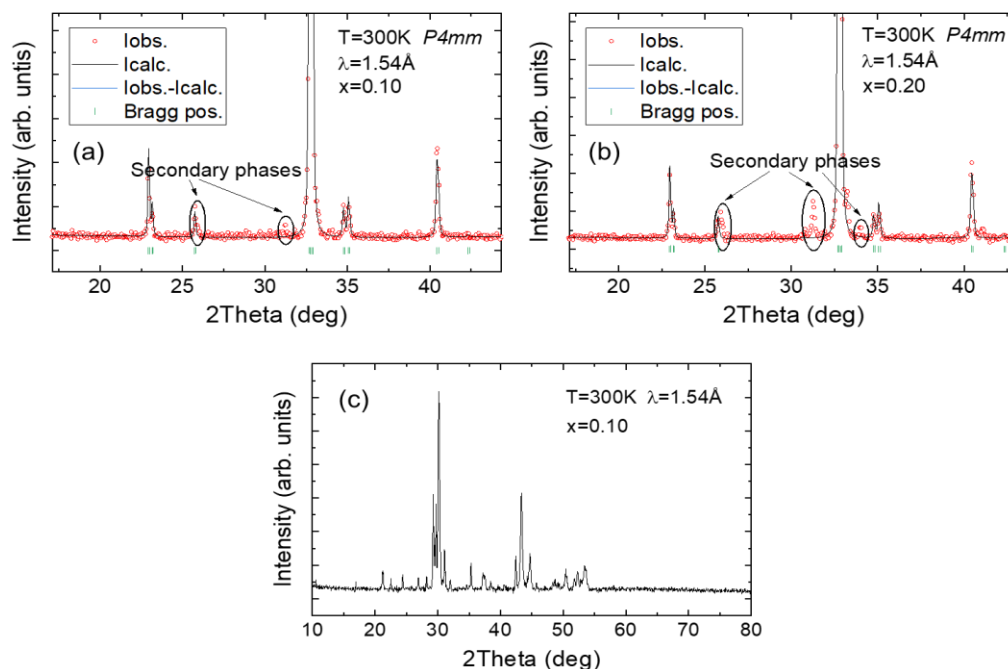


Figure 4.1. Rietveld refinement (black curve) of the YBaCu<sub>1-x</sub>Mn<sub>x</sub>FeO<sub>5</sub> x-ray diffraction intensities (red circles) with (a):  $x = 0.10$  and (b):  $x=0.20$  showing the secondary phases; (c) the x-ray diffraction pattern showing very poor quality of the  $x=0.10$  sample prepared under the reducing atmosphere.

quality sample. In addition, our collaborator Dr. Javier Blasco (Universidad de Zaragoza) also independently attempted to prepare one composition  $\text{YBaCu}_{0.9}\text{Mn}_{0.1}\text{FeO}_5$ , but the presence of the following secondary phases was again noteworthy:  $\text{YMnO}_3$ ,  $\text{Cu}_2\text{O}$ ,  $\text{YBa}_2\text{Fe}_3\text{O}_{8.09}$  and  $\text{Y}_2\text{Cu}_2\text{O}_5$  were found. Finally, we concluded that the tetragonal  $P4mm$  structure formed by bipyramidal layers could not be stabilized when Mn tries to get introduced substituting the divalent Cu sites to form  $\text{YBaCu}_{1-x}\text{Mn}_x\text{FeO}_5$ . The laboratory x-ray diffraction patterns and their refinements are shown in Figure 4.1.

**Mn substituting Fe:** In parallel, we also tried to prepare  $\text{YBaCuFe}_{1-x}\text{Mn}_x\text{O}_5$  polycrystalline samples with  $x=0.10$  and  $0.20$  aimed at substituting  $\text{Fe}^{3+}$  at Fe sites by  $\text{Mn}^{3+}$ .  $\text{Mn}_2\text{O}_3$  was employed as starting precursor. The Rietveld refinements of laboratory x-ray diffraction patterns showed a single phase and no secondary phases were observed. The refinements of these two compositions are shown in Figure 4.2.

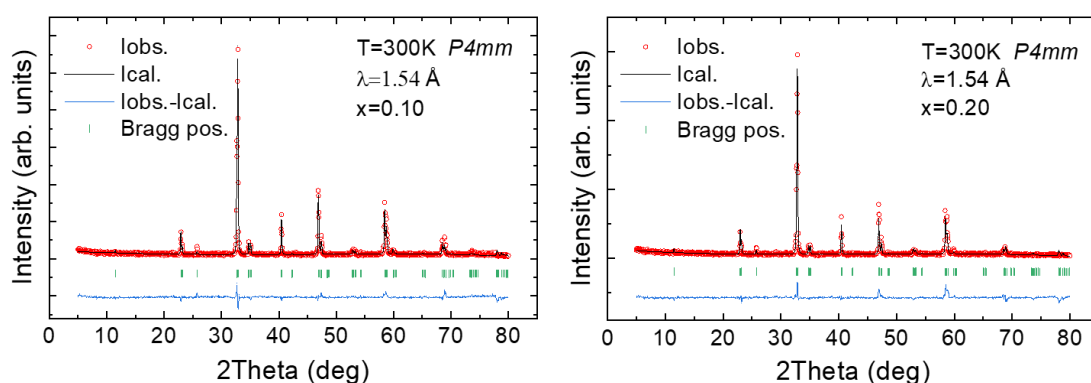


Figure 4.2. Rietveld refinement (black curve) of the x-ray diffraction data (red circles) on two compositions of  $\text{YBaCuFe}_{1-x}\text{Mn}_x\text{O}_5$  with  $x=0.10$  and  $0.20$  polycrystalline samples showing the good quality of single phase. Green bars signal the Bragg diffraction positions and the bottom blue line plots the difference between the experimental and calculated profile intensities.

Looking at the x-ray powder diffraction results, we can see that  $\text{YBaCuFeO}_5$  system shows a strong preference for Mn entering at Fe sites in the crystal structure. Subsequently we prepared more compositions with  $x=0, 0.01, 0.05$  and  $0.15$  (hereafter denoted as Mn-0, Mn-1%, Mn-5%, Mn-10%, Mn-15% and Mn-20%). All compositions were confirmed to be single-phase and of good quality as indicated by the laboratory x-

ray diffraction. To prevent the possible oxidation of Mn cations, we prepared a second set of Mn-10% samples under an argon atmosphere following the same conditions as described earlier. Furthermore, in order to increase the degree of Fe/Cu chemical disorder in bipyramids, another two samples of Mn-10% and Mn-20% were prepared utilizing different cooling methods. After the last annealing in air at  $T=1100$  °C in the furnace, the samples were immediately quenched into RT water and LN, respectively.

We carried out magnetization measurements to check the magnetic behavior of these series of samples. The direct current (dc) magnetization was measured using SQUID for recording magnetic data below RT under 2 kOe after field cooling (FC). In addition, the temperature dependence of the magnetization was recorded in the interval 300-650K using VSM under the same magnetic field.

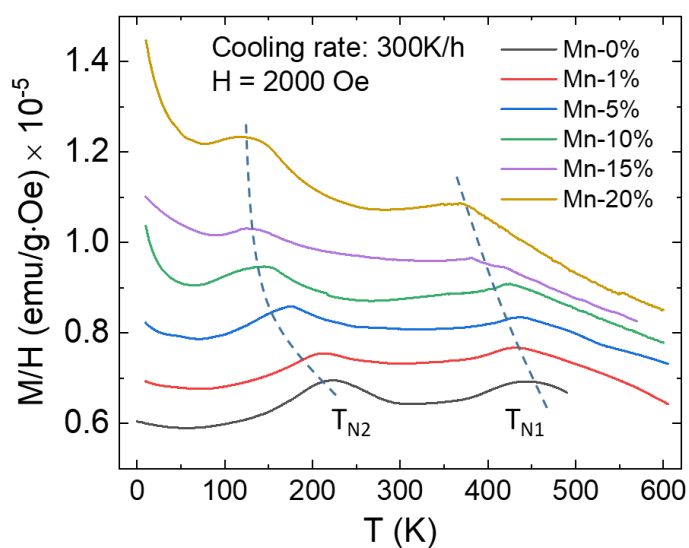


Figure 4.3. Magnetic susceptibility curves (2 kOe) of the YBaCuFe<sub>1-x</sub>Mn<sub>x</sub>O<sub>5</sub> samples prepared using identical cooling rates during the last annealing. Curves were shifted by  $+10^{-6}$  emu g<sup>-1</sup> oe<sup>-1</sup> for clarity. The dashed lines are guides to the eye indicating the evolution of  $T_{N1}$  and  $T_{N2}$  with Mn content.

Figure 4.3 shows the magnetic susceptibility measurements of the five YBaCuFe<sub>1-x</sub>Mn<sub>x</sub>O<sub>5</sub> doped prepared samples and that of YBaCuFeO<sub>5</sub>. Two separated antiferromagnetic transitions take place in all compositions, their corresponding Néel temperatures  $T_{N1}$  and  $T_{N2}$  undergoing a monotonous decrease when the manganese progressively replaces iron in the crystal structure, as shown in the figure. These

magnetization measurements show a general behavior that also support the good quality of our samples.

## **Part I: Samples prepared by a cooling rate of 300 K/h**

### **4.3 Phase composition and structural evolution**

#### **4.3.1 X-ray phase analysis**

The SXPD measurements were performed at 300 K on the BL04-MSPD beamline of the ALBA Synchrotron Light Facility (Barcelona, Spain) using the position sensitive detector MYTHEN. The wavelength,  $\lambda=0.41338$  (4) Å, was determined by measuring a NIST standard silicon. The samples were loaded in borosilicate glass capillaries (diameter of 0.7mm) and kept spinning during data acquisition.

Figure 4.4 displays the refined synchrotron x-ray patterns of  $\text{YBaCuFe}_{1-x}\text{Mn}_x\text{O}_5$  samples. In order to investigate with greater detailed on the evolution of the phase composition, the SXPD patterns collected at  $T=300\text{K}$  were carefully analyzed. Patterns are similar for all compositions and can be well described using the  $P4mm$  symmetry, which gives the best agreement factors and accounts for different spatial disorder of the transition metals (TMs) [46][88]. A thorough inspection of x-ray patterns revealed, however, the occurrence of minor secondary phases alongside the main YBCFO-like phase in all samples doped with Manganese. By a search-and-match analysis of the extra reflections not corresponding to the main phase, they were identified using the HighScore Plus code (Malvern Panalytical). Although the fraction of secondary phases was tiny, their composition could be identified as  $\text{Y}_2\text{O}_3$ ,  $\text{CuO}$ ,  $\text{Y}_8\text{Ba}_5\text{Mn}_4\text{O}_{21}$  and  $\text{Y}_3\text{Ba}_8\text{Cu}_5\text{O}_{18}$ . Their amounts were also determined by a whole-profile Rietveld refinement and have been listed in Table 4.1. The relative weight of secondary phases increases as the doping increases. For  $x \leq 0.05$ , only the two first were detected ( $< 0.25\%$ ).  $\text{Y}_8\text{Ba}_5\text{Mn}_4\text{O}_{21}$  and  $\text{Y}_3\text{Ba}_8\text{Cu}_5\text{O}_{18}$  were only detected in samples with dopings  $x \geq 0.10$ . As shown in Table 4.1 their concentration was always lower than 1%. Secondary phases

containing Fe were not detected. Figure 4.5 illustrates all these refined impurities in the SXPD patterns of the compositions shown in Table 4.1.

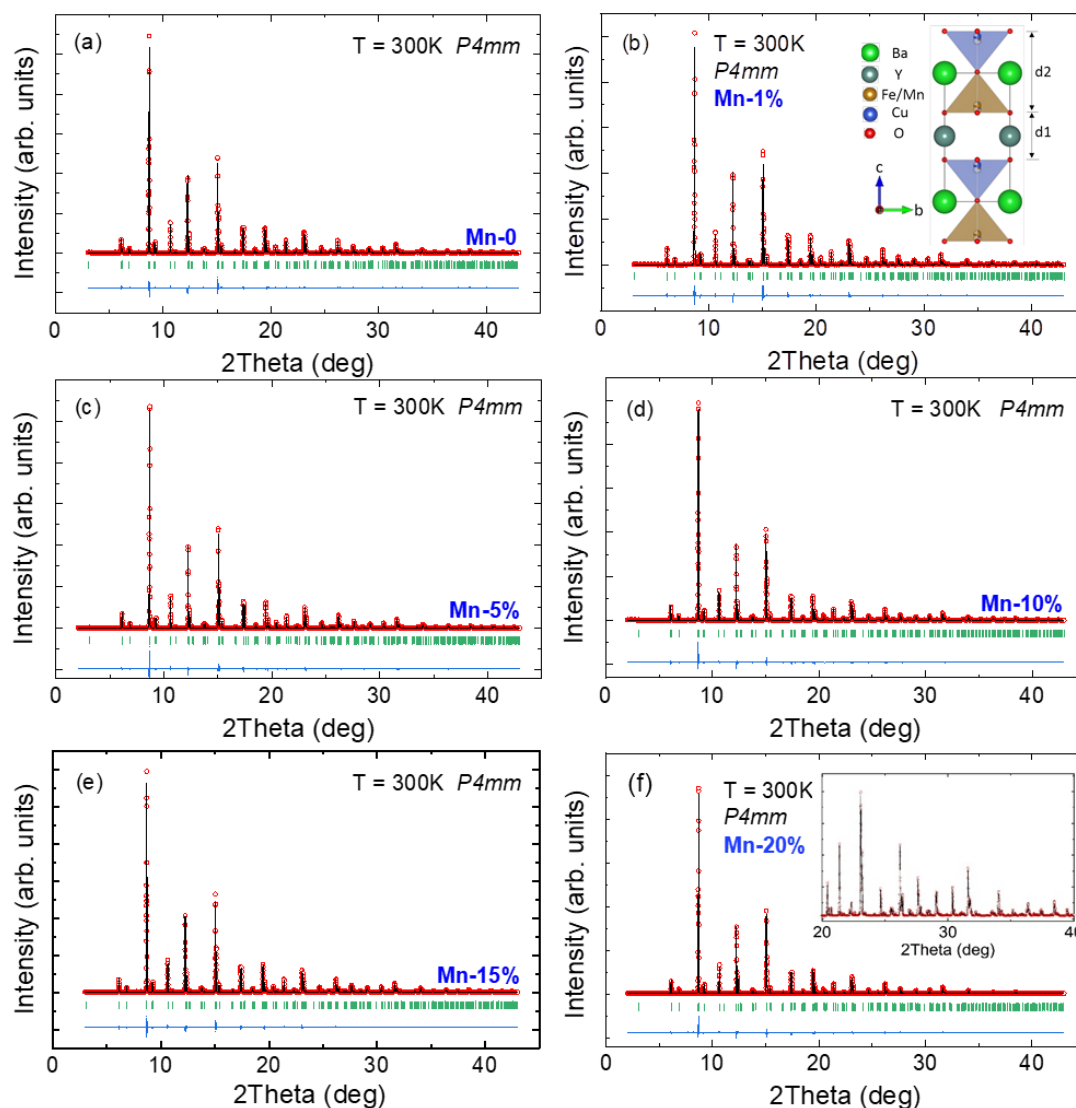


Figure 4.4. Rietveld refinement (black curve) of the synchrotron x-ray powder diffracted intensities (red circles) at 300K. Data collected in MSPD@ALBA ( $\lambda=0.41338(4)$  Å). Green bars are calculated Bragg reflections, bottom blue line is the observed-calculated difference. (a) Mn-0%; (b) Mn-1%. Inset: projection of the  $P4mm$  structure showing the  $d1$  (the separation between bipyramid layers) and  $d2$  (thickness of bipyramid layers) distances; (c) Mn-5%; (d) Mn-10%; (e) Mn-15%; (f) Mn-20%. Inset: details of the high-angles region.

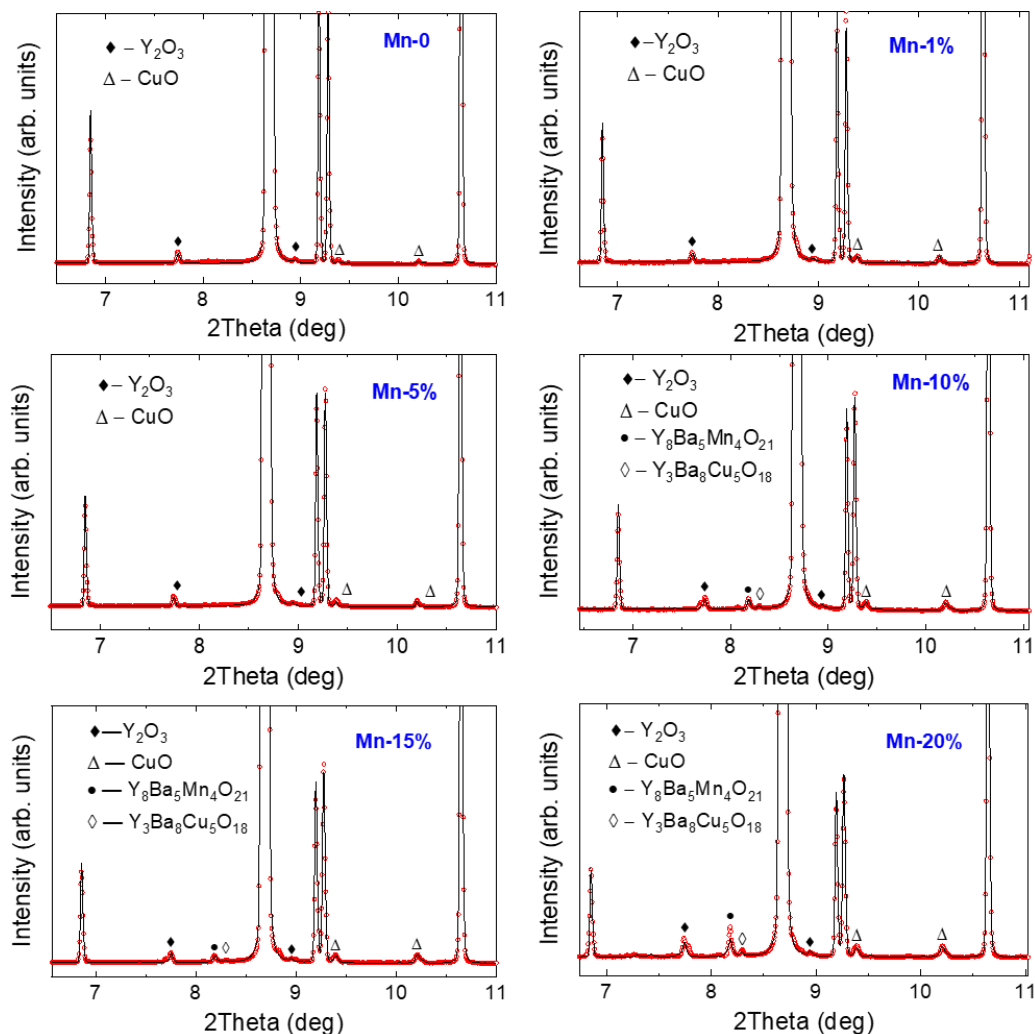


Figure 4.5. Rietveld refinement (black curve) of the secondary phases detected using the synchrotron x-ray powder diffraction data (red circles) from MSPD@ALBA ( $\lambda=0.41338$  (4) Å) at 300K.

**Table 4.1.** Secondary phases (unit in wt%) obtained from SXPd data collected in MSPD@ALBA ( $\lambda=0.41338$  (4) Å).

Mn doping x (%)	Y <sub>2</sub> O <sub>3</sub>	CuO	Y <sub>8</sub> Ba <sub>5</sub> Mn <sub>4</sub> O <sub>21</sub>	Y <sub>3</sub> Ba <sub>8</sub> Cu <sub>5</sub> O <sub>18</sub>	Purity (%)
0	0.27 (3)	0.15 (4)	—	—	99.58
1	0.22 (3)	0.30 (4)	—	—	99.48
5	0.24 (3)	0.25 (9)	—	—	99.51
10	0.30 (3)	0.58 (5)	0.19 (3)	0.09 (3)	98.84
15	0.34 (3)	0.64 (5)	0.28 (4)	0.10 (6)	98.65
20	0.59 (3)	0.92 (5)	0.73 (4)	0.16 (5)	97.60

### 4.3.2 Structural evolution

Table 4.2 reports structural parameters and agreement factors obtained from Rietveld refinement at 300 K as a function of the manganese content. We refined the two transition metal positions and the respective fractions of Cu and (Fe, Mn) ions in each pyramid, the upper (brown) and the lower (blue) pyramids within the unit cell [see inset of Figure 4.4 (b)]. For a proper refinement of the positions and the fractions of the metals in the pyramids, the z-coordinates of the two positions that a given metal M (either Fe/Mn or Cu) occupy in the cell (M1 and M2) were refined under the constraint  $z(\text{M1}) + z(\text{M2}) = 1$ .

**Table 4.2.** Structural parameters at T=300K and agreement factors obtained from the Rietveld refinement of MSPD@ALBA synchrotron data ( $\lambda=0.41338(3)$  Å). (\*: minority fraction; †: occupation of the majority cation in each pyramid). The coordinates of the two positions (M1 and M2) for each metal are related by  $z(\text{M1}) + z(\text{M2}) = 1$ .

YBaCuFe <sub>1-x</sub> Mn <sub>x</sub> O <sub>5</sub>	x=0	x=0.01	x=0.05	x=0.10	x=0.15	x=0.20
a	3.87463(3)	3.87439(3)	3.87354(3)	3.87274(4)	3.87189(4)	3.87052(5)
c	7.66267(5)	7.66349(6)	7.66479(6)	7.66816(8)	7.67013(8)	7.67265(9)
v	115.038(1)	115.036(1)	115.005(2)	115.008(2)	114.987(2)	114.943(2)
z (Y) (0 0 z)	0.5097(5)	0.5096(5)	0.5116(4)	0.5105(5)	0.5036(5)	0.5031(6)
z (Fe1) (½ ½ z)	0.7540(6)	0.7507(7)	0.7551(6)	0.7538(6)	0.7543(7)	0.7524(6)
z (Cu1) (½ ½ z)*	0.7145(3)	0.7156(3)	0.7150(3)	0.7153(2)	0.7184(4)	0.7162(3)
z (Cu2) (½ ½ z)	0.2855(3)	0.2844(3)	0.2850(3)	0.2847(2)	0.2816(4)	0.2838(3)
z (Fe2) (½ ½ z)*	0.2460(6)	0.2493(7)	0.2449(6)	0.2462(6)	0.2457(7)	0.2476(6)
z (O <sub>1</sub> ) (½ ½ z)	0.010(3)	0.008(3)	0.011(3)	0.011(3)	0.009(3)	0.007(3)
z (O <sub>2</sub> ) (0 ½ z)	0.327(1)	0.325(1)	0.327(1)	0.325(1)	0.324(1)	0.320(2)
z (O <sub>3</sub> ) (0 ½ z)	0.693(1)	0.691(1)	0.697(1)	0.696(1)	0.697(1)	0.695(2)
Occ (majority) <sup>†</sup>	0.772(22)	0.764(24)	0.704(22)	0.688(26)	0.671(28)	0.668(28)
$\chi^2$	50.0	67.5	70.9	57.6	61.2	60.8
$R_B$	6.02	5.27	5.44	4.57	3.80	4.90
$R_f$	7.28	6.24	7.16	5.97	4.30	5.90

**Table 4.3.** Refined structural parameters at 300 K using the space group  $P4mm$  and main interatomic distances (Å) for the same undoped ( $x=0$ ) sample from SXPB and high-resolution NPD data. Synchrotron and neutron patterns were collected respectively in MSPD@ALBA ( $\lambda=0.41338$  (4)Å) and in D2B@ILL ( $\lambda= 1.594$  Å). The structure for the YBCFO sample reported in Ref. [44] is also compared in the table.

YBaCuFeO <sub>5</sub>	MSPD (this work)	D2B (this work)	HRPT (Ref. [44]*)
a	3.87463(3)	3.87424(1)	3.87325(1)
c	7.66267(5)	7.66036(3)	7.6655(3)
z (Y) (0 0 z)	0.5097(5)	0.5036(7)	0.5053(16)
z (Ba) (0 0 z)	0	-0.0112(4)	0
z (Cu1) ( $\frac{1}{2}$ $\frac{1}{2}$ z)	0.7145(3)	0.7149(4)	0.7144(7)
z (Fe1) ( $\frac{1}{2}$ $\frac{1}{2}$ z)	0.7540(6)	0.7466(4)	0.7484(8)
z (Cu2) ( $\frac{1}{2}$ $\frac{1}{2}$ z)	0.2855(3)	0.2851(4)	0.2856(7)
z (Fe2) ( $\frac{1}{2}$ $\frac{1}{2}$ z)	0.2460(6)	0.2534(4)	0.2516(8)
z (O1) ( $\frac{1}{2}$ $\frac{1}{2}$ z)	0.010(3)	0.0112(4)	0.0179(15)
z (O2) (0 $\frac{1}{2}$ z)	0.327(1)	0.3233(6)	0.3265(15)
z (O3) (0 $\frac{1}{2}$ z)	0.693(1)	0.6921(6)	0.6947(15)
Occ (majority)	0.772(22)	0.624(20)	0.703(2)
$\chi^2$	50.0	8.93	1.98
$R_B$	6.02	2.50	3.81
$R_f$	7.28	1.64	3.86
d(Fe-Oa)	1.962(16)	2.027(4)	2.066
d(Fe-Ob)	1.992(4)	1.982(1)	1.980
d(Cu-Oa)	2.107(16)	2.098(4)	2.052
d(Cu-Ob)	1.963(4)	1.959(1)	1.962
d(Fe-Cu)	0.303 (5)	0.247 (4)	0.261

Table 4.3 compares the structural results of the Rietveld fits for the YBCFO reference sample of this work obtained from high-resolution SXPB and NPD data. Moreover, they are also compared to the reported structure of YBCFO sample in ref.[44]. Figure 4.6 plots the Rietveld refinement of the high-resolution NPD data recorded on D2B at ILL for our undoped ( $x=0$ ) YBCFO sample. All these comparisons confirm the reliability of our structural refinements.



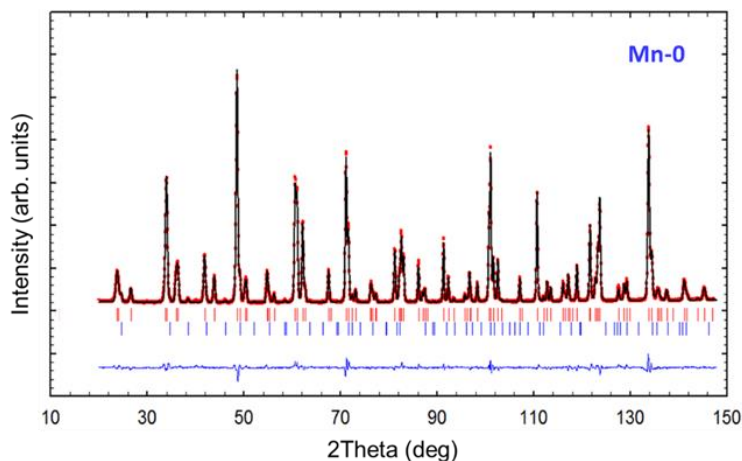


Figure 4.6. Rietveld refinement (black curve) of the D2B neutron diffraction pattern (red points) collected at 300 K ( $\lambda = 1.594 \text{ \AA}$ ) for the YBCFO ( $x=0$ ) sample. The bottom blue line is the difference between the experimental and calculated intensities. The first row of red bars correspond to the structural phase and the second row (blue) to the collinear magnetic phase.

Figure 4.7 (a) plots the evolution of the cell dimensions as a function of the Mn doping. There is an overall shrinkage of the unit cell volume with increasing the Mn concentration which is principally produced by a contraction of the  $a$  parameter and the  $a$ - $b$  ( $b=a$ ) plane. On the contrary, this figure shows a systematic increase of the  $c$  parameter and of the tetragonal distortion represented by the quotient  $c/2a$ . The observed expansion of the vertical  $c$  axis is likewise closely associated to the evolution of  $d_1$  and  $d_2$ , the two main distances that characterize the  $[\text{CuFeO}_9]$  bilayers of corner-sharing square pyramids [46]. They are shown in Figure 4.4 (b). Distance  $d_1$  refers to the separation between bilayers and  $d_2$  represents the thickness of each individual bilayer, i.e. the height of the unit formed by two corner-sharing  $\text{MO}_5$  square pyramids (bipyramid; M: metal). In this structure the height ( $d_2$ ) of the  $\text{CuFeO}_9$  bipyramids is longer than the distance  $d_1$  between them ( $d_1 < d_2$ ).

The evolution of the characteristic distances  $d_1$  and  $d_2$  with different doping level was illustrated in Figure 4.7 (b). There is a monotonous expansion of the separation between bipyramids ( $d_1$ ):  $\Delta d_1 \approx +0.072 \text{ \AA}$  up to Mn-20% sample. Moreover, the thickness of the bipyramid layer ( $d_2$ ) decreases:  $\Delta d_2 \approx -0.064 \text{ \AA}$  up to 20% Mn. The expansion of  $d_1$  is more pronounced than the contraction of  $d_2$  producing the increase

of  $c$ . The evolution of the ratio  $d1/d2$  is also depicted.

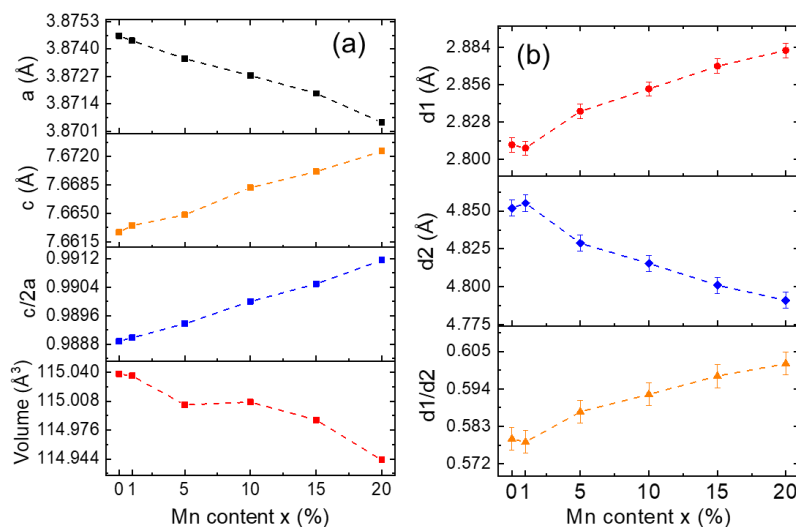


Figure 4.7. (a) Evolution of the cell parameters and volume of  $\text{YBaCuFe}_{1-x}\text{Mn}_x\text{O}_5$  samples with Mn doping; (b) Evolution of the characteristic distances  $d1$  (separation between bilayers),  $d2$  (thickness of bilayers) and the  $d1/d2$  ratio.

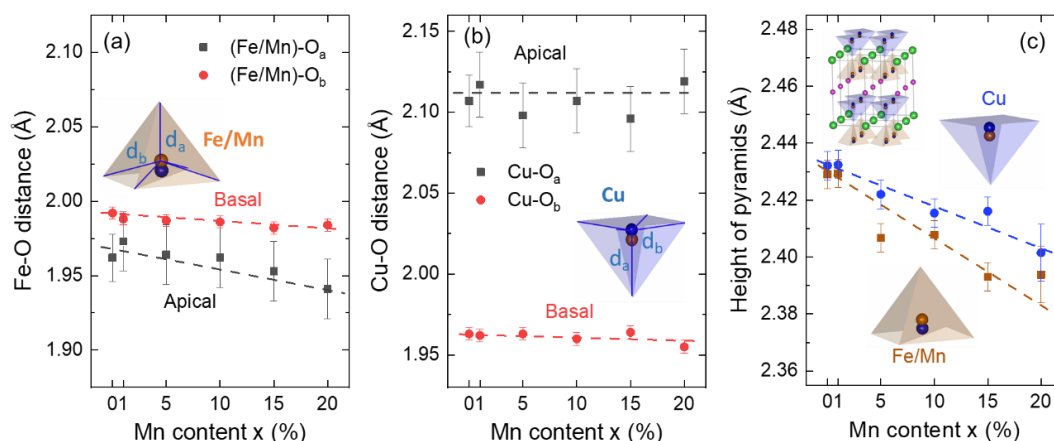


Figure 4.8. Evolution of the (a) (Fe/Mn)-O and (b) Cu-O interatomic distances at room temperature in respectively the upper and lower pyramids of the chemical unit cell, where  $d_a$ =‘apical’ and  $d_b$ =‘basal’ (equatorial) distances in pyramidal coordination. Insets: upper (brown) and lower (blue) pyramids in the unit cell. (c) Height of the  $[\text{Fe/Mn}]\text{O}_5$  and  $\text{CuO}_5$  pyramids. Inset: projection of the structure showing the  $[\text{CuFeO}_9]$  bilayers of corner-sharing square pyramids (green atoms: Ba; red: Y). The color of each pyramid corresponds to the color of the dominant cation in it.

A look to the refined interatomic distances reveals very small variations with Mn content. We can see in Figure 4.8(b) that the Jahn-Teller (J-T) splitting between basal and apical distances around Cu is preserved along the series. No apparent changes are detected in either the large difference between the interatomic Cu-O<sub>a</sub> (apical) or Cu-O<sub>b</sub>

(basal) distances of the CuO<sub>5</sub> pyramids (the J-T distortion around Cu<sup>2+</sup> sites ( $t_{2g}^6 e_g^3$ )). It is thus confirmed that the large splitting between shorter Cu-Ob bonds and a much longer apical Cu-Oa distance is not modified. On another hand Mn<sup>3+</sup> is also a potential J-T active ion due to its nominal  $t_{2g}^3 e_g^1$  electronic configuration. For the case of a Mn<sup>3+</sup>O<sub>5</sub> coordination polyhedron, Millange *et al.* reported the crystal structure of the related oxide YBaMn<sub>2</sub>O<sub>5</sub> [89]. In this compound, having a similar structure as YBaCuFeO<sub>5</sub>, the occurrence of Mn<sup>2+</sup>/Mn<sup>3+</sup> charge order (perfect order in the A and B sites of the perovskite) results in the presence of two different sites for the two manganese ions and  $P4/nmm$  symmetry. The bipyramids are formed by one regular and one distorted pyramid. For the pyramidally coordinated Mn<sup>3+</sup>, the  $d_z^2$  orbital extends along  $c$  and the unoccupied  $d_x^2-y^2$  orbital along [110] and [1-10], producing four basal Mn-Ob distances of 1.917 Å and one apical Mn-Oa distance of 2.048 Å [89]. This large J-T splitting would produce an enlargement of the apical Fe-Oa bonds if Mn<sup>3+</sup> adopted the same electronic configuration in YBaCuFe<sub>1-x</sub>Mn<sub>x</sub>O<sub>5</sub>. Interestingly, the evolution of the apical and basal distances displayed in Figure 4.8(a) strongly suggests that in this series Mn ions do not adopt the J-T configuration  $t_{2g}^3 e_g^1$  with the  $d_z^2$  orbital pointing along [001]. The expected enlargement in the apical Fe-Oa distance as a larger fraction of Mn substitutes Fe atoms is at odds with these results. Instead, Figure 4.8(a) suggests a slight shrinking in the average Fe-Oa bond of the (Fe,Mn)O<sub>5</sub> pyramids when increasing the presence of Mn. Although a variety of orbitally ordered and disordered states have been observed in different manganites containing Mn<sup>3+</sup> ions during the last decades, a very specific feature in YBaCuFe<sub>1-x</sub>Mn<sub>x</sub>O<sub>5</sub> is the concurrence of two potential strong J-T active cations (Cu<sup>2+</sup> and Mn<sup>3+</sup>) in bipyramids where CuO<sub>5</sub> and MnO<sub>5</sub> units are sharing the apical oxygen. The evolution of the interatomic distances could indicate that the robust J-T distortion confirmed in CuO<sub>5</sub> pyramids is impeding the deformation of the MnO<sub>5</sub> polyhedra in the CuMnO<sub>9</sub> bipyramids. The simultaneous coexistence in a bipyramid of (i) a J-T distorted Cu<sup>2+</sup> pyramid, very elongated, and (ii) a J-T  $t_{2g}^3 e_g^1$  Mn<sup>3+</sup> ion with the  $d_z^2$  orbital pointing parallel to the Cu-Oa bond along  $z$ , very likely, has a

too high energy penalty. The same conclusion is drawn by the evolution of the heights in the upper (Fe) and lower (Cu) pyramids displayed in Figure 4.8(c). Additional spectroscopic studies (preferably on single crystals) are needed to get a more complete description of the local electronic structure in this series.

Given the importance of how Fe/Cu atoms are distributed throughout the crystal structure, Table 4.2 also unveils the fraction of Cu atoms that occupy Fe sites. A first appealing result in this series, which were prepared using the same cooling rate is that the presence of a third metal (Mn) systematically increases the degree of Fe/Cu chemical disorder. A certain chemical disorder is a prerequisite for the magnetic order in this structure to evolve from the commensurate to the incommensurate phase. So, from the evolution of the occupation at B-sites depicted in Figure 4.9, one can see that chemical disorder increases from  $n_d \sim 23\%$  without Mn up to  $n_d \sim 33\%$  in the Mn-20% sample ( $n_{oc}[\text{minority}] = n_d$ , level of chemical disorder). It is worth underlying that this is a remarkable relative raise ( $\sim 40\%$ ) achieved in samples prepared using the same synthesis process and an identical cooling rate of 300 K/h.

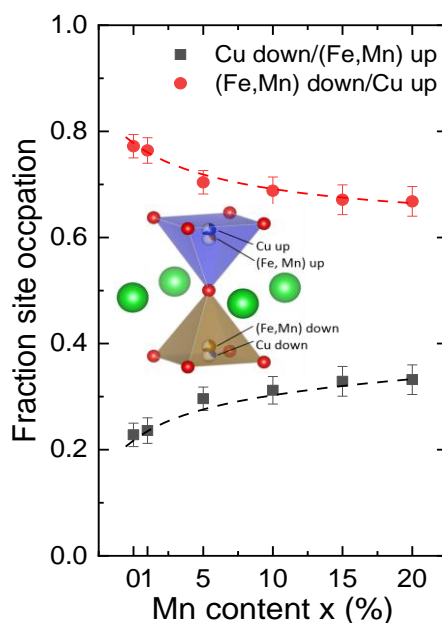


Figure 4.9. Evolution with Mn doping of the average site occupation in the bipyramids of  $\text{YBaCuFe}_{1-x}\text{Mn}_x\text{O}_5$  samples prepared following the same cooling process (300 K/h).

## 4.4 Neutron powder diffraction analysis

### 4.4.1 Magnetic transitions

NPD experiments were carried out at the high-flux reactor of the Institut Laue Langevin (Grenoble, France) using the high intensity diffractometer D1B ( $\lambda=2.52$  Å). The polycrystalline samples were loaded inside a cylinder vanadium sample holder. With cryofurnace in D1B, NPD patterns were collected at fixed selected temperatures and in continuous mode following temperature ramps within the range 10 to 500 K with a heating rate of 3 K/min.

In Figure 4.3, we plotted the magnetic susceptibility measurements of YBaCuFe<sub>1-x</sub>Mn<sub>x</sub>O<sub>5</sub> samples, as performed in a dc magnetic field of 2 kOe in FC condition from 10 K to 600 K. As expected, the Néel temperature undergoes a certain decrease when reducing the concentration of Fe<sup>3+</sup> ions in the structure. Two separated magnetic transitions were observed in all compositions, associated respectively to the onset of the CM ( $T_{N1}$ ) and the ICM ( $T_{N2}$ ) magnetic orders. This was further confirmed by neutron diffraction.

All compositions were characterized by neutron diffraction in the 10 K-500 K range, using the D1B diffractometer. Upon cooling from 500K two distinct sets of new magnetic Bragg reflections appear at  $T_{N1}$  and  $T_{N2}$ . First, new peaks indexed as  $(h/2, k/2, l/2)$  appear at  $T_{N1}$  ( $>350$  K, for all the samples), associated to the propagation vector  $\mathbf{k}_1 = (1/2, 1/2, 1/2)$  (A-point of the Brillouin Zone). Upon further cooling new magnetic peaks compatible with the incommensurate propagation vector  $\mathbf{k}_2 = (1/2, 1/2, 1/2 \pm q)$  emerge at  $T_{N2}$  ( $<250$  K for all the samples) and persist down to base temperature. The T-x phase diagram for YBaCuFe<sub>1-x</sub>Mn<sub>x</sub>O<sub>5</sub> samples is shown in Fig. 4.10(a).

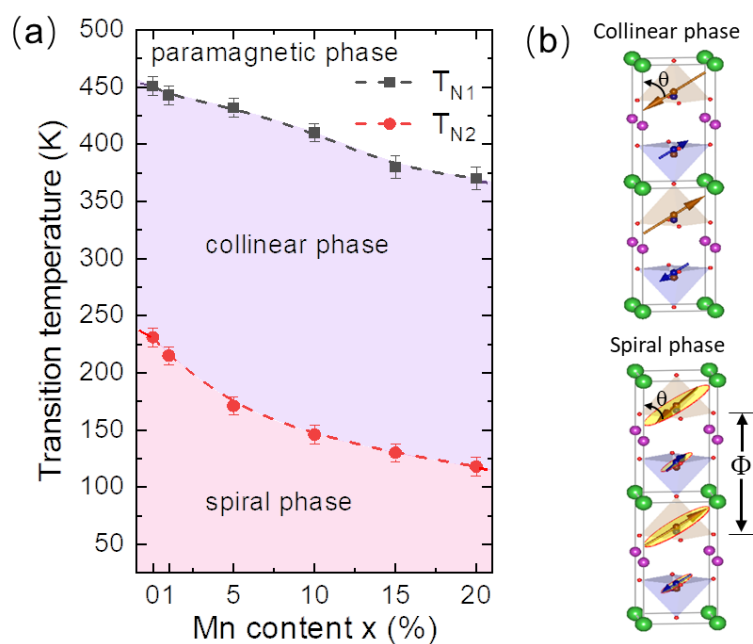


Figure 4.10. (a) T-x phase diagram for  $\text{YBaCuFe}_{1-x}\text{Mn}_x\text{O}_5$  samples. The phase boundaries describe the onset of the magnetic phase according to neutron diffraction data. (b) Sketch of the CM collinear ( $T_{N1}$ ) and ICM spiral ( $T_{N2}$ ) magnetic phases showing the tilting angle  $\theta$ . The rotation angle  $\Phi$  between successive spins along the  $c$  axis deviates from  $180^\circ$  in the ICM phase. For clarity, the average magnetic moment is depicted in each pyramid in the structure using the color of the majority metal.

The partial decrease of  $T_{N1}$  is due to a combination of factors: lattice and structural tuning effects, the increase of chemical disorder and also the changes in the NN exchange constants due to the substitution of Fe by Mn atoms. The decrease of the spiral transition temperature ( $T_{N2} = T_S$ ) is not explained by lattice effects or the increase of the Fe/Cu cation disorder that would raise  $T_S$ . In the light of the model developed by Scaramucci and co-workers [84][85] the decrease should be mainly attributed to the changes in the magnetic exchange couplings parallel to the  $c$  axis, but not only. Essential ingredients of the model are the exchange interactions within the bipyramids. So, a fraction of the strong AFM  $\text{Fe}^{3+}\text{-O-Fe}^{3+}$  bonds (the strongest coupling) would be substituted by the much weaker  $\text{Fe}^{3+}\text{-O-Mn}^{3+}$  (or  $\text{Mn}^{3+}\text{-O-Mn}^{3+}$ ) AFM coupling. In the mentioned theoretical Heisenberg model, the presence of a fraction of very strong AFM  $\text{Fe}^{3+}\text{-O-Fe}^{3+}$  bonds is required. They act as dilute impurity bonds in that generate enough frustration to induce a local canting of the FM spin pairs in the  $\text{Fe}^{3+}\text{-Cu}^{3+}$

bipyramids. If instead of a FM Fe-Cu pair, the bipyramid is formed by a Mn<sup>3+</sup>-Cu<sup>3+</sup> pair (with, respectively, single and double d<sub>z</sub><sup>2</sup> orbital occupation) the Goodenough-Kanamori-Anderson (GKA) rules [76][90][91] also predict ferromagnetic exchange between them. Instead, an AFM coupling is predicted if the single e<sub>g</sub> occupation in Mn<sup>3+</sup> ions would occur in d<sub>x</sub><sup>2</sup>-y<sup>2</sup> orbitals. In the model the long range coupling between locally-canted spins takes place favored by the orientation of these impurity bonds always parallel to the *c* axis [84][85].

On the other hand, some of the pristine J<sub>ab</sub> antiferromagnetic exchanges (Cu-Cu, Fe-Cu and Fe-Fe pairs) in the *ab* plane would probably be substituted by ferromagnetic couplings, associated to Cu<sup>2+</sup>-Mn<sup>3+</sup> or Fe<sup>3+</sup>-Mn<sup>3+</sup> NNs pairs in the plane, thus disturbing the AFM correlations perpendicular to *c*. It should also be pointed out that our structural results are at odds with the expected evolution for the usual J-T configuration in pyramidally coordinated Mn<sup>3+</sup> (with the d<sub>z</sub><sup>2</sup> orbital pointing along the vertical axis of the pyramid). Therefore, further investigations of the local electronic structure would be desirable to unambiguously determine some of the actual new exchange couplings associated to the presence of Mn.

Figure 4.11 compares the low-angle region of the neutron patterns collected at 10 K for all compositions. A systematic evolution is observed when increasing the amount of Mn substitution. As Mn replaces Fe both the ICM and CM magnetic phases coexist, but the relative weight of the latter grows with *x*. Thus, in Mn-20% both phases still coexist but the CM phase is largely dominant over the ICM one. This evolution in the relative intensities of the magnetic peaks associated to the CM and the ICM propagation vectors indicates that they are due to two separate magnetic phases (not a multi-*k* structure).

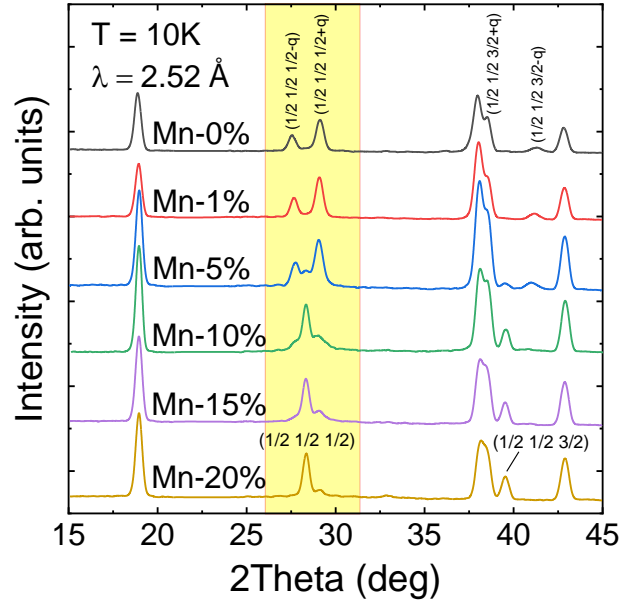


Figure 4.11. Low-angle region of the neutron diffraction patterns collected at 10 K (D1B@ILL,  $\lambda = 2.52 \text{ \AA}$ ) for samples with increasing levels of Mn content.

#### 4.4.2 Temperature dependence

NPD patterns were collected using the continuous mode in the high intensity diffractometer D1B, with excellent resolution at low-Q and a high efficiency position sensitive detector covering the angular range up to  $129^\circ$ . Around 50 patterns were recorded in the range 10 K-500 K, with a temperature step of 9 K between successive patterns. Figure 4.12(a) plots a T-Q projection of the neutron-diffracted intensities in a selected angular range, around the  $(1/2 \ 1/2 \ 1/2)$  reflection. The evolution of the main magnetic reflections is shown between 10 K and 500 K, illustrating the onset and evolution of the two magnetic phases. The splitting of the  $\mathbf{k}_1 = (1/2, 1/2, 1/2)$  reflections into two satellites signals the onset of the ICM modulation associated to the translational symmetry along the  $c$  axis. The magnetic modulation parameter  $q(T)$  appears at  $T_{N2}$  and progresses until it reaches its maximum amplitude  $q_0$ .

Neutron powder diffraction data are compatible with an ICM spiral phase below  $T_{N2}$ :

$$\mathbf{m}_{lj}(\mathbf{k}) = M_R(\mathbf{m})(\mathbf{u}_j) \cos(2\pi\{\mathbf{k} \cdot \mathbf{R}_l + \Phi_j\}) + M_I(\mathbf{m})(\mathbf{v}_j) \sin(2\pi\{\mathbf{k} \cdot \mathbf{R}_l + \Phi_j\}) \quad (\text{eq. 4.1})$$



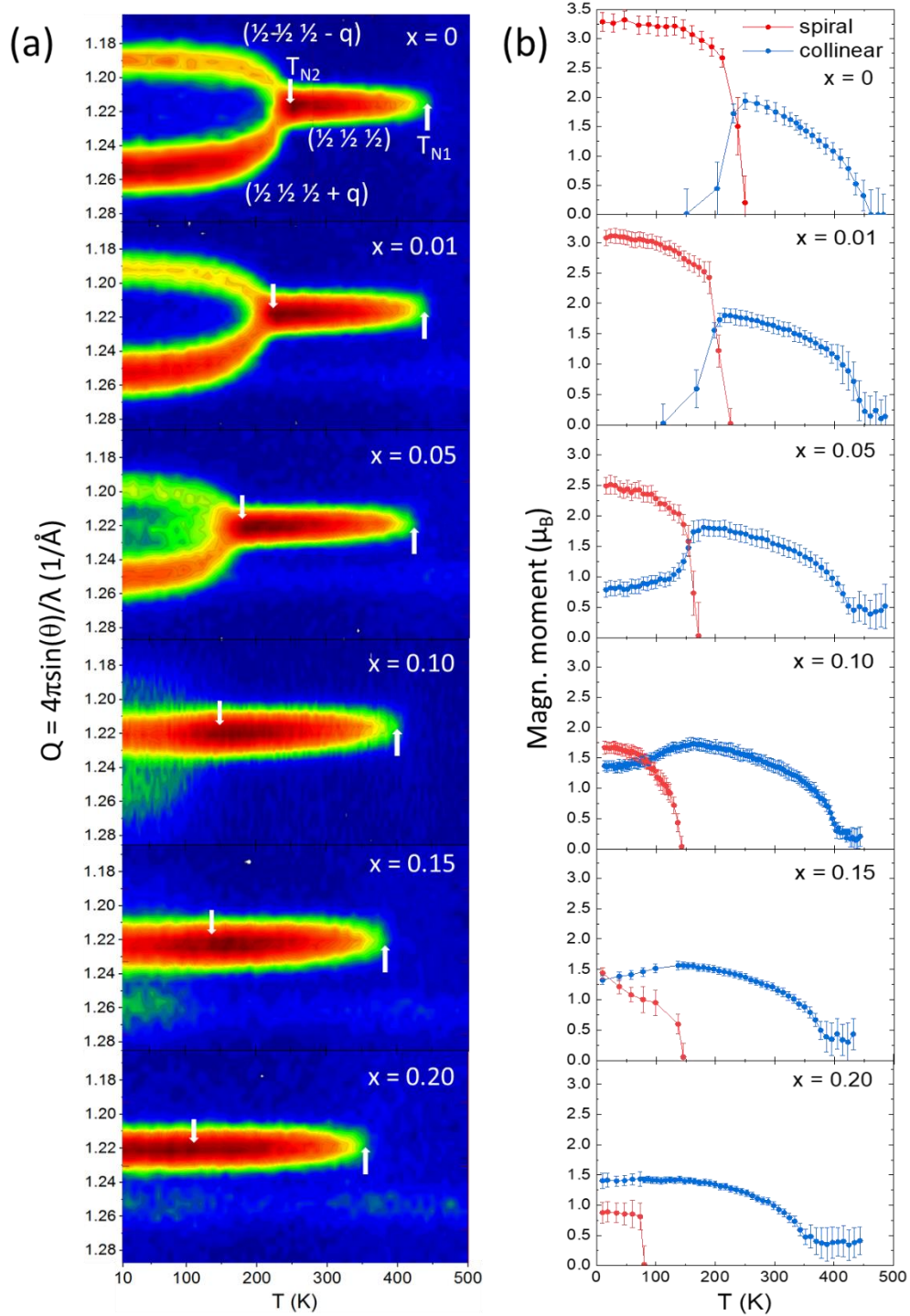


Figure 4.12. (a) T-Q projection of the temperature dependence for the neutron-diffracted intensities around  $(\frac{1}{2} \frac{1}{2} \frac{1}{2})$  reflection. Evolution with the Mn content (D1B@ILL,  $\lambda = 2.52$  Å). (b) T-dependence of the (average) ordered magnetic moments associated to the CM and ICM phases.

where  $\mathbf{m}_j$  is the magnetic moment of the atom  $j$  in the unit cell  $l$ ,  $\mathbf{R}_l$  is the vector joining the arbitrary origin to the origin of unit cell  $l$ , and  $\Phi_j$  is a magnetic phase.  $\mathbf{u}_j$  and  $\mathbf{v}_j$  in eq. [4.1] define the orientation of the two perpendicular axes that fix the plane of the

helix, where  $M_R$  (real) and  $M_I$  (imaginary) amplitudes determine the ellipse that envelops the magnetic moments. Due to the intrinsic limitations of the data collected on powder samples (distinct magnetic peaks can share the magnitude of momentum transfer wave vector) it is not possible to independently refine parameters such as the real and imaginary amplitudes ( $M_R$  and  $M_I$ ), forcing us to fix their ratio using constraints. The moments at the  $\text{Cu}^{2+}$  and  $\text{Fe}^{3+}$  sites of the cell were restricted to the same inclination angle  $\theta$  in the neutron refinements. The phase difference  $\varphi$  between the magnetic moments at the two sites was fixed to  $180^\circ$  as found in the YBCFO single-crystal study of ref. [86], and in earlier refs. [44][45][21]. The relative intensities of the two satellites ( $1/2 \ 1/2 \ 1/2 \pm q$ ) in Figure 4.14 indicate that  $\varphi$  does not deviate from  $180^\circ$  by doping. In the Figure 4.12(b) we have plotted the refined (average) magnetic moments for each one of these phases and their evolution up to 500K. In these figures the ICM and CM magnetic moments are referred to the full amount of sample. Moreover, their values correspond to ordered moments averaged over Fe and Cu sites, and (for the spiral phase) in the limit  $M_R \gg M_I$ .

Regarding the magnetic moments the neutron patterns were refined within two imposed limits: (i)  $m(\text{Fe})=5m(\text{Cu})$  (as the ratio of their respective unpaired spins), for the lowest-disorder case; and (ii)  $m(\text{Fe})=m(\text{Cu})$ , for the highest-disorder limit. In addition, for the ICM/spiral phase we considered two limits in the refinements: the limit  $M_R \gg M_I$  (high eccentricity) and the circular ellipse model ( $M_R=M_I$ ). Similar agreement factors were obtained in all cases.

The evolution of the ordered moments with the fraction of Mn shown in Figure 4.13(a) and Table 4.6 reveals that the ordered moment at Fe/Mn sites decreases faster than expected when substituting  $S=5/2$   $\text{Fe}^{3+}$  spins by  $S=2$   $\text{Mn}^{3+}$  spins. Moreover, it neither can be ascribed to the increase of chemical disorder between divalent and trivalent ions. Instead, the observed evolution should be attributed to enhanced magnetic frustration by the presence of Mn ions. The magnitude and the sign of some of the pristine interactions should change when  $\text{Fe}^{3+}$  is substituted by  $\text{Mn}^{3+}$  increasing

frustration. So, for example, the GKA rules for the  $\text{Mn}^{3+}/\text{Cu}^{2+}$  and  $\text{Mn}^{3+}/\text{Fe}^{3+}$  pairs of NNs in this square-pyramidal arrangement predicts FM couplings within the  $ab$  plane.

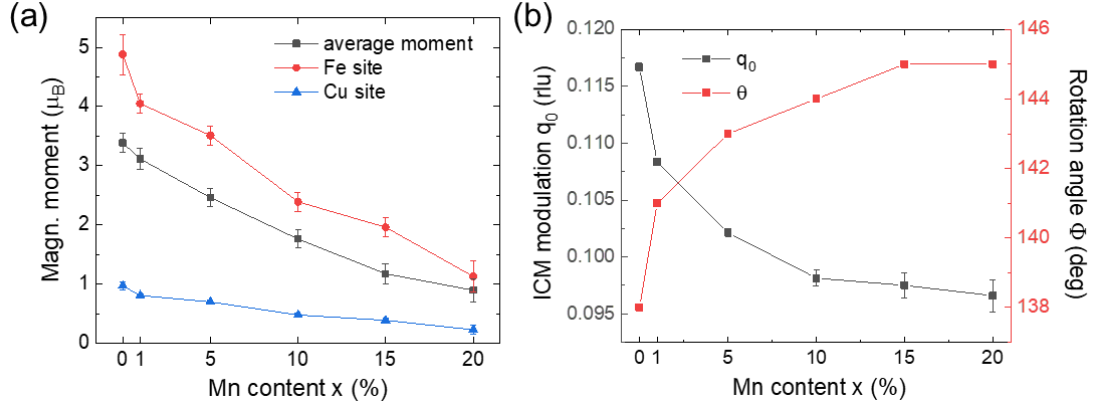


Figure 4.13. Evolution of the ICM magnetic phase with Mn content. (a) Ordered magnetic moments at 10 K (referred to the full sample and  $M_R \gg M_I$ ). Blue and red dots correspond to the case where a constraint in the form  $m(\text{Fe})=5m(\text{Cu})$  gets applied. Black dots correspond to the case where the same average moment is refined at Cu and Fe sites; (b) ICM  $q_0$  modulation component and associated spin rotation angle  $\Phi$  ( $\Phi$ ) between successive bilayers.

This is in contrast to the pristine compound (YBCFO), where NN couplings in that plane are always AFM, independently of the  $\text{Fe}^{3+}/\text{Cu}^{2+}$  distribution. Within a bipyrmaid formed by two elongated  $\text{Cu}^{2+}$  ( $3d^4$ ) and  $\text{Mn}^{3+}$  ( $3d^9$ ) pyramids (with the occupied  $d_z^2$  orbital along  $[001]$ ) one would expect FM coupling along  $c$ . However, the formation of such Jahn-Teller Cu-Mn bipyramids is presumably energetically more expensive than other configurations.

In addition, the evolution with the Mn content of the incommensurability parameter  $q_0$  is plotted in Figure 4.13(b).  $q_0$  corresponds to the maximum amplitude of the ICM modulation. The amplitude  $q_0$  of the incommensurability is a measurement of the magnetic rotation of the spin moments between two successive bilayers or, in other words, between two successive unit cells along the  $c$  axis [see Figure 4.10(b)]. In the same plot of the Figure 4.13(b) we show the  $\Phi$  values as determined for the different compositions. The  $q_0$  ( $x_{\text{Mn}}$ ) evolution is clearly nonlinear and reaches a kind of asymptotic or constant value for  $x > 10\%$  Mn of  $q_0 \approx 0.098$  rlu ( $\Phi = 215.3^\circ$ ). This value is

far from the commensurate limit. Therefore, this evolution suggests that increasing  $x$  further than 10% Mn produces a reduction of the ICM phase in favor of the CM collinear order, whose spatial distribution is related or conditioned by the local distribution of Mn ions.

#### 4.4.3 Easy axis and magnetic plane inclination

As already said, the angle  $\theta$  represents the angular distance (tilting) between the  $c$  axis and the direction of the spins, namely (i) the collinear spins direction  $\mathbf{u}$  in the CM phase ( $T < T_{N1}$ ) or (ii) the rotation plane of the helix in the spiral ICM magnetic phase ( $\mathbf{u}$ - $\mathbf{v}$  plane at  $T < T_{N2}$ ). Due to the tetragonal symmetry the orientation of the moments in the  $\mathbf{ab}$  plane cannot be determined from neutron diffraction data on powder samples. Hence, for simplicity, the director vector  $\mathbf{u}$  can be taken as within the  $\mathbf{ac}$ -plane,  $\mathbf{v}$  being thus parallel to the  $\mathbf{b}$  axis. A  $\theta$  value close to  $0^\circ$  means that the easy-axis is close to the  $c$  axis, whereas for  $\theta \approx 90^\circ$  the easy-axis is within the  $\mathbf{ab}$ -plane. In the  $P4mm$  structure when  $\theta$  adopts intermediate values (different to  $0$  or  $90^\circ$ ) the magnetic arrangement according to  $\mathbf{k}_1$  or  $\mathbf{k}_2$  translational symmetries requires the concurrent activation of magnetic modes belonging to distinct irreducible representations (magnetic *irreps*) [44]. The temperature evolution of the tilting angle  $\theta$  was refined for all the samples between 10K and the onset of the paramagnetic phase using the ratio  $m(\text{Fe})=5m(\text{Cu})$ . Below  $T_{N2}$  we used the  $M_R \gg M_I$  limit that allows us to minimize the imprecision (errors) in the determination of  $\theta$ , maximizing accuracy. The full diffraction patterns were analyzed for all temperature values, using different magnetic phases for the sequential refinements above and below  $T_{N2}$ , respectively. Initially we used the structures showed in Table 4.2 and the six free structural coordinates in the structure ('z' coordinates) were refined as a function of temperature (in addition to temperature factors, cell dimensions, magnetic phases, etc..) but they did not show any thermal evolution and remained constant. The extracted magnetic parameters showed a good convergence and their refined values were the same both refining and keeping invariant the structural z-

coordinates. Figure 4.14 illustrates the results obtained for the six different compositions of YBaCuFe<sub>1-x</sub>Mn<sub>x</sub>O<sub>5</sub> studied.

The evolution of  $\theta$  (T, x) plotted in Figure 4.14 allows us to extract several appealing conclusions. First, within each magnetic regime the tilting  $\theta$  remains practically constant. We observe this behavior in all compositions. This result is at odds with some early interpretations of a continuous decrease of  $\theta$  when lowering temperature in YBCFO. Second, from present results the orientation of the easy axis is stable in the collinear regime, and equally the tilt of the plane of the helix does not appreciably vary below  $T_{N2}$ . However, we observe a sudden fall of the inclination around  $T_{N2}$ , coinciding with the CM-to-ICM transformation. Indeed Figure 4.14 shows a sudden drop of the tilting at the transition in all samples. Third, interestingly, the descent looks more pronounced by increasing the amount of substituted metal. Only in the sample with the highest doping (Mn-20%) the weakness of the ICM reflections precludes unambiguously determining its  $\theta$  value.

The refined magnetic moments [ $m(\text{Fe})=5m(\text{Cu})$ ] and tilting angles  $\theta(x)$  obtained refining the CM collinear phase at 300K and the ICM phase at 10K are given in Table 4.6. For the latter, the moments found using the two extreme models  $M_r \gg M_i$  (*Model1*) and  $M_r = M_i$  (*Model2*) are both shown. As expected, the refined moments using a sinusoidal modulated order (*Model1*) are greater than those obtained for a circular spiral (*Model2*). The value found at the Fe positions of YBCFO with *Model1* at 10 K (4.9(2)  $\mu_B/\text{Fe}$ ) is very close to the atomic moment for Fe<sup>3+</sup> ions. Although this value is too high and hardly compatible with the amount of chemical disorder in the sample, it cannot be taken to rule out *Model1* because it results from imposing a constraint over the ordered moments [ $m(\text{Fe})=5m(\text{Cu})$ ] in the bipyramid that represents the limit of full cationic order. A projection of the refined ICM magnetic order at 10K using *Model2* ( $M_r = M_i$ , circular spiral) is shown in Figure 4.15 for all doped compositions.

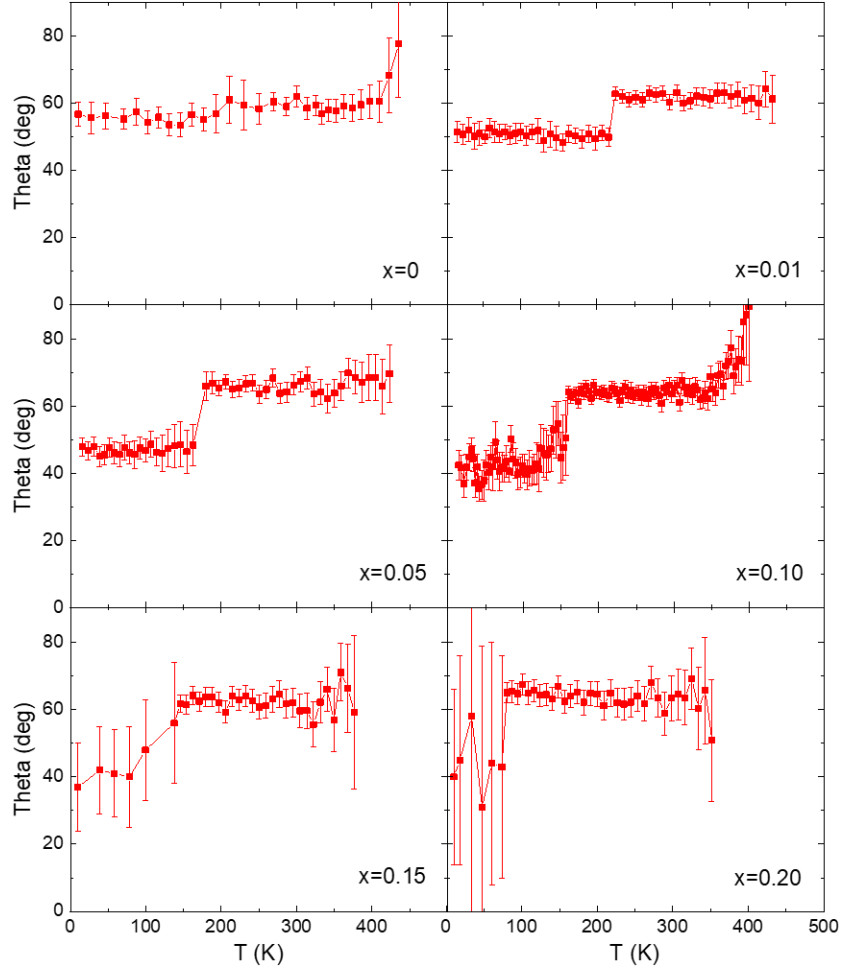


Figure 4.14. Temperature evolution of the inclination angle  $\theta$  of the collinear spins ( $T_{N2} < T < T_{N1}$ ) and of the helix rotation plane ( $T < T_{N2}$ ) in  $\text{YBaCuFe}_{1-x}\text{Mn}_x\text{O}_5$  samples for the different Mn contents.

**Table 4.4.** Refined Magnetic moments [imposing  $m(\text{Fe})=5m(\text{Cu})$ ] and inclination angles ( $\theta$ ) obtained refining the CM collinear phase at 300K and the ICM phase at 10K. At low temperature, the refined moments correspond to models  $M_r \gg M_i$  (*Model1*) and  $M_r = M_i$  (*Model2*).

sample	300 K (CM)		10 K (ICM)			
	<i>Collinear</i>		<i>Model1</i> ( $M_i \sim 0$ )		<i>Model2</i> ( $M_r = M_i$ )	
	$m(\text{Fe})$ ( $\mu_B$ )	Theta (deg)	$m(\text{Fe})$ ( $\mu_B$ )	Theta (deg)	$m(\text{Fe})$ ( $\mu_B$ )	Theta* (deg)
Mn-0	2.34 (2)	59 (2)	4.9 (2)	55 (5)	3.61 (4)	55
Mn-1%	2.31 (2)	62 (2)	4.1 (2)	52 (5)	2.94 (3)	52
Mn-5%	2.15 (2)	66 (2)	3.5 (2)	47 (6)	2.19 (3)	47
Mn-10%	1.91 (2)	64 (2)	2.4 (2)	43 (8)	1.78 (3)	43
Mn-15%	1.42 (2)	65 (3)	1.9 (2)	35 (12)	1.48 (3)	35
Mn-20%	1.36 (2)	65 (4)	1.1 (2)	55 (52)	0.86 (4)	55

Theta\* in Model2 is fixed to its refined value in Model1.

In Figure 4.16(a) we have represented the dependence of the tilting angle  $\theta$  in the CM collinear phase (at 300 K) and in the ICM regime (at 10K) with the amount of Mn. Hereafter we will associate the direction fixed by the Theta angle ( $\theta$ ) as the easy-axis of the system for each magnetic phase (although the tetragonal symmetry does not allow identifying the direction within the **ab**-plane). We find that the orientation (tilting) of the magnetic easy-axis in the ICM phase differs from the CM collinear phase because  $\theta_{ICM} < \theta_{CM}$ . Moreover, this difference systematically increases with  $x$ , being a measure of the previously mentioned drop at the CM-ICM transition. Most interestingly, the evolution shown in Figure 4.16(a) indicates that Mn substitution brings about a systematic reorientation of the plane of the helix. In such a way, the rotation plane tends to move away from the tetragonal **ab** plane approaching the **c** axis. Such evolution appears also illustrated in Figure 4.16(b). The observed rate is  $\Delta\theta/\Delta x \approx -1.33$  deg/%Mn. So, comparing the samples with  $x=0$  and  $x=0.15$  one can see a reorientation of the spiral plane (easy axis) of  $\Delta\theta \sim -20^\circ$ , from  $55^\circ$  to  $35^\circ$ . We must stress upon the fact that here the orientation of the plane of the helix respect to the **c** axis determines if the spiral order is of cycloid- ( $\theta \rightarrow 0^\circ$ ) or helix-type ( $\theta \rightarrow 90^\circ$ ). Consequently, the ICM magnetic phase in YBaCuFe<sub>1-x</sub>Mn<sub>x</sub>O<sub>5</sub> would evolve from an inclined helix towards a cycloid by increasing the Mn content (see Figure 4.16(b)). It is thus important to recall at this point that for an electrical polarization  $\mathbf{P}$  with origin at the antisymmetric Dzyaloshinskii–Moriya interaction, its dependence with the orientation of the helix in this system would be described by  $\mathbf{P} \propto \mathbf{r}_{12} \times (\mathbf{S}_1 \times \mathbf{S}_2)$ , being in this case  $\mathbf{r}_{12}$  the **c** axis and  $\mathbf{S}_1$  and  $\mathbf{S}_2$  the spins at Cu and Fe sites of a bilayer[22][23]. In the non-collinear case the spin-chirality  $\mathbf{Q} = \mathbf{S}_1 \times \mathbf{S}_2 \neq 0$ , and the module of the polarization would be  $P \propto Q \cdot \sin(90-\theta) = Q \cdot \cos(\theta)$ , namely, proportional to  $\cos(\theta)$ .



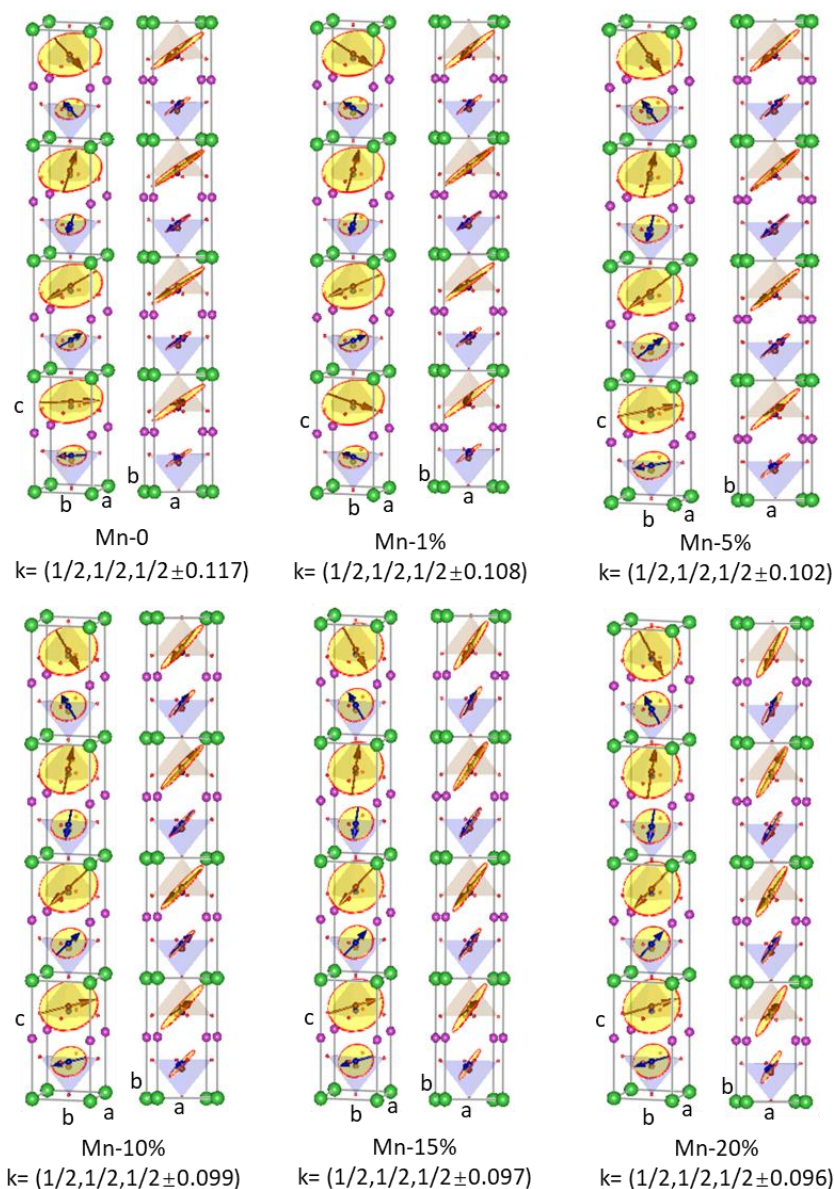


Figure 4.15. Two projections of the refined ICM spiral order at 10 K (with  $M_r = M_i$ , as described in Table 4.6) in  $\text{YBaCuFe}_{1-x}\text{Mn}_x\text{O}_5$  samples with  $x=0, 0.01, 0.05, 0.10, 0.15$  and  $0.20$  Mn.

We performed additional refinements to study how the obtained  $\theta$  angle changes with the constraint that relates Fe and Cu magnetic moments. As shown in Figure 4.16(a), by using  $m(\text{Fe})=m(\text{Cu})$ ,  $\theta$  turns out to be systematically shifted down by  $\approx 12^\circ$ . The Rietveld refinement of the neutron diffraction patterns at 300 K and 10 K for all Mn doped samples are shown in Figure 4.17 and Figure 4.18.



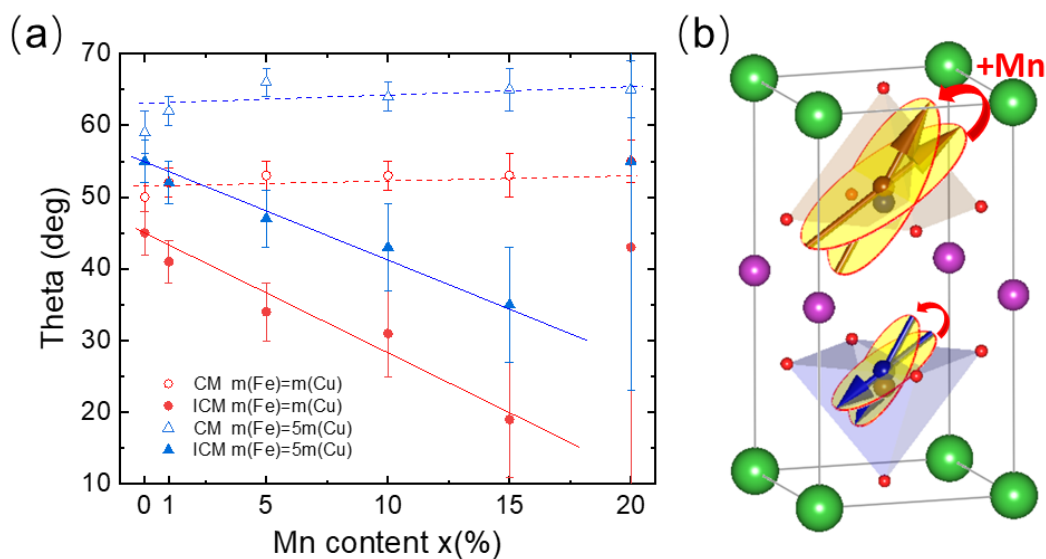


Figure 4.16. (a) Inclination angle ( $\theta$ ) in the CM collinear (300 K, empty symbols) and ICM spiral phases (10 K, full symbols) in YBaCuFe<sub>1-x</sub>Mn<sub>x</sub>O<sub>5</sub> as a function of Mn content. The plot compares the refined values using two models (constraints): (Blue)  $m(\text{Fe})=5m(\text{Cu})$  and (Red)  $m(\text{Fe})=m(\text{Cu})$ . (A nearly constant shift is observed between both). (b) Projection of the evolution of the tilting of the spiral rotation plane ( $\theta$ ) in the ICM phase by increasing the Mn content. For clarity, the average magnetic moment is depicted in each pyramid (shared by three distinct metals) with the color of the majority metal.

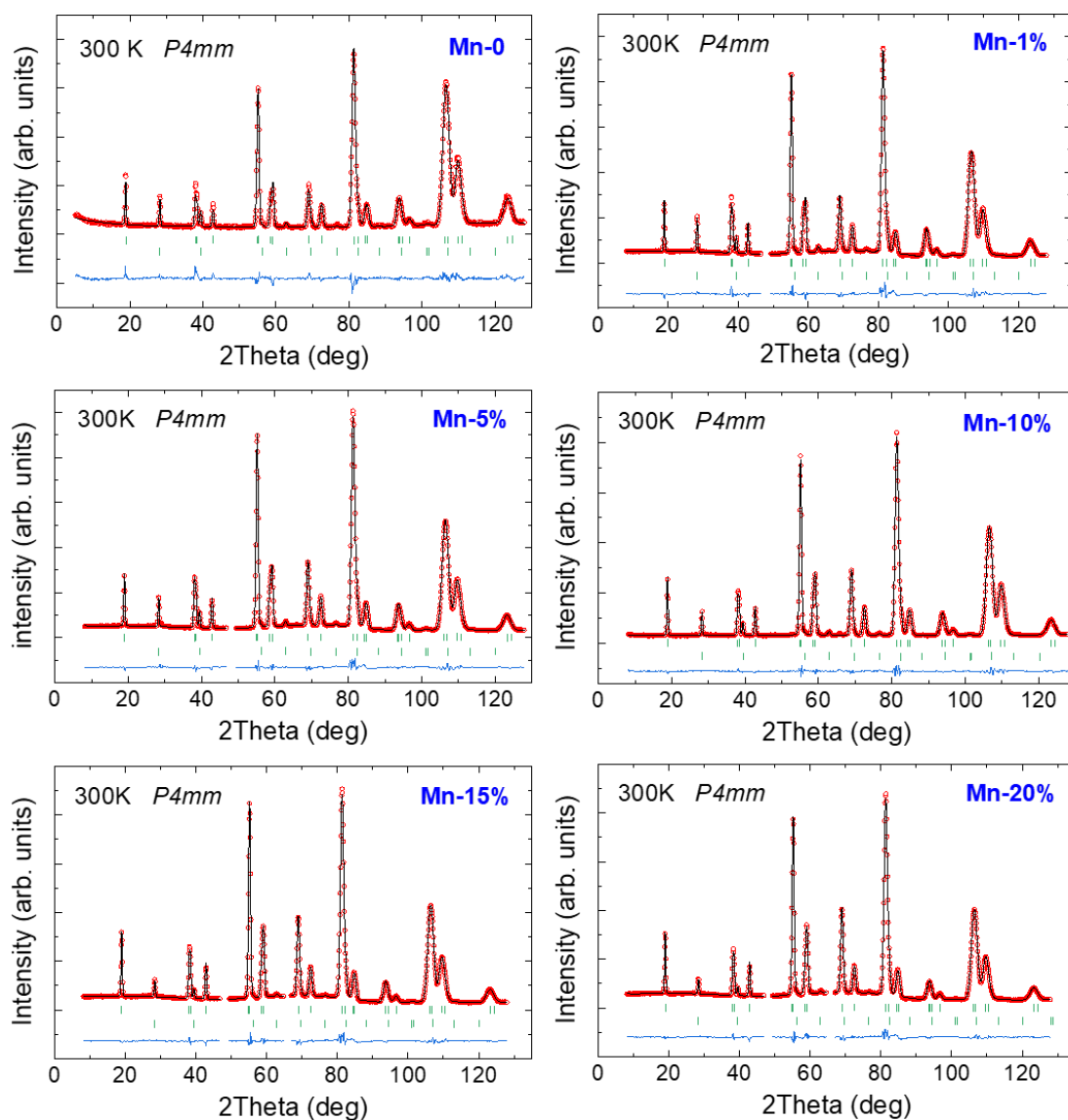


Figure 4.17. Rietveld refinement (black curve) of the neutron diffraction patterns (red circles) collected at 300 K (D1B@ILL) for **Mn-0** ( $R_B$ :3.74,  $R_f$ :2.39,  $R_M$ :17.1,  $\chi^2$ :2.93); **Mn-1%** ( $R_B$ :2.41,  $R_f$ :1.33,  $R_M$ :16.0,  $\chi^2$ :14.6) ; **Mn-5%** ( $R_B$ :0.975,  $R_f$ :0.575,  $R_M$ :3.29,  $\chi^2$ :7.61); **Mn-10%** ( $R_B$ :0.827,  $R_f$ :0.485,  $R_M$ :15.0,  $\chi^2$ :3.43); **Mn-15%** ( $R_B$ :1.83,  $R_f$ :1.01,  $R_M$ :20.5,  $\chi^2$ :10.20); **Mn-20%** ( $R_B$ :2.25,  $R_f$ :1.26,  $R_M$ :21.6,  $\chi^2$ :11.3). The bottom blue line represents the difference between the experimental and calculated intensities. The rows of bars correspond to all allowed reflections for the structural and magnetic phases.

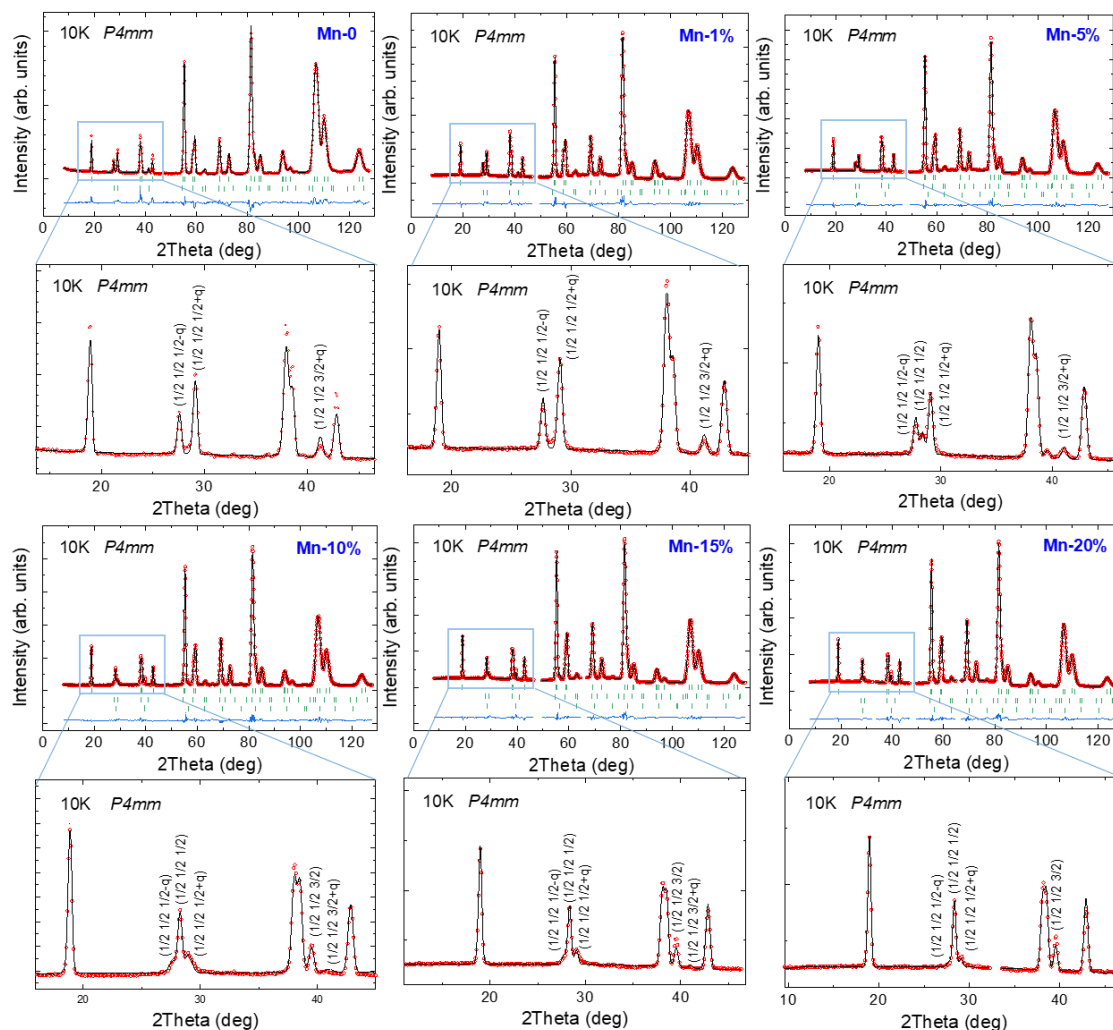


Figure 4.18. Rietveld refinement (black curve) of the neutron diffraction patterns (red circles) collected at 10 K (D1B@ILL) for **Mn-0** ( $R_B$ :3.34,  $R_f$ :2.05,  $R_M$ :13.6,  $\chi^2$ :11.50); **Mn-1%** ( $R_B$ :1.67,  $R_f$ :0.94,  $R_M$ :6.9,  $\chi^2$ :12.3); **Mn-5%** ( $R_B$ :2.12,  $R_f$ :1.22,  $R_M$ :15.6,  $\chi^2$ :13.2); **Mn-10%** ( $R_B$ :0.98,  $R_f$ :0.57,  $R_M$ :12.9,  $\chi^2$ :7.60); **Mn-15%** ( $R_B$ :1.86,  $R_f$ :1.04,  $R_M$ :23.3,  $\chi^2$ :10.20); **Mn-20%** ( $R_B$ :2.25,  $R_f$ :1.29,  $R_M$ :43.0,  $\chi^2$ :12.3). The bottom blue line is the difference between the experimental and calculated intensities. Rows of bars correspond to allowed reflections for the structural, ICM magnetic (circular spiral) and CM magnetic phases. The expanded low-angle region is also shown for each composition, refined using the average moment [ $m(\text{Fe})=m(\text{Cu})$ ].

## **Part II: Samples prepared with different cooling methods or atmosphere**

We also prepared two compositions with  $x=0.10$  and  $0.20$ , where the annealing conditions were the same as for the previous  $\text{YBaCu}(\text{Fe}_{1-x}\text{Mn}_x)\text{O}_5$  samples, the only difference being the final cooling method. After the last annealing, these samples were immediately quenched into the RT water or into LN. Hereafter, we denote these two samples as Mn-10%\_CW, Mn-10%\_CN, Mn-20%\_CW and Mn-20%\_CN. Since the spiral ordering temperature in the perovskite  $\text{YBaCuFeO}_5$  can be increased by more than 150 K through a controlled manipulation of the Fe/Cu chemical disorder [45], we are here aimed at maximizing the chemical disorder of two  $x=0.10$  and  $x=0.20$  samples with fast cooling to discover the tuning possibilities on the spiral phase enabled by this procedure. After the magnetization measurements, we employed XAS to further study the electronic states of the different cations in these differently cooled samples as well as in the rest of samples presented in Part I. Another  $x=0.10$  sample was prepared using argon gas as atmosphere during the whole annealing process and cooled with a 300 K/h rate for the purpose of preserving the oxidation states of cations in the compound. Hereafter we denote this sample as Mn-10%\_Ar. Then, studies of high-resolution and high-intensity neutron diffraction data were carried out to determine the correct oxygen stoichiometry and magnetic properties of these samples.

### **4.5 Magnetization measurement**

The magnetic susceptibility of the two compositions  $x=0.10$  and  $x=0.20$  samples prepared by different cooling methods, are plotted in Figure 4.19, the third sample prepared cooling in air at 300 K/h is also included for comparison. In the two compositions, treated with a fast cooling rate, the Néel temperature  $T_{N2}$  exhibits a clear raise (a shift of  $\sim+60$  K for both compositions) compared with samples prepared with a normal cooling. We also see that we got very similar  $T_{N2}$  values for the samples cooled

using water and LN. The two Néel transitions occurred in the magnetization curves also got reflected in the neutron diffraction measurements that will be presented later in this chapter.

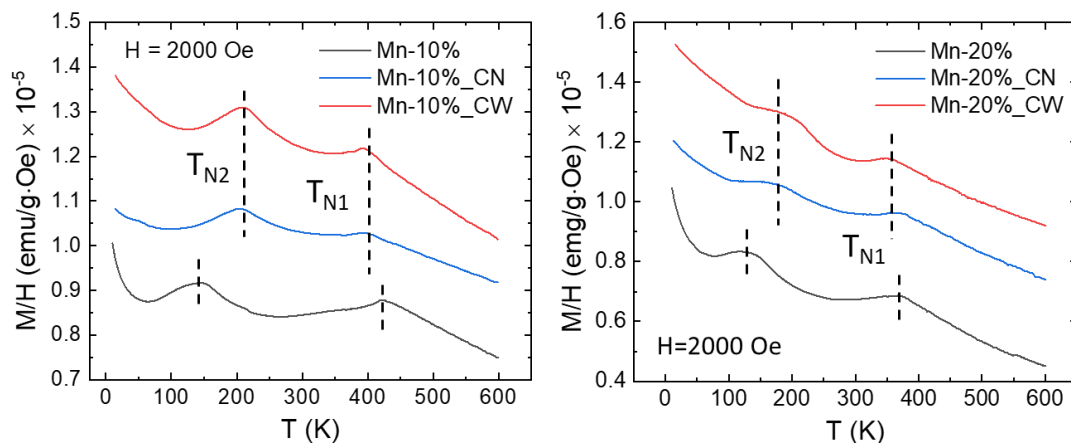


Figure 4.19. Magnetic susceptibility curves of the  $x=0.10$  and  $0.20$  samples prepared using different cooling methods after the last annealing. The two magnetic anomalies marked with dashed lines associated to the CM collinear ( $T_{N1}$ ,  $\mathbf{k}_1$ ) and ICM spiral ( $T_{N2}$ ,  $\mathbf{k}_2$ ) magnetic phases. Curves have been shifted by  $+10^{-6}$  emu  $g^{-1}$  Oe $^{-1}$  for clarity.

## 4.6 X-ray absorption spectroscopy

XAS measurements at the Cu, Fe and Mn  $L_{2,3}$  edges were performed in the HECTOR cryomagnet endstation at the BL29-BOREAS beamline of the ALBA Synchrotron Light Facility (Barcelona, Spain). The samples were mounted on Cu-made sample holders and in-situ under UHV conditions similarly as explained in the precedent chapter.

First of all, we performed XAS measurements on the samples presented in Part I. Figure 4.20 shows the XAS spectra recorded across the Mn  $L_{2,3}$  edges for all samples in the YBaCu(Fe $_{1-x}$ Mn $_x$ )O $_5$  series that were cooled down at a 300 K/h rate, in air. We can see that the spectral shape varies along the series; for the case of a very low Mn content ( $x=0.01$  and  $0.05$ ), the measured XAS firmly reminds to an octahedrally-coordinated Mn $^{4+}$ -based system such as MnO $_2$  or SrMnO $_3$  [92], also shown in the bottom part of the Figure. This is evident by looking at the sharp Mn  $L_3$  pre-peak arising

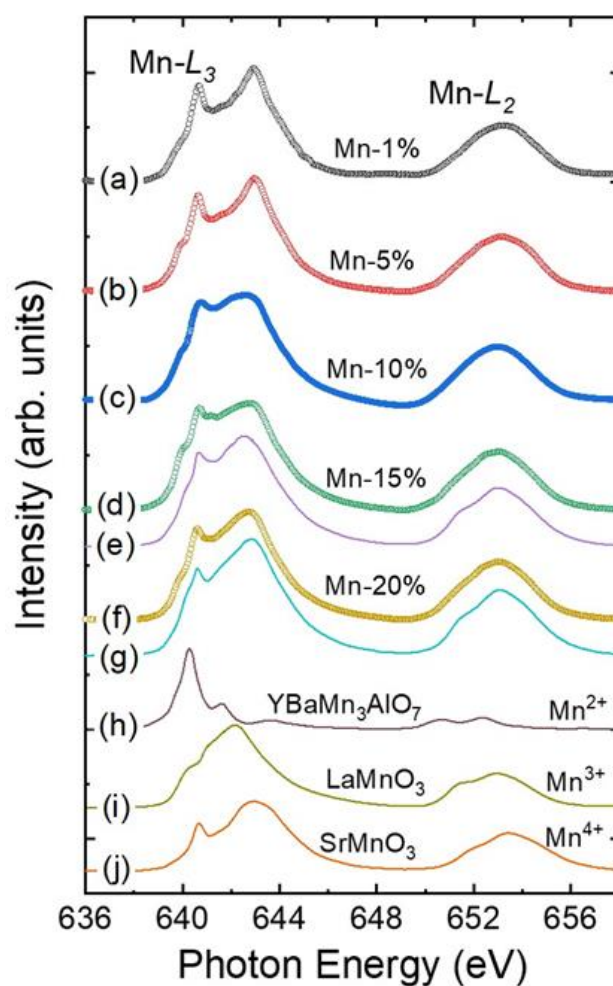


Figure 4.20. Mn- $L_{2,3}$  XAS spectra recorded at 300 K and semiempirical simulations. (h), (i), and (j) are spectra extracted from ref. [92] and used here as references. Mn-1% and Mn-5% XAS spectra are consistent with reference spectra (j); Mn-10% and Mn-15% XAS spectra can get reproduced using the same simulated spectrum (e); simulation (e) and (g) are performed by the weighted addition of reference spectra (i) and (j). Curves have been vertically shifted for clarity.

at  $\sim 640.6$  eV. In contrast, in samples with a higher Mn concentration ( $x \geq 0.10$ ) both this pre-peak and the main Mn  $L_3$  peak at nearly 643 eV appear softened. This can get well accounted for by semiempirical simulations based on the weighed addition of  $\text{Mn}^{3+}$  and  $\text{Mn}^{4+}$  references XAS spectra in a ratio of approximately 1:2, which vary little for all three heaviest Mn-doped samples studied,  $x=0.10$ , 0.15 and 0.20, as summarized in Table 4.5. A  $\text{LaMnO}_3$  XAS spectrum [92] was used as a trivalent Mn cation reference here. It seems thus that there are two well-defined regions for what concerns the local electronic structure around Mn atoms once they get incorporated into the YBCFO

lattice, as a function of the degree of cationic substitution: below  $x=0.10$ , Mn is fully tetravalent, for  $x=0.10$  and  $0.15$  we find about two thirds of all Mn cations keep being  $4+$  and one third becoming trivalent, and finally, for  $x=0.20$  the abundance of  $Mn^{3+}$  diminishes back to about one fourth of the total Mn cations.

**Table 4.5.** Oxidation state of Mn ions in  $YBaCuFe_{1-x}Mn_xO_5$  and their relative abundance as determined by the weighted addition of Mn reference XAS spectra. This gets expressed both by percentage (upper values) and per f.u. (lower values).

sample	$Mn^{2+}$	$Mn^{3+}$	$Mn^{4+}$
Mn-1%	---	---	100% 0.01
Mn-5%	---	---	100% 0.05
Mn-10%	---	34% 0.034	66% 0.066
Mn-15%	---	34% 0.05	66% 0.10
Mn-20%	---	25% 0.05	75% 0.15

We have seen that the XAS spectra at Mn  $L_{2,3}$  edges in  $YBaCuFe_{1-x}Mn_xO_5$  undergo a noteworthy evolution as a function of Mn content. To complete the picture, Figure 4.21 displays the XAS of the studied samples across the Fe and Cu  $L_{2,3}$  edges. Basically, we can observe that the oxidation state of Fe is not modified against different Mn doping levels and it always appears in a high spin and trivalent state. In addition, the oxidation state of Cu is also preserved well in all studied samples showing a typical  $Cu^{2+}$  XAS profile [83]. In contrast to Mn, the local electronic structure of Fe and Cu thus very stable within the compositional range studied in the series.

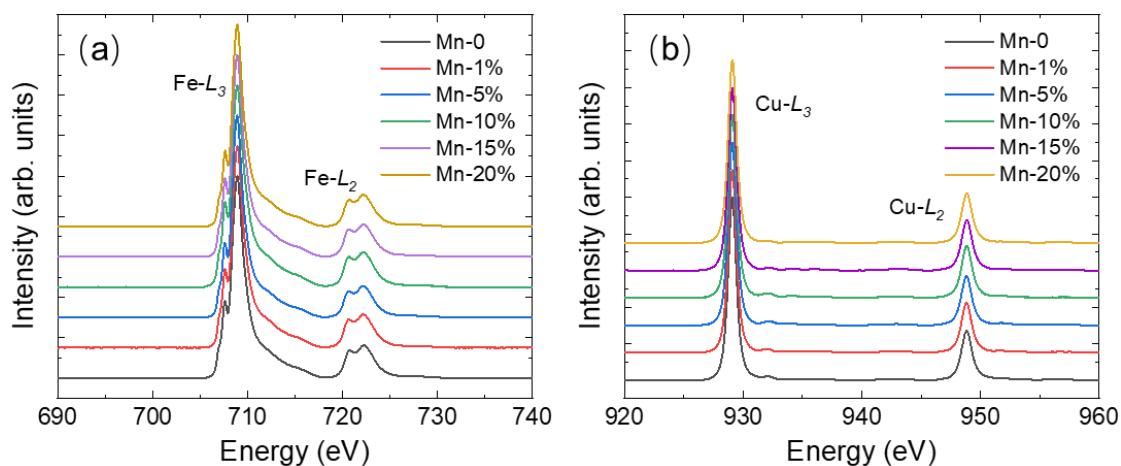


Figure 4.21. XAS spectra across the Fe and Cu  $L_{2,3}$  edges, respectively, for each composition. Some curves have been vertically shifted for clarity.

Secondly, we performed XAS measurement on the three Mn-10%\_CW, Mn-10%\_CN and Mn-10%\_Ar samples. The dependence of the average Mn oxidation state as a function of the cooling methods and atmosphere used is summarized in Figure 4.22. Four experimental XAS spectra are shown here, together with the  $x=0.10$  sample prepared in air and cooled with the rate 300 K/h as comparison. In addition, following the experimental spectra, the best simulated curves are also plotted for each one. As earlier commented, the Mn-10% sample cooled down in air at a rate 300 K/h turns out to be approximately composed of 1/3 of  $\text{Mn}^{3+}$  and 2/3 of  $\text{Mn}^{4+}$  cations, which gets spectroscopically reflected on the large Mn  $L_3$  edge pre-peak structure at 640.6 eV. For the Mn-10%\_Ar sample, where an argon atmosphere was instead employed (at the same cooling rate 300 K/h), this pre-peak gets smoothed and traces of the “fingered” Mn  $L_3$  edge XAS fine structure typical of  $\text{Mn}^{3+}$  Oh ions are visible. Indeed, we find that trivalent Mn is dominant here, the  $\text{Mn}^{3+}:\text{Mn}^{4+}$  ratio lying at nearly 3:2. Namely, manganese gets reduced in average, which correlates well with a less oxidizing surrounding atmosphere.

The effects of quenching are even more dramatic. So, when the cooling of the sample is carried out by immersion into a liquid, be it RT water or LN, the experimental XAS spectra suggest that further electronic changes affecting Mn cations take place. In the latter case, Mn appears mostly as 3+ (70%), and the main novelty is that a substantial



quantity of Mn<sup>2+</sup>, nearly as large as that of Mn<sup>4+</sup>, now appears too. This is spectroscopically noticed by the feature arising at 640.0 eV, as a shoulder, typical of Mn<sup>2+</sup>-based system. This evolves into a well-defined peak in the XAS spectrum of the Mn-10%\_CW sample. Our simulations indicate that almost one third of total Mn is found here in a divalent state. It seems that this cationic species grows at the expense of or Mn<sup>4+</sup>, the quantity of Mn<sup>4+</sup> remaining fairly stable with respect to the sample quenched in LN. The proportion of Mn ions in the different oxidation state in each sample is summarized in Table 4.6 below.

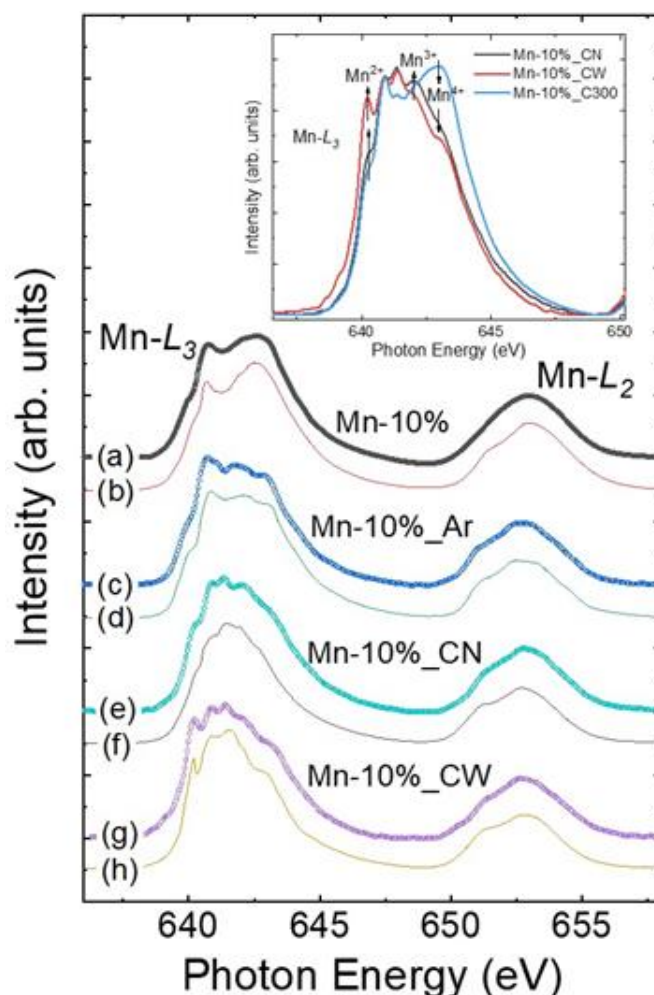


Figure 4.22. Room temperature experimental (symbols) and simulated (solid lines) Mn  $L_{2,3}$  spectra of  $x=0.10$  sample subjected to different cooling methods and environmental atmosphere conditions. Simulated curves correspond to best fits using the weighted addition of reference spectra shown in Figure 4.20 [92]. All curves have been vertically shifted for clarity.

**Table 4.6.** Oxidation states and relative abundance of Mn ions in  $\text{YBaCuFe}_{0.90}\text{Mn}_{0.10}\text{O}_5$  samples as determined by the weighted addition of references. They are expressed by percentage (upper values) and per f.u. (lower values).

Sample	$\text{Mn}^{2+}$	$\text{Mn}^{3+}$	$\text{Mn}^{4+}$
Mn-10%_CN	12% 0.012	72% 0.072	16% 0.016
Mn-10%_CW	30% 0.03	57% 0.057	13% 0.013
Mn-10%_Ar	---	59% 0.059	41% 0.041

To complete the picture, we also exhibit here the XAS spectrum across the Fe and Cu  $L_{2,3}$  edges in Figure 4.23. In general, we observe that Fe is in a resilient high spin and trivalent state in all samples [82], with just minimal changes showing up for the Mn-10%\_CW sample that might be due to a residual presence of  $\text{Fe}^{2+}$  ions. The spectra shown in Figure 4.23 agree well with the expected electronic configuration of octahedral  $\text{Fe}^{3+}$  ( $3d:t_{2g}^3e_g^2$ ) and  $\text{Cu}^{2+}$  ( $3d:t_{2g}^6e_g^3$ ) [83] in oxide materials. However, weak secondary spectroscopic features were found about 2.5 eV beyond the Cu  $L_3$  absorption edge, which is particularly evident for Mn-10%\_CN. This is due to the presence of a certain amount of Cu atoms in a monovalent state [93].

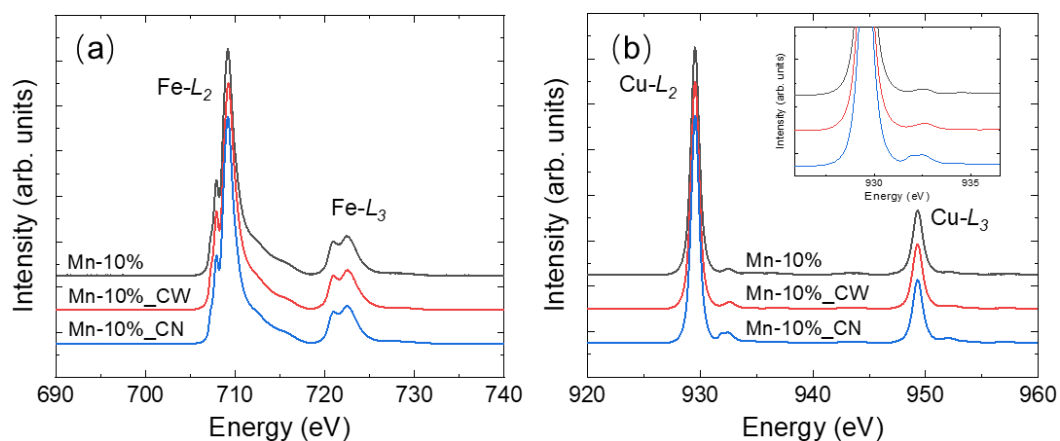


Figure 4.23. XAS spectra across the (a) Fe and (b) Cu  $L_{2,3}$  edges, respectively, for the three Mn-10% samples studied, which underwent different cooling methods. Inset in (b) focuses on the secondary peaks beyond the main peak found between 932 and 933 eV. Some curves have been vertically shifted for clarity.

As a summary to the above XAS measurement results, we can conclude that in this complicated Mn doped YBCFO system, the oxidation states of Fe and Cu are comparatively stable, in spite of a little quantity of monovalent copper appearing in the fast-cooled sample. The most affected cation is the Mn cation. As a function of the samples' cooling method chosen to finalize the synthesis process, they display a different average Mn oxidation states, based on the presence of Mn<sup>2+</sup>, Mn<sup>3+</sup> and Mn<sup>4+</sup> in a variable ratio. A remarkable feature of the nominal Mn<sup>3+</sup> doping is the generated concurrence of two potential strong J-T active cations (Cu<sup>2+</sup> and Mn<sup>3+</sup>) in bipyramids where CuO<sub>5</sub> and MnO<sub>5</sub> units are sharing the apical oxygen [47]. For these two pyramidally coordinated cations, the d<sub>z<sup>2</sup></sub> orbital extends along c thus creating a strongly distorted and elongated pyramid along this direction, respectively. However, following the structural evolution of Fe/Mn-O<sub>a</sub> apical distances studied in section 4.3.2, we did not find a large splitting between them and the four basal Fe/Mn-O<sub>b</sub> bonds. For the crystal structure of YBCFO, which consists of an ordered array of layers containing the large Ba<sup>2+</sup> ions plus two corner-sharing square pyramids separated by Y<sup>3+</sup> sheets, when introducing a certain amount of Mn<sup>3+</sup> to replace the Fe sites, the bipyramids formed by Cu<sup>2+</sup> and Mn<sup>3+</sup> cations would presumably produce a local deformation and generate local internal strain within the crystal lattice due to their J-T effect, thus imposing a perturbation to the local YBCFO structure. Combined with the absence of J-T effect of Mn in the structural analysis and the XAS results, we have deduced that in order to avoid this energetically costly deformation, the Mn cations tend to alter their valence state as a compromise solution. Actually, for the YBaCuFe<sub>1-x</sub>Mn<sub>x</sub>O<sub>5</sub> sample cooled with a 300 K/h rate, the Mn shows strong tendency to be oxidized from Mn<sup>3+</sup> to Mn<sup>4+</sup> (which is J-T inactive) and, considering the ionic radius (Mn<sup>3+</sup> VI HS 0.645 Å and Mn<sup>4+</sup> VI HS 0.53 Å) of these two cations, the latter is more likely helpful to against the lattice deformation. For the case of the samples prepared by fast cooling, the situation is even more complex. Since these sample were quenched immediately by immersion into RT water and LN from high temperature, Mn<sup>3+</sup> cations may undergo different oxidation

and reduction processes. Similarly, there are many reports investigating related Cu-Mn-based oxides [94][95][96][97]. For instance, Daniel P. Shoemaker *et al.* reported on the  $\text{CuMn}_2\text{O}_4$ , which is structurally very complex as a consequence of incoherent J-T distortions and multiple valence states of the two cations in conjunction with site disorder [94]. The sample was prepared using water-quenched method after last annealing to ensure a monophase. Ideally, in the structure of  $\text{CuMn}_2\text{O}_4$ , the tetrahedral and octahedral sites are occupied by J-T active  $\text{Cu}^{2+}$  and  $\text{Mn}^{3+}$  respectively. However, the neutron scattering analysis suggests that there is ~30% of Mn on the tetrahedral site with compensating Cu on the octahedral site. The bond valence analysis of the Reverse Monte Carlo supercell reveals that the electronic state of both J-T ions gets disproportionated to higher and lower valence states as a means of avoiding their J-T tendency [94]. The findings in this report and our deductions illustrated above, expectedly, could provide a possible interpretation to the Mn valence flexibility in the Mn doped YBCFO samples.

## 4.7 Neutron powder diffraction analysis

### 4.7.1 Oxygen stoichiometry determination

The XAS characterization was accompanied by a study of the oxygen stoichiometry using neutrons that confirms the complexity of these compounds doped with Mn. From the result of XAS, we know that the valence of Fe and Cu in the system gets well preserved against Mn introduction, whereas the oxidation state of Mn suffers a remarkable evolution as a function of its concentration and the different cooling methods employed. This has motivated us to detect the correct oxygen stoichiometry which, we can anticipate, that will not remain unaffected (as five O atoms per f.u.) due to the oxidation state of Mn.

As D1B is not optimized for monitoring precise structural details, additional neutron measurements were performed on high resolution D2B diffractometer in ILL,

where we collected long NPD datasets at 300K to optimize the statistics. Careful Rietveld refinements were performed aiming to determine the oxygen stoichiometry and other fine structural details. The information obtained is listed in Figure 4.24 and Table 4.7. In this structure the d<sub>2</sub>-bilayers of corner-sharing square pyramids ([CuFeO<sub>9</sub>]) are separated by the rare-earth layer free from oxygen. In this layer the oxygen vacancies occupy the *1b*: (1/2, 1/2, *z*) position of multiplicity  $m/M=1/8$  (hereafter named as the extra-oxygen position, O<sub>e</sub>). The presence of oxygen of this empty site in YBCFO has been refined without constraining the total oxygen content. For these samples studied, the refinements converged to the same values, within the errors, repeating the adjustments using different initial conditions, relaxation factors, etc.. In these refinements the *z* coordinate of O<sub>e</sub> could not be refined and it got fixed to be within the plane of Yttrium atoms ( $z(\text{Oe})=z(\text{Y})$ ). As in previous refinements, given the low proportion of Mn, we also fixed  $z(\text{Mn})=z(\text{Fe})$ . Cationic vacancies were not detected by neutron diffraction. Quantitatively, we could confirm the presence of extra oxygen atoms in Mn-10% and Mn-20% samples, with respective occupations of 0.0031 (4) and 0.0076 (5) in the O<sub>e</sub> site (Table 4.7). This implies  $\delta \neq 0$  in YBaCu(Fe<sub>1-x</sub>Mn<sub>x</sub>)O<sub>5+ $\delta$</sub> : being  $\delta = 0.025$  (3) in Mn-10% and 0.061(4) in Mn-20%.

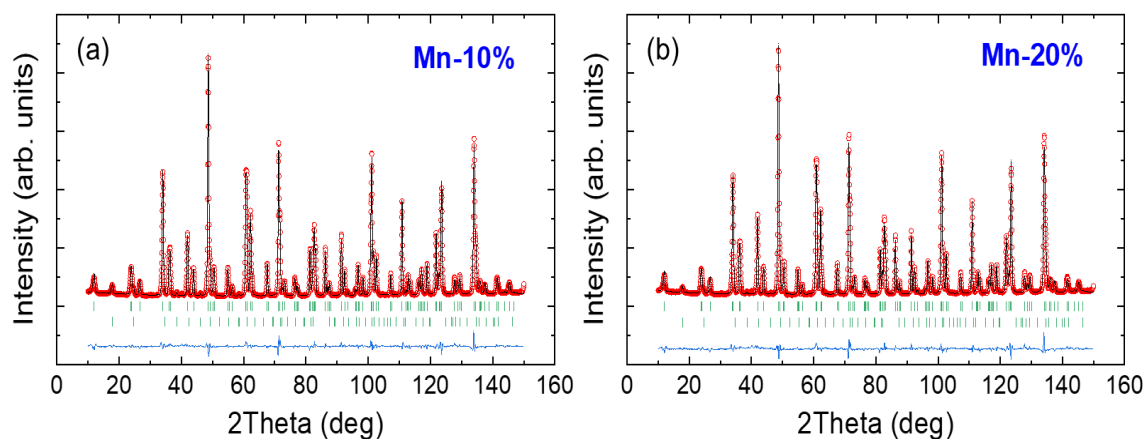


Figure 4.24. Rietveld refinements without constrained oxygen stoichiometry (black line) of D2B neutron diffraction patterns ( $\lambda=1.594$  Å) in high-flux mode (red circles, experimental points) collected at 300 K. The bottom blue line is the difference. Two rows of green bars are Bragg positions of structural phase (first row) and the CM magnetic phase (second row). (a) Mn-10% ( $\chi^2$ : 6.23,  $R_B$ : 2.40,  $R_f$ : 1.58,  $R_M$ : 12.8), (b) Mn-20% ( $\chi^2$ : 7.76,  $R_B$ : 3.14,  $R_f$ : 2.00,  $R_M$ : 14.1).

**Table 4.7.** Rietveld refinement of the oxygen stoichiometry from D2B NPD data at 300 K of  $\text{YBaCuFe}_{1-x}\text{Mn}_x\text{O}_{5+\delta}$  for  $x=0.10$  and  $0.20$ . In the  $P4mm$  structure, the oxygen vacancies occupy the  $1b$ :  $(1/2, 1/2, z)$  position (point symmetry  $4mm$  and multiplicity  $m/M=1/8$ ). The magnetic moment of Fe and Cu were constrained by  $m(\text{Fe})=5m(\text{Cu})$  in the refinement, and Theta represents the angular distance between the  $c$  axis and the direction of the spins.

$\text{YBaCuFe}_{1-x}\text{Mn}_x\text{O}_{5+\delta}$	Mn-10%		Mn-20%	
	$\delta=0$	$\delta$ refined	$\delta=0$	$\delta$ refined
Oe site occupation:				
(m/M)	---	0.0031 (4)	---	0.0076 (5)
$\delta$	---	0.025 (3)	---	0.061 (4)
$z(\text{Oe})=z(\text{Y})$	0.5114 (8)	0.5113 (8)	0.5123 (8)	0.5120 (8)
$m(\text{Fe})$ ( $\mu_B$ )	1.95 (3)	1.95 (3)	1.55 (5)	1.55 (5)
Theta (deg)	67 (5)	67 (5)	57 (6)	57 (6)
$\text{Mn}^{3+}/\text{f.u.}$	---	0.034	---	0.050
$\text{Mn}^{4+}/\text{f.u.}$	---	0.066	---	0.150

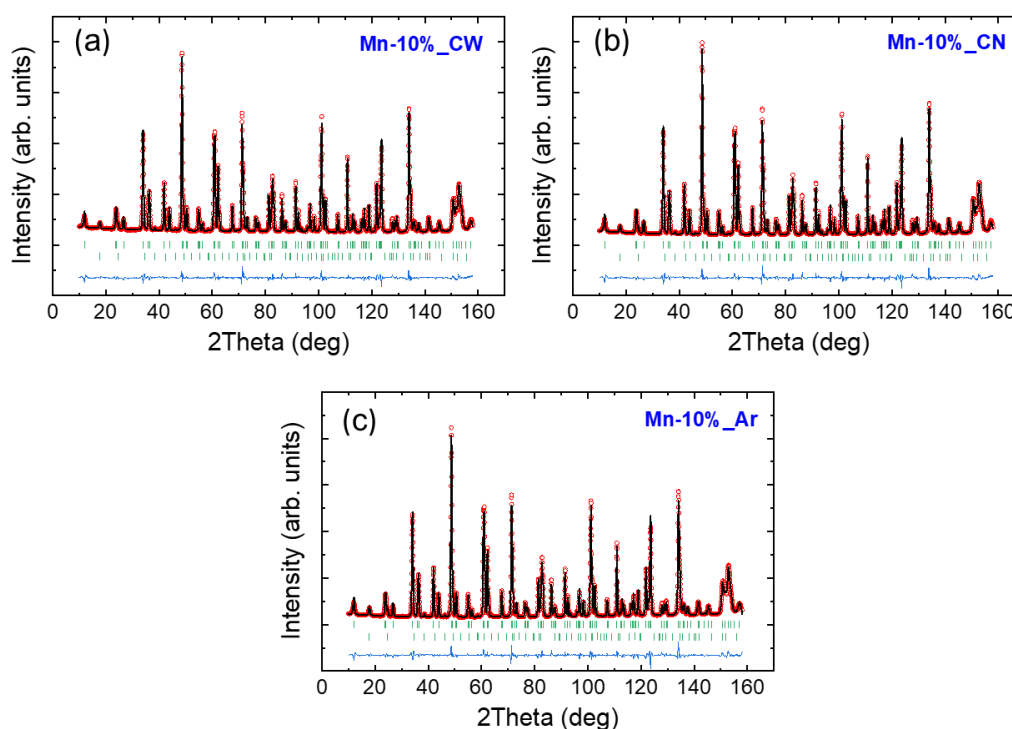


Figure 4.25. Rietveld refinements (black line) of D2B neutron diffraction patterns ( $\lambda=1.594 \text{ \AA}$ ) in high-flux mode (red circles, experimental points) collected at 300 K. The bottom blue line is the difference between experimental and calculated intensity. Two rows of green bars are Bragg positions of structural phase (first row) and the CM magnetic phase (second row). (a) Mn-10%\_CW ( $\chi^2$ : 9.37,  $R_B$ : 2.95,  $R_f$ : 2.04,  $R_M$ : 14.1), (b) Mn-10%\_CN ( $\chi^2$ : 11.5,  $R_B$ : 3.01,  $R_f$ : 1.94,  $R_M$ : 12.5), (c) Mn-10%\_Ar ( $\chi^2$ : 15.0,  $R_B$ : 2.86,  $R_f$ : 1.87,  $R_M$ : 10.9).

**Table 4.8.** Rietveld refinement of the oxygen stoichiometry from D2B NPD data at 300 K of YBaCuFe<sub>0.90</sub>Mn<sub>0.10</sub>O<sub>5+ $\delta$</sub>  prepared by different conditions. In the  $P4mm$  structure oxygen vacancies occupy the  $1b$ :  $(1/2, 1/2, z)$  position (point symmetry  $4mm$  and multiplicity  $m/M=1/8$ ). The magnetic moment of Fe and Cu were constrained by  $m(\text{Fe})=5m(\text{Cu})$  in the refinement, and Theta represents the angular distance between the  $c$  axis and the direction of the spins.

Sample	Mn-10%		Mn-10%_CW	Mn-10%_CN	Mn-10%_Ar
	$\delta = 0$	$\delta$ refined	$\delta$ refined	$\delta$ refined	$\delta$ refined
Oe site occupation:					
$(m/M)$	0	0.0031(4)	0.0016 (4)	0.0015 (4)	0.0003 (4)
$\delta$		0.025(3)	0.013 (3)	0.012 (3)	0.002 (3)
$z(\text{Oe}) = z(\text{Y})$	0.5114 (8)	0.5113(8)	0.5111 (8)	0.5113 (8)	0.5138 (8)
$m(\text{Fe})$ ( $\mu_B$ )	1.95 (3)	1.95(3)	1.79 (3)	1.86 (3)	2.08 (3)
Theta (deg)	67 (5)	67(5)	59 (5)	60 (5)	80 (10)

Likewise, we performed an oxygen stoichiometry study on the samples prepared by different cooling methods. The information obtained from the Rietveld refinements of the D2B neutron diffraction data are shown in Figure 4.25 and Table 4.8.

The presence of extra oxygen atoms can modify the mean valence of the three metal ions: Cu, Fe and Mn. However, the XAS spectra did not reflect changes in the oxidation state of Cu and Fe species, which kept their respective divalent and trivalent valences even in the specimens with the highest doping level. The study of the oxygen stoichiometry confirmed that there is a tendency to incorporate a small proportion of extra oxygen content at the position occupied by oxygen vacancies in the YBCFO structure. We can associate these oxygen atoms to the presence of Mn-Oe bonds in the MnO<sub>6</sub> octahedral environment. Therefore, from the present results the proportion of MO<sub>6</sub> octahedral in Mn-10% and Mn-20% samples would be 2.5% and 6.1%, respectively, and in Mn-10%\_CW and Mn-10%\_CN samples, this value keeps reduced to 1.2%. Within the error, we did not detect extra oxygen in the Mn-10%\_Ar sample.

### 4.7.2 Structural characterization

The structural information of the samples synthesized by different cooling methods was also carefully analyzed using the D2B neutron diffraction data. The structural parameters obtained from Rietveld refinements are listed in the Table 4.9. An interesting finding is the effect of fast cooling to the Fe/Cu chemical disorder of samples. For the slow cooling rate of 300 K/h, the Mn-10% sample shows  $n_d \sim 25\%$  occupation of Fe in Cu site, and vice versa (level of chemical disorder). Whereas for the both fast cooling sample, this value increases to  $\sim 30\%$ , clearly indicating that these compositions get more chemically disordered when fast cooling procedure is employed.

The evolution of different structural parameters as a function of cooling approaches is presented in Figure 4.26. In contrast with what observed in the samples prepared under a 300 K/h cooling rate, when samples get cooled at fast rate, a decreasing tendency is observed for the  $c$  parameter, in addition to a contraction of the tensile tetragonal distortion and a volume decrease. The contraction of  $c$  in the vertical direction can be associated to the changes in  $d_1$  and  $d_2$ , the two main distances characterizing the  $[\text{CuFeO}_9]$  bilayers of corner-sharing squared pyramids. As shown in 4.26 (b), the decrease of  $d_1$  is more pronounced than the expansion of  $d_2$ , so the lattice parameter  $c$  decreases. A look to the Fe/Cu to oxygen distances, they also give expected changes. As we concluded in the XAS characterization section, in Mn-10%\_CW and Mn-10%\_CN samples, there is a certain amount of  $\text{Mn}^{2+}$  in the material. Considering that the  $\text{Mn}^{2+}$  has a much larger ionic radius than  $\text{Mn}^{3+}$  and  $\text{Mn}^{4+}$  ( $\text{Mn}^{2+}$ : 0.83 Å,  $\text{Mn}^{3+}$ : 0.645 Å,  $\text{Mn}^{4+}$ : 0.53 Å, all being in VI coordination, HS) [48], it is reasonable to conclude that its presence in these samples increases the average Fe/Mn to oxygen distance, which in turn produces an inverse effect on the Cu to oxygen distance. The same evolution can also be observed on the height of Fe/Cu pyramids, as shown in Figure 4.26 (e).



**Table 4.9.** Structural parameters at T=300 K from Rietveld refinement of D2B neutron diffraction data ( $\lambda=1.594$  Å). The coordinates of the two positions (M1 and M2) for each metal are related by  $z(M1)+z(M2)=1$ . (\*: minority fraction; +: occupation of the majority cation in each pyramid).

sample	Mn-10%	Mn-10%_CW	Mn-10%_CN	Mn-10%_Ar
a (Å)	3.87218 (2)	3.87233 (1)	3.87254 (1)	3.87170 (2)
c (Å)	7.66519 (4)	7.66209 (4)	7.66263 (4)	7.66718 (4)
v (Å <sup>3</sup> )	114.930 (1)	114.893 (1)	114.913 (1)	114.932 (1)
z (Y) (0 0 z)	0.5174 (7)	0.5095 (7)	0.5089 (8)	0.5152 (7)
z (Fe1) (½ ½ z)	0.7572 (4)	0.7510 (3)	0.7509 (3)	0.7545 (4)
z (Cu1) (½ ½ z)*	0.7091 (4)	0.7129 (3)	0.7128 (3)	0.7095 (4)
z (Cu2) (½ ½ z)	0.2909 (4)	0.2871 (3)	0.2873 (3)	0.2905 (4)
z (Fe2) (½ ½ z)*	0.2428 (4)	0.2490 (3)	0.2491 (3)	0.2455 (4)
z (O <sub>1</sub> ) (½ ½ z)	0.0219 (7)	0.0209 (7)	0.0208 (7)	0.0210 (8)
z (O <sub>2</sub> ) (0 ½ z)	0.3375 (5)	0.3191 (7)	0.3182 (7)	0.3360 (6)
z (O <sub>3</sub> ) (0 ½ z)	0.7084 (5)	0.6891 (7)	0.6883 (7)	0.7058 (6)
Occ (majority) <sup>+</sup>	0.748 (20)	0.716 (20)	0.691 (20)	0.774 (20)

The different extra oxygen content between Mn-10% and the fast-cooled Mn-10%\_CW and Mn-10%\_CN samples offers us some meaningful conclusions. On the one hand, the XAS results show that in Mn-10% sample, the proportion of Mn<sup>4+</sup> is almost two times greater than Mn<sup>3+</sup> (Mn<sup>4+</sup>: Mn<sup>3+</sup>= 2:1), while in the case of Mn-10%\_CW and Mn-10%\_CN sample, most of the Mn<sup>4+</sup> cations turned into Mn<sup>3+</sup> and Mn<sup>2+</sup>, remaining only up to ~15% in each of these two samples. So, more extra oxygen should be incorporated in the sample Mn-10% than the other two Mn-10%\_CW and Mn-10%\_CN samples. On the other hand, the extra oxygen detected should occupy the oxygen vacancies in the YBCFO structure, namely, the position between bipyramids. Then a Mn-O<sub>e</sub> bond would be generated, producing the appearance of MnO<sub>6</sub> octahedra in the lattice. From Table 4.9, we know that there will be a larger proportion of octahedra in normal cooled sample than in the fast-cooled samples. It is worth noting here that, because of the two metal-to-apical oxygen bonds in the octahedrally

coordinated configuration, the metal to apical oxygen distance should be shorter compared with the distance in pyramidally coordinated configuration. This is in agreement with the Figure 4.26 (c), where we can see that the Fe/Mn-O<sub>a</sub> distance in Mn-10% is shorter than its counterpart in Mn-10%\_CW and Mn-10%\_CN samples.

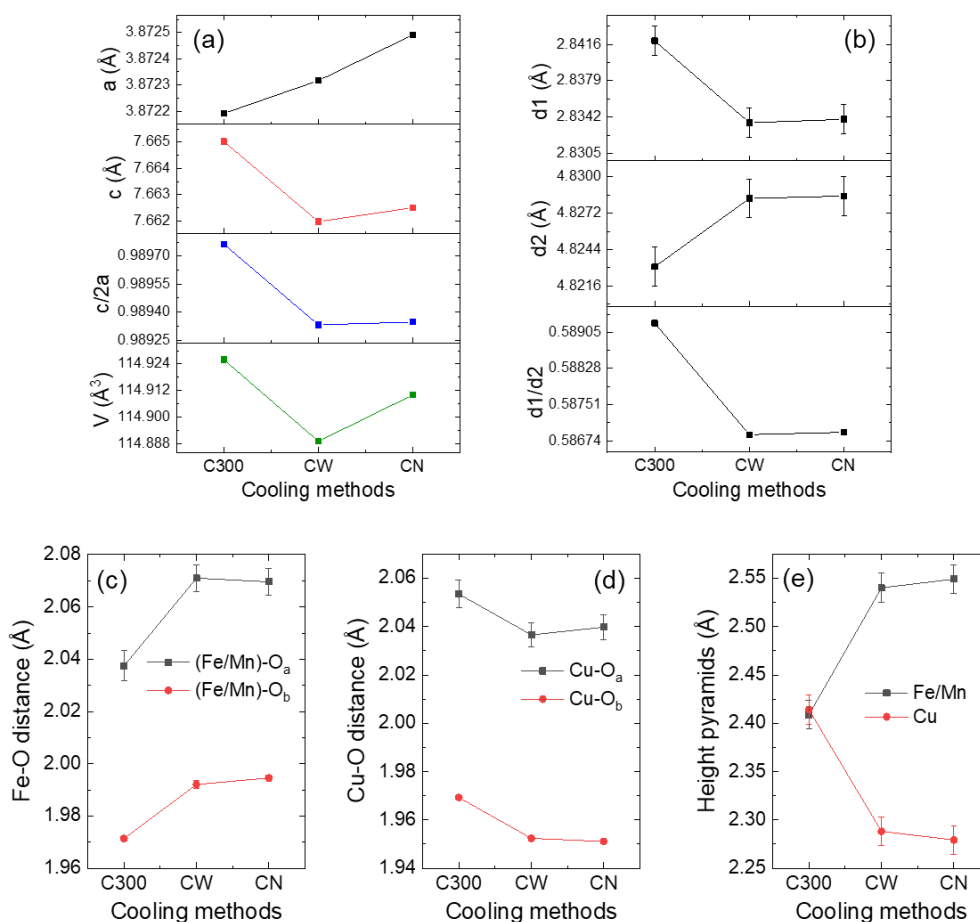


Figure 4.26. Structural evolution of the three  $x=0.10$  samples prepared with different cooling methods extracted from Rietveld refinement of D2B neutron diffraction data recorded at  $T=300$  K. (a) the evolution of cell parameters and volume. (b) the evolution of the characteristic distances  $d_1$  (the separation of bipyramids) and  $d_2$  (the thickness of the bipyramids). (c) (Fe/Mn)-O and (d) Cu-O interatomic distances in respectively pyramids of the chemical unit cell. (e) Height of the  $[\text{Fe/Mn}]\text{O}_5$  and  $\text{CuO}_5$  pyramids.

### 4.7.3 Temperature dependence

Temperature-dependent NPD measurements were also conducted in the high intensity diffractometer D1B for the two compositions  $x=0.10$  and  $x=0.20$  samples, as prepared using different cooling methods. Diffraction patterns were collected in the

range 10 K-500 K, with a temperature step of 9 K between consequent patterns. Long-time integration of 20 min per pattern was also recorded on each sample at T=10 K for improved statistics.

The long-time integration NPD patterns recorded at 10 K were plotted in Figure 4.27, which compares the evolution of the main magnetic reflections of the two compositions in the low-angle region. Evident changes in the intensity of the main magnetic peaks are visible for both compositions in the samples quenched in water and liquid nitrogen. For the three samples with  $x=0.10$ , when applying with a fast cooling, the collinear phase which is characterized by the  $(1/2\ 1/2\ 1/2)$  peak greatly diminishes. Instead, the spiral phase characterized by the two satellites  $(1/2\ 1/2\ 1/2\pm q)$  is more dominant in Mn-10%\_CW and Mn-10%\_CN samples. This change also takes place in  $x=0.20$  samples, although less pronounced: when applied with fast cooling, the two spiral satellites get moderately enhanced, but the collinear phase still predominates.

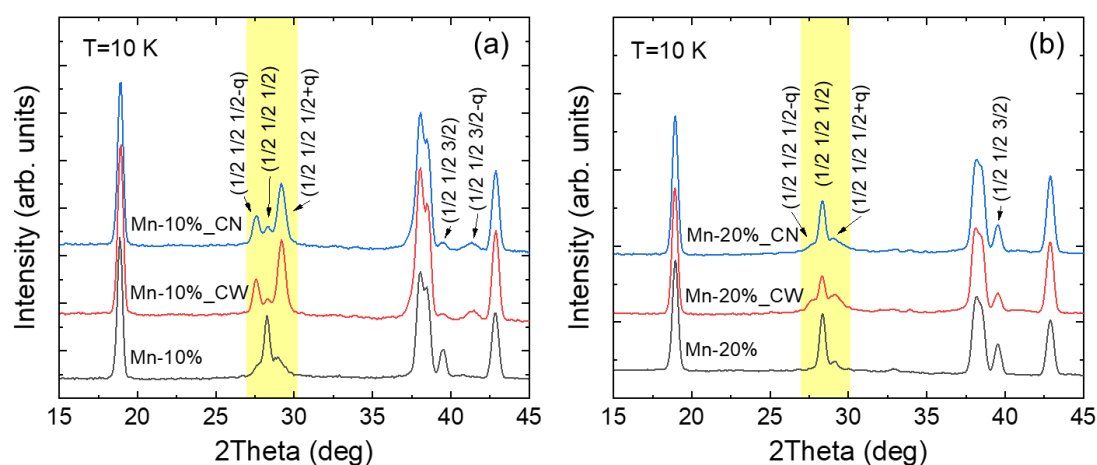


Figure 4.27. Low-angle region of the neutron diffraction patterns collected at T=10 K in D1B ( $\lambda=2.52\ \text{\AA}$ ) for each sample showing the main magnetic reflections of (a) three samples with  $x=0.10$  and (b) three samples with  $x=0.20$ .

Temperature dependence NPD patterns allow us to study more comprehensively the magnetic properties of these samples prepared by different cooling approaches. For both compositions, the T-2Theta contour map of neutron-diffracted intensities as a function of temperature, temperature dependence of the averaged magnetic moments

associated to the CM and ICM phases and the evolution of the inclination angle  $\theta$  with respect to the  $c$  axis in both phases are depicted in Figure 4.28. Looking at the (a) and (d) panel sets in this Figure, two magnetic phase transitions can be observed at  $T_{N1}$  and  $T_{N2}$ , which signal the onset temperatures from paramagnetic phase to AF1 CM phase and CM phase to AF2 ICM phase, respectively. These two transition temperature values are consistent with our magnetization measurements studied in section 4.5. For both compositions  $x=0.10$  and  $0.20$ , in contrast with the sample prepared with 300 K/h cooling rate, the two fast-cooled samples witnessed a remarkable increase for  $T_{N2}$ , especially for the lower Mn-doped set. In addition, the two spiral satellites strengthened, resulting in a more split and distinguishable spiral phase. The increase of the spiral transition temperature cannot be explained by lattice effect of the changes happened on the inter- or intra-bipyramids, namely,  $d1$  and  $d2$ , which would raise  $T_{N2}$ . On the contrary, the preparation-dependent chemical disorder could provide additional insight on this phenomenon. Our high-resolution neutron diffraction analysis has confirmed that, for the composition  $x=0.10$ , the fast-cooled samples have a higher chemical disorder of  $\sim 30\%$ , compared with a value  $\sim 25\%$  for the normal cooling samples. It has been shown in the previous reports that site and/or bond defects in a magnetically ordered lattice may, in some particular conditions, give rise to a spiral magnetic order [98][99]. In addition, according to the disorder-based mechanism proposed by Scaramucci and co-workers [84], a magnetic spiral can be stabilized through the introduction of a few strong, randomly distributed frustrating bonds in systems featuring a single crystallographic direction. Considering our samples, the more chemically disordered, the more FM spin pairs in  $\text{Fe}^{3+}\text{-O-Cu}^{2+}$  bipyramids will be replaced by strong AFM  $\text{Fe}^{3+}\text{-O-Fe}^{3+}$  (two orders larger in absolute value than the FM Cu-Fe coupling) dimers which act as frustrating bonds in this system, and generating enough frustration to induce a local canting and thus turning the collinear order into a spiral one [84][45].

In Figure 4.28 (b) and (e), we plotted the evolution of the refined magnetic

moments for both collinear and spiral phases of each sample up to 500 K. In these figures, the collinear and spiral magnetic moments are referred to the full amount of sample and their values were calculated as averaged over Fe and Cu sites, particularly, for the spiral phase, we use the limit  $M_R \gg M_I$ . The temperature dependence of the inclination angle  $\theta$  was also refined for both compositions in the range between 10 K and  $T_{N1}$  using the same conditions reported in Section 4.6.3, as shown in Figure 4.28 (c) and (f). The fast-cooled samples show similar results to those samples prepared by cooling at 300 K/h. Firstly, for both compositions, the inclination angle  $\theta$  in both collinear and spiral phases remain a constant value. Only in the spiral phase of  $x=0.20$  samples, the weak reflection intensities do not allow the sequential refinement, resulting in large error bars and inconsistent values with temperature. Secondly, the inclination angle in the collinear phase does not vary within the three samples with the same doping level. And we also observed a sudden fall once below  $T_{N2}$  in all the samples. In the case of the three  $x=0.10$  samples, for the spiral phase, a  $\sim 10^\circ$  constant difference between the fast-cooled samples and the normally-cooled sample, as shown in the Table 4.10. Here we should point out that, contrarily to those samples prepared with increasing Mn doping level [47], when the samples are the same doping amount, fast cooling will impose an opposite effect on the orientation of the magnetic spiral plane, evolving from a cycloid ( $\theta \rightarrow 0^\circ$ ) towards a helix-type ( $\theta \rightarrow 90^\circ$ ).

The refined magnetic moment of Fe site and inclination angle  $\theta$  at 300 K and 10 K for all samples are summarized in the Table 4.10. The temperature dependence of the ICM modulation vector  $q$  for the three  $x=0.10$  samples is depicted in Figure 4.29 (a). Theoretically, the parameter  $q$  appears at  $T_{N2}$  and progresses until it reaches the maximum amplitude  $q_0$ . However, from the figure, the beginning of  $q$  doesn't evolve from the  $T_{N2}$ , this is most probably because the low ICM phase reflection intensities around the transition temperature cannot stabilize a  $q$  value for the refinement. The difference is remarkable between the normally-cooled and fast-cooled samples.

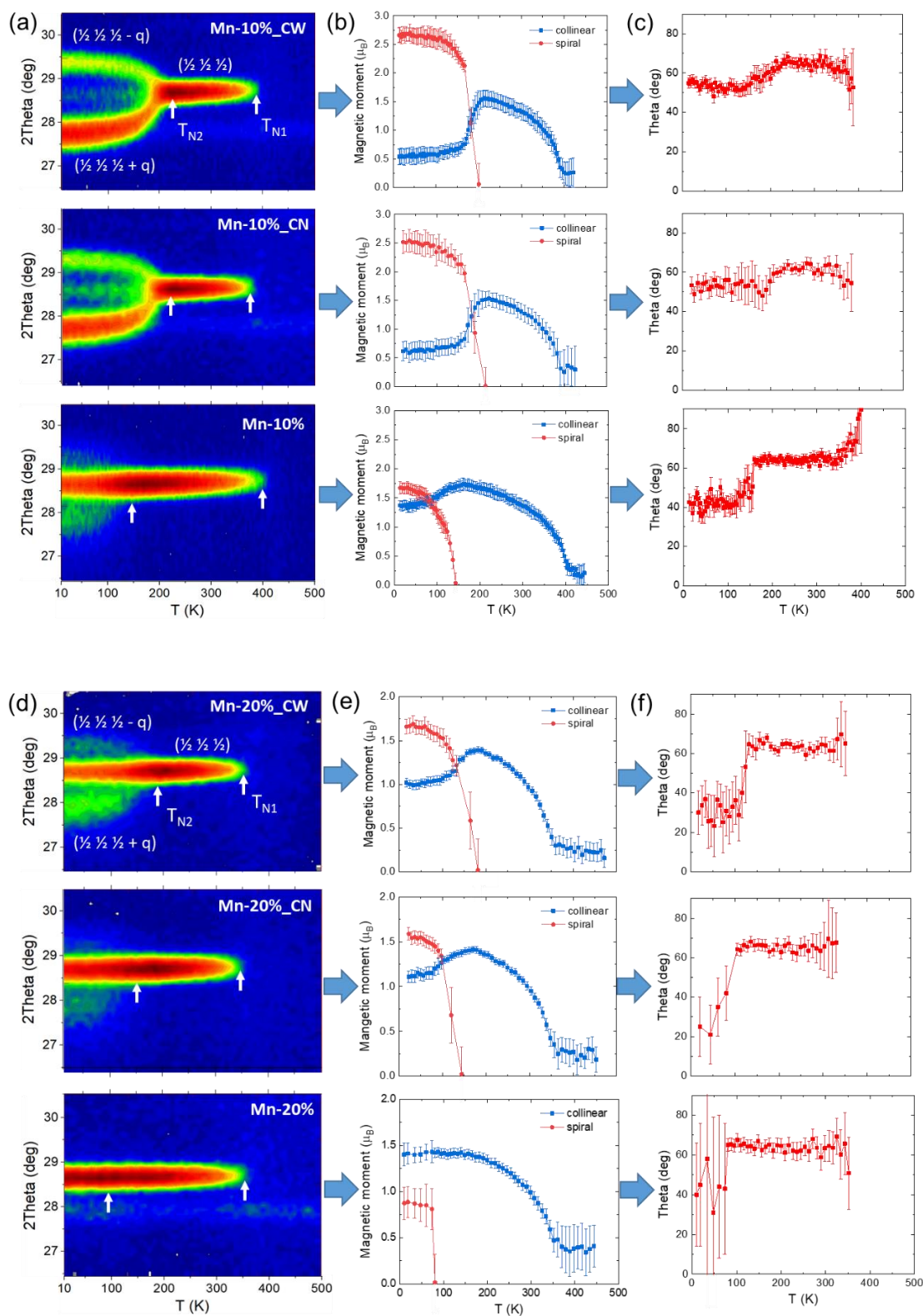


Figure 4.28. Temperature dependence of NPD measurements on the two compositions  $x=0.10$  and  $0.20$  prepared using different cooling methods of the : (a) and (d) T-2Theta projection of the neutron-diffracted intensities around the  $(1/2 1/2 1/2)$  reflection; (b) and (e) The evolution of average ordered magnetic moments associated to the CM and ICM phases; (c) and (f) The evolution of the inclination angle  $\theta$  of the collinear spins and the spiral rotation plane with respect to the  $c$  axis.

**Table 4.10.** Refined magnetic moments [imposing  $m(\text{Fe})=5m(\text{Cu})$ ] and inclination angles ( $\theta$ ) obtained by refining the collinear phase at 300 K and the spiral phase at 10 K. At 10 K, the refined magnetic moments correspond to *Model 1* ( $M_i \sim 0$ ) and *Model 2* ( $M_i = M_r$ ). Theta ( $\theta$ ) in *Model 2* is fixed to its refined values in *Model 1*.

Sample	300 K (CM)		10 K			
	<i>Collinear</i>		<i>Model 1</i> ( $M_i \sim 0$ )		<i>Model 2</i> ( $M_i = M_r$ )	
	m(Fe) ( $\mu_B$ )	Theta (deg)	m(Fe) ( $\mu_B$ )	Theta (deg)	m(Fe) ( $\mu_B$ )	Theta (deg)
Mn-10%	1.91 (2)	64 (2)	2.4 (2)	43 (8)	1.78 (3)	43
Mn-10%_CW	1.77 (2)	61 (2)	3.5 (2)	53 (7)	2.69 (3)	53
Mn-10%_CN	1.81 (2)	62 (2)	3.5 (2)	54 (7)	2.56 (3)	54
Mn-20%	1.36 (2)	65 (5)	1.1 (2)	55 (52)	0.86 (4)	55
Mn-20%_CW	1.22 (2)	65 (5)	2.3 (2)	40 (9)	1.76 (3)	40
Mn-20%_CN	1.25 (2)	68 (5)	2.1 (2)	36 (15)	1.57 (3)	36

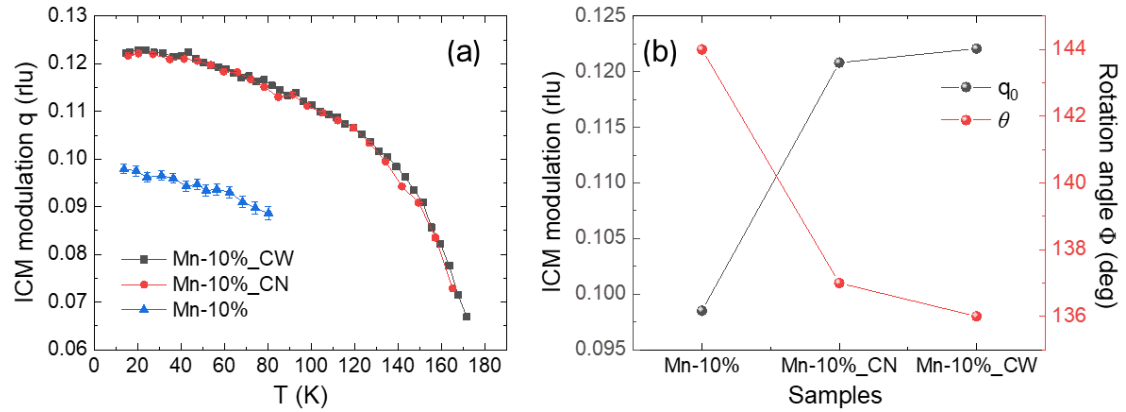


Figure 4.29. (a) Evolution of the ICM modulation  $q$  as a function of temperature for the three samples prepared with different cooling approaches; (b) ICM modulation  $q_0$  component and associated spin rotation angle  $\Phi$  ( $\Phi$ ) between successive bilayers.

The fast cooling method unambiguously favors the generation of the two spiral satellites or, in other words, the ICM phase. In addition, for the three samples, we observed a smooth and continuous increase of  $q$ , characteristic of second-order phase transitions, this suggests that the collinear-to-spiral transition changes progressively, but clearly not a first-order transition. In the Figure 4.29 (b), we show the maximum amplitude of the ICM modulation  $q_0$  for the three samples and their corresponding spin rotation angle  $\Phi$  between successive bilayers. The  $q_0$  for the two fast-cooled samples

is higher than 0.12 r.l.u. in contrast with 0.10 r.l.u. for the normally-cooled sample. This provides another evidence of the enhancement of the ICM phase at the expense of the CM collinear order in samples submitted to a quenching-type cooling process.

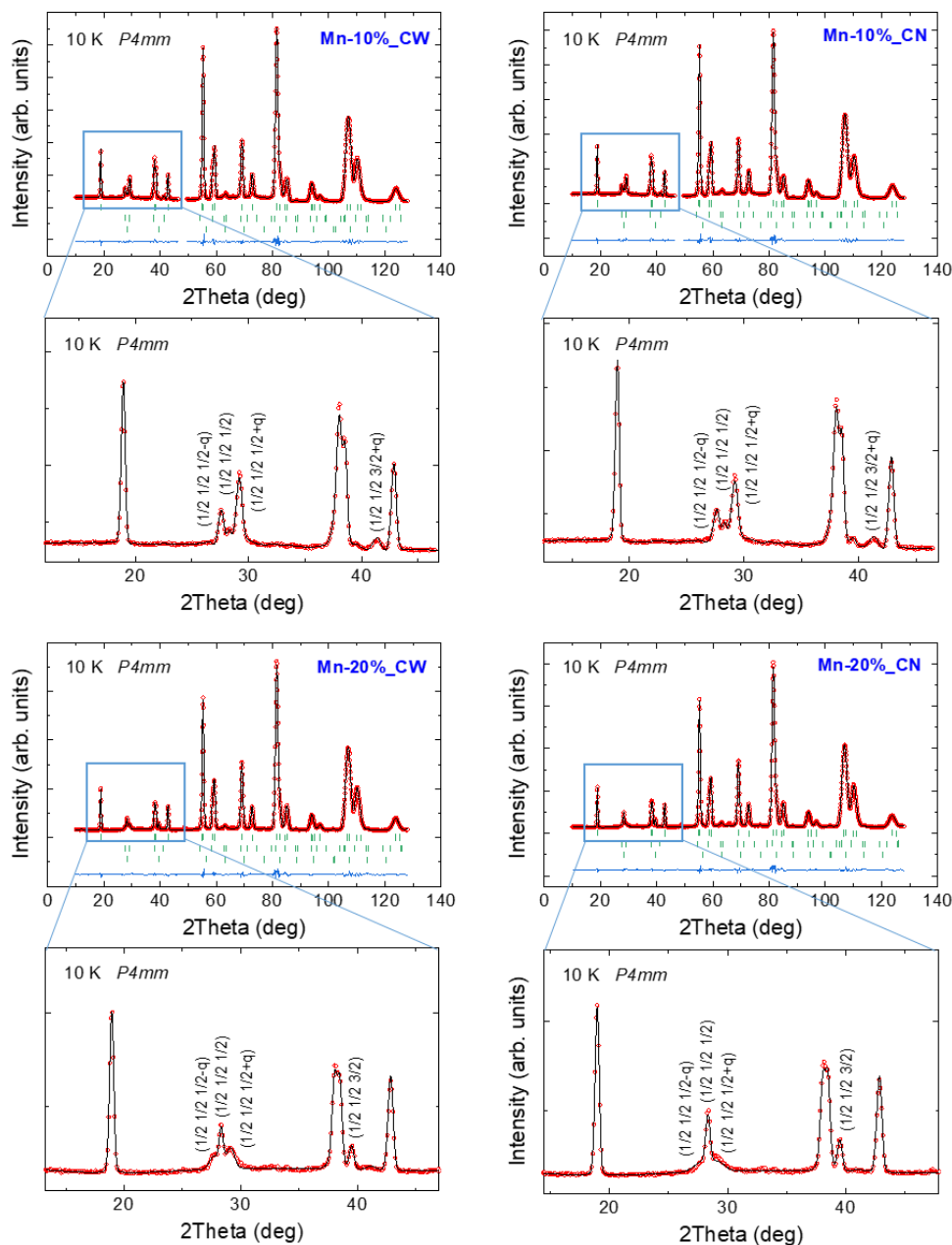


Figure 4.30. Rietveld refinement (black curve) of the neutron diffraction patterns (red circles) collected at 10 K (D1B@ILL) for **Mn-10%\_CW** ( $R_B$ :1.56,  $R_f$ :0.90,  $R_M$ :12.7,  $\chi^2$ :13.6); **Mn-10%\_CN** ( $R_B$ :1.42,  $R_f$ :0.84,  $R_M$ :13.8,  $\chi^2$ :11.5); **Mn-20%\_CW** ( $R_B$ :1.13,  $R_f$ :0.65,  $R_M$ :11.3,  $\chi^2$ :6.32); **Mn-20%\_CN** ( $R_B$ :1.18,  $R_f$ :0.68,  $R_M$ :14.8,  $\chi^2$ :6.83). Bottom blue line is the difference between the experimental and calculated intensities. Rows of bars correspond to allowed reflections for the structural, ICM magnetic (circular spiral) and CM magnetic phases. The expanded low-angle region is also shown for each composition, refined using the average moment [ $m(\text{Fe})=m(\text{Cu})$ ].



## 4.8 Summary and conclusions

In this chapter we have presented a detailed structural and magnetic characterization and analysis of the Mn doped YBaCuFe<sub>1-x</sub>Mn<sub>x</sub>O<sub>5</sub> high-T<sub>c</sub> multiferroic candidate using a combination of data collected from various experimental techniques such as SXPD, NPD and XAS. We prepared and investigated the properties of YBCFO when trivalent Fe is partially substituted by Mn, with the aim of increasing the spin-orbit coupling effects acting on the B'-sites of the perovskite. In addition, the study was extended to two selected compositions (x=0.10 and 0.20) prepared by quenching into room temperature water and liquid nitrogen, with the aim of increasing the chemical disorder. This allowed us establishing a comparison of the fast and normally-cooled samples.

### Part I:

The AA'BB'O<sub>5</sub> perovskites (A=Y, A'=Ba, B=Cu, B'=Fe) are composed of bipyramidal layers and exhibit complete order of A and A' cations but only partial order of B and B'. Since the B-site ordering is sensitive to the cooling process during the last annealing, all compositions were prepared under identical conditions and a cooling rate of 300 K/h. We found that the overall Fe/Cu cation disorder at the B'-sites was concomitantly increased by Mn doping from n<sub>d</sub>~23% without Mn up to n<sub>d</sub>~33% in the Mn-20% sample. This represents a new alternative strategy to tune the Fe/Cu chemical disorder in this structure.

The T-x magnetic phase diagram for the YBaCuFe<sub>1-x</sub>Mn<sub>x</sub>O<sub>5</sub> family has been built up to the paramagnetic state. We found that the tilting angles  $\theta_{col}$  ( $\theta_{CM}$ ) and  $\theta_{spiral}$  ( $\theta_{ICM}$ ) adopt constant values for a given composition, and within each magnetic regime they do not change upon temperature variations. Within the error  $\theta_{col}$  shows no dependence on the Mn content. In contrast,  $\theta_{spiral}$  exhibits a strong dependence on it. Namely, the introduction of Mn produces a progressive reorientation of the rotation plane of the magnetic spiral ( $\theta_{spiral}$ ): from nearly perpendicular to almost parallel to the *c* axis. Therefore, Mn doping is capable to transform a helical-type spin order ( $\mathbf{k} // \mathbf{Q}$ ) into a

cycloidal one ( $\mathbf{k} \perp \mathbf{Q}$ ), which may critically determine the ferro-electric and magnetoelectric behavior in these systems.

We have evidenced a strong competition (incompatibility) between the tendencies towards a J-T distortion in  $\text{Cu}^{2+}$  and  $\text{Mn}^{3+}$  ions in this perovskite. The energy penalty associated to the deformation of the lattice necessary to accommodate the J-T distortion in both  $\text{Cu}^{2+}$  and  $\text{Mn}^{3+}$  pyramidal polyhedra is too high, particularly in the  $\text{CuMnO}_9$  units. As a consequence, the system preserves the J-T deformation around  $\text{Cu}^{2+}$  sites by avoiding the presence of J-T distorted  $\text{Mn}^{3+}\text{O}_5$  pyramids. This is achieved by electronic segregation through a self-oxidation process assisted by the capture of extra oxygen within the rare-earth layer (the oxygen vacancy layer).  $\text{Mn}^{3+}$  is thus precluded at low-doping levels and substituted by the smaller  $\text{Mn}^{4+}$  ion, whereas Cu and Fe atoms respectively keep their original divalent and trivalent valences.

### **Part II:**

Magnetization measurements show a remarkable increase of the spiral transition temperature  $T_{\text{N}2}$  for the two fast-cooled (quenched) samples with composition  $x=0.10$  and  $0.20$ . This reaches  $\sim 60$  K for both samples as compared with the normally-cooled (300 K/h) samples with the identical composition.

The aforementioned prevalence of Mn cations in a tetravalent state in normally-cooled Mn-doped YBCFO evolves into a richer diversity of Mn cationic species when considering the samples prepared by rapid cooling due to submersion into RT water and LN. Specifically, the fast cooling method reduced the generation of tetravalent Mn cations, becoming for instance  $\sim 15\%$  of total Mn cations in the two fast-cooled  $x=0.10$  samples. Interestingly, on top of  $\text{Mn}^{3+}$  cations, there also appears a certain amount of  $\text{Mn}^{2+}$ .

We saw that the cooling-by-quenching methods produced an increase in the Fe/Cu chemical disorder. For the two studied fast-cooled samples, we also observed an increase in the (Fe/Mn)-Oa and a decrease in the Cu-Oa bondlengths. This is mainly due to two reasons: (i) the ionic radius of  $\text{Mn}^{2+}$  is much larger than that of  $\text{Mn}^{3+}$  and

Mn<sup>4+</sup>; and (ii) the oxygen excess in the crystal lattice generates an octahedral configuration around some of the Mn atoms.

Neutron diffraction data have unveiled that the samples underwent a fast-cooling process present a higher spiral transition temperature  $T_{N2}$ , especially for  $x=0.10$ . This could be ascribed to the mechanism proposed by Scaramucci and co-workers, namely, the larger the chemical disorder, the more Cu/Fe pairs will be replaced by the strong AFM Fe/Fe pair defects (the concentration being low enough so as to not dominate over the Fe/Cu order that produce local canting), increasing the frustration level in the system which favors the stabilization of the spiral.

Finally, the inclination angles  $\theta$  in the fast-cooled samples for both collinear and spiral phases present similar features to those seen in the normally-cooled samples. For the CM phase,  $\theta_{\text{col}}$  remains constant and independent from the cooling approach employed. Meanwhile, for the ICM phase,  $\theta_{\text{spiral}}$  keeps constant for each sample, but the fast-cooling samples show larger values ( $\sim 10^\circ$ ) as compared with the 300 K/h cooled ones, which tunes the spiral order from a cycloid ( $\theta \rightarrow 0^\circ$ ) towards a helix-type ( $\theta \rightarrow 90^\circ$ ).

## Chapter 5

# New strategy to rise the spiral temperature in YBaCuFeO<sub>5</sub> by Cu/Co substitution

### 5.1 Introduction

The interesting multiferroic candidate YBaCuFeO<sub>5</sub> with the perovskite structure AA'BB'O<sub>5</sub> allows different design possibilities based on cationic substitutions. By means of cationic substitutions in the A/A'-site of this perovskite ( such as in Y(Ba, Sr)CuFeO<sub>5</sub>, where Ba<sup>2+</sup> gets partially substituted by the smaller Sr<sup>2+</sup>) it is possible to notably raise the spiral ordering temperature up to ~395 K [46]. However, spontaneous polarization has not been observed in Sr-doped samples and several works attribute this lack of FE in Sr-doped YBaCuFeO<sub>5</sub> to a negligible DM interaction due to a configuration of the helical spin rotation plane parallel to the **ab**-plane [86][100]. In REBaCuFeO<sub>5</sub> the magnetic properties can be also favorably tuned by using larger rare-earths [45]. But this strategy ends up by generating defects in the orderly stacking of RE and Ba planes.

As an alternative strategy to upgrade the properties of YBaCuFeO<sub>5</sub>, in the last chapter we investigated the cationic substitution at the trivalent B'-site aimed to

increase the spin-orbit coupling and the magnetoelectric response by using  $3d^4$  Mn<sup>3+</sup> ions ( $L=2, S=2$ ) to partially substitute the highly symmetric Fe<sup>3+</sup> ions ( $3d^5, L=0, S=5/2$ ). So, in the YBaCuFe<sub>1-x</sub>Mn<sub>x</sub>O<sub>5</sub> family, we proved that the presence of the Mn produces a progressive reorientation of the plane of the magnetic spiral in the ICM phase [47]. Although this tuning of the spiral plane inclination is able to transform the helical magnetic spin order into a cycloidal one (which might critically determine the ferroelectric and magnetoelectric behavior), we found a systematic reduction in the spiral ordering temperature when increasing the Mn content.

In this chapter, we focus on the cationic substitution at the divalent B-site of this perovskite. We have comprehensively investigated the partial substitution of Cu<sup>2+</sup> by Co<sup>2+</sup> in the YBaCuFeO<sub>5</sub> perovskite and explored its influence of the magnetic properties of this material. As we know the basic structure of YBCFO is formed by [CuFeO<sub>9</sub>] bipyramids of corner-sharing Cu<sup>2+</sup>O<sub>5</sub> and Fe<sup>3+</sup>O<sub>5</sub> units. In contrast to the flattened Fe<sup>3+</sup>O<sub>5</sub> square pyramids, the Cu<sup>2+</sup>O<sub>5</sub> pyramids are notably elongated along *c*-axis due to the J-T distortion around Cu<sup>2+</sup> ( $t_{2g}^6 e_g^3$ ), which shows a large difference between the interatomic distances of Cu to apical and basal oxygens. The divalent cobalt ion presents HS state in most of cobalt oxides, and it is a non-J-T ion. Here the proposed substitution acts on the divalent B-site of this perovskite, preserving the trivalent B'-site occupied by Fe-III which is key for the strong AFM coupling of Fe-O-Fe bonds.

In many cobaltites the (high spin) ground state configuration of  $3d^7$  Co<sup>2+</sup> cations if surrounded by six oxygen anions creating a local  $O_h$  cubic symmetry is  $t_{2g}^5 e_g^2$ , as shown in Figure 5.1(a). Such state may be split under a local symmetry lowering, e.g. by a tetragonal or orthorhombic distortion. The degeneracy in the  $t_{2g}$  subshell, will be thus lifted. This can be seen from the total energy-level diagram shown in the Figure 5.1(b). When the  $3d$  spin-orbit interaction is not considered ( $\xi=0$  case), we find three low-lying quartets within the first 0.1 eV. In electron language, each of them would correspond to the hole occupying one of the three  $t_{2g}$  orbitals. The importance of the lifted degeneracy is that the orbital occupation will no longer be isotropic, i.e., the Co-

ion charge distribution will be highly nonspherical. If we enable a non-zero spin-orbit coupling ( $\xi \neq 0$  case), the energy level diagram reveals that there is indeed a large amount of mixing due to the spin-orbit interaction. So, N. Hollmann, Z. Hu, *et al.*[101] found that the  $3d$  spin-orbit interaction has a major influence on the energies and nature of the low-lying states of the  $\text{CoWO}_4$  system. The magnetic moment of Co atoms contains both a spin and an appreciable orbital component. This results in a strong coupling of the magnetic moment direction to the crystal structure, which permits to estimate the single-ion anisotropy of  $\text{Co}^{2+}$  ions.

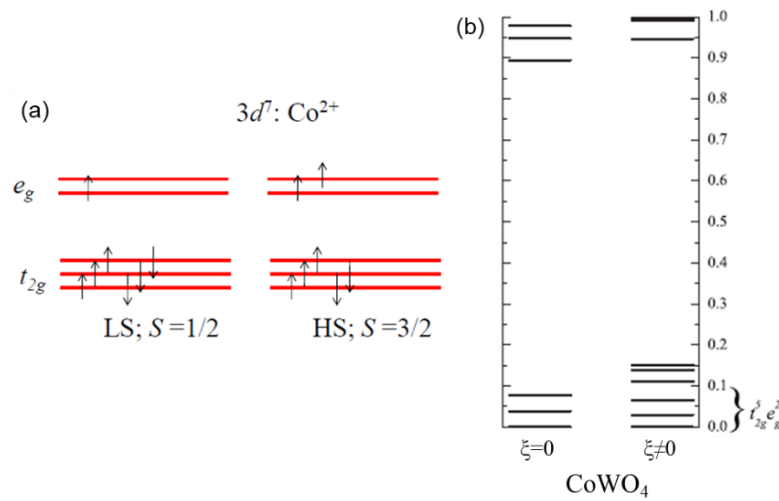


Figure 5.1. (a) The electronic configuration of the  $3d^7$ :  $\text{Co}^{2+}$  ion with low spin (LS) and high spin (HS) state; (b) The energy-level diagram for  $\text{Co}^{2+}$  ion, excluding and including the  $3d$  spin-orbit coupling  $\xi$ . Only the states up to 1 eV are shown, figure adapted from reference [101].

Over the past decades, there were many works done on the structural and magnetic properties of transition metal oxide containing  $\text{Co}^{2+}$  related to its spin-orbit coupling and single-ion magnetic anisotropy natures [102][103][104][105][106][107]. Thus, in this work, the substitution of Cu by Co was supposed to help increasing the magnetic anisotropy and the spin-lattice coupling thanks to the significant orbital moment contribution from  $\text{Co}^{2+}$  ions. This should have a direct incidence over the characteristic and stability of the spiral.

## 5.2 Sample synthesis and basic characterization

Polycrystalline samples YBaCu<sub>1-x</sub>Co<sub>x</sub>FeO<sub>5</sub> with  $x = 0, 0.01, 0.03, 0.04, 0.05, 0.06, 0.065, 0.075, 0.08, 0.10, 0.125, 0.15, 0.20$  and  $0.25$  (hereafter we denote samples by their % of Co substitution) have been prepared by the conventional solid-state reaction method, a general line of the process consisted of successive procedures is listed below:

- (i) High purity oxides of Y<sub>2</sub>O<sub>3</sub>, BaCO<sub>3</sub>, CuO, Co<sub>3</sub>O<sub>4</sub>, and Fe<sub>2</sub>O<sub>3</sub> were employed as starting materials to prepare polycrystalline samples. Evaporation of the moisture of the precursor oxides BaCO<sub>3</sub>, CuO, Fe<sub>2</sub>O<sub>3</sub> and Co<sub>3</sub>O<sub>4</sub> in a stove at 100 °C for 10 hours to avoid weighing errors. In case of Y<sub>2</sub>O<sub>3</sub>, a pre-annealing process was carried out at 900 °C for 10 hours in a furnace to promote the evaporation of possible carbonates;
- (ii) Determination of the stoichiometric amounts of the precursor oxides required by the reaction;
- (iii) Weighing, mixing, and homogenization of above oxides, finally completely homogeneous fine powder was obtained;
- (iv) Pressing of the fine powder into pellets using a cylindrical mold under a pressure 12 tons and hold for 20min (pellets size after pressing: 20mm in diameter and 5mm in thickness);
- (v) Annealing process of the pellets using a tubular furnace at 1100 °C for 50 hours in air atmosphere, with an initial positive temperature ramp of 300 °C/h and final negative ramp of 300 °C/h to cool the sample down to room temperature.
- (vi) Checking of as prepared samples using laboratory x-ray powder diffraction.

**Laboratory x-ray diffraction:** In order to assure the good quality of each composition, all samples were checked by laboratory x-ray diffraction. The x-ray diffraction patterns were collected using a Siemens D-5000 diffractometer and Cu K<sub>α</sub> radiation ( $\lambda=1.54 \text{ \AA}$ ). Some diffraction patterns on compositions with  $x=0.03, 0.05, 0.10$  and  $0.15$  and their Rietveld refinements are shown in Figure 5.2. All compositions were observed to be single-phase and no secondary phases were detected.

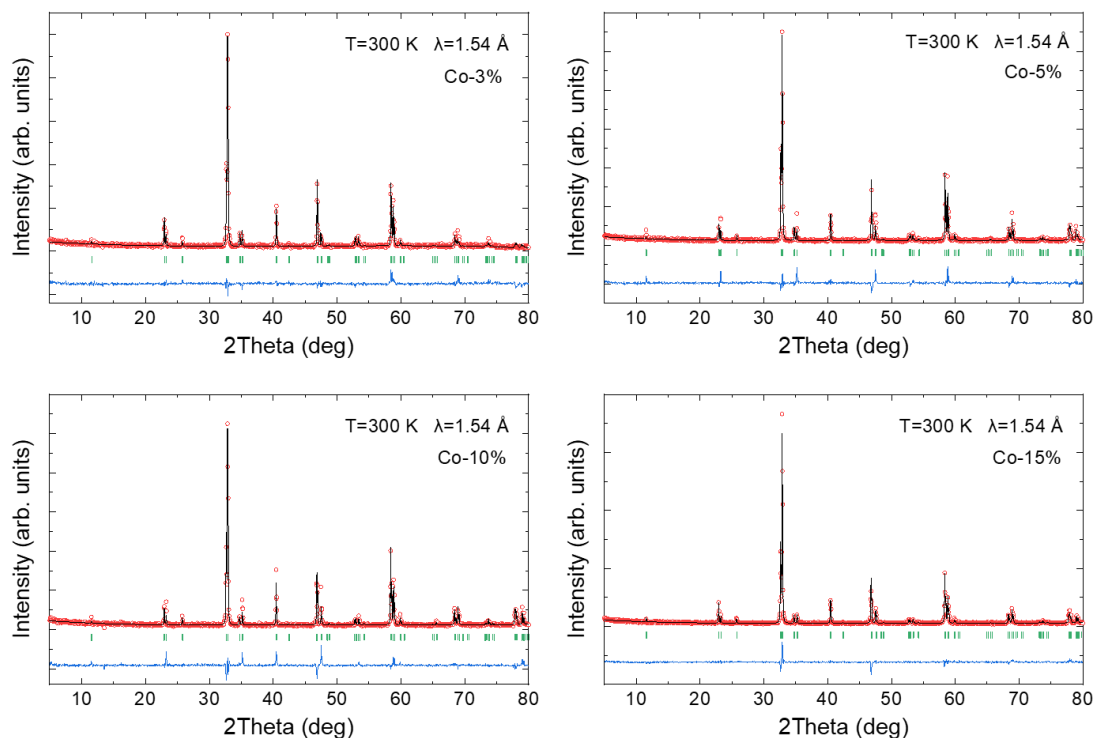


Figure 5.2. The Rietveld refinement (black line) of laboratory x-ray intensities (red circles) on  $\text{YBaCu}_{1-x}\text{Co}_x\text{FeO}_5$  with  $x=0.03, 0.05, 0.10$  and  $0.15$ . The row of green bars is the Bragg positions and the bottom blue line is the difference between experimental and calculated profile intensities.

**Magnetization:** Magnetic susceptibility measurements were also performed to study the magnetic phase transitions. A SQUID was employed to measure the magnetic data below RT under a magnetic field of 2 kOe in the condition of FC. Moreover, the magnetization upon warming was recorded in the temperature interval 300-550 K using a VSM in the PPMS, under the same magnetic field.

The measured magnetic susceptibility curves for all the compositions are depicted in Figure 5.3. The curves have been divided into two groups and plotted in panel (a) and (b). As we know that for the susceptibility curve of  $\text{YBaCuFeO}_5$ , namely, Co-0 sample, there are two transition temperatures at  $T_{N1}$  and  $T_{N2}$ , which correspond to the onset of AF1 collinear and AF2 spiral phase. For the cases of Co doped samples, two transition temperatures were also observed, as indicated by the two black arrows for each curve in panel (a) of Figure 5.3. The most interesting finding is, for  $T_{N2}$ , a different evolution compared with the  $\text{YBaCuFe}_{1-x}\text{Mn}_x\text{O}_5$  family which showed a decreasing



evolution upon doping content. The samples in panel (a) present an increasing tendency of  $T_{N2}$  against the Co substitution level, increased by more than 120 K from Co-0 (~230 K) to Co-6.5% (~355 K), well beyond RT. The  $T_{N1}$  undergoes a slight decrease upon Co doping which suggests that the magnetic collinear order has not been affected greatly when increasing the Co concentration in the solid solution.

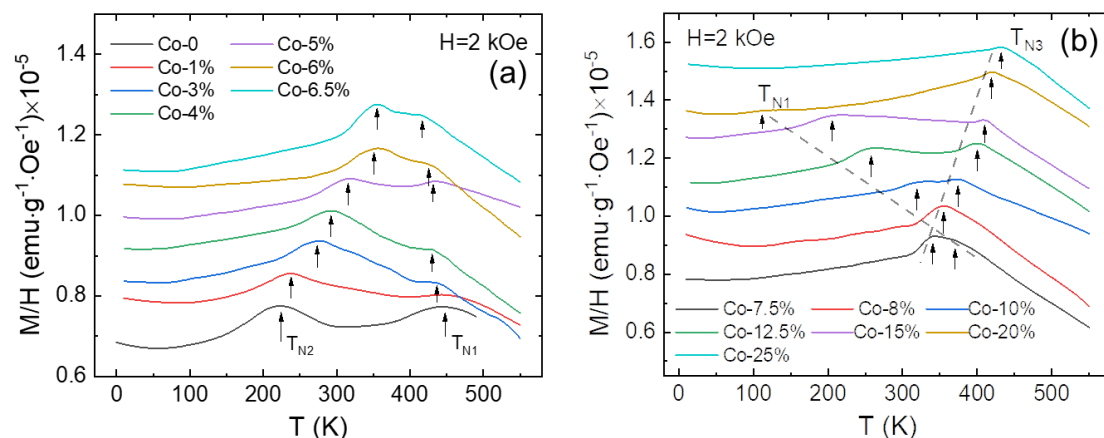


Figure 5.3. The measured magnetic susceptibility curves (2 kOe) for all the compositions in panel (a)  $0 \leq x \leq 6.5\%$  and (b)  $7.5\% \leq x \leq 25\%$ . Curves were shifted by  $+10^{-6} \text{ emu} \cdot \text{g}^{-1} \cdot \text{Oe}^{-1}$  for clarity. Dashed lines in panel (b) are guided lines for  $T_{N1}$  and  $T_{N3}$ .

The magnetic susceptibility curves for YBaCu<sub>1-x</sub>Co<sub>x</sub>FeO<sub>5</sub> ( $7.5\% \leq x \leq 25\%$ ) samples are shown in panel (b). It displays a different behavior in contrast to the samples in panel (a). Firstly, continue to increase the Co doping level, in the Co-7.5%, the two transition temperatures get closer to each other compared with Co-6% sample. And in the Co-8%, only one maximum was observed. Afterwards, when  $x > 8\%$ , two distinct transition temperatures appear again and undergo a modest increasing for  $T_{N3}$  and a fast decreasing tendency for  $T_{N1}$ , as guided by the dashed lines in panel (b). Here we should point out that, in this panel,  $T_{N1}$  is the onset temperature of the AF1 collinear phase, the same as in panel (a); while  $T_{N3}$  signals another onset temperature of a new AF collinear phase. This new transition will be confirmed, described and discussed later on in this chapter when we present the neutron diffraction results. The two groups of samples deserve further detailed investigation due to their attractive magnetic characteristics.

### 5.3 X-ray absorption spectroscopy

We performed XAS measurements with the purpose of assessing the electronic states of the different metals in the  $\text{YBaCu}_{1-x}\text{Co}_x\text{FeO}_5$  compounds and, in particular, with the aim of checking if the Co by Cu substitution is isovalent, namely, whether cobalt ions are indeed divalent, and occupy  $\text{Cu}^{2+}$  sites. The measurements at the Cu, Fe and Co  $L_{2,3}$  edges on  $\text{YBaCu}_{1-x}\text{Co}_x\text{FeO}_5$  samples with  $x=0.01, 0.05, 0.10$  and  $0.25$  were conducted in the HECTOR cryomagnet endstation at the BL29-BOREAS beamline of the ALBA Synchrotron Light Facility (Barcelona, Spain). The investigated samples were mounted on the Cu-made sample holders and in-situ cleaved under UHV conditions similarly as described in the previous chapters.

The XAS spectra across the Fe and Cu  $L_{2,3}$  edges are shown in Figure 5.4. In general, the spectrum of Fe and Cu present very similar spectroscopic features, respectively, and they do not show large variations upon Co doping level. At the Fe  $L_{2,3}$  edges, it is easy to observe that the XAS spectra corresponds to a high spin ( $S=5/2$ ) and trivalent electronic state [81][82]. Meanwhile, for the case of Cu  $L_{2,3}$  edges, we found the expected  $3d^9$  configuration [83]. This means that the oxidation states of Fe and Cu were well preserved during the preparation process of all samples.

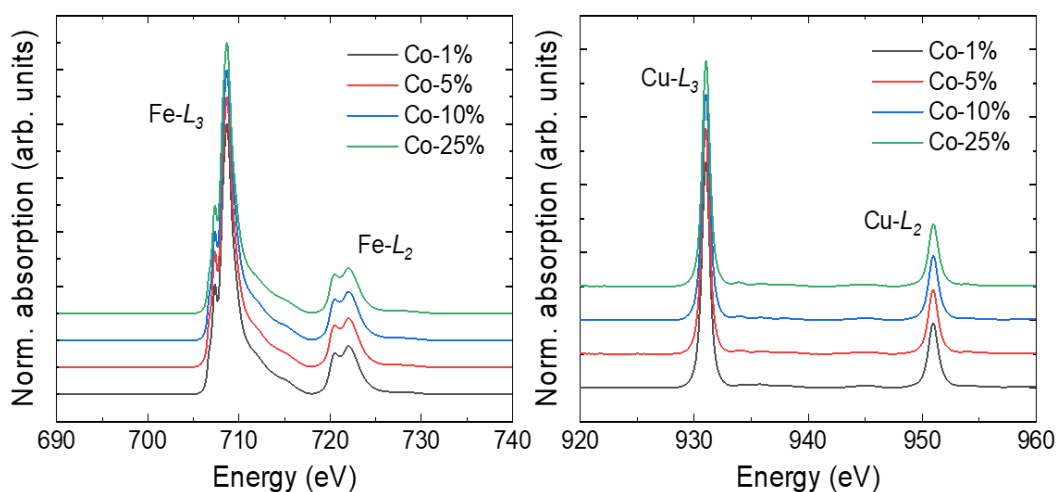


Figure 5.4. XAS spectra across the Fe (left) and Cu (right)  $L_{2,3}$  edges, for  $\text{YBaCu}_{1-x}\text{Co}_x\text{FeO}_5$  with  $x=0.01, 0.05, 0.10$  and  $0.25$ . Curves are vertically shifted for clarity.

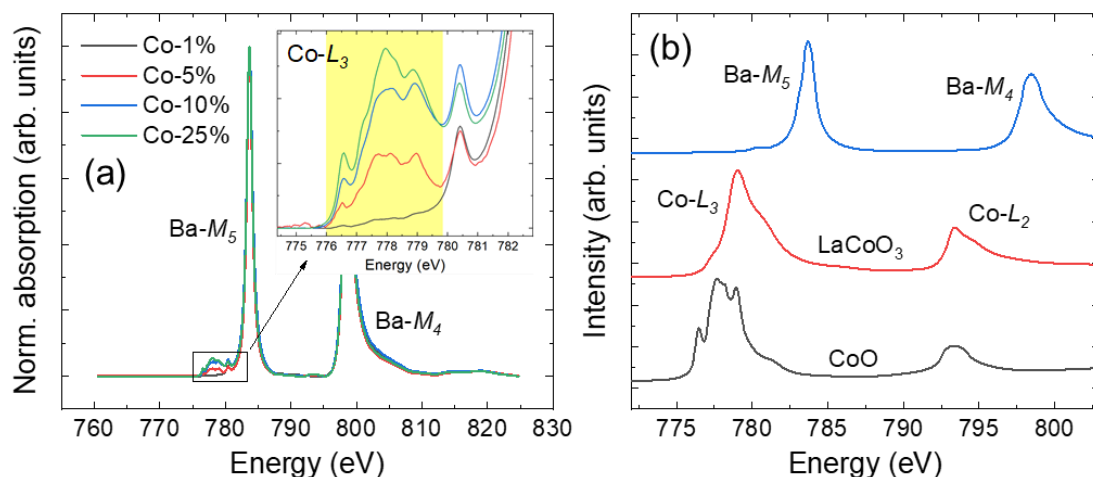


Figure 5.5. (a) XAS spectra across the Co  $L_{2,3}$  edges for YBaCu<sub>1-x</sub>Co<sub>x</sub>FeO<sub>5</sub> samples with  $x=0.01$ ,  $0.05$ ,  $0.10$  and  $0.25$ . The inset in panel (a) focuses on the Co  $L_3$  edge. (b) XAS spectra provided as references across the Co  $L_{2,3}$  and the Ba  $M_{4,5}$  edges of the compounds CoO (Co<sup>2+</sup>), LaCoO<sub>3</sub> (Co<sup>3+</sup>) [102] and Ba<sub>1.60</sub>Ce<sub>0.20</sub>Na<sub>0.20</sub>Ca(BO<sub>3</sub>)<sub>2</sub> (Ba<sup>2+</sup>) [108].

The experimental XAS spectra across the Co  $L_{2,3}$  edges for the four compositions are plotted in Figure 5.5 (a). It is worth noting that the Co  $L_{2,3}$  and Ba  $M_{4,5}$  absorption edges lie very close in energy, but the absorption cross section of Ba  $M_{4,5}$  is comparatively much larger. As a result, we observe a strong and sharp peak centered at  $\sim 784$  eV, in the high energy side of the Co  $L_3$  edge. The partial overlap hinders a proper analysis of Co  $L_3$  spectroscopic features. A similar problem takes place at the Co  $L_2$  edge, even aggravated due to its weaker XAS intensity. However, if zoomed (Fig. 5.5(a), inset), the Co  $L_3$  XAS region (776-780 eV) reveals an analyzable signal for most samples. Only for the Co-1% sample, we do not see almost any spectroscopic trace in the region, probably due to the very low concentration of Co. The other three compositions show comparable signals. The spectra of Co-5% and Co-10% are very similar, being composed of three main spectroscopic features. The first one peaks at 776.5 eV, followed by a broader, multi-component structure in between 777.5 eV and 778.5 eV and with a final rather incisive peak at 779 eV. All these energy positions match well with those found in a prototypical Co<sup>2+</sup>-based compound like CoO, as shown in the Figure 5.5 (b). This confirms that the oxidation state of cobalt in Co-5% and Co-10% samples is 2<sup>+</sup>. The XAS spectrum of Co-25% presents little differences

with respect to the lower doped samples. A sharper peak is found at  $\sim 778$  eV, which may reflect small structural and electronic changes, although the overall profile of the XAS spectrum continues being exclusive of divalent cobalt.

## 5.4 Synchrotron x-ray powder diffraction

The SXRPD measurements for all compositions were performed at 300 K at the BL04-MSPD beamline of the ALBA Synchrotron Light Facility (Barcelona, Spain) using the position sensitive detector MYTHEN. The wavelength,  $\lambda=0.413378$  (4) Å, was determined by measuring a NIST standard silicon. The samples were loaded in borosilicate glass capillaries (diameter in 0.7mm) and kept spinning during data acquisition.

Figure 5.6 displays the refined synchrotron x-ray powder diffraction patterns of the  $\text{YBaCu}_{1-x}\text{Co}_x\text{FeO}_5$  samples for all the compositions. All the patterns are similar and can be well described by the  $P4mm$  space group. In all the compositions, impurity phases such as  $\text{YFeO}_3$  and  $\text{CuO}$  were detected in low-angle regions, their amount systematically increase with the Co doping level, being 0.47% wgt and 0.30% wgt, respectively, in the Co-20% sample.

The structural parameters and agreement factors for each composition obtained from the Rietveld refinement at 300 K are listed in the Table 5.1. Similarly, as we did for the  $\text{YBaCuFe}_{1-x}\text{Mn}_x\text{O}_5$  samples, we refined the two split positions and occupations for Fe and (Cu, Co) respectively in each pyramid, and the z-coordinates of Fe and Cu in upper and lower pyramids were constrained by  $z(\text{M1})+z(\text{M2})=1$ , as shown in the Figure 5.7 (a) and Table 5.1 (the z-coordinates of Co atoms were constrained to be the same as for Cu). Figure 5.7 (b) shows the refined Fe/(Cu, Co) chemical disorder in the upper and lower pyramids. In the previous chapter we confirmed that the introduction of a third metal like Mn aiming to occupy the Fe sites progressively increases the Fe/Cu chemical disorder. To our surprise, the SXRPD refinements indicate that the Fe/Cu chemical disorder in the  $\text{YBaCu}_{1-x}\text{Co}_x\text{FeO}_5$  family is preserved and shows no dependence on the

Co content within the experimental error. As prior discussed, the degree of chemical disorder plays a key role on the magnetic frustration and the exchange interactions between the metals of the structure. At this point it is then important to highlight that a remarkable finding here is that the partial substitution of  $\text{Cu}^{2+}$  by  $\text{Co}^{2+}$  does not produces additional chemical disorder. We have determined a chemical disorder (see Table 5.1 and Figure. 5.7) of  $\sim 36\%$  in our set of  $\text{YBaCu}_{1-x}\text{Co}_x\text{FeO}_5$  samples, independently from their Co content.

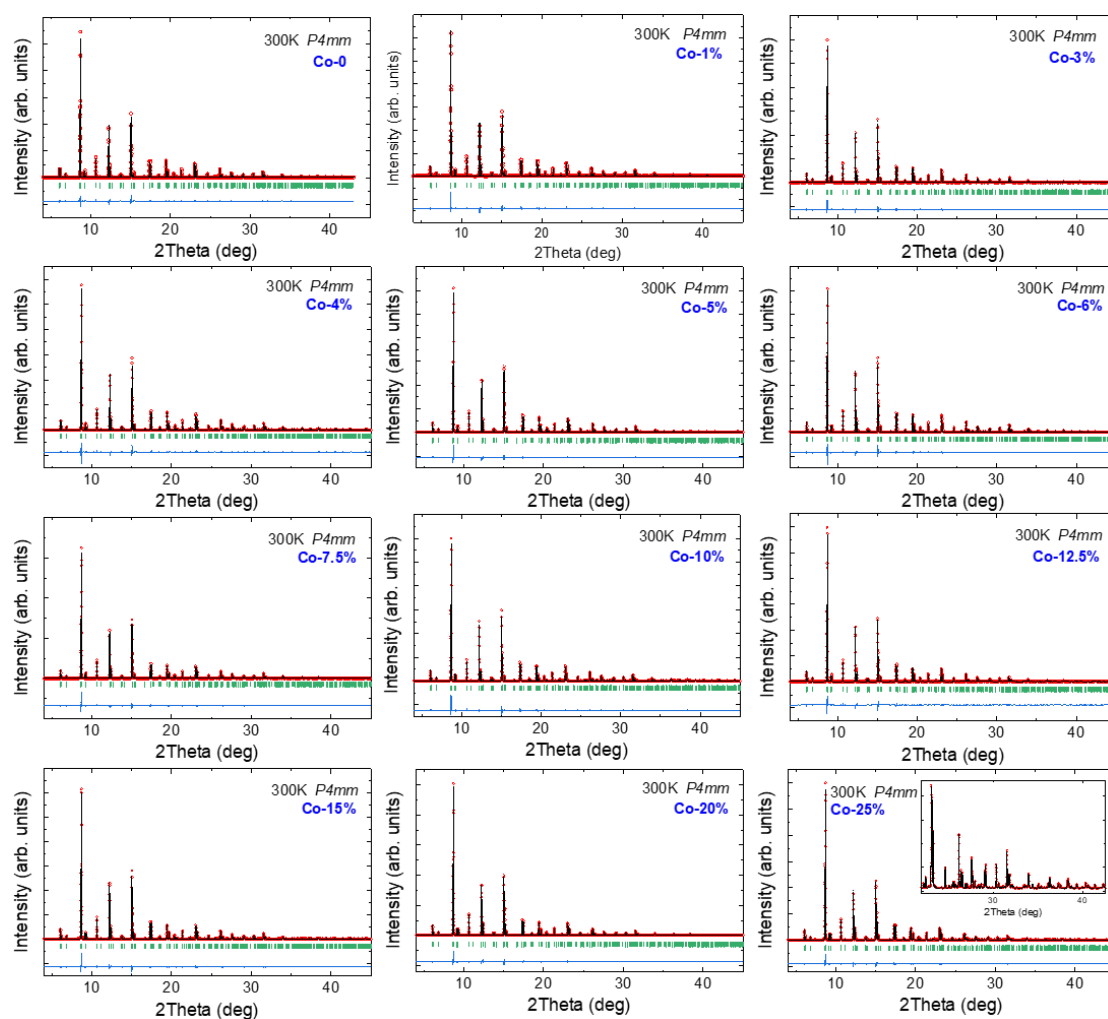


Figure 5.6. Rietveld refinement (black curve) of the synchrotron x-ray intensities (red circles) at 300 K of each composition. Bottom blue line is the observed-calculated difference, the row of green bar represents the calculated Bragg positions. Inset in the Co-25%: Details of the high-angle region.

**Table 5.1.** Structural parameters at T=300 K and agreement factors obtained from Rietveld refinement of synchrotron x-ray diffraction patterns ( $\lambda = 0.413378$  (3) Å). The coordinates of the two positions (M1 and M2) for each metal are related by  $z(\text{M1})+z(\text{M2})=1$ . (\*: the dominant cation in the pyramid).

YBaCu <sub>1-x</sub> Co <sub>x</sub> FeO <sub>5</sub>	x=0.01	x=0.03	x=0.04	x=0.05	x=0.06	x=0.065
a (Å)	3.87446 (3)	3.87500 (3)	3.87552 (3)	3.87612 (3)	3.87644 (3)	3.87651 (3)
c (Å)	7.66256 (6)	7.66072 (6)	7.65902 (6)	7.65753 (6)	7.65672 (6)	7.65672 (6)
V (Å <sup>3</sup> )	115.026 (2)	115.030 (2)	115.036 (2)	115.049 (2)	115.056 (2)	115.060 (2)
z (Y) (0 0 z)	0.51177 (32)	0.51146(33)	0.51189 (26)	0.51123 (23)	0.51194 (29)	0.51152 (28)
z (Fe1) (½ ½ z)*	0.75485 (54)	0.75441 (55)	0.75429 (67)	0.75415 (60)	0.75401 (73)	0.75395 (70)
z (Cu1) (½ ½ z)	0.71524 (23)	0.71545 (23)	0.71549 (23)	0.71553 (25)	0.71584 (32)	0.71579 (28)
z (Cu2) (½ ½ z)*	0.28476 (23)	0.28455 (23)	0.28451 (23)	0.28447 (25)	0.28416 (32)	0.28421 (28)
z (Fe2) (½ ½ z)	0.24515 (54)	0.24559 (55)	0.24571 (67)	0.24585 (60)	0.24599 (73)	0.24605 (70)
z (O1) (½ ½ z)	0.00318 (234)	0.00325 (243)	0.00329 (234)	0.00359 (278)	0.00386 (258)	0.00412 (262)
z (O2) (0 ½ z)	0.32611 (94)	0.32557 (96)	0.32541 (117)	0.32515 (102)	0.32503 (133)	0.32469 (120)
z (O3) (0 ½ z)	0.69488 (93)	0.69453 (95)	0.69451 (116)	0.69446 (102)	0.69442 (133)	0.69440 (120)
Occ (Fe1)	0.639 (20)	0.638 (20)	0.637 (20)	0.632 (20)	0.632 (20)	0.634 (20)
$\chi^2$	70.4	69.4	49.9	72.5	63.0	74.8
$R_B$	5.35	5.34	7.81	6.00	10.2	6.77
$R_f$	6.24	5.97	7.94	7.05	8.56	6.41

YBaCu <sub>1-x</sub> Co <sub>x</sub> FeO <sub>5</sub>	x=0.075	x=0.10	x=0.125	x=0.15	x=0.20	x=0.25
a (Å)	3.87688 (3)	3.87807 (3)	3.87880 (3)	3.87977 (3)	3.88101 (3)	3.88275 (3)
c (Å)	7.65555 (6)	7.65183 (6)	7.64992 (6)	7.64648 (6)	7.64350 (6)	7.63636 (6)
V (Å <sup>3</sup> )	115.064 (2)	115.079 (2)	115.094 (2)	115.099 (2)	115.128 (2)	115.124 (2)
z (Y) (0 0 z)	0.51077(37)	0.51040(27)	0.50985(27)	0.50951(28)	0.50899(29)	0.50826(29)
z (Fe1) (½ ½ z)*	0.75390(54)	0.75360(59)	0.75311(56)	0.75247(57)	0.75210(56)	0.75142(51)
z (Cu1) (½ ½ z)	0.71608 (23)	0.71617 (25)	0.71635 (23)	0.71746 (24)	0.71779 (24)	0.71849 (22)
z (Cu2) (½ ½ z)*	0.28392(23)	0.28383(25)	0.28365(23)	0.28254(24)	0.28221(24)	0.28151(22)
z (Fe2) (½ ½ z)	0.24610 (54)	0.24640 (59)	0.24689 (56)	0.24753 (57)	0.24790 (56)	0.24858 (51)
z (O <sub>1</sub> ) (½ ½ z)	0.00455 (256)	0.00429 (266)	0.00468 (254)	0.00389 (263)	0.00381 (269)	0.00396 (215)
z (O <sub>2</sub> ) (0 ½ z)	0.32516(101)	0.32371(118)	0.32351(111)	0.32153(122)	0.32008(117)	0.31836(117)
z (O <sub>3</sub> ) (0 ½ z)	0.69481(99)	0.69412(115)	0.69425(108)	0.69303(118)	0.69256(113)	0.69177(113)
Occ (Fe1)	0.631 (20)	0.632 (20)	0.631 (20)	0.632 (20)	0.631 (20)	0.630 (20)
$\chi^2$	78.5	82.4	65.1	75.3	53.3	52.1
$R_B$	5.41	5.45	5.46	4.73	4.33	4.65
$R_f$	6.49	6.86	6.84	5.91	4.97	4.44

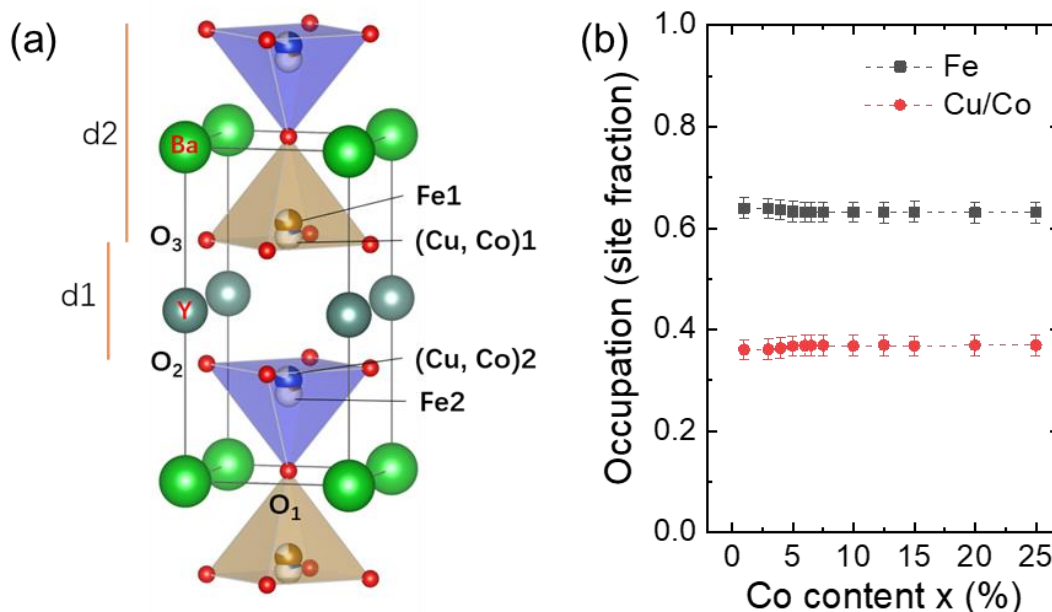


Figure 5.7. (a) Three-dimensional crystal structure of the YBaCu<sub>1-x</sub>Co<sub>x</sub>FeO<sub>5</sub> samples. In the structure, Fe1 and (Cu, Co)1 accommodate in the upper pyramid, Fe2 and (Cu, Co)2 occupy the lower pyramid. The distance d1 refers to the separation of bipyramid units and d2 is the thickness of the bipyramids. (b) Refined occupation values for each metal in Fe1 (upper) pyramid as a function of Co content. The disorder measures the fraction of atoms different from Fe1 at the Fe1 pyramid ( $n_d = 1 - \text{Occ}(\text{Fe1})$ ).

The experimental values found for the lattice parameters, volume (also included in the Table 5.1) and interatomic distances as a function of Co content are reported in Figure 5.8, as extracted from the Rietveld refinements of SXRPD data. In contrast with the studied samples belonging to the YBaCuFe<sub>1-x</sub>Mn<sub>x</sub>O<sub>5</sub> family, a systematic increase of the cell parameter  $a$  and a decrease of  $c$  were observed. Moreover, a reduction of the tetragonal distortion ( $c/2a$  ratio) accompanies the expansion of the volume, although these changes are very small. The contraction of the  $c$  parameter possibly results from the changes occurred in d1 and d2, the separation between the bipyramid layers and the average thickness of these layers, respectively, as shown in Figure 5.7 (a). Looking at the evolution of d1 and d2, we see an increase in the separation between bipyramid layers of up to  $\Delta d1 \approx +0.025$  Å in the heaviest Co-doped sample (Co-25%), as well as a compression in the thickness of the bipyramids of  $\Delta d2 \approx -0.051$  Å. Since the change in d2 is more pronounced than that in d1, we end up having a decrease in the cell parameter  $c$ . The evolution of the ratio d1/d2 is also plotted in Figure 5.8 (b).



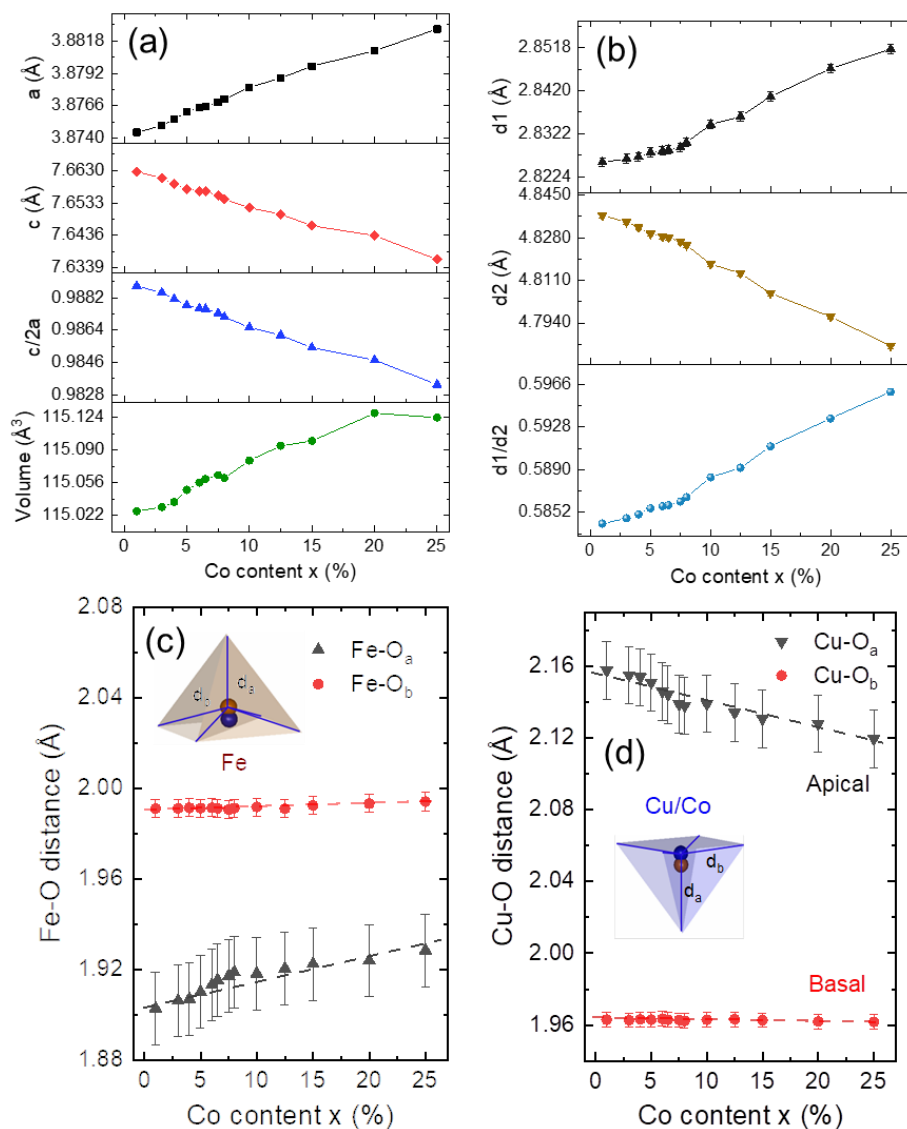


Figure 5.8. Evolution of lattice parameters and interatomic distances as a function of Co content  $x$ : (a) the cell parameters and volume; (b) the characteristic distances of  $d1$  and  $d2$  and the ratio  $d1/d2$ .  $d1$  is the distance of the separation between bipyramids and  $d2$  refers to the thickness of bipyramids; (c) and (d) the interatomic distances of Fe-O and (Cu/Co)-O in upper pyramid (brown) and lower pyramid (blue), respectively. The  $d_a$  and  $d_b$  in pyramids refer to the “apical” and “basal” distances in a pyramidal coordination.

The variation on metal-to-oxygen distances is rather appealing. The two basal distances, Fe-O<sub>b</sub> and Cu-O<sub>b</sub>, adopt a nearly constant value and show no dependence on the increasing Co doping level. On the contrary, at the same time, the two apical distances Fe-O<sub>a</sub> and Cu-O<sub>a</sub> undergo a continuous increasing and decreasing tendency, respectively. The J-T splitting between basal and apical distances around Cu<sup>2+</sup> ( $3d^9$ :  $t_{2g}^6 e_g^3$ ) is clear along the whole series. Nevertheless, it diminishes upon the addition of

Co because the Cu-O<sub>a</sub> distance also decreases. Indeed, under the addition of Co<sup>2+</sup>, Cu<sup>2+</sup> in the square pyramids gets progressively replaced by the former, which is a non Jahn-Teller-active ion. This produces an average shrinkage of the lattice along the [001] direction, overcoming the fact that the ionic size of Co<sup>2+</sup> (0.67 Å) is a bit larger than that of Cu<sup>2+</sup> (0.65 Å) [87] under V-coordination. Finally, we also see that Fe-O<sub>a</sub> follows a modest increasing tendency along the series, due to the displacement of the apical O1 towards the Cu position.

## 5.5 Neutron powder diffraction

NPD experiments were also conducted at the high-flux reactor of the Institut Laue Langevin (Grenoble, France) using the high intensity diffractometer D1B ( $\lambda=2.52$  Å). The polycrystalline samples were loaded inside the cylinder vanadium sample holder. Using the cryofurnace in D1B, NPD patterns were collected at fixed selected temperatures for 10 min to acquire good statistics. In addition, neutron diffraction patterns were also recorded in a continuous mode following temperature ramps within 10 K to 500 K range, with a heating rate of 3 K/min. For all the compositions presented above, we will here intentionally divide this YBaCu<sub>1-x</sub>Co<sub>x</sub>FeO<sub>5</sub> family into two parts or doping ranges:

(1) Doping range 1:  $0 \leq x \leq 7.5\%$  (DR1) and

(2) Doping range 2:  $8\% \leq x \leq 25\%$  (DR2)

as we will show that these two groups exhibit qualitatively distinct properties and magnetic behaviors.

Figure 5.9 plots the stacked low-angle region of neutron diffraction patterns recorded at 10 K for the samples in the two groups of doping ranges: light doping (DR1) and heavy doping (DR2). The systematic evolution of the main magnetic reflections in each group is displayed. Firstly, for the DR1 samples (Figure 5.9(a)) we observe that the ICM magnetic phase progressively decreases at expenses of an increase of the CM collinear magnetic phase. Both orders largely coexist within the DR1 range until for

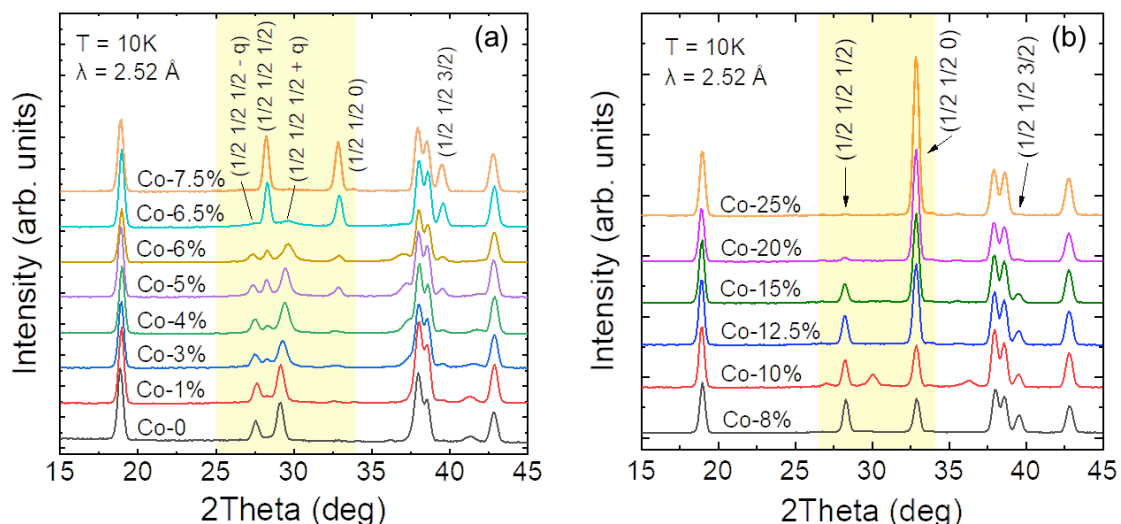


Figure 5.9. Low-angle region of the neutron diffraction patterns recorded at 10 K (d1b@ILL,  $\lambda=2.52$  Å) for the two groups of doping range samples: (a) for DR1 samples ( $0 \leq x \leq 7.5\%$ ) and (b) for DR2 samples ( $8\% \leq x \leq 25\%$ ).

$x=7.5\%$  Co the spiral order has vanished. Additionally, Figure 5.9(a) discloses that a second CM phase ( $\mathbf{k}_3=(1/2, 1/2, 0)$ ) gradually shows up being apparent for  $x \geq 5\%$  Co. Coinciding with the disruption of the spiral order, both  $\mathbf{k}_1$  and  $\mathbf{k}_3$  phases are initially reinforced for  $x \geq \sim 6\%$  Co. However, in the heavily doping range (Figure 5.9 (b)) one can see that then the  $\mathbf{k}_1=(1/2, 1/2, 1/2)$  type reflections begin to decline in favor of the third  $\mathbf{k}_3=(1/2, 1/2, 0)$  magnetic phase, which gets gradually dominant and finally it is the only magnetic phase present in YBaCu<sub>0.75</sub>Co<sub>0.25</sub>FeO<sub>5</sub> sample (our highest doping).

### 5.5.1 Temperature dependence: new insight on the phase evolution

**DR1 samples:** The magnetic susceptibility measurements carried out in section 5.2 displayed very attractive results for DR1 samples ( $0 \leq x \leq 7.5\%$ ), where we saw a systematic increase of the spiral ordering temperature by more than 120 K upon Co doping, stabilizing the magnetic spiral up to 355 K, well beyond RT. All these compositions were measured by neutron diffraction in the 10 K to 500 K temperature interval, which enabled us to study the magnetic transitions and investigate the evolution of the different magnetic phases.

For DR1 samples, the T-Q projection of the temperature dependence for the neutron-diffracted intensities around the (1/2 1/2 1/2) reflection is plotted in Figure 5.10 (a). As expected, upon cooling two sets of new magnetic Bragg reflections appear at  $T_{N1}$  and  $T_{N2}$ . Below  $T_{N1}$  (>375 K, for DR1 samples) the magnetic reflections can be indexed as  $(h/2, k/2, l/2)$ , and the unitary propagation vector is  $\mathbf{k}_1 = (1/2, 1/2, 1/2)$  (A point of the Brillouin Zone). Upon further cooling, two new split satellite magnetic peaks emerge at  $T_{N2}$  associated to the ICM propagation vector  $\mathbf{k}_2 = (1/2, 1/2, 1/2 \pm q)$ , which persist down to the lowest temperature. It is needed to point out here that below  $T_{N2}$ , the ICM phase is always accompanied by the CM collinear phase, which does not fully disappear and it can be seen clearly in Co-3%, Co-5% and Co-6% samples. The magnetic spiral modulation  $q$  (T) appears at  $T_{N2}$  ( $=T_S$ ) and progressively evolves to its maximum amplitude  $q_0$  at the lowest temperature. The two transition temperatures are listed in the Table 5.2 below.

The temperature dependence of the neutron diffraction data is compatible with the emergence of an ICM spiral magnetic phase below  $T_{N2} = T_S$ :

$$\mathbf{m}_{lj}(\mathbf{k}) = M_R(\mathbf{m})(\mathbf{u}_j) \cos(2\pi\{\mathbf{k} \cdot \mathbf{R}_l + \Phi_j\}) + M_I(\mathbf{m})(\mathbf{v}_j) \sin(2\pi\{\mathbf{k} \cdot \mathbf{R}_l + \Phi_j\})$$

where  $\mathbf{m}_{lj}$  is the magnetic moment of the atom  $j$  in the unit cell  $l$ ,  $\mathbf{R}_l$  is the vector joining the arbitrary origin to the origin of unit cell  $l$ , and  $\Phi_j$  is a magnetic phase.  $\mathbf{u}_j$  and  $\mathbf{v}_j$  define the orientation of the two perpendicular axes that fix the plane of the helix, where  $M_R$  (real) and  $M_I$  (imaginary) amplitudes determine the ellipse that describes the amplitudes of the magnetic moment components. In this structure it is not possible to independently refine parameters such as the real and imaginary magnetic moments components, because of the intrinsic limitations of the neutron powder diffraction data (different magnetic reflections can share the magnitude of momentum transfer wave vector), thus forcing us to fix their ratio using constrains. According to previous studies in these perovskites the moments at the  $\text{Cu}^{2+}$  and  $\text{Fe}^{3+}$  sites were restricted to the same inclination angle  $\theta$  in the neutron refinements. The phase difference  $\varphi$  between the magnetic moments at the two sites was fixed to  $180^\circ$  as previously found in the pure

YBCFO [21][44][45][86].

Moreover, apart from the magnetic phases described above, new magnetic reflections that cannot be indexed using  $\mathbf{k}_1$  or  $\mathbf{k}_2$  appeared upon cooling at a very similar onset temperature as that of phase  $\mathbf{k}_2$  (we denote this onset temperature as  $T_{N3}$ ) and also persist down to the base temperature. These novel magnetic peaks were visible from the Co-5% sample and are compatible with the commensurate propagation vector  $\mathbf{k}_3 = (1/2, 1/2, 0)$ . The  $\mathbf{k}_3$  component becomes clearly stronger increasing the Co content above the 6% of Co, when the  $\mathbf{k}_2$  loses preeminence, resulting in the very weak  $\mathbf{k}_2$  satellites in Co-6.5% sample. Finally, for Co-7.5%, the ICM phase  $\mathbf{k}_2$  component is completely gone and only the collinear phases  $\mathbf{k}_1$  and  $\mathbf{k}_3$  are present, as shown in the Figure 5.10 (a). It thus seems that there is an intense magnetic phase competition between the CM  $\mathbf{k}_3$  and ICM  $\mathbf{k}_2$  phases for  $x[\text{Co}] \geq 5\%$  in the present family. This novel phenomenon will be discussed later on in this chapter. Accordingly, the evolution of the ordered magnetic moment for the two main magnetic phases of each composition has been plotted in Figure 5.10 (b). Here, the CM and ICM ordered magnetic moments are averaged over the full sample volume. Moreover, the magnetic moments were refined averaged over the Fe and Cu sites. Additionally, for the ICM phase, the limit  $M_R \gg M_I$  was imposed.

For DR1 samples, the neutron diffraction results reflecting the evolution of the ordered spiral magnetic moment at 10 K while increasing the Co substitution level are shown in Figure 5.11. The fraction of spiral domains or the frustration level is hardly modified increasing the presence of  $\text{Co}^{2+}$  at  $\text{Cu}^{2+}$  sites up to the 6% of Co doping. That doping marks a change to a new scenario in which the stability and presence of the spiral order suddenly falls off. It is interesting to recall here that the level of Cu/Fe disorder is practically constant and the evolution observed essentially cannot be ascribed to changes in the B-site disorder (namely, to changes in the density of improper AFM Fe/Fe bonds).

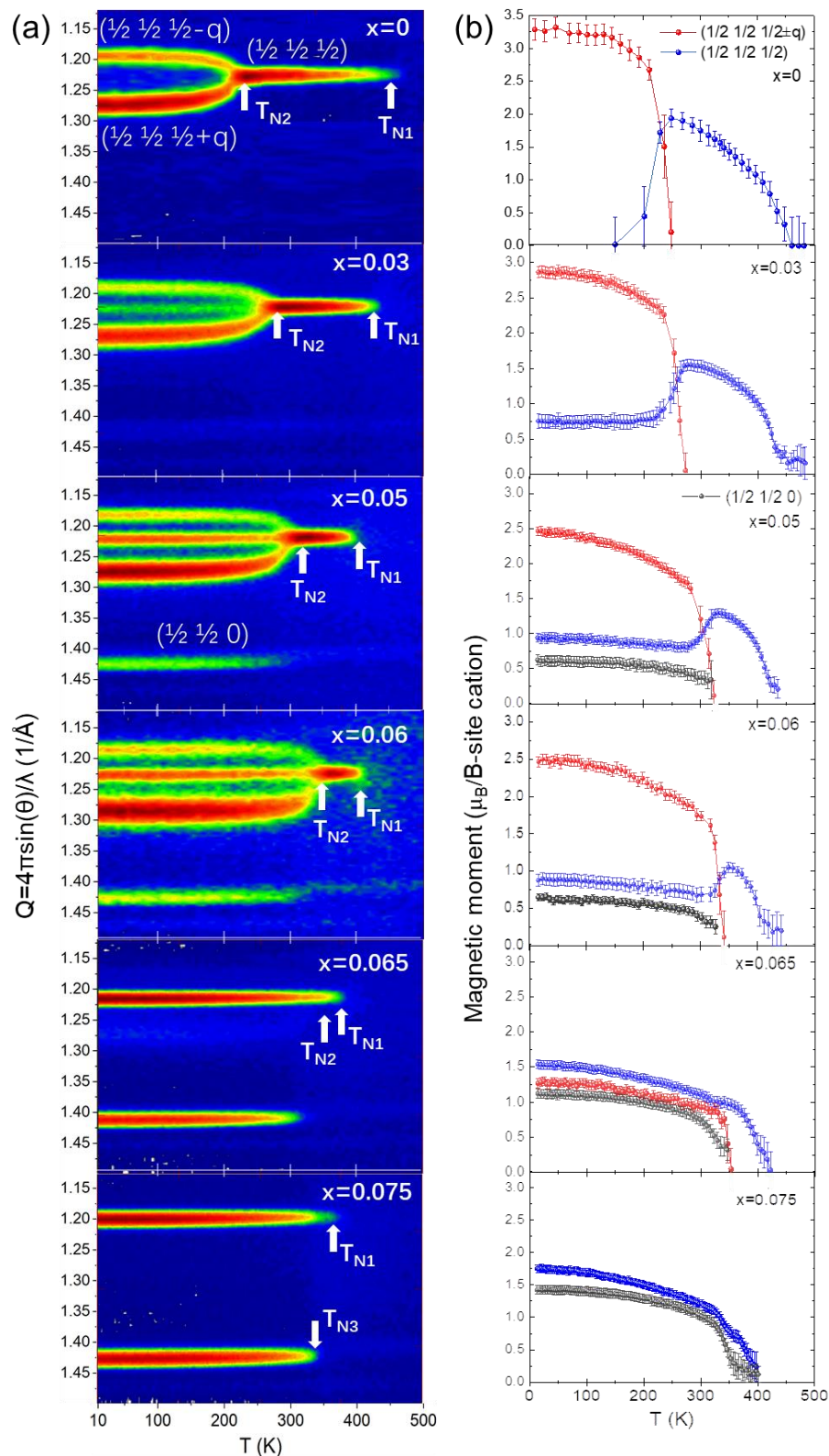


Figure 5.10. YBaCu<sub>1-x</sub>Co<sub>x</sub>FeO<sub>5</sub> samples in doping range 1 (DR1). (a) T-Q projection of the temperature dependence for the neutron-diffracted intensities around the  $(\frac{1}{2} \frac{1}{2} \frac{1}{2})$  reflection. (b) Average ordered magnetic moment (referred to the full sample volume) associated to the CM and ICM phases as a function of temperature. The red, blue and black symbols correspond to magnetic domains with  $(\frac{1}{2}, \frac{1}{2}, \frac{1}{2}\pm q)$ ,  $(\frac{1}{2}, \frac{1}{2}, \frac{1}{2})$  and  $(\frac{1}{2}, \frac{1}{2}, 0)$  wave vectors, respectively.

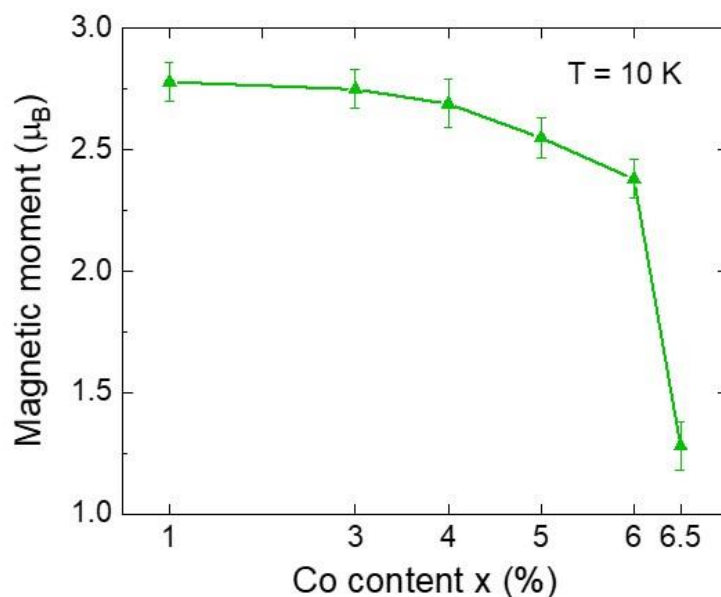


Figure 5.11. Evolution with Co of the ordered magnetic moment (referred to the full sample volume and  $M_R \gg M_I$ ) of the spiral magnetic phase at 10 K (DR1 samples).

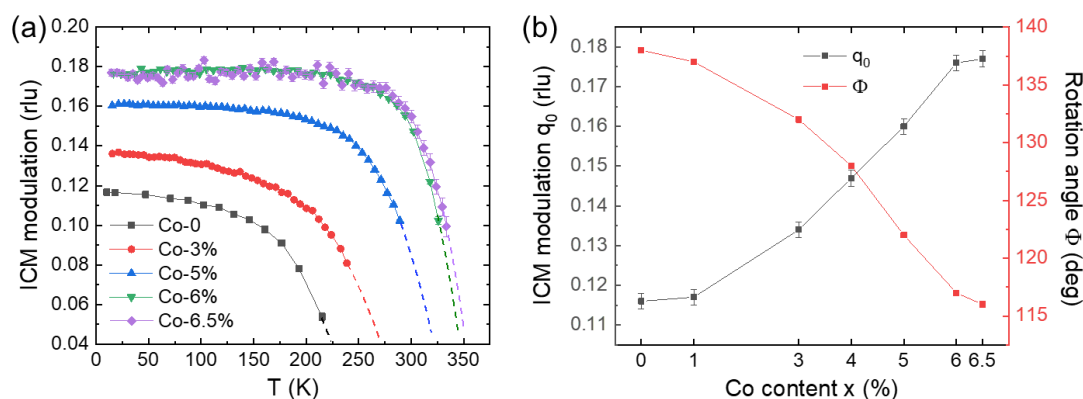


Figure 5.12. Modulation ( $q_s$ ) of the incommensurate spiral in YBaCu<sub>1-x</sub>Co<sub>x</sub>FeO<sub>5</sub> perovskites within the doping range DR1 ( $x < 7.5\%$ ). (a) Temperature dependence of the modulation and spiral transition temperatures ( $T_S = T_{N2}$ ). The dashed lines are guides for the eye. (b) Dependence of the modulation on Co content at 10 K. The associated spin rotation angle  $\Phi$  between equivalent moments in successive bilayers is also shown.

The temperature dependence of the incommensurability  $q$  is shown in Figure 5.12(a) for the DR1 samples. As shown in Figure 5.10 this parameter of the magnetic spiral modulation vector  $\mathbf{k}_2$  is also a measurement of the angular rotation of the spin moments between two successive unit cells along the [001] direction. For the samples with very low Co content we observe a smooth, continuous decrease of  $q$  on warming, characteristic of a second-order phase transition. This behavior gets progressively

substituted by a more abrupt collapse of  $q$  for the samples with higher  $T_s$  transition temperatures ( $x \geq 6\%$ ) suggesting that the CM to ICM phase transition transforms from second to first order. The ground state  $q_0$  values (at 10 K) are shown in Figure 5.12(b) for the different samples. In the same plot, one can also see the evolution of the spin rotation angle  $\Phi$  for each composition, where  $\Phi = \pi + \varphi = \pi + 2\pi q_0$  ( $\varphi = 2\pi q$  is the twist angle (canting) formed by the two spins of a bipyrmaid in the spiral phase). Such evolution of  $q_0$  and  $\Phi$  dependences on  $x$  indicates that the incommensurability is gradually strengthened when increases the Co content in the DR1 samples, as expected from the evolution of the spiral transition temperature. In addition, notice the abrupt changes occurring above the Co-6.5% doping that signal an apparent interruption of the described evolution.

**Table 5.2.** Some related parameters of structural and neutron results about the DR1 samples. The “ $n_d$ ” stands for the chemical disorder and  $n_d = 1 - \text{Occ}(\text{Fe}1)$ .

Sample	$T_{N1}(\text{K})$	$T_{N2}(\text{K})$	$T_{N3}(\text{K})$	$n_d$	$q(\text{r.l.u.})$	$d_2(\text{\AA})$	$\text{Fe-O}_a(\text{\AA})$	$\text{Cu-O}_a(\text{\AA})$
Co-1%	447(8)	236(8)	---	0.361(20)	0.117(2)	4.837(1)	1.903(16)	2.158(16)
Co-3%	425(8)	277(8)	---	0.362(20)	0.134(2)	4.834(1)	1.906(16)	2.155(16)
Co-4%	420(8)	296(8)	---	0.363(20)	0.147(2)	4.832(1)	1.907(16)	2.154(16)
Co-5%	413(8)	320(8)	320(8)	0.368(20)	0.160(2)	4.829(1)	1.910(16)	2.151(16)
Co-6%	403(10)	350(10)	350(10)	0.368(20)	0.176(2)	4.828(1)	1.913(16)	2.146(16)
Co-6.5%	390(12)	355(12)	355(12)	0.366(20)	0.177(2)	4.827(1)	1.915(16)	2.144(16)
Co-7.5%	370(12)	---	362(12)	0.369(20)	---	4.826(1)	1.916(16)	2.142(16)



**DR2 samples:** For the DR2 samples ( $8\% \leq x \leq 25\%$ ), the temperature dependence of the neutron-diffracted intensities around the magnetic reflections  $(1/2 \ 1/2 \ 1/2)$  and  $(1/2 \ 1/2 \ 0)$  have been plotted in Figure 5.13. As observed in the Figure 5.10, the extra magnetic phase with propagation vector  $\mathbf{k}_3=(1/2, 1/2, 0)$  was firstly detected in Co-5% sample. Upon Co doping this magnetic phase gets stronger and develops a higher onset temperature  $T_{N3}$ . For the sample Co-8%, the two magnetic CM phases  $\mathbf{k}_1$  and  $\mathbf{k}_3$  were observed displaying the same transition temperature ( $T_{N1}=T_{N3}$ ). Then, increasing further the fraction of  $\text{Cu}^{2+}/\text{Co}^{2+}$  substitution,  $T_{N3}$  increased whereas  $T_{N1}$  showed an opposite tendency. The evolution of the onset temperatures for the two CM phases  $\mathbf{k}_1$  and  $\mathbf{k}_3$  is shown in Table 5.3 and Figure 5.14, as determined from neutron data. One can see that the  $T_{N1}$  decreases much faster than the increase of  $T_{N3}$ . Actually, the  $\mathbf{k}_1$  CM phase got progressively suppressed. Eventually, for the sample Co-25%, the  $\mathbf{k}_1$  CM phase disappeared and got completely replaced by the  $\mathbf{k}_3$  CM phase.

Figure 5.15 shows the evolution of the average ordered magnetic moment at 10 K with the Co substitution level for the two CM phases with propagation vectors  $\mathbf{k}_1=(1/2, 1/2, 1/2)$  and  $\mathbf{k}_3=(1/2, 1/2, 0)$ . An increasing and decreasing tendency was observed, respectively, for these two magnetic phases raising the Co content. It is worth noticing that around the composition  $\text{YBaCu}_{0.90}\text{Co}_{0.10}\text{FeO}_5$ , Figure 5.13 reveals the presence of an additional minority phase compatible with the new propagation vector  $\mathbf{k}_4=(1/2, 1/2, \pm q)$ . Its ICM nature is confirmed by the detection of two new magnetic reflections, satellites of the  $(1/2 \ 1/2 \ 0)$  one. For that reason, the CM ordered magnetic moments in the sample Co-10% are lower than expected regarding the evolution plotted in the Figure 5.15 for the two CM phases.

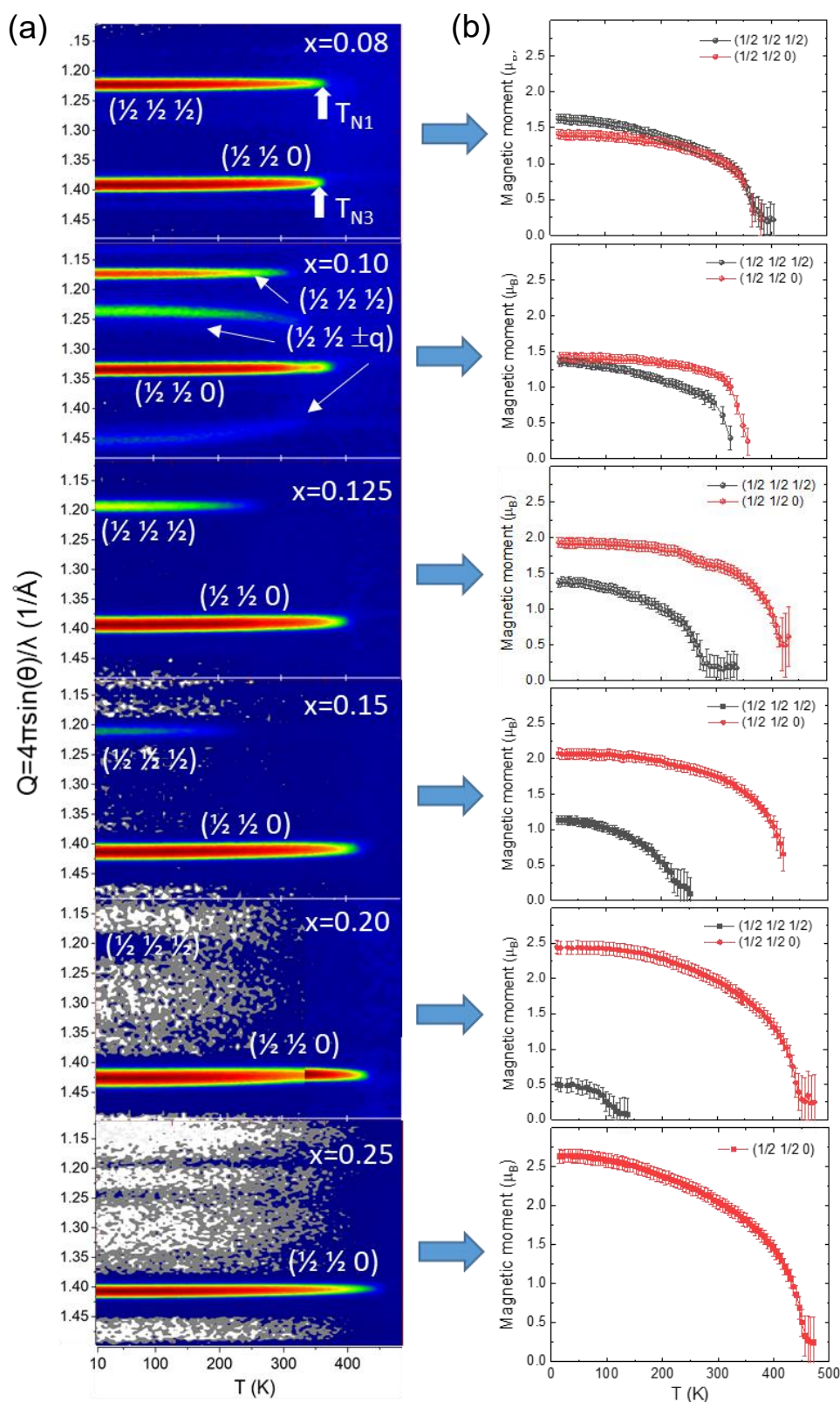
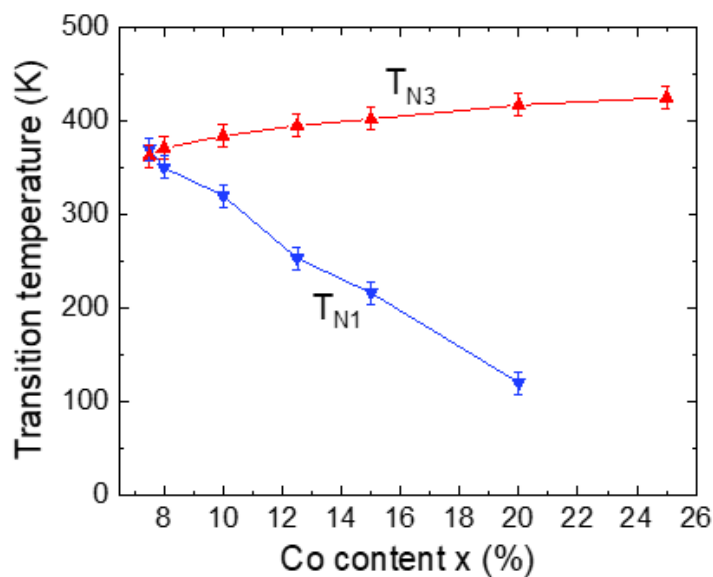
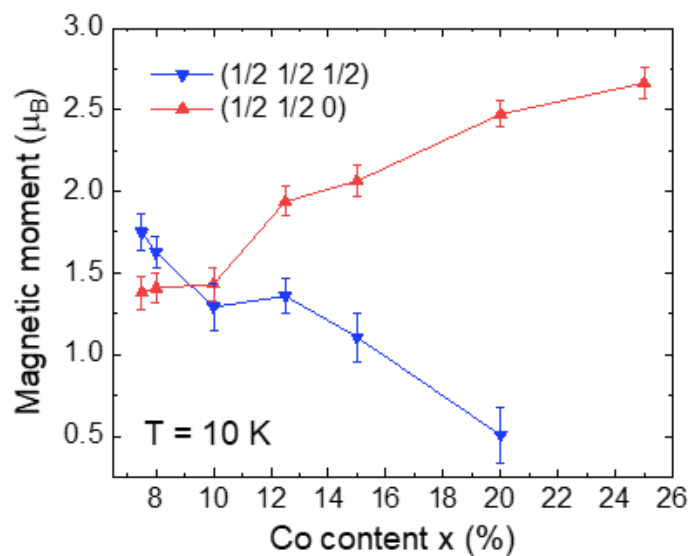


Figure 5.13. (a): T-Q projection of the temperature dependence for the neutron-diffracted intensities around the  $(\frac{1}{2} \frac{1}{2} \frac{1}{2})$  and  $(\frac{1}{2} \frac{1}{2} 0)$  reflections, for the DR2 samples. (b): the ordered averaged magnetic moments associated to the two CM phases as a function of temperature corresponding to (a). The red and black symbols correspond to the  $(\frac{1}{2}, \frac{1}{2}, 0)$  and  $(\frac{1}{2}, \frac{1}{2}, \frac{1}{2})$  phases, respectively.

**Table 5.3.** The onset temperatures for the two CM phases  $\mathbf{k}_1$  and  $\mathbf{k}_3$  as determined from the neutron diffraction measurements for DR2 samples.

Sample	Co-8%	Co-10%	Co-12.5%	Co-15%	Co-20%	Co-25%
$T_{N1}$ (K)	350(12)	320(12)	253(12)	216(12)	120(12)	---
$T_{N3}$ (K)	371(12)	384(12)	395(12)	402(12)	417(12)	425(12)

Figure 5.14. The evolution of the  $T_{N1}$  and  $T_{N3}$  onset temperatures versus Co content  $x$  for DR2 samples, determined by neutron measurements.Figure 5.15. Evolutions of the average ordered magnetic moment (referred to the full amount of sample and  $M_R \gg M_I$ ) of the two CM magnetic phases characterized by the propagation vector  $\mathbf{k}_1=(1/2, 1/2, 1/2)$  and  $\mathbf{k}_3=(1/2, 1/2, 0)$  at 10 K upon the Co content  $x$ .

### 5.5.2 Magnetic phase diagrams: huge increase of $T_s$ by Co substitution

According to the temperature dependent neutron diffraction results, a  $T$ - $x$ [Co] magnetic phase diagram for DR1 samples was built up first, as shown in Figure 5.16. The two magnetic transition temperatures determined by neutron diffraction data are consistent with the previous magnetization measurements. Regarding the evolution of  $T_{N1}$  and  $T_{N2}$  ( $=T_s$ ) in the figure, the former displays a modest decrease while the latter shows a huge increase from  $T_s \sim 230$  K in the non-doped sample Co-0 up to  $T_s \sim 355$  K in the Co-6.5% sample. In the Co-7.5%, the spiral phase was not detected.  $T_s = 355$  K found in the Co-6.5% sample is the highest spiral ordering temperature obtained for this series prepared by a controlled cooling rate of 300 K/h. In addition, as observed in the Figure 5.10, the novel CM magnetic phase  $\mathbf{k}_3 = (1/2, 1/2, 0)$  starts to arise in the Co-5% sample. It seems that this phase “separates” from the main  $\mathbf{k}_1$  and  $\mathbf{k}_2$  phases, and it progressively gets stronger increasing the Co content until  $x=0.075$ . We call this region as the “*Phase separation region*”, presented using the slashes in the phase diagram. In this region the  $\mathbf{k}_2$  and  $\mathbf{k}_3$  phases coexist, extending from  $x=0.05$  until the spiral phase disappears.

The decrease of  $T_{N1}$  can be safely attributed to the crystal lattice and structural tuning effects and the concomitant variations of magnetic NN exchange interactions caused by the substitution of Cu by Co atoms. Such as the increase of  $d_1$  (decreasing  $J_{c1}$ ) or the weakening of the FM coupling inside the bipyramids when the Cu/Fe pair is substituted by AFM Co/Fe. The huge increase of  $T_{N2}$  is however more intriguing, although it should be stressed here that a priori both the B-site chemical disorder and the  $d_1$  and  $d_2$  distances can play an active role on the transition temperature  $T_{N2}$ . First, it is shown in Figure 5.7(b) that, within the error, the chemical disorder of DR1 samples has not been varied by the addition of the third metal Co to the Cu sites, the associated chemical disorder was determined to be  $\sim 36\%$ , invariant under doping. Second, the structural analysis presented in the Figure 5.8(b) shows that the distance  $d_1$  has been increased by  $0.003(1)$  Å from Co-1% to Co-6%, whereas the  $d_2$  has been shrunk by

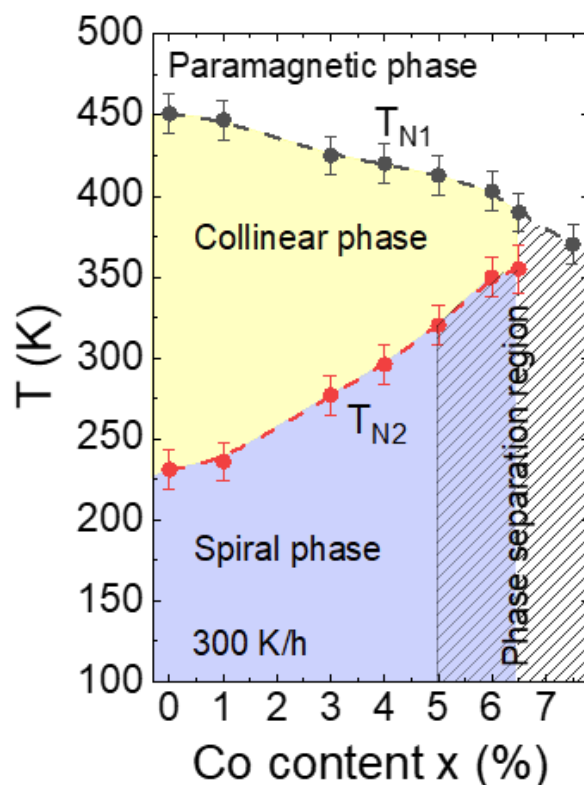


Figure 5.16. The  $T$ - $x$ [Co] phase diagram for the  $\text{YBaCu}_{1-x}\text{Co}_x\text{FeO}_5$  series prepared by a controlled cooling rate 300 K/h. The phase boundaries correspond to the onset of the magnetic phases as observed from neutron diffraction data. In the *phase separation region*,  $\mathbf{k}_3$  magnetic domains coexist with the spiral  $\mathbf{k}_2$  phase (in addition to  $\mathbf{k}_1$  domains). Around 7.5% Co, the spiral phase is absent.

0.008(1) Å, almost three times in contrast to the variation happened on  $d_1$ . Third, in order to explain the huge stability achieved in the spiral order, the most relevant and important effect is the modification of the bipyramidal thickness  $d_2$  parallel to the  $c$  axis. The crucial point being that in the bipyramids occupied by two Fe atoms, the strong AFM Fe-O1-Fe exchange coupling ( $J_{c2}$ ) is further strengthened due to the contraction of  $d_2$  (and so of the Fe-O1-Fe straight bond). The strong AFM exchange generated in  $\text{Fe}_2\text{O}_9$  bipyramids (present by disorder) is thus reinforced and raises the frustration level (competition with the FM  $J_{c2}$  exchange from Fe-O1-Cu bonds in “ordered”  $\text{FeCuO}_9$  bipyramids). Therefore, the contraction of  $d_2$  imposes a positive effect on the degree of magnetic frustration within the layered bipyramids structure, thus increasing the spiral ordering temperature  $T_s$ . In other words, we conclude that we have obtained a huge increase of the spiral ordering temperature which is an additive

consequence of the combination of the high chemical disorder and, most important, the contraction of the bipyramidal thickness  $d_2$ . The remarkable achievement then is that the stability of the spiral magnetic phase has been displaced beyond ambient temperature using a new strategy based on the disruption of the J-T distortion in  $\text{CuO}_5$  pyramids. The disturbance of the J-T distortion has been made possible thanks to the insertion of divalent magnetic but non-J-T  $\text{Co}^{2+}$  ions in  $\text{Cu}^{2+}$  sites.

Previous work done by M. Morin and coworkers on the  $\text{YBaCuFeO}_5$  layered structure gives additional support to our interpretation of these experimental results. In  $\text{YBaCuFeO}_5$  samples with different Fe/Cu chemical disorder, the  $T_S$  was raised up to  $T_S \approx 310$  K for the most disordered sample [45][46]. Furthermore, in their another work dedicated to extend the stability range of the magnetic spirals, they prepared (i)  $\text{REBaCuFeO}_5$  samples in which the  $\text{Y}^{3+}$  was replaced by isovalent rear earth  $\text{RE}^{3+}$  ( $\text{RE}=\text{Lu}$  to  $\text{Dy}$ ) with the purpose of elongating  $d_1$  and (ii)  $\text{YBa}_{1-x}\text{Sr}_x\text{CuFeO}_5$  series where the  $\text{Ba}^{2+}$  was partially substituted by smaller  $\text{Sr}^{2+}$  aiming at compressing  $d_2$ . The first approach lifted the  $T_S$  to 312 K, whereas the latter boosted the  $T_S$  to 375 K for  $x[\text{Sr}]=0.4$ . In agreement with our findings, the manipulation of  $d_2$  is much more efficient than  $d_1$  for tuning the spiral ordering temperature [46].

The temperature dependent neutron diffraction illustrated in Figure 5.10 and the evolution of the spiral magnetic moment in Figure 5.11 can help us to understand the “*Phase separation region*” better. As observed in Figure 5.10, the collinear AF3  $\mathbf{k}_3$  phase starts to arise markedly in the Co-5% sample, but it exists already, very incipiently at lower doping (Figure 5.9(a)). This is probably a consequence of the introduction of Co ions in the bipyramids. The reason is that in a bipyramid occupied by a  $\text{Co}^{2+}/\text{Fe}^{3+}$  pair or even  $\text{Co}^{2+}/\text{Cu}^{2+}$  pair (instead of  $\text{Cu}^{2+}/\text{Fe}^{3+}$ ) the exchange coupling is AFM (instead of FM), according to the Goodenough-Kanamori-Anderson (GKA) rules [76][90][91]. This AFM intra-pyramidal coupling favors  $k_z=0$  instead of  $k_z=1/2$  and therefore, our substitution proportionally favors a residual magnetic phase with wave vector  $\mathbf{k}_3=(1/2, 1/2, 0)$ . We call that residual phase separation at this initial stage

as “induced phase separation” (induced by Cobalt). When increasing the Co content, between 5% and 7%, the AF3 phase competes with the other two. In an independent parallel process, the spiral phase collapses at  $x=6.5\%$  Co (Figure 5.11). When  $T_{N2}$  approaches or meets  $T_{N1}$ , yielding a multicritical point. The “spiral order by disorder mechanism” requires and cannot avoid a commensurate collinear phase preceding the chiral incommensurate magnetic order. A paramagnetic/spiral phase boundary of finite size is not possible. The disappearance of the spiral should be ascribed to the strong AFM couplings between Fe-Fe bonds which become so large that the FM coupling of the bipyramids occupied by Cu-Fe can no longer compete. This favors a magnetic structure where all NN couplings are AFM, corresponding to the magnetic phase with  $\mathbf{k}_3$ . The evolution of the spiral magnetic moment in Figure 5.11 confirms that picture. The spiral magnetic moment decreases only a little up to 6% of Co doping (induced phase separation). Whereas for the Co-6.5% sample, the magnetic moment undergoes a sudden drop, which indicates that there is a large modification of the magnetic frustration in the system. Further increases the Co content, the spiral phase is completely absent beyond the triple point, when the continuous evolution of the collinear-to-spiral phase transition intersects the paramagnetic-to-collinear-spiral transition line. After this multi-critical point [109], the phase separation is termed as “critical phase separation”.

Apart from the  $T$ - $x$ [Co] phase diagram, the  $T$ - $d_2$  and  $T$ - $q_0$  phase diagrams for the YBaCu<sub>1-x</sub>Co<sub>x</sub>FeO<sub>5</sub> family ( $0 \leq x \leq 6.5\%$ ) are also plotted in Figure 5.17, which correlates the two transition temperatures with the bipyramidal thickness  $d_2$  and the incommensurability  $q_0$ , keeping fix the Fe/Cu disorder. The  $\mathbf{k}_2$  spiral phase coexists with the new  $\mathbf{k}_3$  collinear phase when  $x$ [Co]  $\geq 5\%$ , this is illustrated by the “*Phase separation region*” in both figures. Actually, below  $x$ [Co]=5%, there is already  $\mathbf{k}_3$  phase, but its proportion is so small that it is hardly detected. In Figure 5.17(a), a negative linear correlation can be extracted between the two parameters,  $T_{N2} = -11452.60d_2 + 55639.64$ . In this material, when the Fe/Cu chemical disorder is fixed, the

modification of the thickness of the bipyramid layers ( $d_2$ ) is an efficient way to tune the magnetic frustration and control the spiral ordering temperature. On the other hand, in Fig. 5.17(b), a positive linear relationship can be found between  $T_{N2}$  and the incommensurability  $q_0$ , ( $T_{N2} = 10.89 + 1933.57q_0$ ), which is consistent with the mathematical model developed by Scaramucci and coworkers [84][85].

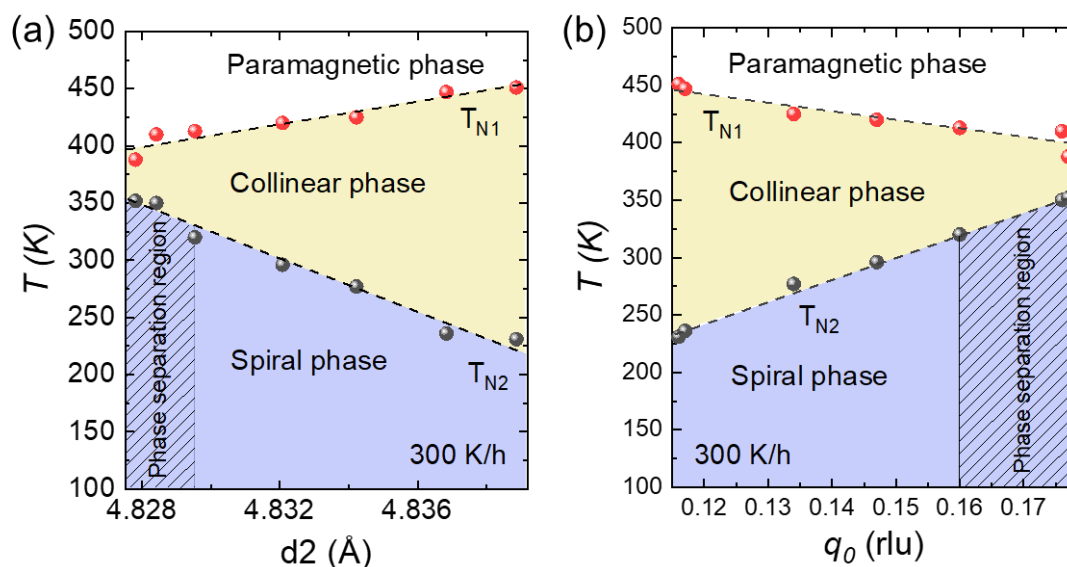


Figure 5.17. The (a)  $T$ - $d_2$  and (b)  $T$ - $q_0$  phase diagram for the  $\text{YBaCu}_{1-x}\text{Co}_x\text{FeO}_5$  family ( $0 \leq x \leq 6.5\%$ ). The  $T_{N1}$  and  $T_{N2}$  are determined from the  $T$ -dependence neutron diffraction data;  $q_0$  and  $d_2$  are Rietveld refined values using the neutron and synchrotron diffraction data, respectively.

Another interesting observation for the  $\text{YBaCu}_{1-x}\text{Co}_x\text{FeO}_5$  family is the previously referred linear relationship between the spiral ordering temperature and the modulation  $q_0$  (periodicity of the spiral) as shown in Figure 5.18, in which our samples have been plotted with other series of samples investigated in the reference [46]. The modulation  $q_0$  for our family has been pushed to a value of 0.177 (3), and also the spiral ordering temperature has been managed to raise up to  $T_s = T_{N2} = 355(12)$  K, reaching the triple point by keeping constant the chemical disorder. Without the need of having a very strong disorder we have thus reached very high spiral temperatures, comfortably far from RT. In addition, we show in the figure that the linear relationships for each family are not identical (see Figure 5.18). They intersect the horizontal axis in different points



(non-zero points on the  $q_0$  axis). This suggests that there is a minimum  $q_0$  point (non-zero) for the stabilization of the spiral phase. Such a result is in contrast with previous assumptions [46] which used the same linear relationship across the origin for all the families.

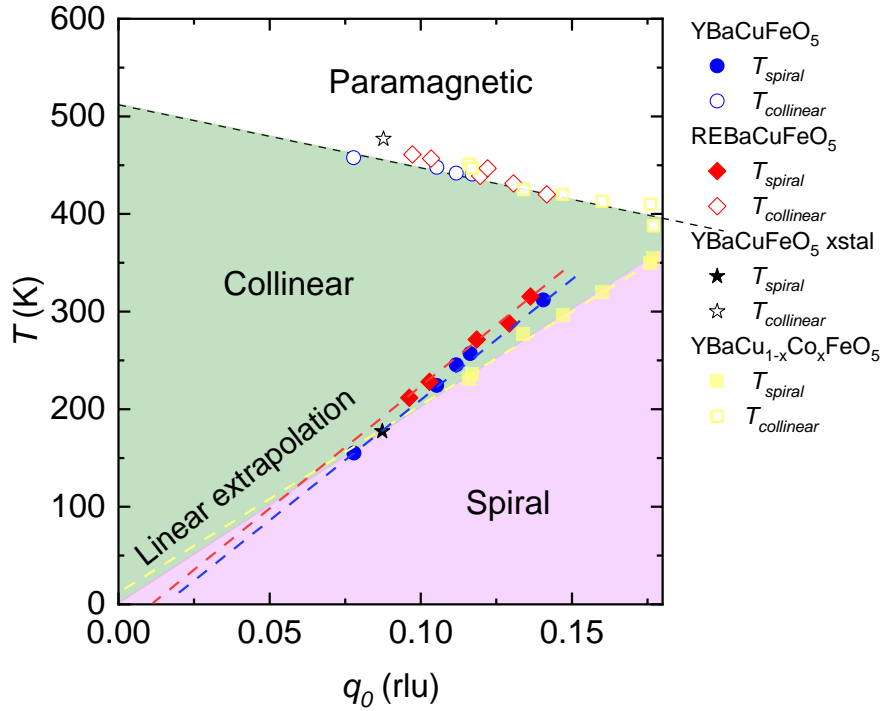


Figure 5.18. Linear relationship between the spiral ordering temperature  $T_s$  and the ground-state magnetic spiral modulation  $q_0$  for our YBaCu<sub>1-x</sub>Co<sub>x</sub>FeO<sub>5</sub> ( $0 \leq x \leq 0.065$ ) series compared to other family of samples from reference [46].

### 5.5.3 Impact of Co doping on the easy axis and magnetic anisotropy

In this section we have investigated the impact of the Cu<sup>2+</sup> by Co<sup>2+</sup> substitution on the magnetic anisotropy of YBCFO, by means of neutron diffraction. The orientation of the magnetic easy axis, defined by the angle  $\theta$  is illustrated in Figure 5.19 for collinear and spiral phases.

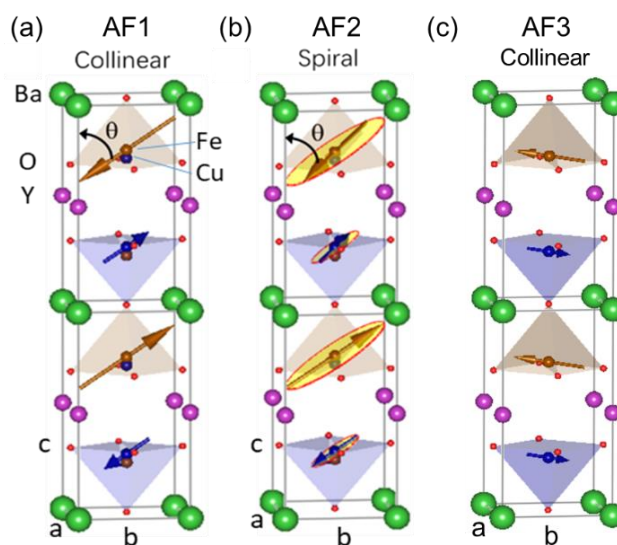


Figure 5.19. Schematic figure showing the inclination angle  $\theta$  in the (a) AF1 collinear  $\mathbf{k}_1$  and (b) AF2 spiral  $\mathbf{k}_2$  phases. (c) Projection of the refined AF3 collinear  $\mathbf{k}_3$  phase in Co-8% which shows a different magnetic coupling inside the bipyramid as compared with AF1 collinear phase.

### 5.5.3a DR1 samples: tilting of the magnetic plane by Co doping

Neutron powder diffraction data allowed us to refine the inclination angle  $\theta$  in both the collinear and spiral phases of DR1 samples as a function of temperature. As explained in Chapter 4, the inclination angle  $\theta$  indicates the angular distance between the direction of magnetic spins and the  $c$  axis, as shown in the Figure 5.19, namely (i) the collinear magnetic spin direction  $\mathbf{u}$  in the CM phases and (ii) the rotation plane of the helix in the spiral ICM magnetic phase ( $\mathbf{u}$ - $\mathbf{v}$  plane). We recall here that due to the tetragonal symmetry of the parent cell, it is not possible from NPD to distinguish the orientation of the easy axis component parallel to the  $ab$  plane. So, following the same procedure as for the  $\text{YBaCuFe}_{1-x}\text{Mn}_x\text{O}_5$  family, for simplicity, the director vector  $\mathbf{u}$  can be taken as within the  $ac$ -plane,  $\mathbf{v}$  being thus parallel to the  $b$  axis. A  $\theta$  value close to  $0^\circ$  means that the easy-axis is close to the  $c$  axis, whereas for  $\theta \approx 90^\circ$  the easy-axis would be within the  $ab$ -plane. In the  $P4mm$  structure when  $\theta$  adopts intermediate values (different to 0 or  $90^\circ$ ) the magnetic arrangement according to  $\mathbf{k}_1$  or  $\mathbf{k}_2$  translational symmetries requires the concurrent activation of magnetic modes belonging to distinct irreducible representations (magnetic *irreps*)[44]. The temperature evolution of the

inclination angle  $\theta$  was refined for all the compositions between 10 K and the onset of the paramagnetic phase using the constraint  $m(\text{Fe})=m(\text{Cu})$  (refining the average moment). Refinements of the spiral phase were done using the  $M_R \gg M_I$  limit that allows us to maximize the accuracy of the inclination angle of the spin rotation plane. Figure 5.20 plots the results obtained from sequential refinements (Fullprof), performed for the six DR1 samples. For the Co-6.5% sample, the weak intensities of the magnetic satellites from the spiral makes not possible to refine sequentially the evolution of the inclination angle  $\theta_s$  in this phase, so just the evolution of inclination angle  $\theta_c$  for the collinear phase is shown. In the case of the Co-7.5% sample, the spiral phase is completely gone, and only the inclination of the collinear phase could be refined.

The behavior of the easy-axes illustrated in Figure 5.20 brings us some captivating conclusions. Firstly, the inclination angle  $\theta_s$  of the spin rotation plane in the spiral phase preserves practically constant values as a function of temperature for each composition. Secondly, the inclination of the easy axis in the collinear phase remains also very stable as a function of temperature for the set of DR1 samples. Not only that but comparing samples with different Co doping samples (and similar Fe/Cu disorder) we have found that the orientation of the collinear easy axis remains invariant ( $\theta_c = 50^\circ \pm 3^\circ$ ), in all the DR1 compositions. Of importance is that we observed a sudden drop in the tilting of the magnetic axis across the collinear–spiral transition at  $T_S$ . Interestingly, we can observe that the nearly constant  $\theta_s$  (T) values in the spiral phase noticeably decrease while increasing the Co substitution level, from a value of  $\sim 45^\circ$  in the Co-0 sample to  $\sim 13^\circ$  in the Co-6% sample.

Furthermore, with the aim of thoroughly investigate the impact of Co doping on the features of the spiral order, we have carefully refined the quality neutron diffraction patterns collected at 10 K at D1B for the compositions with  $x=0, 0.01, 0.03, 0.04, 0.05, 0.06, 0.065$ . The best Rietveld refinements are shown in Figure 5.21. The refined magnetic moments [imposing  $m(\text{Fe})=m(\text{Cu})$ ] and the inclination angles obtained for the ICM non-collinear phase are given in Table 5.2. As in previous chapters, two models

were used to refine the magnetic moments: (i)  $M_r \gg M_i$  (*Model 1*) and (ii)  $M_r = M_i$  (*Model 2*). As expected, the refined moments using a sinusoidal modulated order (*Model 1*) are larger than those obtained for a circular spiral (*Model 2*). A projection of the refined ICM spiral magnetic order at 10 K using *Model 2* is shown in Figure 5.23 for all the compositions investigated.

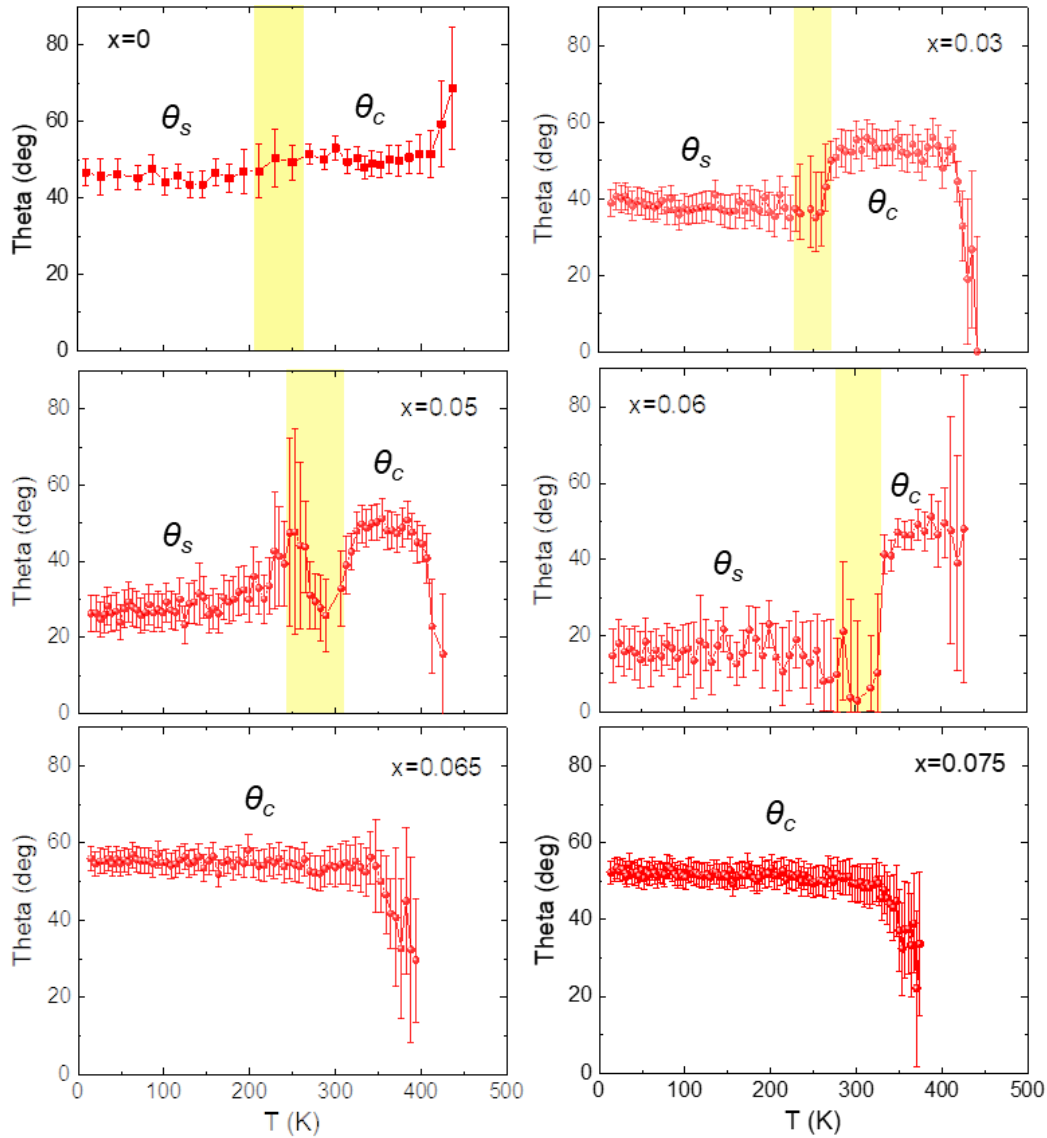


Figure 5.20. DR1 samples ( $\text{YBaCu}_{1-x}\text{Co}_x\text{FeO}_5$  ( $0 \leq x \leq 7.5\%$ )). T-evolution of the easy axes. Evolution of the inclination angles as a function of temperature for the collinear spin order ( $\theta_c$ ,  $T_S < T < T_{N1}$ ) and for the spiral rotation plane ( $\theta_s$ ,  $T < T_S$ ). The transition region has been marked in yellow.

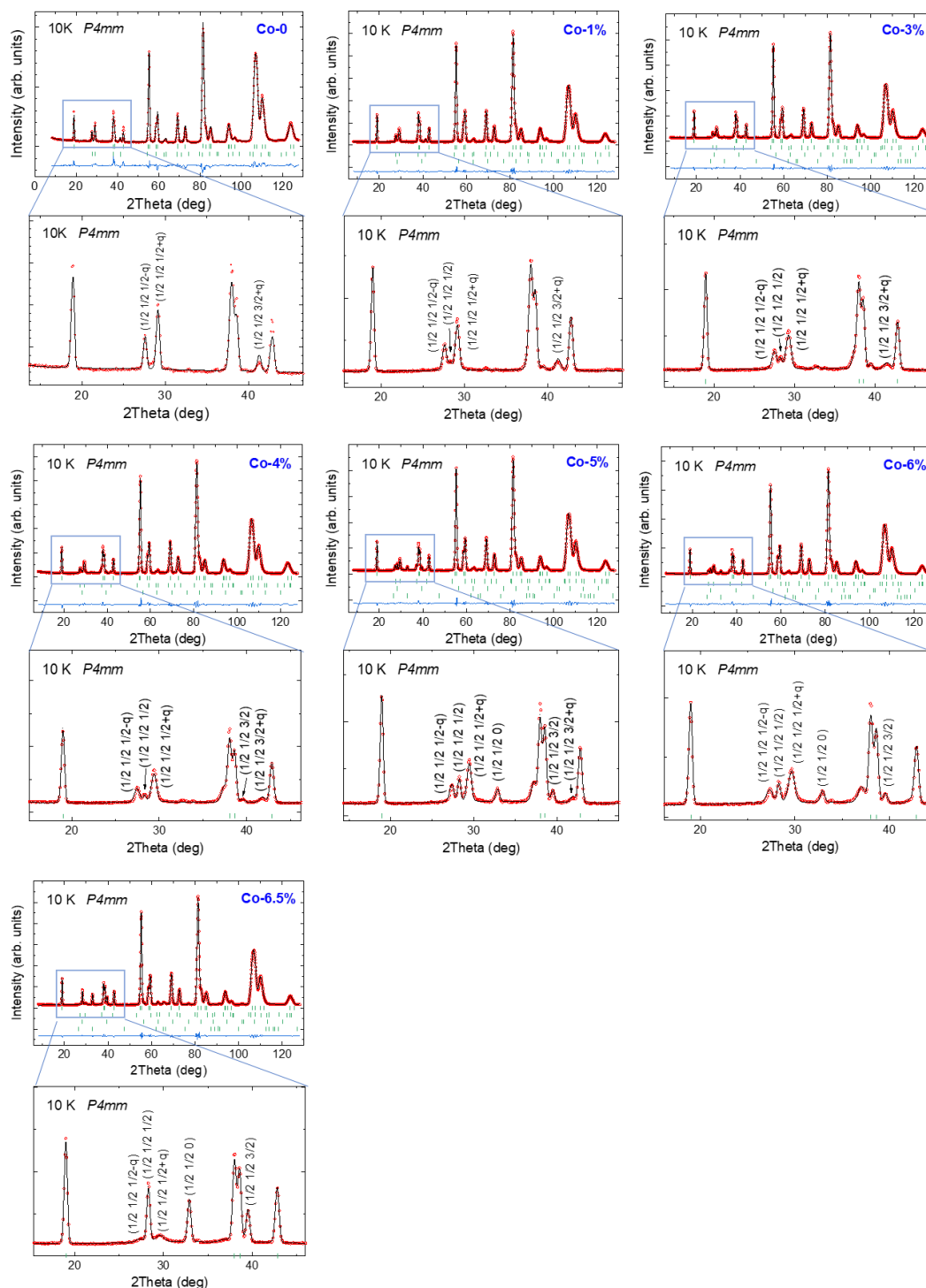


Figure 5.21. DR1 samples. Rietveld refinement of the neutron diffraction patterns collected at 10 K (d1b@ILL) for Co-0 ( $R_B$ : 3.45,  $R_f$ : 2.10,  $R_M$ : 13.6,  $\chi^2$ : 11.1); Co-1% ( $R_B$ : 1.16,  $R_f$ : 0.658,  $R_M$ : 9.44,  $\chi^2$ : 10.2); Co-3% ( $R_B$ : 0.923,  $R_f$ : 0.551,  $R_M$ : 8.71,  $\chi^2$ : 8.63); Co-4% ( $R_B$ : 1.82,  $R_f$ : 1.10,  $R_M$ : 11.7,  $\chi^2$ : 12.1); Co-5% ( $R_B$ : 0.918,  $R_f$ : 0.576,  $R_M$ : 9.83,  $\chi^2$ : 9.48); Co-6% ( $R_B$ : 1.35,  $R_f$ : 0.866,  $R_M$ : 9.84,  $\chi^2$ : 8.4); Co-6.5% ( $R_B$ : 0.720,  $R_f$ : 0.440,  $R_M$ : 11.3,  $\chi^2$ : 8.48). The three rows of green bars represent the allowed reflections for the structural, CM and ICM magnetic phases. The low-angle region has been zoomed-in below each sample's full pattern to show the agreement in the fit of the main magnetic peaks.

Table 5.4. Refined magnetic moments [imposing  $m(\text{Fe})=m(\text{Cu})$ ] and inclination angle  $\theta_s$  of the spin rotation plane in the spiral phase from NPD data at 10 K. Values correspond to models  $Mi\sim 0$  (*Model 1*) and  $Mi=Mr$  (*Model 2*). Theta (deg) in *Model 2* are fixed to its refined values in *Model 1*.

Sample 10 K	<i>Model 1</i> ( $Mi\sim 0$ )		<i>Model 2</i> ( $Mi=Mr$ )	
	$m$ ( $\mu_B$ )	$\theta_s$ (deg)	$m$ ( $\mu_B$ )	$\theta_s$ (deg)
Co-0	3.38 (7)	45 (5)	2.66 (5)	45
Co-1%	2.78 (7)	43 (3)	2.03 (2)	43
Co-3%	2.74 (6)	38 (3)	2.02 (2)	38
Co-4%	2.69 (7)	31 (5)	1.96 (2)	31
Co-5%	2.55 (5)	26 (3)	1.77 (2)	26
Co-6%	2.38 (5)	16 (5)	1.74 (2)	16
Co-6.5%	1.28 (5)	13 (6)	0.93 (2)	13

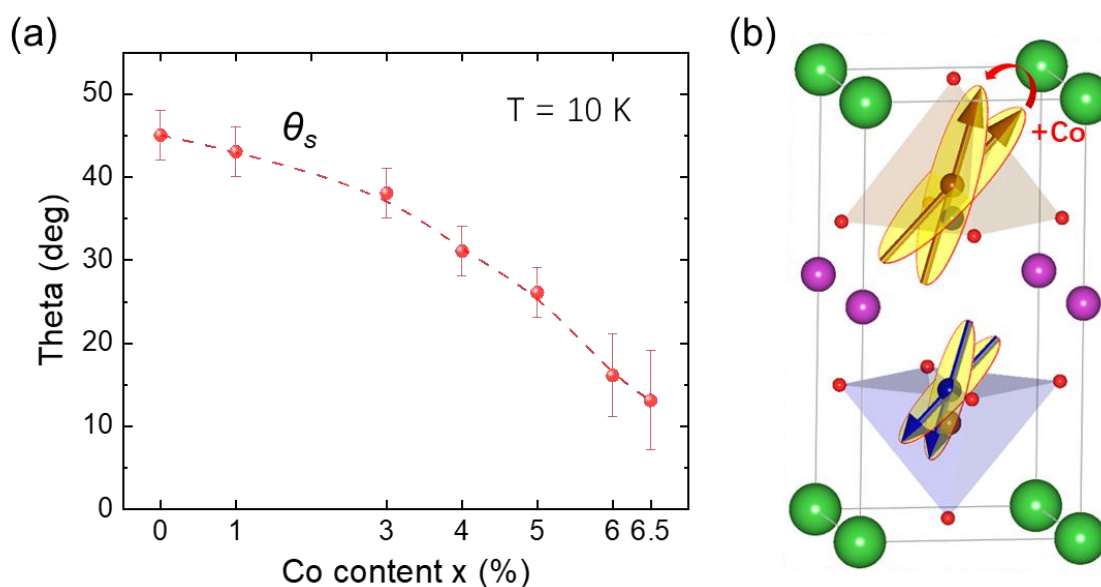


Figure 5.22. (a) Evolution of the inclination angle  $\theta_s$  of the ICM spiral phase as a function of Co content  $x$  obtained at 10 K. (b) A projection showing the evolution of the orientation of the spiral rotation plane by increasing the Co content. For clarity, the average magnetic moment is depicted in each pyramid (shared by three distinct metals) with the color of the majority metal.

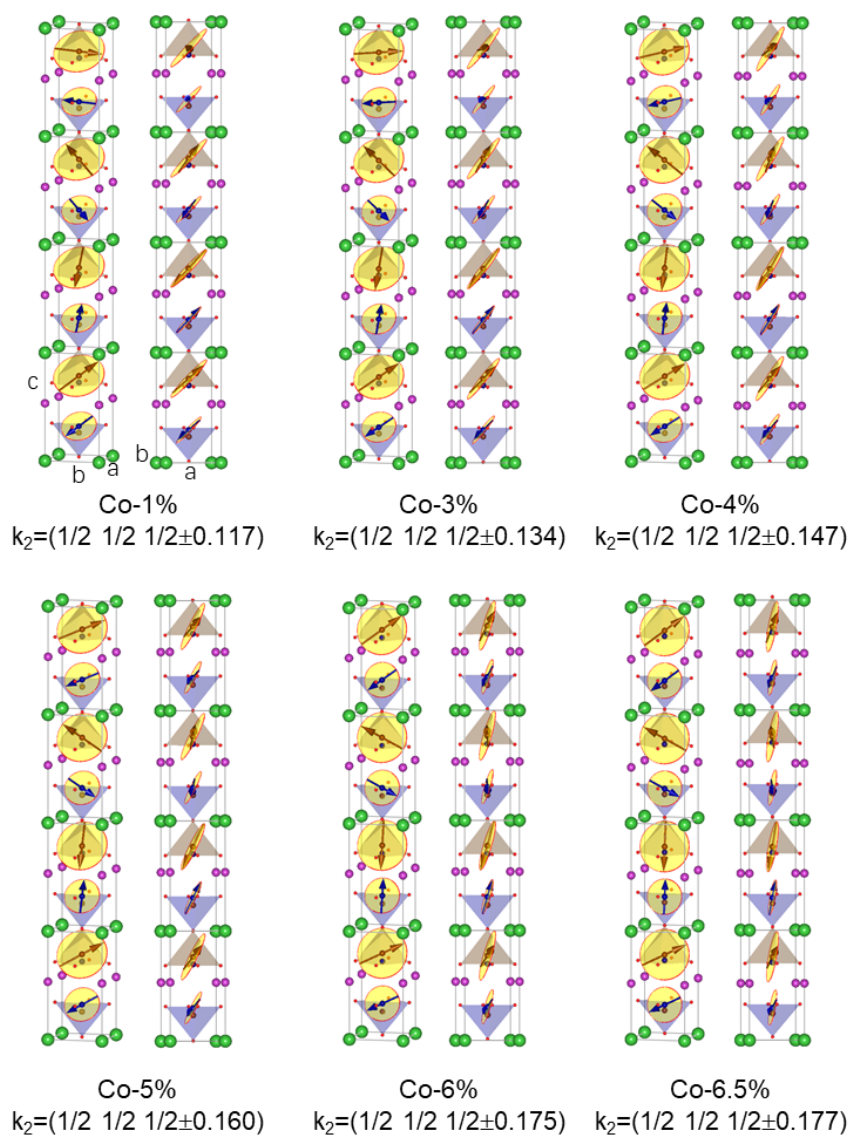


Figure 5.23. Two projections of the refined ICM magnetic spiral order at 10 K using  $M_r=M_i$  (*Model 2*) for YBaCu<sub>1-x</sub>Co<sub>x</sub>FeO<sub>5</sub> family (cooling rate 300K/h) with  $x = 1, 3, 4, 5, 6, 6.5\%$  of Co.

In Figure 5.20 we observed that the constant tilting angle in the spiral phase for each composition is remarkably decreasing by increasing the Co substitution level. Indeed, in Table 5.2, we list the refined tilting angles  $\theta_s$  of the spiral plane obtained at 10 K for the sample Co-0 to Co-6.5%. A decreasing tendency of  $\theta_s$  was observed for this series of samples. Figure 5.22(a) represents the evolution of the tilting angle  $\theta_s$  of the spiral order as a function of the Co content  $x$  as listed in Table 5.2, in samples where the Cu/Fe cation disorder keeps invariant. The tilting angle  $\theta_s$  defines the orientation of the easy-axis in each sample. Interestingly, the evolution in Figure 5.22(a) unveils that

the Cu/Co substitution leads to a systematic reorientation of the magnetic spiral plane, that is to say, the magnetic rotation plane is progressively shifted away from the tetragonal **ab** plane and it proceeds towards the *c* axis. Such evolution is also illustrated in Figure 5.22(b) which visually reproduces the reorientation process of the magnetic spiral plane triggered by increasing the presence of divalent Co. So, by increasing *x* between 0 and 6.5%, there is a reorientation of the magnetic spiral plane (easy-axis) of  $\Delta\theta \approx 32^\circ$ , from  $\sim 45^\circ$  to  $\sim 13^\circ$ .

As mentioned in preceding chapters, the orientation of the magnetic spiral plane respect to the *c* axis (the incommensurate direction) determines if the spiral order is of cycloid ( $\theta \rightarrow 0^\circ$ , nearly parallel to the *c* axis) or helix-type ( $\theta \rightarrow 90^\circ$ , nearly parallel to the **ab** plane). As a consequence, the reorientation of the magnetic spiral plane in this series would evolve from an inclined helix-type towards a more cycloid-type upon increasing the Co content. Let us bring to mind that chirality (**Q**) and polarization (**P**) both change their sign under space reversal but transform differently under time inversion. In terms of invariance “helical spins” and “cycloidal spins” behave similarly to chirality and polarization, respectively. In order to elucidate multiferroic behavior in non-collinear chiral magnets, it is very helpful to distinguish cycloidal from helical spin orders. Polarization **P** induced by the antisymmetric D-M interaction could be described by  $\mathbf{P} \propto \mathbf{r}_{12} \times (\mathbf{S}_1 \times \mathbf{S}_2)$ , being the  $\mathbf{r}_{12}$  the *c* vector and  $\mathbf{S}_1$  and  $\mathbf{S}_2$  the spins at Fe and Cu sites in the bipyramid [22][23]. In the spiral case the spin-chirality  $\mathbf{Q} = \mathbf{S}_1 \times \mathbf{S}_2 \neq 0$ , and  $\mathbf{P} \propto \mathbf{Q} \cdot \sin(90-\theta) = \mathbf{Q} \cdot \cos(\theta)$ , that is, proportional to  $\cos(\theta)$ .



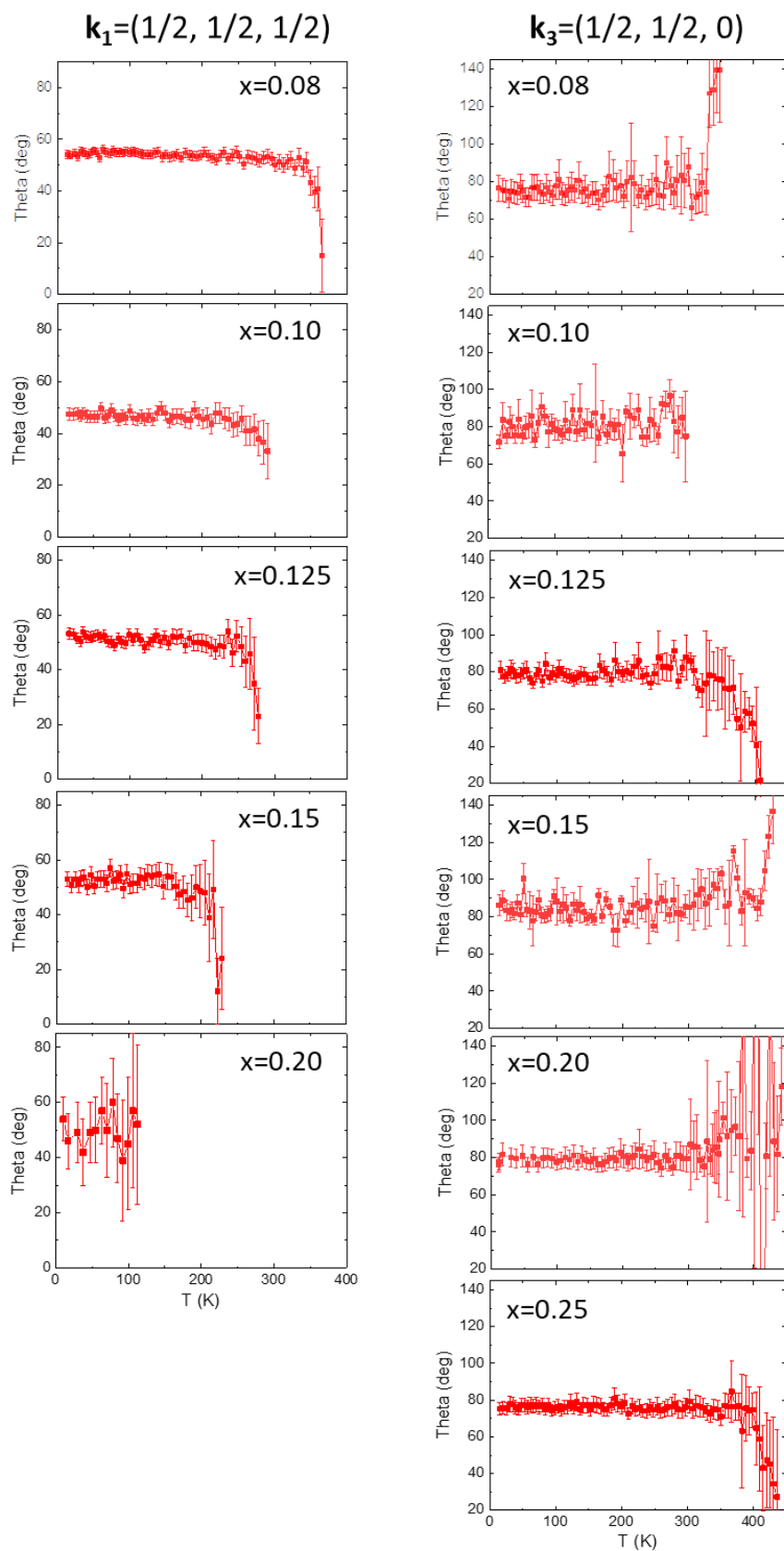


Figure 5.24. DR2 samples ( $\text{YBaCu}_{1-x}\text{Co}_x\text{FeO}_5$  ( $x > 7.5\%$  Co)). Evolution of the inclination angle  $\theta_c$  (magnetic easy-axis) as a function of temperature for the  $\mathbf{k}_1$  and  $\mathbf{k}_3$  collinear phases in  $\text{YBaCu}_{1-x}\text{Co}_x\text{FeO}_5$  (DR2 samples).

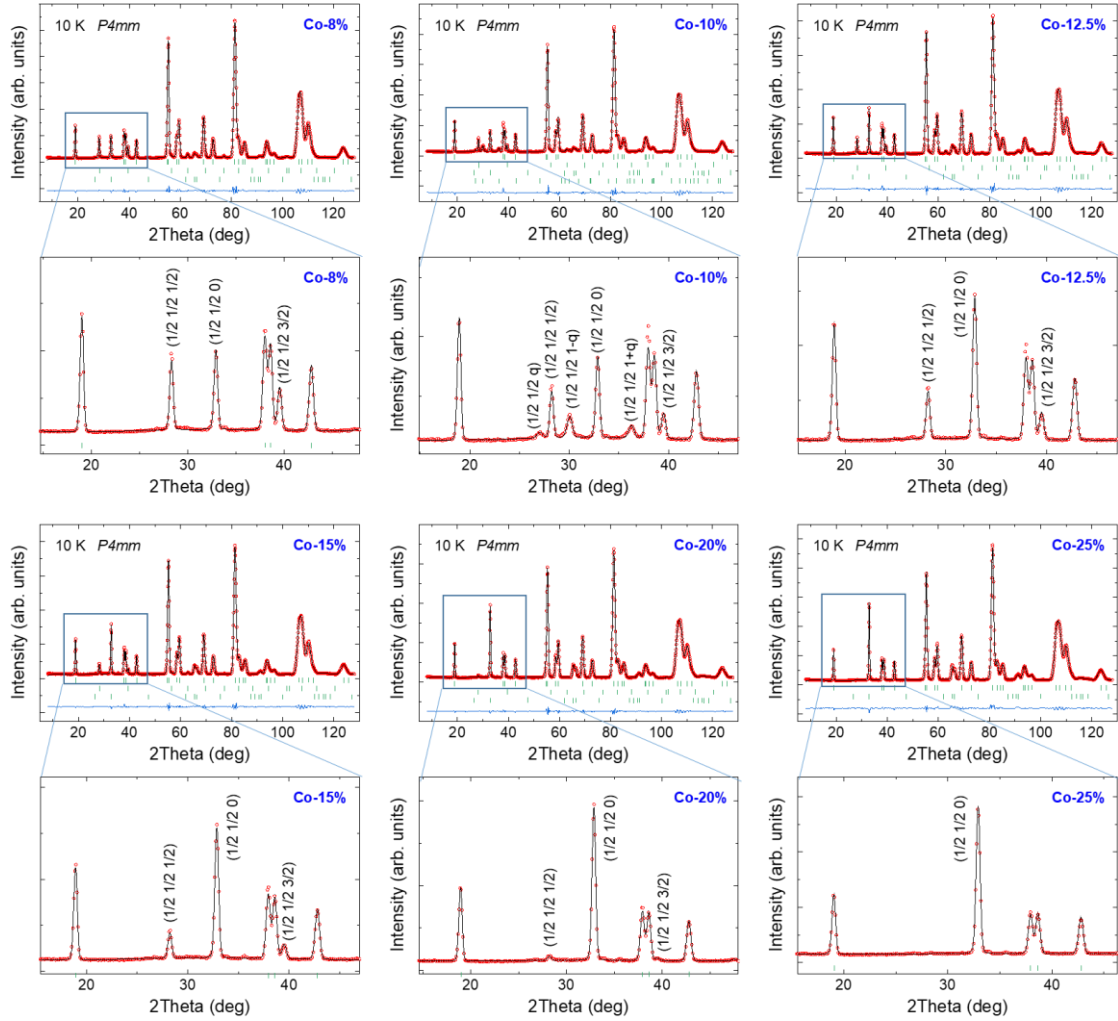


Figure 5.25. DR2 samples. Rietveld refinement of the neutron diffraction patterns collected at 10 K (d1b@ILL) for Co-8% ( $R_B$ : 0.962,  $R_f$ : 0.559,  $R_M$ : 8.72,  $\chi^2$ : 10.1); Co-10% ( $R_B$ : 1.67,  $R_f$ : 0.978,  $R_M$ : 6.75,  $\chi^2$ : 8.94); Co-12.5% ( $R_B$ : 0.887,  $R_f$ : 0.577,  $R_M$ : 4.87,  $\chi^2$ : 7.27); Co-15% ( $R_B$ : 0.784,  $R_f$ : 0.526,  $R_M$ : 4.63,  $\chi^2$ : 5.86); Co-20% ( $R_B$ : 0.889,  $R_f$ : 0.547,  $R_M$ : 3.37,  $\chi^2$ : 4.53); Co-25% ( $R_B$ : 1.05,  $R_f$ : 0.556,  $R_M$ : 7.64,  $\chi^2$ : 9.08). The three rows of green bars represent the allowed reflections for the structural and CM magnetic phases. A low-angle region has been zoomed-in below each sample's full pattern.

### 5.5.3b DR2 samples: easy-axis in the collinear orders of $\mathbf{k}_1$ and $\mathbf{k}_3$

For DR2 samples, our neutron diffraction data have allowed us to obtain information on the two types of competing collinear magnetic domains that concur at high cobalt doping. A proper fit of the magnetic reflections is shown in Figure 5.25. This analysis has enabled us to determine the evolution of the orientation of the AFM collinear spins (easy-axis) as a function of the Co content, for the two CM phases  $\mathbf{k}_1$  and  $\mathbf{k}_3$ . The evolution is plotted in Figure 5.26. The study proves a lack of impact of the

Co content on the collinear easy-axis.

Summarizing, through the study of the magnetic evolution for the two CM phases with propagation vectors  $\mathbf{k}_1$  and  $\mathbf{k}_3$ , we can conclude that: (i) on the one hand, there is an internal magnetic phase competition between the AF1 and AF3 spin arrangements, and the latter progressively replaces the former on increasing the Co substitution level. (ii) On the other hand, the magnetic easy-axis is found to be very different in these two competing collinear phases. We have determined that  $\theta_C \approx 50^\circ \pm 3^\circ$  in the AF1 ( $\mathbf{k}_1$ ) phase, in strong contrast with  $\theta_C \approx 80^\circ$  (3) in the AF3 ( $\mathbf{k}_3$ ) phase. A refined magnetic structure of the AF3 collinear  $\mathbf{k}_3$  phase for Co-8% sample is shown in Figure 5.19(c).

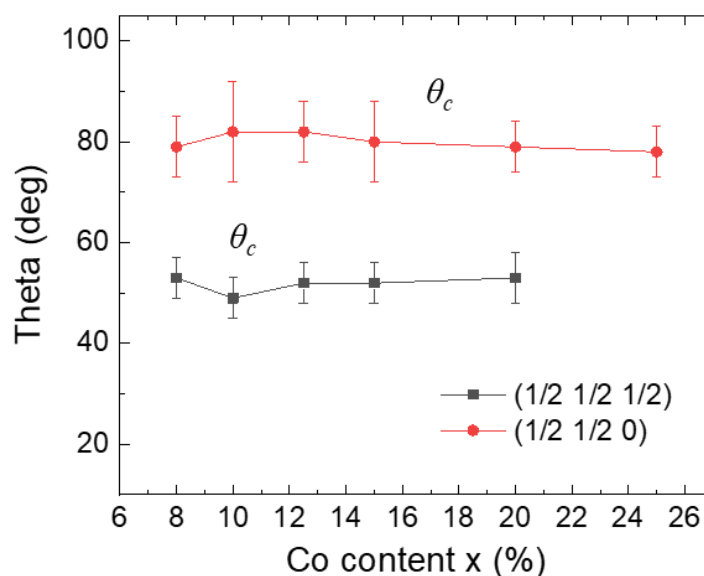


Figure 5.26. Evolution with Co content of the spin orientation (easy-axis) in the two competing collinear phases of YBaCu<sub>1-x</sub>Co<sub>x</sub>FeO<sub>5</sub> compounds with  $x \geq 8\%$  (DR2 samples), characterized by the wave vectors  $\mathbf{k}_1 = (1/2, 1/2, 1/2)$  and  $\mathbf{k}_3 = (1/2, 1/2, 0)$ , as obtained from NPD at 10 K.

## 5.6 Summary and conclusions

In this chapter we have assessed a new strategy addressed to enhance the performance of the high-T chiral magnetic order in the proposed multiferroic YBCFO system. Our new strategy to upgrade the properties of YBaCuFeO<sub>5</sub> has consisted on the generation of chemical pressure in the YBCFO structure by appropriate cationic substitution at the divalent B-site of this perovskite. Our choice was the partial

substitution of the J-T  $\text{Cu}^{2+}$  ions ( $t_{2g}^6 e_g^3$ ) by non-J-T  $\text{Co}^{2+}$  ( $t_{2g}^5 e_g^2$ ). Our aim was to explore the impact of such strategy of the thermal stability and the helicoidal *versus* cycloidal features of the exotic spiral magnetic order driven by disorder in these layered perovskites.

14 different  $\text{YBaCu}_{1-x}\text{Co}_x\text{FeO}_5$  compositions were prepared and investigated, from  $x=0$  up to  $x=0.25$  (25% of Co substituting Cu). Different techniques were applied to their structural, electronic and magnetic characterization, including XAS, SXRPD and NPD. Applying the same post-annealing procedure (300 K/h cooling down to RT) the distinct compositions were stoichiometric (same oxygen content) and presented (within error) the same level of B-site cationic disorder:  $n_d \sim 36(2) \%$ .

The insertion of HS  $\text{Co}^{2+}$  cations is very appealing for several reasons: (i) its valence and ionic size (comparable to  $\text{Cu}^{2+}$ ). (ii) The fact of being non-J-T active. (iii) Its expected highly non-spherical charge distribution and appreciable orbital component. (iv) High single-ion anisotropy. The synchrotron XAS study allowed us to prove that cobalt ions indeed adopted the divalent HS  $\text{Co}^{2+}$  electronic configuration ( $t_{2g}^5 e_g^2$ ), preserving the pristine oxidation states of Cu ( $3d^9:t_{2g}^6 e_g^3$ ) and Fe ( $3d^5:t_{2g}^3 e_g^2$ ) and the oxygen stoichiometry, without modifying the commensurable fraction of oxygen vacancies.

From a careful and thorough structural investigation we demonstrated several very relevant results. The most remarkable being: (i) first, the strong J-T splitting between basal and apical distances characteristic of the  $\text{Cu}^{2+}$  sites is (in average) severely reduced by increasing the Co doping level. (ii) Second, as a result, there is a pronounced atomic shift of the apical oxygen perpendicular to the layers that compresses the large, elongated Cu pyramids, the Cu/Fe bipyramids and hence the thickness of the bipyramid layer. Thus, the separation between successive bipyramid layers increases but the average thickness of these layers strongly decreases with Co. This phenomena produces an average shrinkage of the lattice along  $c$ , in spite of the ionic size of  $\text{Co}^{2+}$  is a bit larger than that of  $\text{Cu}^{2+}$  in pyramidal coordination.

The impact of Co on the magnetic phase diagram of YBCFO was extensively investigated by combining magnetometry and neutron techniques. The successive magnetic transitions were described in the range 10 K to 500 K for Co dopings  $0\% \leq x \leq 25\%$ . From the magnetic point of view, we showed the convenience of distinguishing two very different doping ranges (DR):  $0 \leq x \leq 7.5\%$  (DR1) and  $8\% \leq x \leq 25\%$  (DR2). For the DR1, a huge increase of the spiral transition temperature  $T_S$  was observed up to  $T_S=355(12)$  K for Co-6.5%. Along this doping range two linear relationships were established, between  $T_S$  and  $q_0$  and  $T_S$  and  $d_2$  respectively, which are consistent with the mathematical model developed by Scaramucci and coworkers. The most important effect is the contraction of the bipyramidal thickness  $d_2$ . When the bipyramids are occupied by two Fe atoms, the strong AFM Fe-O1-Fe exchange coupling is further strengthened due to the contraction of  $d_2$  which result in a reinforced frustration level in the system, thus increasing the spiral ordering temperature  $T_S$  (*chemical pressure effect*). So, in the DR1 the *chemical pressure effect* helps the material to reach the point where  $T_{N2}$  meets  $T_{N1}$ , keeping fix the Fe/Cu disorder. A certain magnetic phase separation was also detected in DR1 (mainly for  $x \geq 5\%$  Co) produced by the *Exchange sign change* induced by cobalt: magnetically the addition of Co to the solid solution favors the formation of the new commensurate  $\mathbf{k}_3$  phase due to the AFM  $\text{Co}^{2+}/\text{Fe}^{3+}$  and  $\text{Co}^{2+}/\text{Cu}^{2+}$  pairs in the bipyramids.

Increasing further the Co content, the strong AFM Fe-Fe bonds are reinforced by the decrease of the bipyramidal thickness  $d_2$ . When the FM coupling in the bipyramids occupied by Cu-Fe can no longer compete the magnetic frustration gets unbalanced and falls down. Concerning the DR2, the collapse of the spiral phase when  $T_{N2}$  reaches  $T_{N1}$  drives the material to a *multi-critical point*, and after this point, the material enters the “*Critical phase separation*” regime. The spiral phase has collapsed and it is no longer stable. In this region, AF3 and AF1 orders compete and the second progressively gives way to the first when increasing further the Co content. The FM coupling inside the bipyramids has been substituted by a magnetic structure where all NN couplings are

AFM, corresponding to the new CM  $\mathbf{k}_3$  phase.

Finally, the impact of the Co doping on the easy-axis and anisotropy for this set of samples has been investigated in detail. For DR1 samples, the T-dependence of the magnetic inclination angle (easy-axis) in both the CM and ICM phases remains practically constant for a given composition. We showed that the inclination of the magnetic easy-axis in the collinear AF1 phase shows no dependence on the Co substitution level; secondly, in contrast, the inclination angle of the spin rotation plane in the ICM spiral order shows a strong dependence on the Co content. The tilting of the magnetic spiral plane decreases from  $45^\circ$  in Co-0 down to  $13^\circ$  in Co-6.5%, corresponding to a systematic reorientation of the magnetic spiral plane, changing from a more helical spin order ( $\mathbf{k} // \mathbf{Q}$ ) into a more cycloidal spin order ( $\mathbf{k} \perp \mathbf{Q}$ ), respectively, producing a null or a finite electrical polarization in the improper mechanism for multiferroicity based on the DM interaction. *It should be underlined that the most cycloidal spiral found is as well the most thermally stable ( $T_S$  around 360 K).* For DR2 samples, the easy-axis for the two magnetic collinear phases (with  $\mathbf{k}_1$  and  $\mathbf{k}_3$ ) is stable against temperature. Moreover, the inclination of the magnetic easy-axis in each collinear phase shows no dependence on the Co content. Beyond the critical triple point increasing Co content the AF3 phase ( $\theta_c \sim 80^\circ$ ,  $\mathbf{k}_3$ ) progressively becomes dominant over the AF1 phase ( $\theta_c \sim 50^\circ$ ,  $\mathbf{k}_1$ ).



# Chapter 6

## Characteristics of the spiral magnetic phase in Mg-doped YBaCuFeO<sub>5</sub>

### 6.1 Introduction

In an effort to further increase the thermal stability of the spiral ferroelectric phase, we have initiated a different research line based on cation substitution at the B-site of the perovskite YBCFO. The strategy considers the steric (chemical internal pressure) effects induced from B-sites. In this regard, it is important to notice that the degree of magnetic frustration depends on two opposite nearest neighbors (NN) coupling interactions ( $J_{c1}$  and  $J_{c2}$ ) along the *c*-axis. Their sign and strength depend on the spatial distribution of Fe<sup>3+</sup> and Cu<sup>2+</sup> ions. The AFM  $J_{c1}$  direct exchange acts between successive bipyramids, which are separated by the characteristic distance  $d_1$  along the *c*-axis. This interaction competes with the  $J_{c2}$  exchange within the FeCuO<sub>9</sub> bipyramids (Fe-O1-Cu). But  $J_{c2}$  can be of different sign and magnitude depending on: firstly, the B-site cation disorder; and secondly, the thickness of the bipyramids,  $d_2$  (or, similarly, the M-O1-M' bondlength within the bipyramid). We call  $J_{c2}$  to the FM coupling for the Fe-O1-Cu “ordered” or “proper” configuration, the AFM coupling for the Fe-O1-Fe “disordered” or “improper” configuration. The AFM Cu-O1-Cu “disordered” energy term can be neglected in front of the strong  $J_{c2}$  term.



Furthermore, from the theoretical model developed by Scaramucci et al [84], we presume that a contraction in the height of the bipyramids ( $d_2$  distance) could increase magnetic frustration and should trigger the rise of the spiral stability. Thanks to increasing the  $3d-2p$  orbital overlap across the M-O1-M' superexchange path. So, in the previous chapter, we have thoroughly studied the divalent B-site chemical substitution of  $\text{Cu}^{2+}$  by  $\text{Co}^{2+}$ . A huge increase of the spiral ordering temperature  $T_S=T_{N2}$  was obtained for the DR-I samples doped with Co. Despite this encouraging finding for DR-I samples, the ICM spiral phase was found to coexist with a residue of the CM collinear phase below  $T_{N2}$ . So, apart from increasing the spiral ordering temperature, improving and upgrading the quality of the spiral phase is another essential purpose we need to consider. We also proved that, at variance with doping with Mn the Fe site, the chemical disorder did not vary with Co doping along the series.

Having in mind these previous findings, we decided to investigate YBCFO samples where  $\text{Cu}^{2+}$  is progressively substituted by non-magnetic  $\text{Mg}^{2+}$  ions. The effective ionic radii in V/VI coordination for  $\text{Cu}^{2+}$ ,  $\text{Co}^{2+}$  and  $\text{Mg}^{2+}$  are respectively 0.65/0.73 Å (for  $\text{Cu}^{2+}$ ), 0.67 Å/0.745 Å (for HS  $\text{Co}^{2+}$ ), and 0.66 Å/0.72 Å (for  $\text{Mg}^{2+}$ ) [48]. Even if  $\text{Co}^{2+}$  is slightly bigger than  $\text{Cu}^{2+}$ , it behaves as a smaller cation along the  $c$  axis due to the J-T elongated Cu-O1 bond in J-T distorted  $\text{CuO}_5$  pyramids. Divalent  $\text{Mg}^{2+}$  ions appear as an excellent candidate to substitute  $\text{Cu}^{2+}$  in this structure. The first main reason is that divalent  $\text{Mg}^{2+}$  is smaller than  $\text{Co}^{2+}$ , also non-J-T and practically identical in size to  $\text{Cu}^{2+}$  although in octahedral compounds its size is even smaller than  $\text{Cu}^{2+}$ . Furthermore, since  $\text{Mg}^{2+}$  is non-magnetic, the presence of complex magnetic interactions will be reduced which could favor the formation of a clearer spiral phase. In addition to these two reasons, we would also expect a progressive disruption of the cooperative J-T distortion in the divalent site by the incorporation of Mg. And finally, we aim also at investigating whether the introduction of  $\text{Mg}^{2+}$  favors the Fe/Cu chemical disorder, when compared to pure YBCFO samples prepared under similar final cooling rates. In this respect, in order to maximize the effect and promote chemical

disorder, the  $\text{YBaCu}_{1-x}\text{Mg}_x\text{FeO}_5$  family was prepared by two different cooling protocols after the last annealing: (i) cooling in furnace at a controlled cooling rate 300 K/h; (ii) cooling by immersion into the liquid nitrogen (LN).

## 6.2 Sample synthesis

Polycrystalline samples of composition  $\text{YBaCu}_{1-x}\text{Mg}_x\text{FeO}_5$  with  $x = 0, 0.02, 0.05, 0.075, 0.10, 0.125$  and  $0.15$  have been prepared by the conventional solid-state reaction method. The series of samples were prepared by two different cooling methods after the last annealing: (i) controlled cooling rate of 300 K/h in the furnace and (ii) immediate quenching by submersion into liquid nitrogen. Hereafter we denote samples by indicating their % of substituted Mg. Moreover, in the labelling of the samples prepared by the quenching method we have included the suffix “\_CN” (cooled in nitrogen). The detailed process of the sample preparation can be summarized as follows:

- (i) High purity oxides of  $\text{Y}_2\text{O}_3$ ,  $\text{BaCO}_3$ ,  $\text{CuO}$ ,  $\text{MgO}$ , and  $\text{Fe}_2\text{O}_3$  were employed as precursors to prepare polycrystalline samples. Evaporation of the moisture of the precursor oxides  $\text{BaCO}_3$ ,  $\text{CuO}$ ,  $\text{Fe}_2\text{O}_3$  and  $\text{MgO}$  in a stove at  $100\text{ }^\circ\text{C}$  for 10 hours to avoid weighing errors. In case of  $\text{Y}_2\text{O}_3$ , a pre-annealing process was carried out at  $900\text{ }^\circ\text{C}$  for 10 hours in a furnace to promote the evaporation of possible carbonates;
- (ii) Determination of the stoichiometric amounts of the precursor oxides required by the reaction;
- (iii) Weighing, mixing, and homogenization of above oxides, finally completely homogeneous fine powder was obtained;
- (iv) Pressing of the fine powder into pellets using a cylindrical mold under a pressure 12 tons and hold for 20min (pellets size after pressing: 20mm in diameter and 5mm in thickness);
- (v) Annealing process of the pellets using a tubular furnace at  $1100\text{ }^\circ\text{C}$  for 50 hours in air atmosphere, with an initial positive temperature ramp of 300 K/h. For the cooling process, the first set of samples were cooled down to RT at a controlled

cooling rate of 300 K/h in the furnace and the other set were cooled at a fast cooling rate by immersion into the liquid nitrogen.

## 6.2.1 Laboratory x-ray characterization

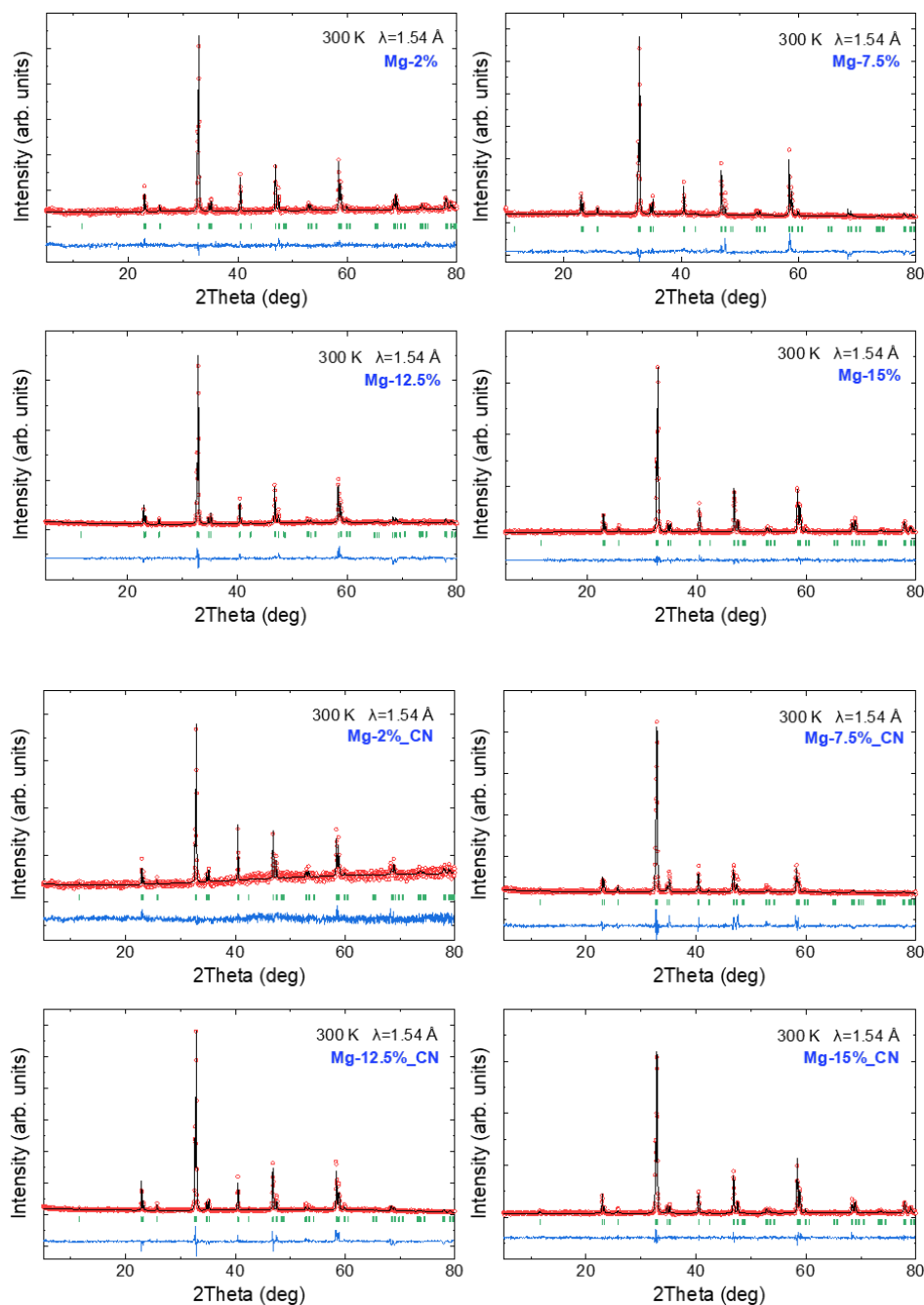


Figure 6.1. Rietveld refinements (black line) of the laboratory x-ray intensities (red circles) of the two sets of YBaCu<sub>1-x</sub>Mg<sub>x</sub>FeO<sub>5</sub> samples (controlled ramp and LN cooling) with  $x=0.02, 0.075, 0.125$  and  $0.15$ . The row of green bars is the Bragg positions and the bottom blue line is the difference between experimental and calculated profile intensities.

The x-ray diffraction patterns were collected using a Siemens D-5000 diffractometer and Cu  $K_{\alpha}$  radiation ( $\lambda=1.54 \text{ \AA}$ ). Figure 6.1 shows the Rietveld refinements of the laboratory x-ray diffraction patterns taken at 300 K on the two sets of samples synthesized by two different final cooling processes. From these refinements, the samples were observed to be single-phase and no impurity reflections were detected.

### 6.2.2 Magnetic characterization

The magnetization measurements were employed to characterize and determine the magnetic transition temperatures of these two sets of samples. The direct current (dc) magnetization was measured using SQUID for recording magnetic data below RT under 2 kOe after field cooling (FC). In addition, the temperature dependence of the magnetization was recorded in the 300-550K interval using VSM under the same magnetic field.

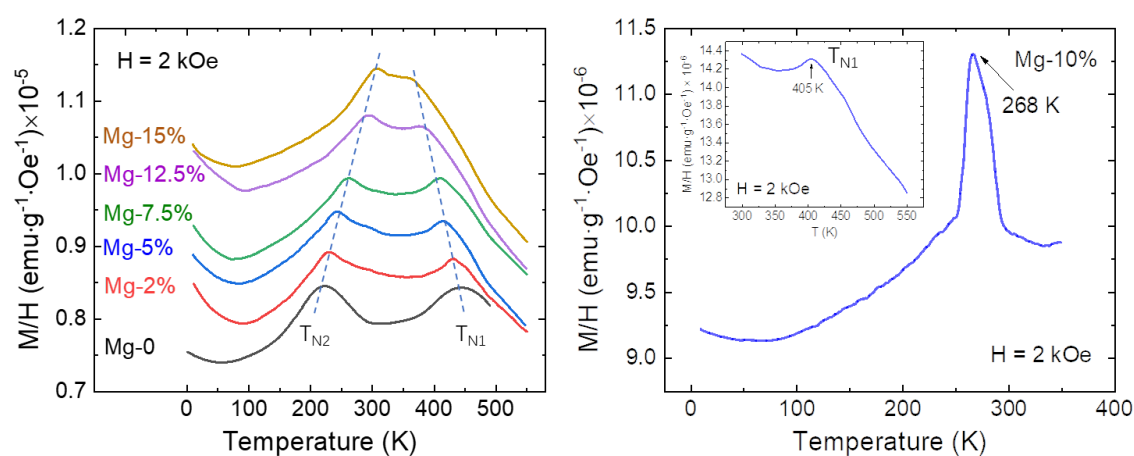


Figure 6.2. The measured magnetization curves for the  $\text{YBaCu}_{1-x}\text{Mg}_x\text{FeO}_5$  samples synthesized using a controlled 300 K/h cooling rate. The curves are vertically shifted by  $+10^{-6} \text{ emu} \cdot \text{g}^{-1} \cdot \text{Oe}^{-1}$  for clarity. The dashed lines in the left panel are eye-guidelines for  $T_{N1}$  and  $T_{N2}$ . The panel in the right shows the magnetization curve for the Mg-10% sample, and the inset displays the magnetization recorded above RT using the VSM.

Figure 6.2 plots the magnetic susceptibility curves for the  $\text{YBaCu}_{1-x}\text{Mg}_x\text{FeO}_5$  samples prepared under the controlled cooling rate 300 K/h. As expected, in the left panel, two Néel temperatures appeared for all the compositions, corresponding as we

will show later to the onset of the CM ( $T_{N1}$ ) and the ICM ( $T_{N2}$ ) magnetic orders. The  $T_{N2}$  underwent an increasing tendency from  $\sim 230$  K for the Mg-0 sample to  $\sim 310$  K for the Mg-15% one. Surprisingly, the Mg-10% sample demonstrated an unexpected magnetic behavior if compared with the rest of compositions. As shown in the right panel, below RT, the susceptibility curve reveals the appearance of what seems a FM-AFM like phase transitions at 268 K for this particular composition. We will come back later to this unexpected observation.

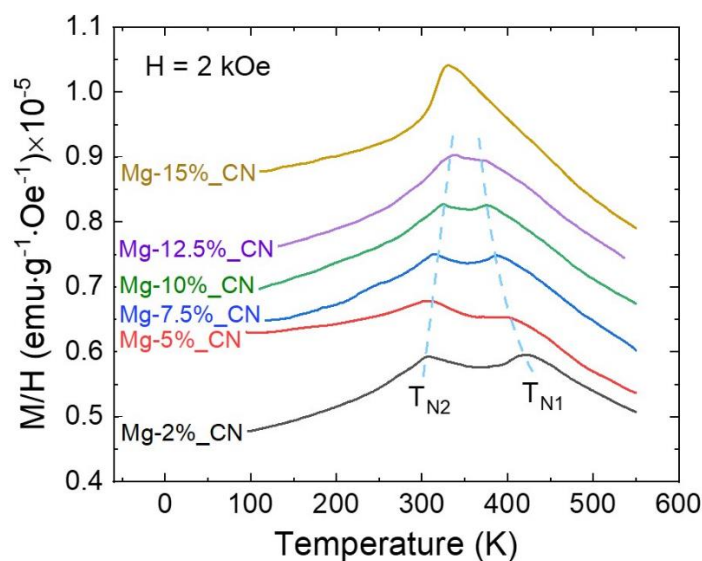


Figure 6.3. Magnetization curves for the YBaCu<sub>1-x</sub>Mg<sub>x</sub>FeO<sub>5</sub> samples synthesized by sudden immersion into liquid nitrogen. The curves are vertically shifted by  $+10^{-6}$  emu $\cdot$ g $^{-1}\cdot$ Oe $^{-1}$  for clarity. The blue dashed lines are eye-guides to ease following the evolution of  $T_{N1}$  and  $T_{N2}$ .

The magnetization measurements for the second set of YBaCu<sub>1-x</sub>Mg<sub>x</sub>FeO<sub>5</sub> samples, (quenched) are shown in Figure 6.3, where one can see that  $T_{N1}$  and  $T_{N2}$  undergo a modest decrease and increase, respectively. These two transition temperatures gradually approach to each other and finally converge for the Mg-15%<sub>CN</sub>. It is worth noting that the change in the cooling process for this set of samples imposed a positive effect to the spiral magnetic ordering temperature  $T_{N2}$  as compared with the first set, although the increase is modest. In addition, it seems from the macroscopic magnetization that only one AF phase transition survives in the Mg-15%<sub>CN</sub> sample. The detailed magnetic phase transitions and a deeper study of the magnetic properties for these sets

of samples will be further investigated by other complementary techniques in next sections. But first, it is convenient to summarize the systematic structural characterization of these layered perovskites where  $\text{Cu}^{2+}$  ions are partially substituted with  $\text{Mg}^{2+}$ .

### 6.3 Synchrotron x-ray powder diffraction

The SXRPD measurements for the two sets of samples were performed at 300 K at the BL04-MSPD beamline of the ALBA Synchrotron Light Facility (Barcelona, Spain) using the position sensitive detector MYTHEN. The wavelength,  $\lambda=0.41252$  (4) Å, was determined by measuring a NIST standard silicon. The powder samples were loaded in borosilicate glass capillaries (diameter in 0.7mm) and kept spinning during data acquisition. Each diffraction pattern used for the Rietveld refinement was averaged from 5 diffraction scans.

**Controlled cooling rate samples:** The Rietveld refinements of the SXRPD patterns for the first set of samples (cooling rate 300 K/h) are plotted in the Figure 6.4. All diffraction patterns can be well described by the  $P4mm$  symmetry. From these patterns, certain secondary phases such as  $\text{Y}_2\text{O}_3$  and  $\text{CuO}$  were detected in all the compositions only in the low angle region, but their amount was confirmed to be lower than ~1% wgt in the heaviest Mg doped sample.

The structural information including the lattice dimensions and coordinates for each atom in the crystal structure as obtained from the Rietveld refinements at 300 K for these samples are summarized in the Table 6.1 together with the best agreement factors. As done in previous chapters, we refined the two split positions and occupations for Fe and (Cu, Mg) respectively in each pyramid, and the z-coordinates of Fe and Cu in upper and lower pyramids were constrained by  $z(\text{M1})+z(\text{M2})=1$ , as shown in the Table 6.1 (the z-coordinates of Mg were constrained to be the same as Cu).

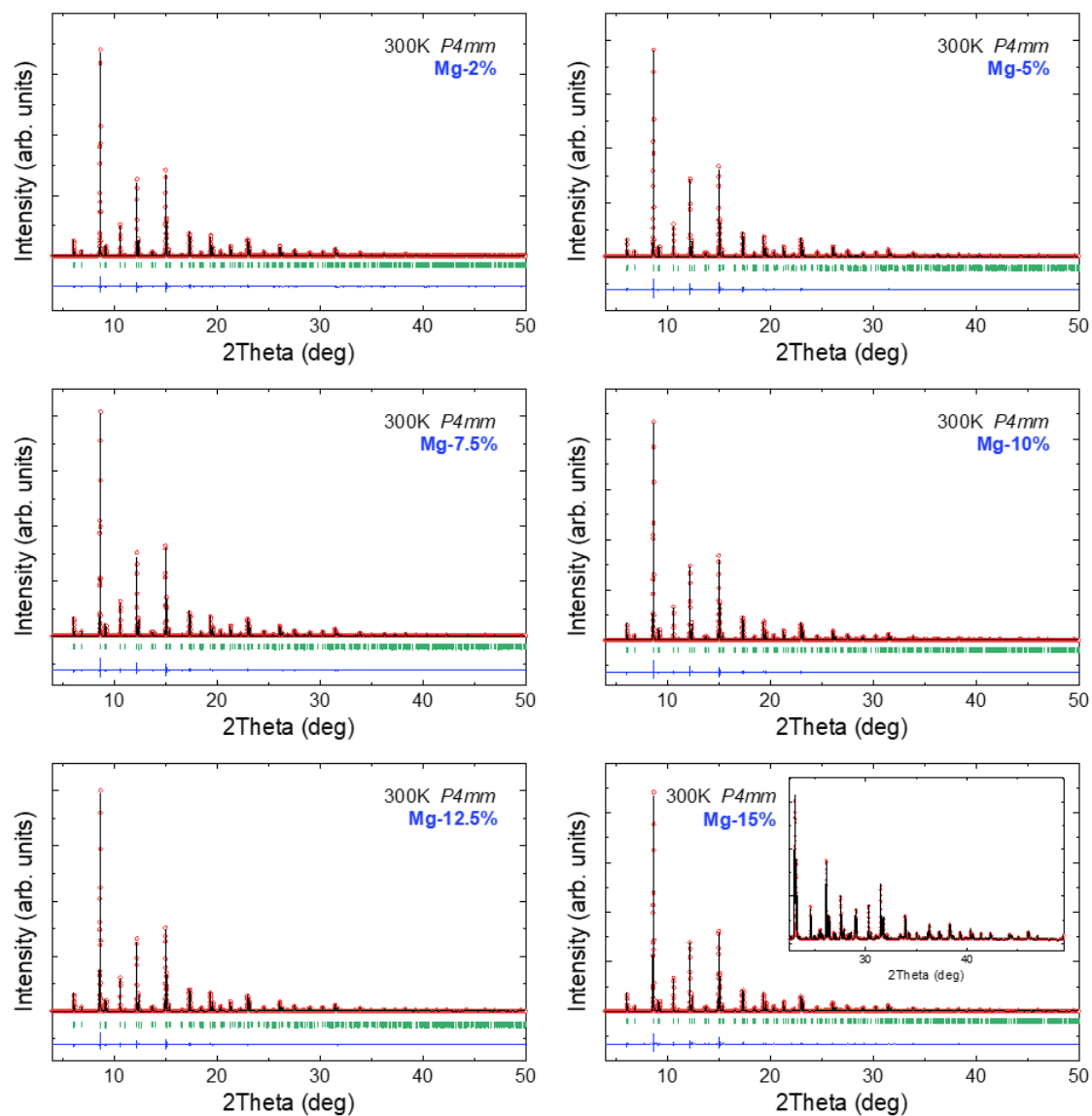


Figure 6.4. YBaCu<sub>1-x</sub>Mg<sub>x</sub>FeO<sub>5</sub> (cooled 300 K/h). Rietveld refinement (black curve) of the synchrotron x-ray diffraction intensities (red circles) performed at 300 K for the samples cooled at a controlled rate of 300 K/h. The row of green bars is the agreed Bragg reflections. Bottom blue line is the difference between the observed and calculated intensities. Inset in the Mg-15%: refinement details of the high-angle region.

**Table 6.1.** Structural parameters at T=300 K and agreement factors obtained from the Rietveld refinement of the mspd@Alba synchrotron diffraction data ( $\lambda = 0.41252$  (4) Å) for the first set of samples. The coordinates of the two positions for the two metals (M1 and M2) are related by  $z(M1)+z(M2)=1$ . (\*: minority fraction; +: occupation of the majority cation in each pyramid). “nd” stands for the chemical disorder ( $n_d = 1 - \text{Occ}(\text{Fe1})$ ).

YBaCu <sub>1-x</sub> Mg <sub>x</sub> FeO <sub>5</sub>	x=0_C300	x=0.02_C300	x=0.05_C300	x=0.075_C300	x=0.10_C300	x=0.125_C300	x=0.15_C300
a (Å)	3.87526 (3)	3.87486 (2)	3.87602 (3)	3.87676 (3)	3.87746 (3)	3.87823 (3)	3.87927 (3)
c (Å)	7.66278 (6)	7.66149 (5)	7.65829 (6)	7.65648 (6)	7.65547 (6)	7.65359 (6)	7.65114 (6)
V (Å <sup>3</sup> )	115.077 (2)	115.034 (2)	115.054 (2)	115.071 (2)	115.098 (2)	115.115 (2)	115.140 (2)
z (Y) (0 0 z)	0.4941 (5)	0.5109 (3)	0.5104 (3)	0.51000 (3)	0.5095 (2)	0.50911 (3)	0.5083 (3)
z (Fe1) (½ ½ z)	0.7446 (5)	0.7525 (5)	0.75214 (5)	0.7519 (5)	0.7519 (6)	0.7509 (6)	0.75100(6)
z (Cu1) (½ ½ z)*	0.7190 (2)	0.7155 (2)	0.7158 (2)	0.7159 (2)	0.7159 (2)	0.7162 (3)	0.7166 (3)
z (Cu2) (½ ½ z)	0.2811 (2)	0.2845 (2)	0.2842 (2)	0.2841 (2)	0.2840 (2)	0.2838 (3)	0.2834 (3)
z (Fe2) (½ ½ z)*	0.2555(5)	0.2475 (5)	0.2479 (5)	0.2481 (5)	0.2480 (6)	0.2491 (6)	0.2490 (6)
z (O <sub>1</sub> ) (½ ½ z)	0.009 (2)	0.012 (2)	0.013 (2)	0.014 (2)	0.015 (2)	0.015 (3)	0.016 (3)
z (O <sub>2</sub> ) (0 ½ z)	0.313 (1)	0.326 (1)	0.326 (1)	0.326 (1)	0.324 (1)	0.324 (1)	0.324 (1)
z (O <sub>3</sub> ) (0 ½ z)	0.681 (1)	0.694 (1)	0.694 (1)	0.694 (1)	0.693 (1)	0.693 (1)	0.693 (1)
Occ (Fe1) <sup>+</sup>	0.684 (22)	0.686 (20)	0.675 (20)	0.677 (20)	0.667 (20)	0.666 (20)	0.682 (20)
n <sub>d</sub>	0.316 (22)	0.314 (20)	0.325 (20)	0.323 (20)	0.333 (20)	0.334 (20)	0.318 (20)
$\chi^2$	97.8	232.0	252.0	249.0	242.0	194.0	203.0
R <sub>B</sub>	4.54	4.76	4.74	4.45	4.22	3.93	3.75
R <sub>f</sub>	2.57	5.61	5.57	5.35	4.91	4.66	4.58



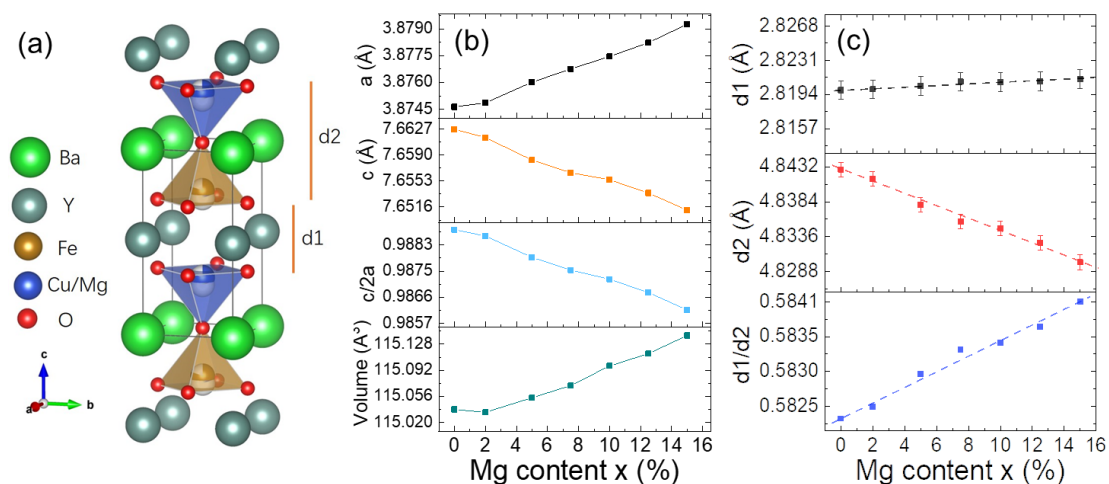


Figure 6.5. YBaCu<sub>1-x</sub>Mg<sub>x</sub>FeO<sub>5</sub> (cooled 300 K/h). (a) Projection of the three dimensional crystal structure ( $P4mm$  symmetry). (b) Evolution of the cell parameters and volume as a function of Mg content  $x$ . (c) Evolution with  $x$ [Mg] of the  $d1$  and  $d2$  distances, and  $d1/d2$  ratio, as shown in (a),  $d1$  refers to the separation between bipyramid layers and  $d2$  is the thickness of the bipyramids.

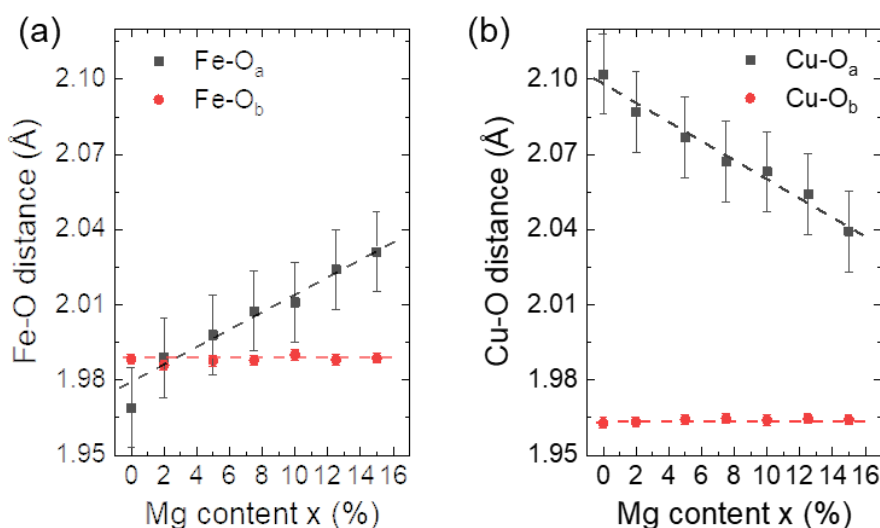


Figure 6.6. YBaCu<sub>1-x</sub>Mg<sub>x</sub>FeO<sub>5</sub> (cooled 300 K/h). Refined interatomic distances of metals to basal (O<sub>b</sub>) and apical (O<sub>a</sub>) oxygen atoms. (a): Fe-O and (b): Cu-O, respectively in upper pyramid (brown, Fe) and lower pyramid (blue, Cu/Mg) within the unit cell shown in Fig. 6.5(a).

The evolution of the cell parameters and volume data displayed in Table 6.1 has been plotted in Figure 6.5 (b). A monotonous increase of the cell parameter  $a$  was observed, in addition to a volume expansion as a function of the Mg content,  $x$ . This is probably due to the slightly larger atomic effective radius of Mg<sup>2+</sup> as compared to Cu<sup>2+</sup> (Mg<sup>2+</sup>: 0.66 Å/0.72 Å and Cu<sup>2+</sup> 0.65/0.73 Å in V/VI coordination [48]). At the same time, the lattice parameter  $c$  and the tetragonal distortion were observed to decrease.

The former should be associated to the variations seen in  $d_1$  and  $d_2$ , as already commented (see Figure. 6.5). Indeed, there is a negligible increase of the  $d_1$  distance ( $\Delta d_1 \approx +0.001 \text{ \AA}$ ), whereas  $d_2$  shrinks by  $\sim 0.012 \text{ \AA}$  upon Mg doping up to Mg-15%. This means a noticeable  $\Delta d_2/\Delta d_1 \approx -12$  from the pure YBCFO up to the Mg-15% sample. The evolution of the  $d_1/d_2$  ratio is also plotted in the same figure.

The evolution of the two metal-to-oxygen distances as a function of Mg content is illustrated in Figure 6.6. Firstly, we can see that the two basal distances Fe-O<sub>b</sub> and Cu-O<sub>b</sub> remain nearly unchanged upon Mg addition. But the two apical distances Fe-O<sub>a</sub> and Cu-O<sub>a</sub> demonstrate an increasing and decreasing tendency, respectively. The J-T splitting between the basal and apical distances around Cu<sup>2+</sup> ( $3d^9: t_{2g}^6 e_g^3$ ) is apparent in Figure. 6.6(b). Interestingly, the evolution of the Cu-O<sub>a</sub> bondlength indicates that in average the J-T effect gets progressively tamed when increasing the Mg content because Mg<sup>2+</sup> ions are not J-T active, contrarily to Cu<sup>2+</sup> ones. Thus, an average shrinkage of the height of the (Cu, Mg)O<sub>5</sub> pyramid along the *c* axis was anticipated and has been observed.

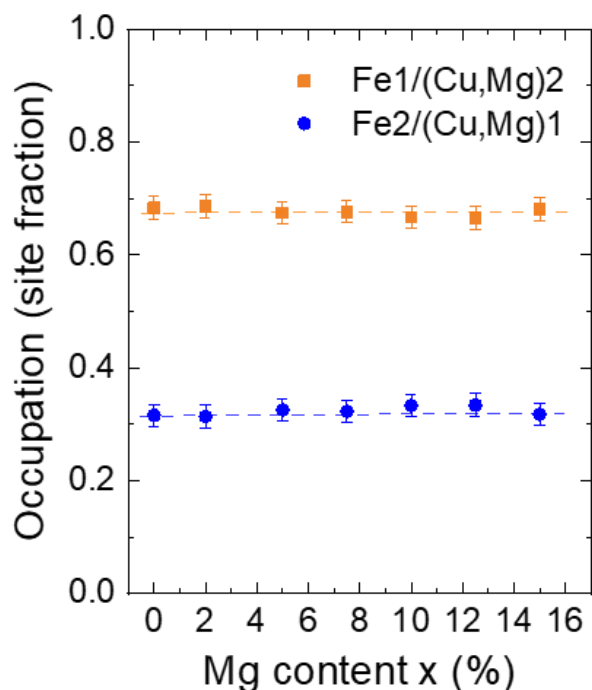


Figure 6.7. YBaCu<sub>1-x</sub>Mg<sub>x</sub>FeO<sub>5</sub> (cooled 300 K/h). The refined occupation of each metal in upper (Fe, brown) and lower (Cu/Mg, blue) pyramid within a unit cell as a function of Mg content *x*.

Figure 6.7 shows the evolution of the refined chemical disorder for the controlled cooling rate samples. From the figure, one can see that, firstly, the chemical disorder remains practically constant, i.e. the addition of the third metal, Mg, did not favor a higher chemical disorder along the series; and secondly, that there are ~32% of Cu/Mg atoms occupying the Fe sites. This sizeable chemical disorder provides a favorable condition for the magnetic order in this structure to evolve from the CM collinear to the ICM spiral magnetic phase. A more detailed description of the effect of chemical disorder on the magnetic properties will be discussed later in the neutron diffraction section. But first, in the following section we will summarize the structural characterization carried out on the Mg-doped series cooled in liquid nitrogen.

**Quenched samples:** The Rietveld refinements of the SXRPD patterns for the second set of samples (cooled by immersion into liquid nitrogen) are plotted in the Figure 6.8. The  $P4mm$  symmetry was used for all these samples. Secondary phase reflections were detected and also identified as Y<sub>2</sub>O<sub>3</sub> and CuO in all the compositions in the low angle region, their amount is confirmed to be lower than ~1% wgt in the most heavily doped sample.

The evolution of the lattice parameters for the quenched samples is plotted in Figure 6.9. On Mg doping,  $a$  and  $c$  are found to enlarge and decrease, respectively, accompanied by a reduction of the tetragonal distortion. The contraction of  $c$  along the  $z$  axis is also directly related to the variations taking place in  $d_1$  and  $d_2$  [Figure. 6.9 (b)]. Upon the addition of Mg,  $d_1$  evolves as  $\Delta d_1 \approx +0.008 \text{ \AA}$  up to the Mg-15%\_CN sample, whereas for  $d_2$  we find  $\Delta d_2 \approx -0.016 \text{ \AA}$ . The fact that the contraction of  $d_2$  is more pronounced than the expansion of  $d_1$  explains the decrease of  $c$ . The unit cell volume also grows with the Mg content  $x$ .

The evolution of the Cu-O and Fe-O bondlengths in the quenched samples as a function of Mg content are displayed in Figure. 6.9 (c) and (d). The two basal distances Cu-O<sub>b</sub> and Fe-O<sub>b</sub> are shown to be rather insensitive, but a remarkable variation takes place on the two apical distances Cu-O<sub>a</sub> and Fe-O<sub>a</sub>. As previously seen, the Cu-O<sub>a</sub>

bondlength reduction can be associated to the decrease in the average J-T splitting around  $\text{Cu}^{2+}$  ions when introducing  $\text{Mg}^{2+}$ . A comparison of the M-O<sub>a</sub> (M: metal) bondlengths between the quenched samples and the controlled cooling rate ones allows to see that the latter varies more notably than the former.

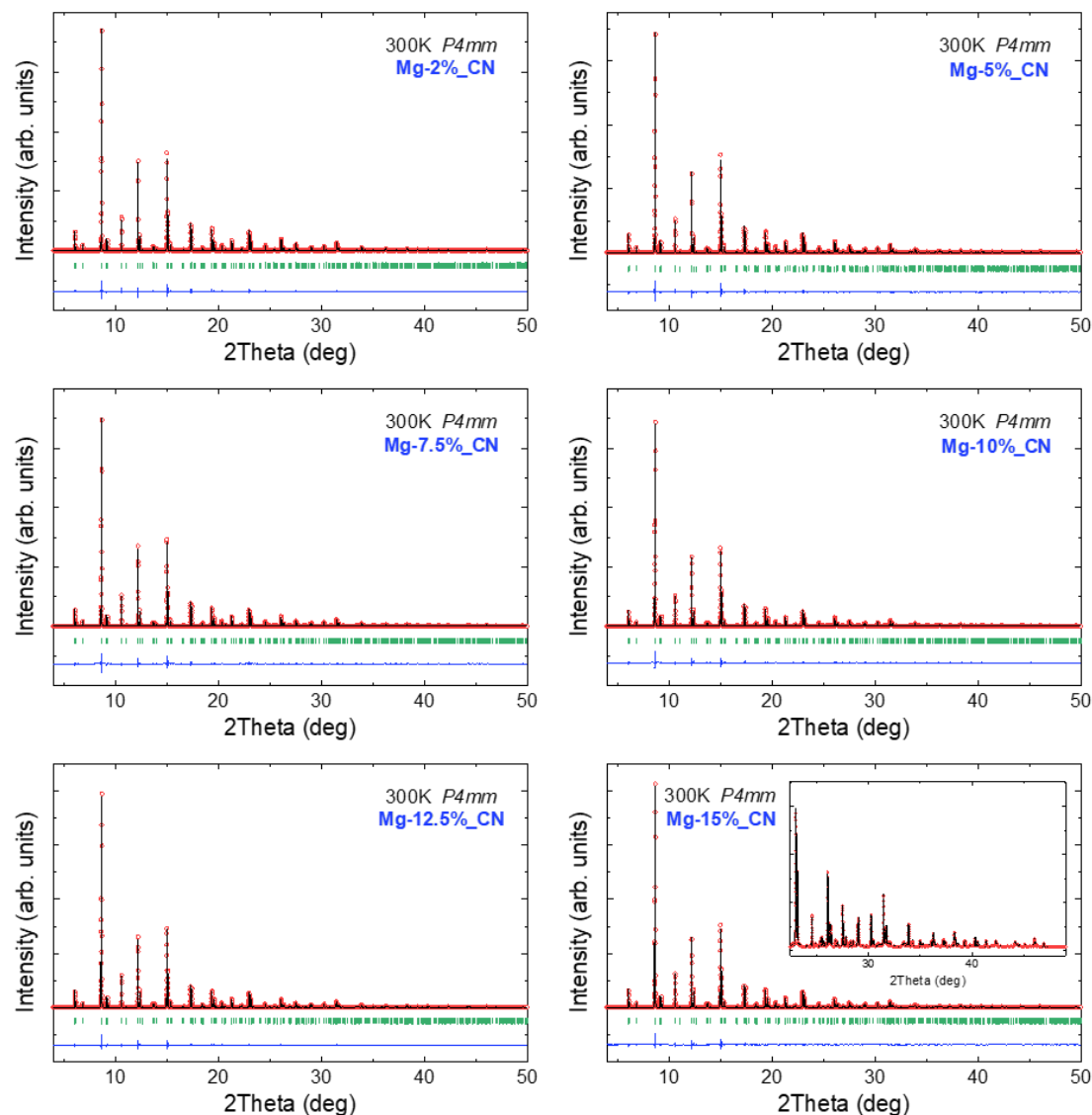


Figure 6.8.  $\text{YBaCu}_{1-x}\text{Mg}_x\text{FeO}_5$  (quenched). Rietveld refinement (black curve) of the synchrotron x-ray diffracted intensities (red circles) performed at 300 K. The row of green bars corresponds to the agreed Bragg reflections. The bottom blue line is the difference between the observed and calculated intensities. Inset in the Mg-15%\_CN: refinement of the high-angle region.

**Table 6.2.** YBaCu<sub>1-x</sub>Mg<sub>x</sub>FeO<sub>5</sub> (quenched). Structural parameters at T=300 K and agreement factors obtained from the Rietveld refinement of the msp@Alba synchrotron diffraction data ( $\lambda = 0.41252$  (4) Å). The coordinates of the two positions for the two metals (M1 and M2) are related by  $z(M1)+z(M2)=1$ . (\*: minority fraction; +: occupation of the majority cation in each pyramid). “n<sub>d</sub>” stands for the chemical disorder (n<sub>d</sub>= 1-Occ (Fe1)).

YBaCu <sub>1-x</sub> Mg <sub>x</sub> FeO <sub>5</sub>	x=0.02_CN	x=0.05_CN	x=0.075_CN	x=0.10_CN	x=0.125_CN	x=0.15_CN
a (Å)	3.87507 (2)	3.87609 (3)	3.87687 (3)	3.87748 (3)	3.87851 (3)	3.87940 (3)
c (Å)	7.65801 (5)	7.65559 (6)	7.65344 (6)	7.65319 (6)	7.65104 (6)	7.64983 (6)
V (Å <sup>3</sup> )	114.994 (2)	115.019 (2)	115.032 (2)	115.076 (2)	115.094 (2)	115.128 (2)
z (Y) (0 0 z)	0.51067 (3)	0.5112 (3)	0.5096 (3)	0.5096 (2)	0.5087 (3)	0.5082 (3)
z (Fe1) (½ ½ z)	0.7521 (5)	0.7539 (5)	0.7514 (5)	0.7517 (6)	0.7506 (6)	0.7499 (6)
z (Cu1) (½ ½ z)*	0.7159 (2)	0.7152 (2)	0.7161 (2)	0.7161 (3)	0.7164 (3)	0.7168 (3)
z (Cu2) (½ ½ z)	0.2842 (2)	0.2849 (2)	0.2839 (2)	0.2839 (3)	0.2836 (3)	0.2832 (3)
z (Fe2) (½ ½ z)*	0.2479 (5)	0.2461 (5)	0.2486 (5)	0.2483 (6)	0.2494 (6)	0.2501 (6)
z (O <sub>1</sub> ) (½ ½ z)	0.014 (2)	0.014 (2)	0.014 (2)	0.014 (2)	0.015 (3)	0.015 (3)
z (O <sub>2</sub> ) (0 ½ z)	0.327 (1)	0.326 (1)	0.326 (1)	0.325 (1)	0.324 (1)	0.324 (1)
z (O <sub>3</sub> ) (0 ½ z)	0.694 (1)	0.695 (1)	0.694 (1)	0.693 (1)	0.693 (1)	0.693 (1)
Occ (Fe1) <sup>+</sup>	0.638 (20)	0.641 (20)	0.638 (20)	0.632 (20)	0.633(20)	0.637 (20)
n <sub>d</sub>	0.362 (20)	0.359 (20)	0.362 (20)	0.368 (20)	0.367 (20)	0.363 (20)
$\chi^2$	285.0	243.0	226.0	181.0	185.0	185.0
R <sub>B</sub>	5.34	5.29	4.81	3.97	3.76	3.63
R <sub>f</sub>	5.93	6.15	5.86	4.75	4.63	4.41

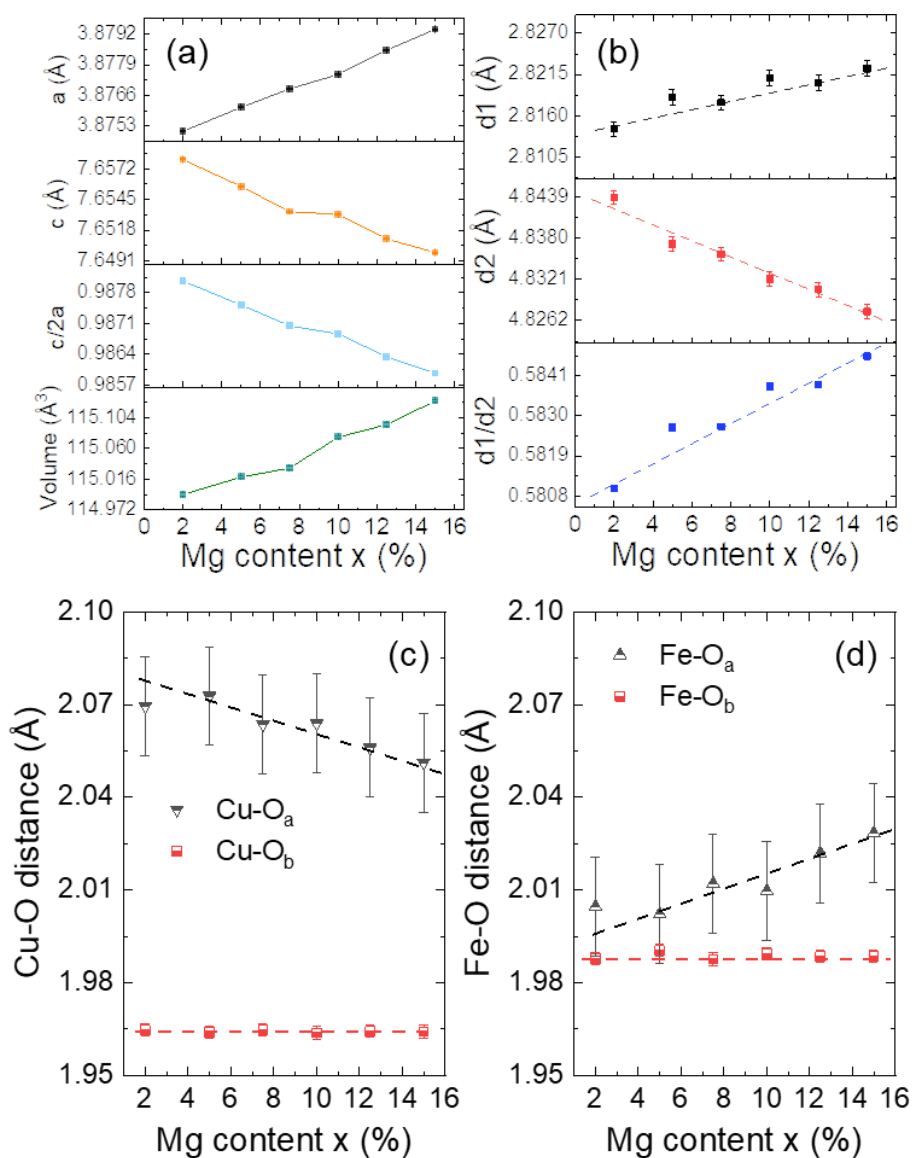


Figure 6.9.  $\text{YBaCu}_{1-x}\text{Mg}_x\text{FeO}_5$  (quenched). (a) Cell parameters and volume; (b)  $d_1$  and  $d_2$  characteristic distances and  $d_1/d_2$  ratio; (c) Cu to apical ( $\text{Cu-O}_a$ ) and Cu to basal ( $\text{Cu-O}_b$ ) oxygen interatomic distances; (d) Fe to apical ( $\text{Fe-O}_a$ ) and Fe to basal ( $\text{Fe-O}_b$ ) oxygen interatomic distances. Evolution with increasing Mg substitution level.

The refined chemical disorder for the quenched samples is plotted in the Figure 6.10. A flat evolution of the chemical disorder was got the same with the normal cooling samples upon increasing Mg content. The difference is this series of samples present a higher chemical disorder ( $n_d \sim 36\%$ ) in contrast with the first set of samples ( $n_d \sim 32\%$ , see Figure. 6.7).

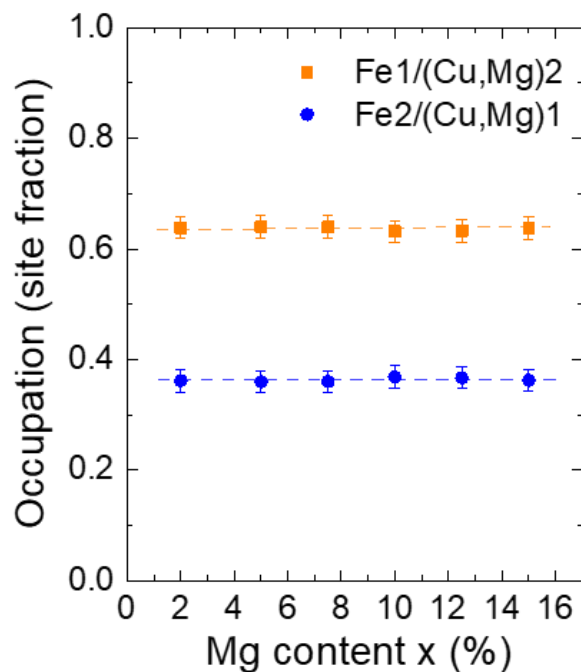


Figure 6.10. Refined values for the Fe and Cu occupation in upper (brown) and lower (blue) pyramids as a function of Mg content  $x$  for the quenched samples.

## 6.4 Neutron powder diffraction

NPD experiments were performed at the high-flux reactor of the Institut Laue Langevin (Grenoble, France) using the high intensity diffractometer D1B ( $\lambda=2.52$  Å). The polycrystalline samples were loaded inside the cylindrical vanadium sample holder. Using cryofurnace, NPD patterns for the quenched samples were collected at fixed selected temperatures at 50 K for 10 min to acquire good statistics. In addition, neutron diffraction patterns were also recorded using the continuous mode following temperature ramps with a heating rate of 3 K/min. Due to the limited time available, for the first set of samples (controlled 300 K/h cooling rate), we measured three compositions:  $x=0.05$ , 0.10 and 0.15 in the 200-440 K range; meanwhile for the second set of samples (quenched), we measured just the two compositions  $x=0.10$  and 0.15 in the slightly more reduced 250-440 K range.

### 6.4.1 Temperature dependence: largest $q_0$ and quality spiral phase observed for a quenched sample

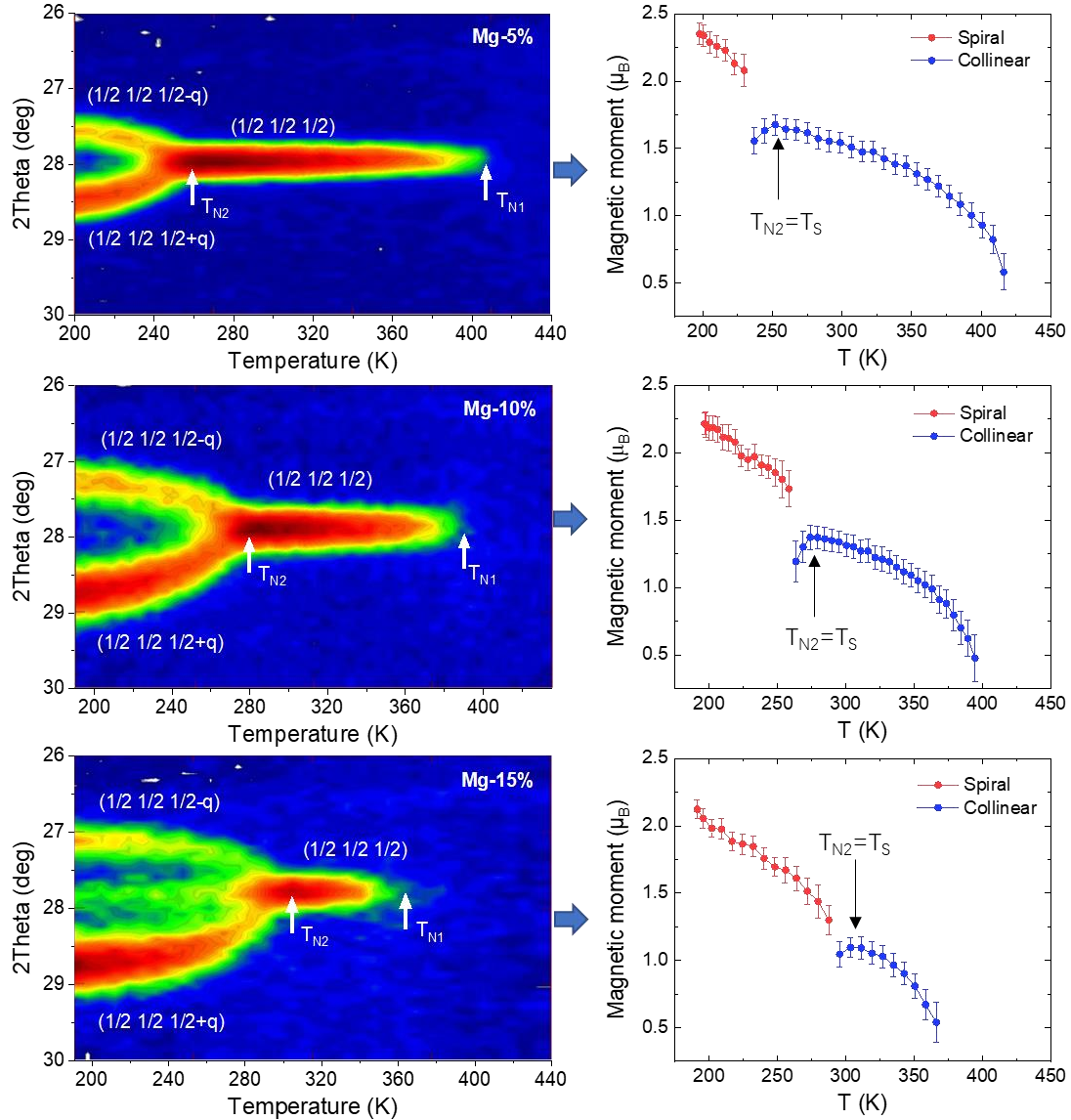


Figure 6.11.  $\text{YBaCu}_{1-x}\text{Mg}_x\text{FeO}_5$  (cooled 300 K/h). T-2Theta contour plots of the temperature dependence for the neutron-diffracted intensities around the  $(1/2 \ 1/2 \ 1/2)$  reflection for the three measured compositions prepared by cooling at 300 K/h and the corresponding average ordered magnetic moment associated to the CM and ICM magnetic phases as a function of temperature. The red and blue symbols correspond to the  $(1/2 \ 1/2 \ 1/2 \pm q)$  and  $(1/2 \ 1/2 \ 1/2)$  magnetic orders, respectively.

**Controlled cooling rate samples:** For the  $x=0.05$ , 0.10 and 0.15 samples in the series, the T-2Theta contour plots of the temperature dependence for the neutron-



diffracted intensities around the  $(1/2, 1/2, 1/2)$  reflection is plotted in the left panel of Figure 6.11. Similarly, as observed for the Mn-doped and Co-doped YBCFO families, two sets of new magnetic Bragg reflections appear at  $T_{N1}$  and  $T_{N2}$  upon cooling. Below  $T_{N1}$ , the magnetic reflection can be indexed as  $(h/2, k/2, l/2)$ , as associated to the propagation vector  $\mathbf{k}_1 = (1/2, 1/2, 1/2)$ . Upon further cooling, two new split satellite magnetic peaks emerge at  $T_{N2}$  which can be characterized by the ICM propagation vector  $\mathbf{k}_2 = (1/2, 1/2, 1/2 \pm q)$  and survive down to the base temperature. We here recall the magnetization measurement that we carried out for the Mg-10% sample, where a singular FM feature was observed to develop around 270 K (Figure. 6.2) under an applied field of 2 kOe. We have explored a possible transient long-range ferromagnetic order in this composition using neutrons (zero field). Actually, we did not detect a spontaneous long-range FM phase in the temperature dependence neutron diffraction data. Since the magnetic reflections for a FM phase get incorporated into the structural reflections, they just produce an increase in the intensity of some structural peaks. Hence, we integrated all the main structural reflections along the whole  $2\theta$  diffraction range, but no abrupt increase of the integrated intensities was observed around 270 K. In order to illustrate this, some selected Bragg reflections and their integrated intensities as a function of temperature are shown in Figure 6.12.

Furthermore, with respect to the observed FM signal in Mg-10% sample under 2 kOe applied field, we also carried out extra magnetization measurements under lower applied magnetic fields (1 kOe and 10 Oe) and a hysteresis loop at 270 K, as shown in Figure 6.13. Both magnetization measurements performed in FC and ZFC conditions clearly display an antiferromagnetic peak at the spiral ordering temperature  $T_{N2} \sim 270$  K, consistent with the NPD measurement. Meanwhile, the hysteresis loop measured at 270 K confirmed that the material is not ferromagnetic. Moreover, we cannot ascribe the observed transient FM signal to a field-induced mechanism. Investigating whether the presence of non-magnetic Mg ions could favor (under particular conditions and very near the emergence of the incommensurate spiral) a fraction of decoupled spins

susceptible to be polarized under field would require more detailed magnetic-history-dependent measurements. From our current data we discard a reproducible transient long-range ferromagnetic component.

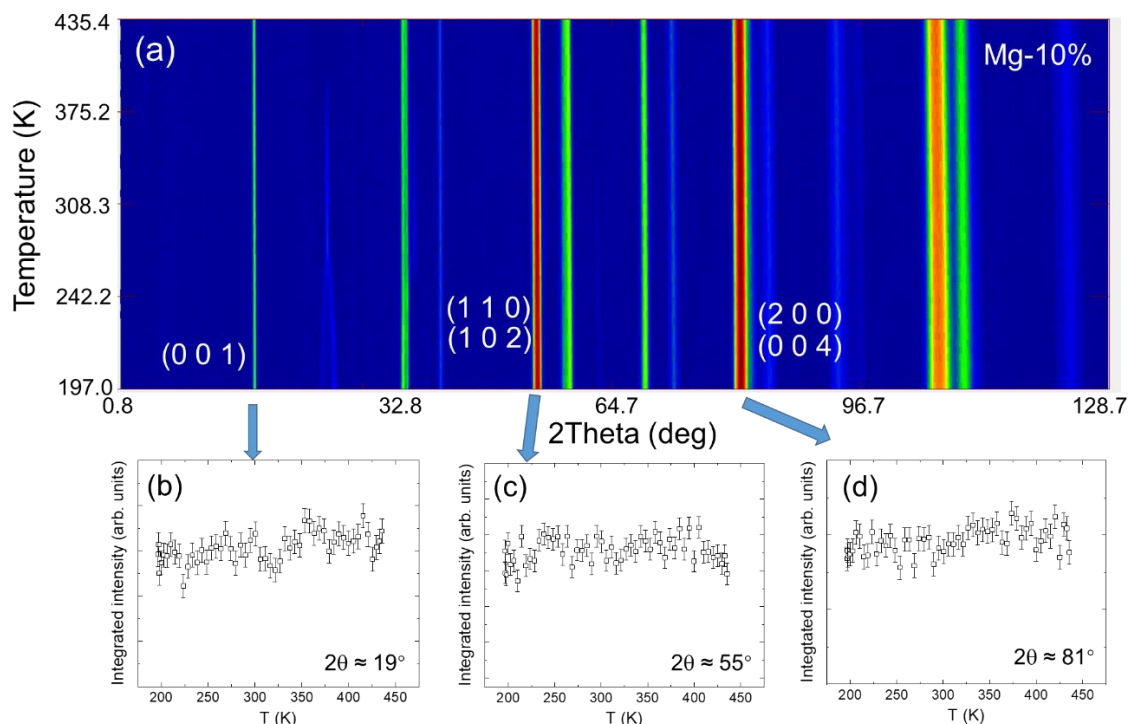


Figure 6.12.  $\text{YBaCu}_{0.90}\text{Mg}_{0.10}\text{FeO}_5$  (cooled 300 K/h). (a) Contour map showing the T-dependence of neutron-diffracted intensities from the Mg-10% sample. Selected integrated structural Bragg reflections are labeled in white; (b), (c) and (d) display the thermal evolution of the integrated intensities from these selected structural Bragg reflections.

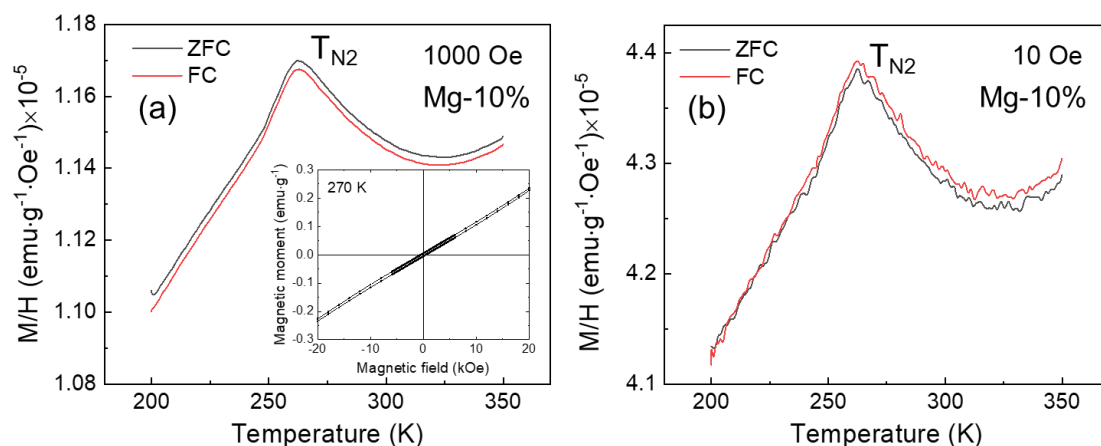


Figure 6.13.  $\text{YBaCu}_{0.90}\text{Mg}_{0.10}\text{FeO}_5$  (cooled 300 K/h). Magnetization measurements performed for the Mg-10% sample in ZFC and FC conditions under (a) 1000 Oe and (b) 10 Oe. Inset in (a): Hysteresis loop measured up to 20 kOe at  $T=270$  K.

For the Mg-15% sample, we observe a residual contribution of the CM phase below  $T_{N2}$ , which keeps present down to the lowest studied temperature. Likewise, the magnetic spiral with incommensurability  $q$  ( $T$ ) appears at  $T_{N2}$  and progressively evolves to its maximum amplitude at base temperature. In the right panel of Figure. 6.11 we have plotted the evolution of the refined average magnetic moments for each of these magnetic phases, as referred to the full amounts of sample, their values being averaged over the Fe and Cu sites, imposing  $M_R \gg M_I$  for the ICM phase.

**Quenched samples:** The low-angle region of the neutron diffraction patterns collected at 50 K for the quenched samples are displayed in Figure 6.14. A systematic evolution is observed in the profile of the main magnetic reflections while increasing the amount of Mg substitution. We can see that the ICM spiral phase dominates below  $T_{N2}$ , the CM collinear phase being completely absent in this thermal region, except for the Mg-15%\_CN sample, where a certain but negligible residue persists. On the other hand, one can also see that the ICM magnetic reflections get better resolved from the structural ones with increasing Mg content, which means that the incommensurability  $q_0$  is gradually growing.

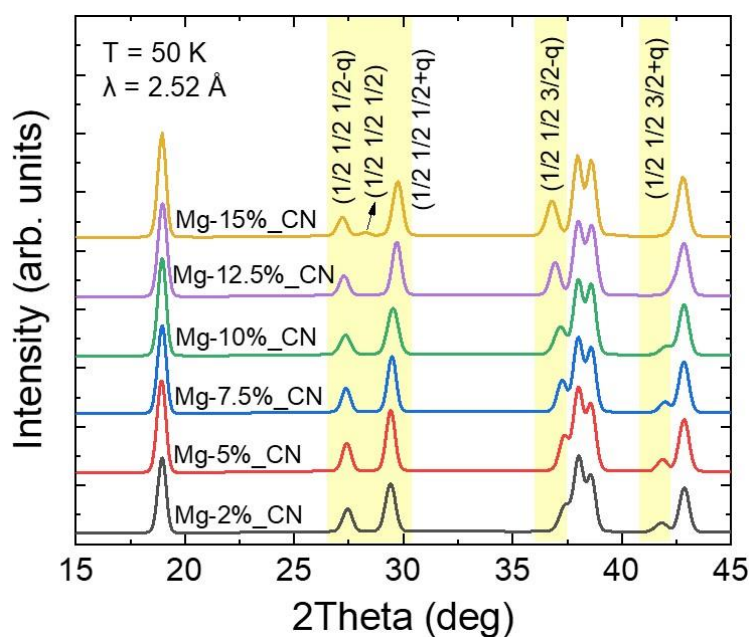


Figure 6.14. YBaCu<sub>1-x</sub>Mg<sub>x</sub>FeO<sub>5</sub> (quenched). Low-angle region of the neutron diffraction patterns collected at 50 K (d1b@ILL) for the quenched sample series.

This is clearly visible in Figure 6.15, which plots the refined ICM modulation incommensurability  $q_0$  at 50 K for the different samples in the series. A maximum amplitude  $q_0 \approx 0.1918$  (2) was obtained for the Mg-15%\_CN sample. This is the largest incommensurability value of the magnetic spiral phase that we have ever found among all our B/B'-site chemically substituted YBCFO samples. The incommensurability  $q_0$  also permits to derive the rotation angle  $\Phi$  of the magnetic spins between two successive unit cells along the  $c$  axis as plotted in the same figure.

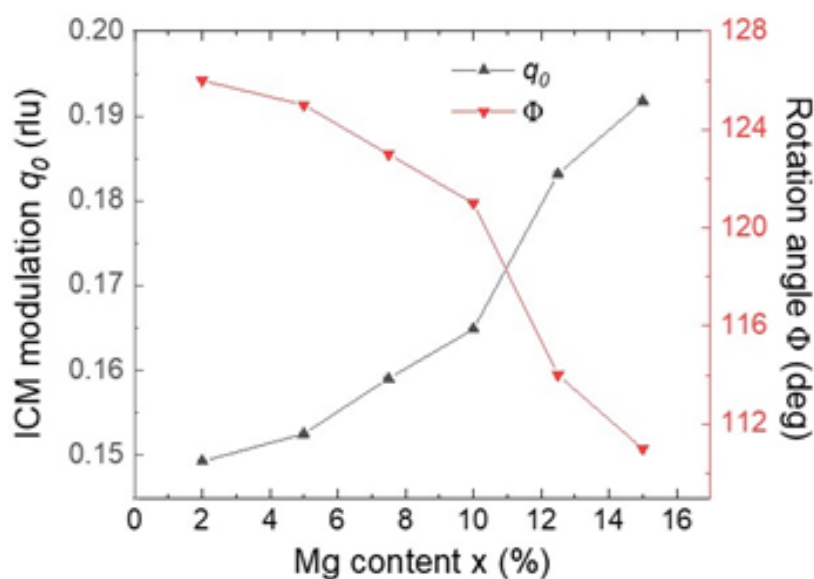


Figure 6.15.  $\text{YBaCu}_{1-x}\text{Mg}_x\text{FeO}_5$  (quenched). ICM modulation  $q_0$  at 50 K and associated spin rotation angle  $\Phi$  between successive bilayers as a function of Mg content  $x$ .

For the two quenched samples studied, the T-2Theta projections of the temperature dependence for the neutron-diffracted intensities around the  $(1/2 \ 1/2 \ 1/2)$  reflection are plotted in the left panel of Figure 6.16. As observed in the case of the controlled cooling rate samples, the CM and ICM phases are clearly distinguishable. For the ICM phase, the two magnetic satellites are more split as compared with the controlled cooling rate samples and the spiral phase dominates without concurrency from the collinear phase, as earlier commented. Interestingly, for the Mg-15%\_CN sample, the CM collinear phase is very weak and detectable in an extremely narrow range above  $T_{N2}$ . The spiral magnetic order is so stable in that composition that  $T_{N2}$  has come very close and is

almost merged with  $T_{N1}$ , the collinear transition temperature. Moreover, the two ICM branches are much more distanced (larger  $q_0$ ). In the right panel of Figure. 6.16 we can see the evolution of the refined average magnetic moments for each one of these phases. For the Mg-15%\_CN sample, the stability range of the magnetic spiral has invaded that of the collinear phase, preventing us to properly trace the collinear order development.

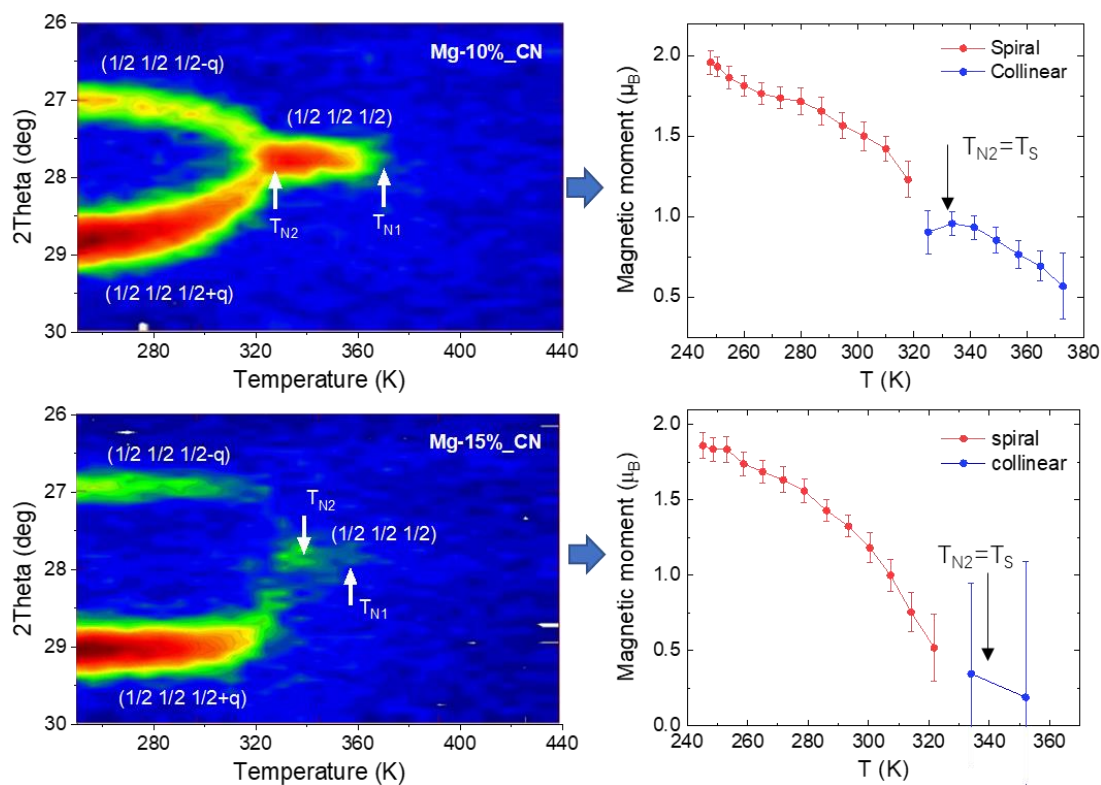


Figure 6.16. YBaCu<sub>1-x</sub>Mg<sub>x</sub>FeO<sub>5</sub> (quenched). T-2Theta contour plot of the temperature dependence for the neutron-diffracted intensities around the  $(1/2, 1/2, 1/2)$  reflection for the two measured compositions prepared by sudden immersion into LN and the corresponding average ordered magnetic moment associated to the CM and ICM phases. The red and blue symbols correspond to the  $(1/2, 1/2, 1/2 \pm q)$  and  $(1/2, 1/2, 1/2)$  magnetic orders, respectively.

### 6.4.2 Magnetic phase diagrams: influence of Mg and the chemical disorder

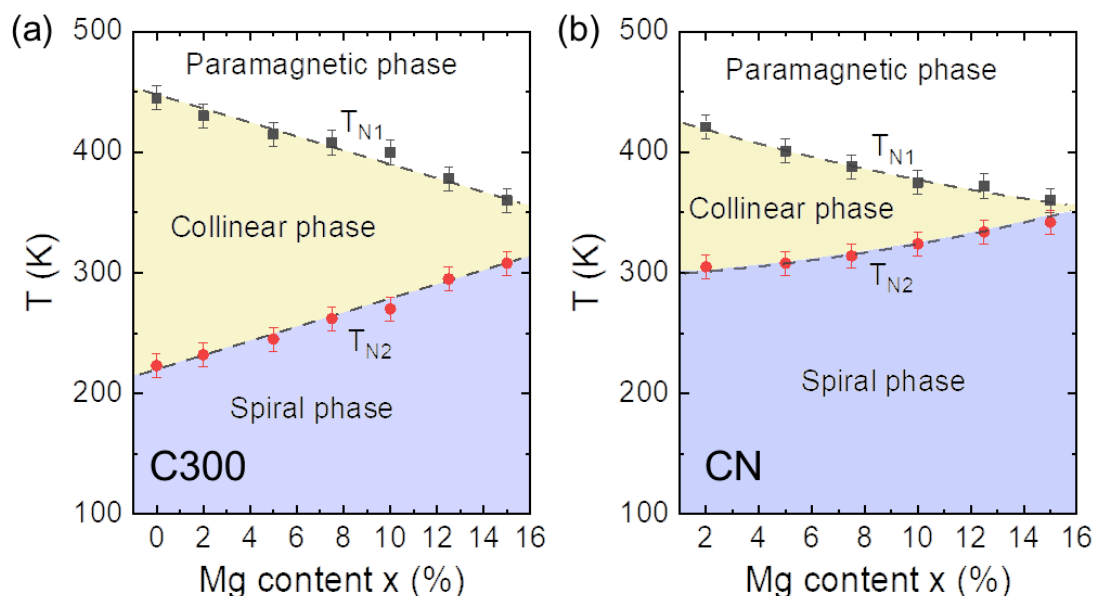


Figure 6.17. The T-x magnetic phase diagrams for the  $\text{YBaCu}_{1-x}\text{Mg}_x\text{FeO}_5$  family prepared applying two different final cooling processes: (a) cooling at a 300 K/h rate; (b) quenched into liquid nitrogen. The phase boundaries correspond to the onset of the collinear and spiral magnetic phases as observed in the magnetization and neutron diffraction measurements.

**Table 6.3.** The transition temperatures obtained from the NPD measurements for the  $\text{YBaCu}_{1-x}\text{Mg}_x\text{FeO}_5$  compounds prepared by different cooling processes and their corresponding chemical disorder ( $n_d$ ).

Controlled 300 K/h rate samples				Quenched samples			
x	$T_{N1}$ (K)	$T_{N2}/T_S$ (K)	$n_d$	x	$T_{N1}$ (K)	$T_{N2}/T_S$ (K)	$n_d$
0	445 (10)	223 (10)	0.316 (20)	0	---	---	---
2	430 (10)	232 (10)	0.314 (20)	2	421 (10)	305 (10)	0.362 (20)
5	415 (10)	245 (10)	0.325 (20)	5	401 (10)	308 (10)	0.359 (20)
7.5	408 (10)	262 (10)	0.323 (20)	7.5	388 (10)	314 (10)	0.362 (20)
10	400 (10)	270 (10)	0.333 (20)	10	375 (10)	324 (10)	0.368 (20)
12.5	378 (10)	295 (10)	0.334 (20)	12.5	372 (10)	334 (10)	0.367 (20)
15	360 (10)	308 (10)	0.318 (20)	15	360 (10)	342 (10)	0.363 (20)

Figure 6.17 plots the T-x[Mg] magnetic phase diagram for the two sets of  $\text{YBaCu}_{1-x}\text{Mg}_x\text{FeO}_5$  compounds prepared by the two different cooling processes. (The transition

temperatures are listed in Table 6.3). The spiral ordering temperature  $T_S (=T_{N2})$  for both sets of samples undergoes an increase with Mg content. For the controlled cooling rate samples [(a) panel], this variation is of a striking  $\sim 90$  K up to  $x=0.15$ ; meanwhile, for the quenched samples [(b) panel],  $T_S$  gets just lifted from  $\sim 300$  K in Mg-2%\_CN to  $\sim 350$  K in Mg-15%\_CN. For the controlled cooling rate samples, we have to stress that the relatively high chemical disorder ( $\sim 32\%$ ) observed in all compositions unambiguously favors a high- $T_S$  spiral phase [45]. More importantly, the variations taking place in  $d_1$  and  $d_2$  also play a significant role for this increase. From Figure. 6.5(c), one can see that there is a small increase for  $d_1$ , while for  $d_2$ , there is a much larger variation of  $\Delta d_2 \sim -0.012$  Å when increasing the Mg concentration. The most relevant effect is the large contraction of  $d_2$  along the  $c$  direction: it implies the contraction of the strongly AFM Fe-O1-Fe  $c$ -bonds, strengthening  $J_{c2'}$  in the improper Fe<sub>2</sub>O<sub>9</sub> bipyramids), which competes with the FM  $J_{c2}$ , from Fe-O1-Cu bonds in proper FeCuO<sub>9</sub> bipyramids. As a result, the remarkable  $d_2$  contraction raises the level of magnetic frustration in the bipyramids structure, thus lifting the stability of the chiral magnetic order. For the quenched samples, the increase of  $T_{N2}$  results from the combined effects associated to (a) the contraction of the  $d_2$  thickness and (b) the larger chemical disorder detected along the series of samples. Concurrently, along the whole series,  $d_1$  evolves as  $\Delta d_1 \sim +0.008$  Å, and  $d_2$  as  $\Delta d_2 \sim -0.016$  Å, i.e.  $d_2$  contraction is twice the elongation of  $d_1$ . The last only produce a secondary weakening of the AFM  $J_{c1}$  direct exchange between successive bilayers.

In Figure 6.18, we study the correlation between the two magnetic ordering temperatures and the incommensurability  $q_0$  found in our quenched samples. The evolution discloses a linear relationship with positive slope between the spiral ordering temperature  $T_S (=T_{N2})$  and the modulation  $q_0$  of the spiral order ( $T_{N2} = A + B \cdot q_S$ ), consistent with the predictions of the model developed by Scaramucci and coworkers [46][84]. Our linear fit in Figure 6.18 yields  $A=188.86$  (10.26) and  $B=797.49$  (61.52).

Furthermore, linear extrapolation of  $T_{N1}$  and  $T_{N2}$  indicate that both temperatures

should merge at  $T_{\max} \approx 348$  K and  $q_0 \approx 0.199$  r.l.u., giving rise to a paramagnetic-collinear-spiral triple point. According to our works [46][110], when approaching the triple point, we expect the magnetic spiral phase for Mg-doped family to be suppressed and replaced abruptly by a new AF3 phase characterized by the propagation vector  $\mathbf{k}_3=(1/2, 1/2, 0)$ , entering into the “Phase separation region”. So  $T_{\max} \approx 348$  K is thus anticipated as the highest spiral ordering temperature among the Mg-doped series samples, slightly lower than in the Co-doped series. Different with the Co-doped family, from Figure 6.16, we did not detect any trace of AF3 phase before the triple point, namely, there is no “induced phase separation”, but only the “critical phase separation” after the triple point. This is favorable difference of the non-magnetic Mg doping respect to the substitution with Co ions.

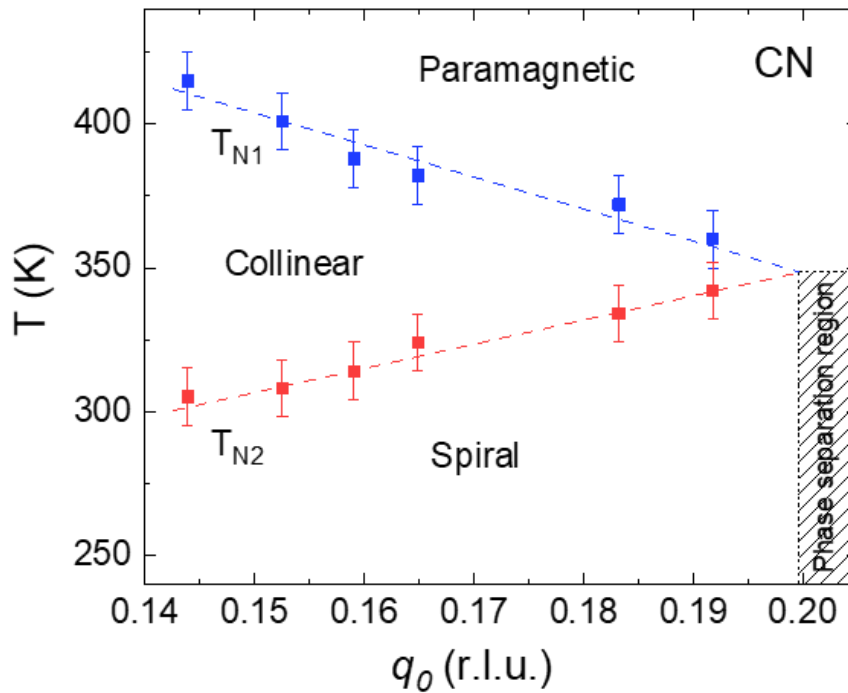


Figure 6.18.  $\text{YBaCu}_{1-x}\text{Mg}_x\text{FeO}_5$  (quenched). Magnetic transition temperatures  $T_{N1}$  and  $T_{N2}$  (Ts) as a function of the incommensurability  $q_0$ .



### 6.4.3 Influence of Mg doping on the easy axis and inclination of the magnetic spiral plane

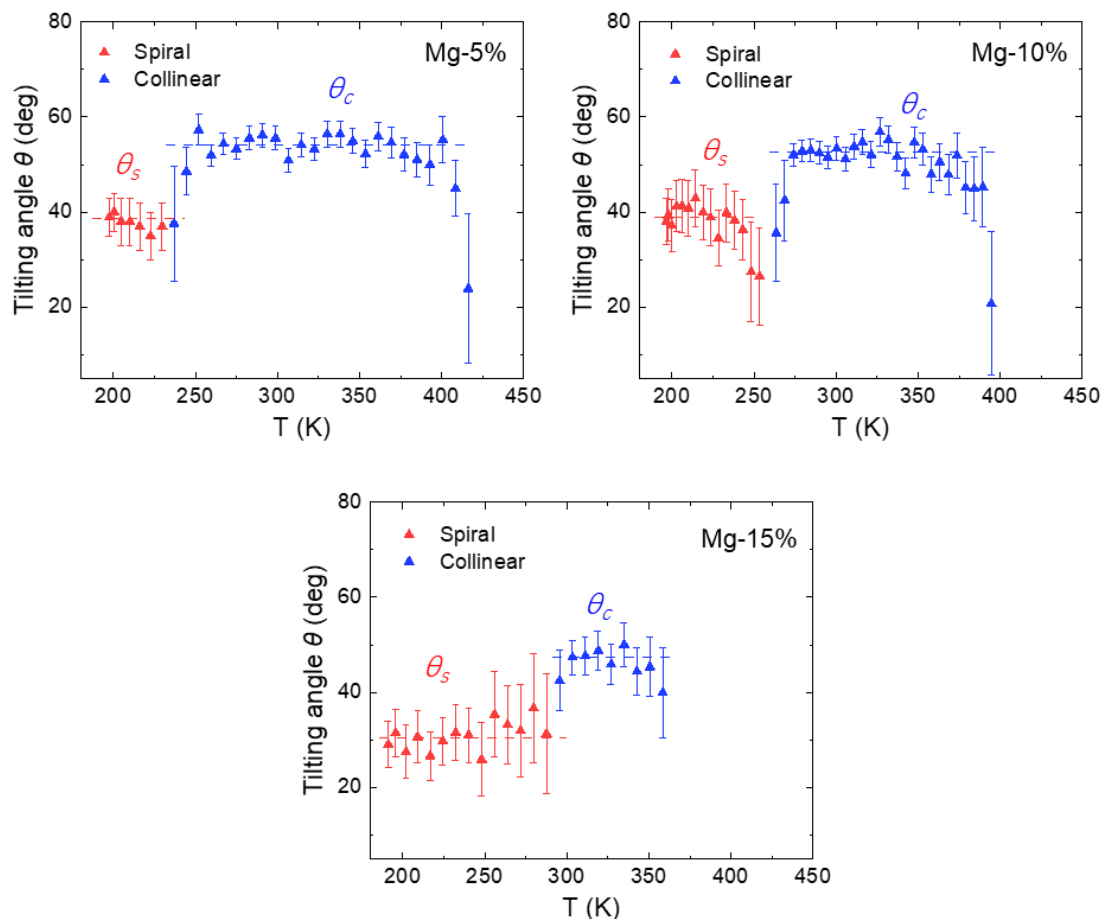


Figure 6.19. YBaCu<sub>1-x</sub>Mg<sub>x</sub>FeO<sub>5</sub> (cooled 300 K/h). The evolution of inclination angle for both spiral and collinear phases as a function of temperature with  $x=0.05, 0.10$  and  $0.15$ .

**Controlled cooling rate samples:** As done for the previously studied families, we also followed the thermal evolution of the inclination angle  $\theta$  in both the CM and ICM phases for three samples analyzed. The temperature dependent neutron diffraction data were collected in the 200 K to 450 K range. The tilting or inclination angle measures, in the collinear CM phase ( $\theta_c$ ), the angular distance between the magnetic spins and the **c** axis; in the spiral ICM phase ( $\theta_s$ ), it refers to the angular distance between the magnetic spiral rotation plane and the **c** axis. Due to the tetragonal symmetry, the orientation of the spins in the **ab** plane cannot be determined from NPD. According to

the magnetic spin configuration built in previous chapters, a  $\theta$  value close to  $90^\circ$  means the easy-axis is nearer to lie within the **ab** plane, while for  $\theta \approx 0^\circ$  the easy-axis is almost parallel to the **c** axis. The inclination angle was refined using the ratio  $m(\text{Fe})=m(\text{Cu})$  in both phases. The  $M_R \gg M_I$  constraint was used in the ICM phase aiming to minimize errors.

Figure 6.19 plots the temperature dependence of the inclination angle for the three studied compositions:  $x=0.05$ ,  $0.10$  and  $0.15$ . Two main conclusions can be extracted with respect to the evolution of the CM and ICM phases. On the one hand, for the CM collinear phase,  $\theta_c$  is nearly constant with the temperature and the values for three compositions are similar to each other. In addition, this constant value is comparable to that found for the  $\text{YBaCu}_{1-x}\text{Co}_x\text{FeO}_5$  family studied in the previous chapter. With respect to the ICM spiral phase, the inclination  $\theta_s$  was also found not to vary significantly with  $T$  for each composition. However, the tilting in Mg-5% and Mg-10% samples is very similar ( $\theta_s \approx 40^\circ$ ), whereas in Mg-15% this adopts a value around  $30^\circ$ . Said otherwise, a reorientation ( $\Delta\theta_s \approx -10^\circ$ ) of the magnetic spiral rotation plane towards the **c** axis was found when moving from low-doped ( $x \leq 0.10$ ) samples to the highest-doped ( $x=0.15$ ) one.

**Quenched samples:** Figure 6.20 displays the tilting angle as a function of temperature for the two quenched samples studied ( $x=0.10$  and  $0.15$ ). The temperature dependent NPD were measured in the 250-440 K range. For the Mg-10%\_CN sample, the inclination angles in the two phases remain practically constant along with the temperature. The constant values found for the CM collinear phase are comparable to those seen in the samples prepared using a controlled cooling rate. For Mg-15%\_CN, due to the weakness of the CM phase and, consequently, low reflection intensities (see Figure. 6.16), the analysis of this phase is not displayed. The inclination  $\theta_s$  also presents a constant value, despite a few points deviating at high temperatures, with large error bars. Interestingly, the tilting of the ICM spiral phase for these two samples is very similar, and no reorientation of the magnetic spiral plane was observed.

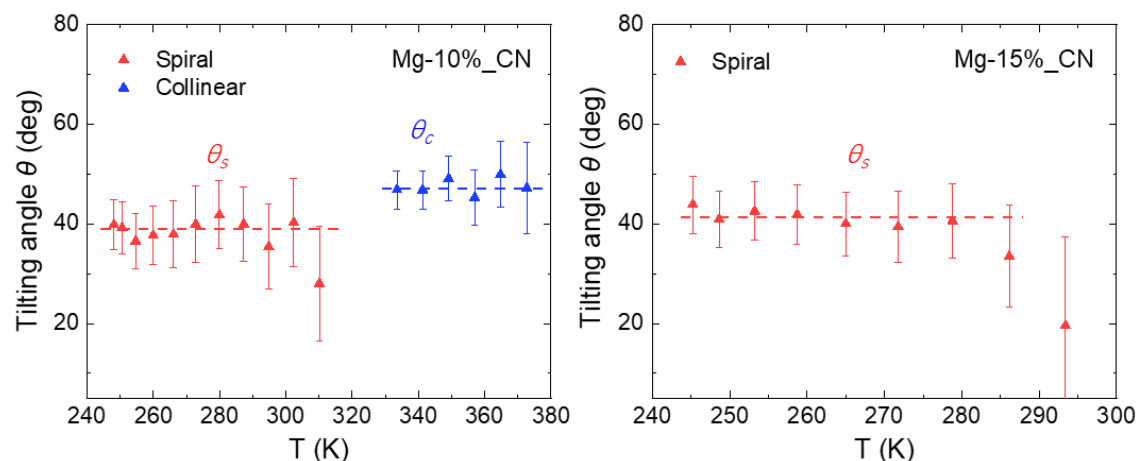


Figure 6.20. YBaCu<sub>1-x</sub>Mg<sub>x</sub>FeO<sub>5</sub> (quenched). Evolution of inclination angle as a function of temperature for YBaCu<sub>1-x</sub>Mg<sub>x</sub>FeO<sub>5</sub> ( $x=0.10$  and  $0.15$ ) prepared by immersion into LN.

**Table 6.4.** YBaCu<sub>1-x</sub>Mg<sub>x</sub>FeO<sub>5</sub> (quenched). Refined magnetic moments [imposing  $m(\text{Fe})=m(\text{Cu})$ ] and inclination angles obtained refining the ICM spiral phase at 50 K. The refined magnetic moments correspond to two models: *Model 1* ( $M_r \gg M_i$ ) and *Model 2* ( $M_r = M_i$ ).

Sample (50 K)	<i>Model 1</i> ( $M_i \sim 0$ )		<i>Model 2</i> ( $M_i = M_r$ )	
	$m(\text{Fe})$ ( $\mu_B$ )	Theta (deg)	$m(\text{Fe})$ ( $\mu_B$ )	Theta (deg)
Mg-2%_CN	2.83 (7)	41 (3)	2.05 (2)	41
Mg-5%_CN	2.77 (6)	39 (3)	2.00 (2)	39
Mg-7.5%_CN	2.73 (7)	38 (3)	1.96 (2)	38
Mg-10%_CN	2.71 (5)	40 (3)	1.95 (2)	40
Mg-12.5%_CN	2.62 (5)	40 (3)	1.87 (2)	40
Mg-15%_CN	2.59 (3)	43 (5)	1.83 (2)	43

The NPD data of the quenched samples collected at fixed 50 K were carefully refined and the Rietveld refinements are presented in Figure 6.21. The obtained results are also summarized in Table 6.4. Regarding the magnetic moments, the neutron patterns were refined using the limit  $m(\text{Fe})=m(\text{Cu})$ . In addition, two models were employed in the refinements: *Model 1* ( $M_r \gg M_i$ ), which corresponds to the high eccentricity case; and *Model 2* ( $M_r = M_i$ ), corresponding to a circular ellipse. Similar agreement factors were obtained in both cases.

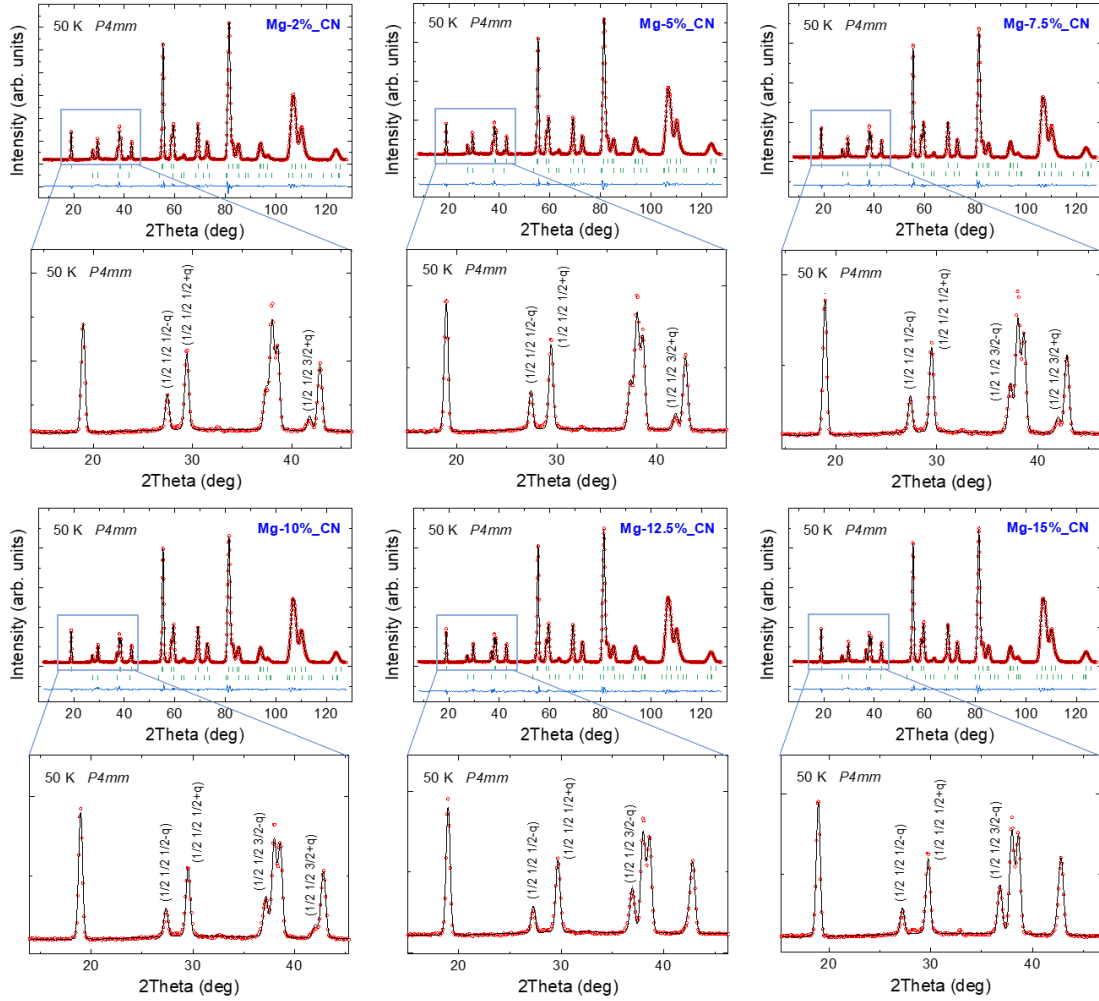


Figure 6.21.  $\text{YBaCu}_{1-x}\text{Mg}_x\text{FeO}_5$  (quenched). Rietveld refinement of the neutron diffraction patterns collected at 50 K (d1b@ILL) for Mg-2%\_CN ( $R_B$ : 1.47,  $R_f$ : 0.922,  $R_M$ : 10.10,  $\chi^2$ : 5.78); Mg-5%\_CN ( $R_B$ : 1.17,  $R_f$ : 0.742,  $R_M$ : 10.2,  $\chi^2$ : 6.15); Mg-7.5%\_CN ( $R_B$ : 2.10,  $R_f$ : 1.24,  $R_M$ : 10.2,  $\chi^2$ : 6.60); Mg-10%\_CN ( $R_B$ : 1.47,  $R_f$ : 0.930,  $R_M$ : 9.66,  $\chi^2$ : 6.00); Mg-12.5%\_CN ( $R_B$ : 1.50,  $R_f$ : 0.938,  $R_M$ : 9.23,  $\chi^2$ : 6.13); Mg-15%\_CN ( $R_B$ : 1.14,  $R_f$ : 0.703,  $R_M$ : 9.35,  $\chi^2$ : 5.23). Rows of bars stand for the allowed Bragg reflections for the structural and magnetic phases. The fitting of low-angle region for the main magnetic peaks are focused below each composition's full pattern.

The inclination angles presented in Table 6.4 are depicted in Figure 6.22. As we can see, the inclination of the magnetic spiral for the compositions  $\text{YBaCu}_{1-x}\text{Mg}_x\text{FeO}_5$  remains at a practically constant value of  $\theta_s \approx 40^\circ$ , within the error. This means that, to first approximation, the spiral rotation plane does not vary upon Mg substitution.

In Figure 6.23, a comparison of the inclination angle in the spiral phase as a function of the incommensurability was plotted for the Mg and Co-doped YBCFO families. Both these two substitutions are in the divalent Cu site, but they

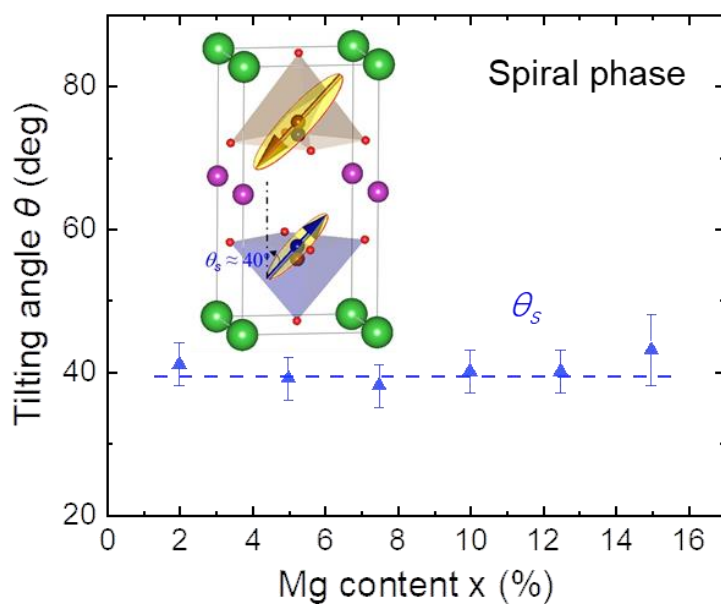


Figure 6.22. YBaCu<sub>1-x</sub>Mg<sub>x</sub>FeO<sub>5</sub> (quenched). The tilting angle ( $\theta_S$ ) in the ICM spiral phase at 50 K in YBaCu<sub>1-x</sub>Mg<sub>x</sub>FeO<sub>5</sub> family as a function of Mg content refining the NPD data. Inset: schematic drawing showing the  $\theta_S$  between the magnetic spiral rotation plane and the  $c$  axis.

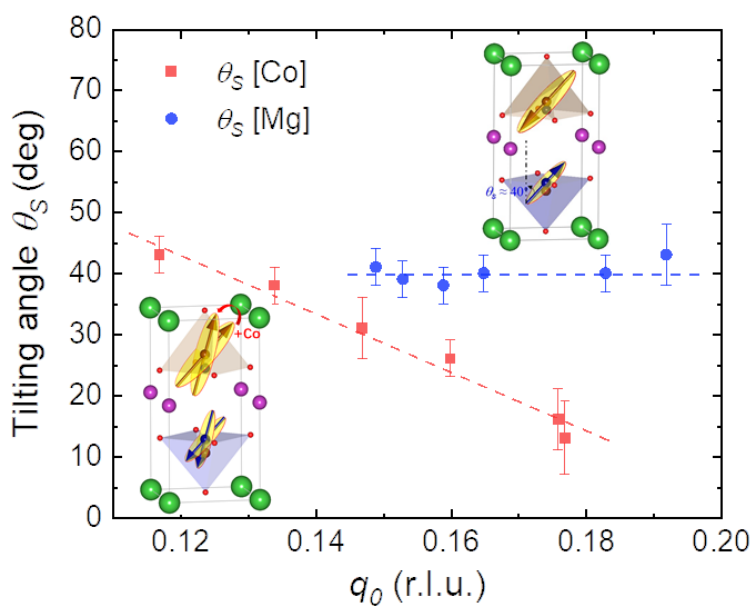


Figure 6.23. YBaCu<sub>1-x</sub>Mg<sub>x</sub>FeO<sub>5</sub> (quenched) and YBaCu<sub>1-x</sub>Co<sub>x</sub>FeO<sub>5</sub> families. The tilting angle ( $\theta_S$ ) in the ICM spiral phase as a function of their incommensurability  $q_0$ . Inset: schematic drawing showing the evolution of  $\theta_S$ .

demonstrate different properties concerning the anisotropy in the chiral phase. As we can see from the figure, the former (Mg-doped) presents a practically constant  $\theta_S$  value. Increasing Mg substitution does not modify the spiral rotation plane. While for the latter, the tilting angles were modified a lot with increasing the Co content, the magnetic

rotation plane of the spiral underwent a counterclockwise turn, favoring cycloidal order. This illustrates the different impact of the two substitution of  $\text{Cu}^{2+}$  ions on the magnetic anisotropy of the spiral phase in YBCFO compounds. On the other hand, we have achieved a much larger spiral modulation ( $q_0 \approx 0.192$  r.l.u.) in the Mg-doped YBCFO family compared with the largest  $q_0 \approx 0.177$  r.l.u. in the Co-doped YBCFO family. This enables to increase the magnetic modulation range  $q_0$  for the YBCFO-based chiral magnets.

## 6.5 Summary and conclusions

To summarize, we have managed to synthesize the  $\text{YBaCu}_{1-x}\text{Mg}_x\text{FeO}_5$  family with two different cooling methods: (i) inside a furnace at a controlled 300 K/h rate; (ii) quenched into liquid nitrogen. After carefully analyzing the SXRPD and NPD data we have arrived to new findings.

The magnetization measurements on both sets of samples unveil interesting magnetic phase transitions. For the controlled cooling rate samples, a systematic increasing of the magnetic spiral ordering temperature  $T_{\text{N}2}$  was found for an increasing Mg content in the solid solution, approaching 308 K in the Mg-15% sample. For the quenched samples, a positive correlation was also found in  $T_{\text{N}2}$  along with the Mg content, reaching  $T_{\text{N}2} \approx 342$  K in the case of the Mg-15%\_CN sample.

The structural information for these two sets of samples was extracted by analyzing the SXRPD data. The SXRPD patterns were compatible with the  $P4mm$  symmetry and best agreement factors were obtained. A systematic increasing and decreasing tendency were found for the cell parameters  $a$  and  $c$ , respectively, for both sets of samples, as a function of Mg content; meanwhile, a progressive elongation and contraction were observed for the two characteristic distances,  $d_1$  and  $d_2$ , respectively. The interesting finding here lies in the Fe/Cu chemical disorder which remains constant values for the two groups of samples. For the controlled cooling rate samples, the occupation of Fe and Cu was found to be  $\sim 32\%$ , whereas for the LN- quenched samples,

the distribution of Fe and Cu got more randomly distributed, we obtained ~36% for this set of samples.

The magnetic properties were characterized and studied by NPD. For the set of controlled cooling rate samples, two AF transition temperatures were found at  $T_{N1}$  and  $T_{N2}$  by checking the T-dependent neutron diffracted intensities and they are consistent with our magnetization measurements. Particularly, for the aforementioned FM phase in the Mg-10% sample, we did not observe the FM signal by integrating the neutron diffracted intensity. The study of the easy-axis was carried out investigating the tilting angles along with the temperature. For these three samples, firstly, we found that the tilting angle remains practically constant in the CM and ICM phases, and that the tilting in the CM phase is insensitive to the Mg substitution level, whereas for the ICM phase, there is a change of  $\Delta\theta \approx -10^\circ$  from the Mg-5% and Mg-10% ( $\theta \approx 40^\circ$ ) to the Mg-15% sample ( $\theta \approx 30^\circ$ ). Therefore, a reorientation of nearly  $10^\circ$  was found for the magnetic rotation helix, approaching to the **c** axis.

The quenched samples show a more interesting behavior. The observed  $T_{N1}$  and  $T_{N2}$  are consistent with the magnetization measurements by checking the T-dependent NPD data. The spiral phases are observed to be alone in the two samples, without the residue of collinear phase. For the Mg-15%<sub>CN</sub> sample, the CM phase is nearly vanished, and the two transition temperatures approach each other. The largest incommensurability  $q_0 \approx 0.1918$  (2) r.l.u. was obtained for the Mg-15%<sub>CN</sub> sample. The easy-axis of the magnetic spins in the ICM phase for the two studied samples was also extracted. The tilting angles for these two samples were also found to be constant in both the CM and ICM phases, within the error, but different to those seen for the controlled cooling rate samples. The reorientation of the magnetic rotation plane was found unchanged from Mg-10%<sub>CN</sub> to Mg-15%<sub>CN</sub>. The NPD patterns collected at 50 K for the quenched samples were carefully analyzed. The tilting angle  $\theta_s$  was found constant and independent on the Mg content, with the angles adopting an intermediate value of  $\sim 40^\circ$ .

A T-x magnetic phase diagram was built for the samples prepared by the two different cooling methods. A positive and negative correlation were found for  $T_{N2}$  and  $T_{N1}$  as a function of Mg content for both sets of samples. The tuning of the spiral ordering temperature ( $T_{N2}$ ) was found to be more pronounced for the quenched samples, and  $T_{N2} \sim 342$  K was achieved in the Mg-15%\_CN sample. The increasing of  $T_{N2}$  is a consequence of the combined effect of chemical disorder and the variations in  $d1$  and  $d2$ . Both the chemical disorder and contraction of  $d2$  produce a rise of the degree of magnetic frustration in the bipyramids structure, generating a positive effect on the magnetic spiral ordering temperature  $T_{N2}$ .





# Chapter 7

## Fabrication and characterization of the single crystal $\text{YBaCuFe}_{0.95}\text{Mn}_{0.05}\text{O}_5$

### 7.1 Introduction

Simultaneous coupling of magnetic order and ferroelectric order parameters results in the new class of (spin induced) type-II multiferroics. The importance of this kind of coupling is not just lies in the fundamental research, but also in the application such as spintronics and the generation of new memory devices. In great part of the referenced spin-induced type-II multiferroic materials, such as  $\text{FeVO}_4$ ,  $\text{MnWO}_4$  and  $\text{TbMnO}_3$ , the electric polarization is induced by a spiral type magnetic configuration of the spins [30][39]. Most of the chiral magnetoelectric multiferroics discovered or investigated in recent years are geometrically frustrated magnets where the spin-orbit coupling favors non-collinear (spiral) magnetic ordering through the DM mechanism. However, the low transition temperatures (normally  $T_S < 100$  K for spiral orders) and relatively small electric polarizations typically limit the potential applications of most type-II multiferroic materials.

$\text{CuO}$  and  $\text{YBaCuFeO}_5$  (YBCFO) are the two widely known type-II multiferroics which are exceptions to the above rules and show both magnetism and strong electric

polarization at temperatures around 200 K. Cupric oxide has been paid much attention and extensively studied to show the multiferroic behavior between 190 and 220 K, in which a formation of a non-collinear antiferromagnetic phase is accompanied [111]. Whereas, the magnetic structure of YBCFO is far less known due to the difficulty in the growth of high-quality single crystals. Previous reports on polycrystalline or powder samples of YBCFO have demonstrated that a strong ferroelectric response at  $T_s$  around 230 K where the CM spin magnetic order undergoes a transition to the ICM spin magnetic order [44][21][112]. Since the magnetic and ferroelectric behavior are anisotropic, the measurements using powder or polycrystalline samples, therefore, limit the detailed study of the mechanism behind the strong magnetoelectric coupling at such a high temperature. In addition, YBCFO displays an extraordinary tunability of its ICM (spiral) ordering temperature ( $T_s=T_{N2}$ ) by manipulating the Cu/Fe chemical disorder in the bipyramids by means of the synthesis procedure [45]. Likewise, beyond cation disorder, the strength of the main magnetic interactions can be also tuned by chemical pressure [46].

The relevance of the spin-orbit coupling in this structure is not clear yet. The similarity of  $\text{Mn}^{3+}$  and  $\text{Fe}^{3+}$  ionic sizes (both  $\approx 0.58 \text{ \AA}$  in pyramidal coordination [48]) opens the possibility to increase the spin-orbit coupling in  $\text{YBaCuFe}_{1-x}\text{Mn}_x\text{O}_5$  through the partial substitution of highly symmetric  $\text{Fe}^{3+}$  ions ( $3d^5$ ,  $L=0$ ,  $S=5/2$ ) with  $3d^4$   $\text{Mn}^{3+}$  ions ( $L=2$ ,  $S=2$ ). We recently reported [47] that in polycrystalline  $\text{YBaCuFe}_{1-x}\text{Mn}_x\text{O}_5$  samples prepared with identical cooling rates, the presence of Mn produces a progressive reorientation of the tilt  $\theta_{\text{spiral}}$  of the rotation plane of the spins in the spiral phase. It moves away from the **ab** plane where the DM-based models predict null spontaneous polarization. So far, the spontaneous polarization has not been reported in samples with  $T_s \geq 300 \text{ K}$  nor in single crystals, a proper determination of the Mr/Mi ratio which is of importance for ferroelectricity requires quality single-crystal neutron diffraction data. The absence of ferroelectricity in YBCFO crystals could be associated to the chemical disorder or the specific features of the spiral (Mr/Mi ratio or tilting of

the spiral rotation plane, for instance). In the recent work [86] on a YBCFO single crystal, the authors did not observe the spontaneous polarization because the neutron powder diffraction data compatible with a helical spiral magnetic order (parallel to the **ab** plane), which, reversely, gives more importance of our Mn doped YBCFO single crystal.

So, along this chapter, we present a detailed investigation on the fabrication and properties of a single crystal  $\text{YBaCuFe}_{0.95}\text{Mn}_{0.05}\text{O}_5$ . That is, YBCFO was partially doped with Mn ions at the trivalent Fe positions. According to the results presented in the Chapter 4, this doping should favor the rotation plane of the magnetic spins in the chiral magnetic phase which does not parallel to the **ab** plane. In this chapter, we have described the preparation and growth of the single crystal and its characterization using different techniques (mainly synchrotron and neutron diffraction and high-resolution transmission electron microscopy (HRTEM)). In the Chapter 4, we have studied a polycrystalline sample with the same composition of the crystal, therefore the properties of the single crystal will be presented in a comparative way emphasizing the similarities or not between these two bulk samples.

## **7.2 Growth of the Mn-doped YBCFO single crystal by the TSFZ method**

### **7.2.1 Rod preparation**

- (i) First of all, the polycrystalline powder of the composition  $\text{YBaCuFe}_{0.95}\text{Mn}_{0.05}\text{O}_5$  should be prepared. The detailed procedures to prepare the powder are described in Chapter 4;
- (ii) The powder was loaded in a thin rubber tube and subsequently packed with cylindrical shape using a vacuum bump and then compacted under 1500 bars of isostatic pressure;
- (iii) The obtained solid cylindrical rod was further compacted by sintering at 1100

$^{\circ}\text{C}$  for 50 h in air. The final dimensions of the rod were 4 mm in diameter and about 80 mm in length. The rod was then cut into two pieces, the longer part was used as feed rod and the shorter one used as seed rod;

- (iv) To grow an incongruently melting compound, a proper solvent rod is required. In this work, a small chip-like solvent rod which consisted of  $\text{CuO}$  with 2 wt%  $\text{B}_2\text{O}_3$  was employed in the growth [53]. The dimensions of the small solvent chip are 3 mm in diameter and 3 mm in height.

Some key procedures of the preparation of the rod are shown in the Figure 7.1.



Figure 7.1. Procedures of the preparation of the polycrystalline  $\text{YBaCuFe}_{0.95}\text{Mn}_{0.05}\text{O}_5$  rod: (a) the powder was packed with cylindrical shape using the vacuum bump; (b) the powder was further packed with the isostatic press; (c) the resulting packed rod with cylindrical shape after the previous procedures; (d) the furnace used to perform the sintering/annealing process for the rod.

### 7.2.2 Single crystal growth

The single crystal growth was performed with a four-mirror optical furnace

(Crystal System Corp., Japan) using the TSFZ method. In the furnace, four 400 Watt halogen lamps were used as the heating source. The feed rod was hanged straightly on the upper shaft and the seed rod was fixed on the lower shaft, aligning and centering the two rods by rotating the shafts in order to keep the two rods well-aligned in the same centerline during their growing process of opposite rotations.

The chip-like solvent was put on the top of the seed rod before growing. Once turned on the furnace, the two rods were rotated at 25 rpm in opposite directions. Firstly, the top of the solvent and the bottom of the feed rod are partially melted and connected. Then, the top of the seed rod and the bottom of the solvent are melted and connected. The growth of the single crystal started based on a stable and homogenous melted zone. After adjusting the pulling rate, the composition of the solvent was in equilibrium after several hours of growth, and the single-crystal with the desired  $\text{YBaCuFe}_{0.95}\text{Mn}_{0.05}\text{O}_5$  composition start to precipitate. After several days of stable growth, a large high-quality single crystal was obtained. A screenshot of the controlling panel during the crystal growth process and the as grown single-crystal are shown in the Figure 7.2.

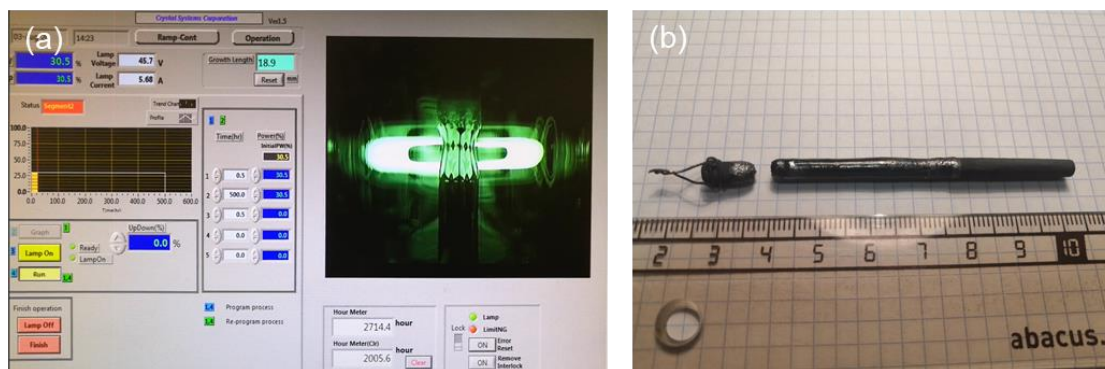


Figure 7.2. (a) The crystal growth computer controlling panel; (b) The as grown single-crystal.

## 7.3 Characterization and discussion

### 7.3.1 Structural characterization

High resolution transmission electron microscopy (HRTEM) images were

obtained at 200kV using the field-emission gun FEI Tecnai F20 S/TEM electron microscope. Samples for transmission electron microscopy (TEM) observation were obtained by gentle mechanical grinding of single crystals. Multislice image simulations were carried out with the EMS software package [113]. In addition, a small pellet of the single crystal was pulverized into powder, the structural analysis of the single crystal sample was performed on the basis of SXRPD data collected at room RT, in the MSPD beamline of the ALBA Synchrotron (Barcelona, Spain), using  $\lambda=0.41252 \text{ \AA}$ . Finally, single-crystal neutron diffraction measurements on a small piece which cut from the large single crystal bar were carried out at the D9 four-circle neutron diffractometer in ILL, in which a large set of 833 nuclear Bragg reflections (456 independent) were collected at 50 K using  $\lambda=0.836 \text{ \AA}$  to obtain a good structural model that allowed us to determine the Fe/Cu cationic order and interatomic distances.

***Transmission electron microscopy:***

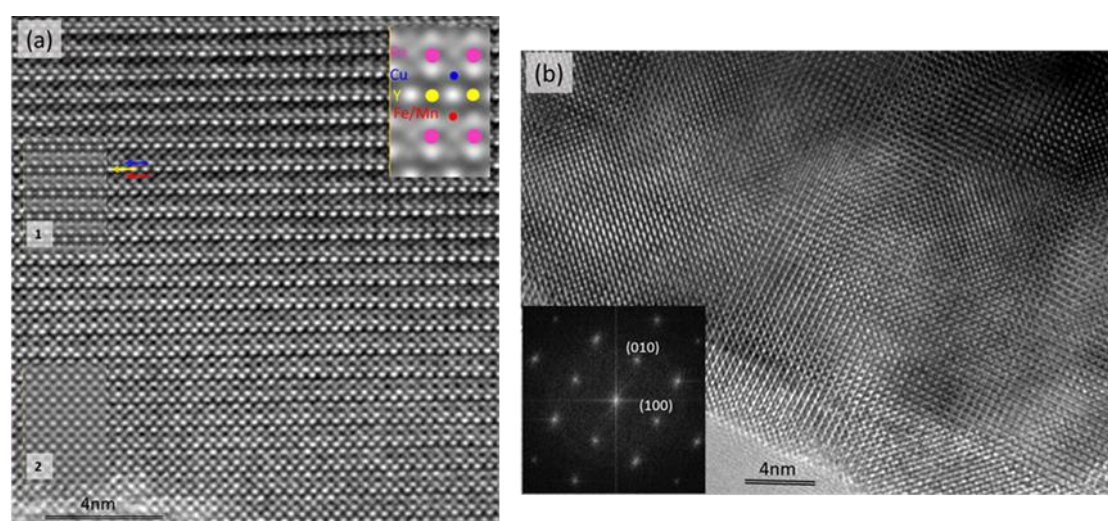


Figure 7.3.  $\text{YBaCuFe}_{0.95}\text{Mn}_{0.05}\text{O}_5$ . (a) HRTEM image of the single crystal viewed along the  $[100]$  zone axis. Insets labelled **1** and **2** are simulations for thickness values of 4.6 and 1.5 nm, respectively (defocus 68 nm). The inset at the upper right corner shows the position of atomic columns. (b) HRTEM image of the same sample viewed along the  $[001]$  zone axis. The inset shows the corresponding fast Fourier transform.

Figure 7.3(a) shows a HRTEM image of the single crystal sample taken along the  $[100]$  zone axis. Image simulations for two different thicknesses (4.6 and 1.5 nm) at a

defocus value of 68nm are over-imposed as insets 1 and 2, respectively, where atom columns are seen dark. Still in this figure, the upper right inset shows the atomic positions on the simulated image. The prominent bright fringes correspond to the Y planes of the crystal structure, as indicated by a yellow arrow. It can be observed that, in the thicker region, the contrast above and below these planes is not symmetric: the atomic planes containing the Cu ions are brighter than those containing the Fe(Mn) ones, giving rise to a characteristic double fringe contrast. This contrast effect, on the other hand, disappears in the thinner area close to the edge of the crystallite at the bottom of the image. It is interesting to note that image simulations using crystal data from a non-Mn doped sample revealed symmetric contrast about the prominent fringes. Therefore, the double fringe contrast can be attributed to the differential distortion of the Cu and Fe sites induced by the selective Mn doping. A more careful inspection reveals lateral variations of the Cu-plane intensity in the thicker area which, on the basis of the above considerations, can be interpreted as variations in the level of lattice distortion induced by concomitant variations of the Mn concentration.

The HRTEM image shown Figure 7.3(b) corresponds to the basal plane of the structure (zone axis [001]). The most apparent feature of the image is a patched like contrast defining very small domains, 4-6 nm in size. This nanostructure was observed in all crystallites observed in this orientation. Dark contrasts in these HRTEM images indicate inhomogeneous strains, while according to image simulations, the elongated shape of the bright dots observed, for instance, in the right side of the image correspond to  $\langle 110 \rangle$  tilts of the lattice away from the zone axis. The fast Fourier transform (see inset) shows diffuse scattering effects around the spots which can be associated to local disorder and strain inhomogeneities observed in the image. It is worthy to mention that this patched nanostructure was not observed in images obtained from non-doped samples.



***Crystal structure: single-crystal neutron diffraction versus synchrotron diffraction of powdered samples:***

Figure 7.4(a) shows the refined SXRPD pattern (at 300 K) for the powdered single crystal sample ( $\chi^2$ : 70.7,  $R_B$ : 6.26,  $R_f$ : 6.36), and Figure 7.4(b) the neutron integrated intensity refinement (at 50 K) for the nuclear reflections of the single-crystal ( $\chi^2$ : 1.12,  $R_F$ : 2.95,  $R_F^2W$ : 4.23). In addition, the refined SXRPD pattern of the Mn-5% polycrystalline powder sample ( $\chi^2$ : 70.9,  $R_B$ : 5.44,  $R_f$ : 7.16) was also plotted in the Figure 7.4(c) as comparison. The atomic positions and the occupancies of the Cu and Fe[Mn] ions in the two pyramids of the unit cell were refined. The z-coordinates of the same metal in upper and lower positions were constrained by  $z(\text{M1})+z(\text{M2})=1$  for the SXRPD data. The positions of the different oxygen atoms were refined separately. The detailed structural information obtained for these specimens is summarized in Table 7.1. A key feature with strong influence on the magnetic properties is the Fe/Cu chemical disorder. For that reason, the partial occupation by the Cu and Fe[Mn] of the upper and lower pyramids in the structure was carefully refined. The results about the chemical disorder in these samples with identical composition are given in Table 7.1. The proper occupancy (Occ) in the pyramids was 0.70 (2) for the polycrystalline powder sample, and for the powdered single crystal, we obtained a value of 0.81 (3) refining the SXRPD data and 0.89 (3) refining the single-crystal neutron diffraction data. Remarkably, this implies that  $\approx 30\%$  of nominal Fe pyramids are occupied by Cu in the polycrystalline powder sample, whereas in the single crystal this is so only in  $\approx 11\%$  of the pyramids (a proper occupation  $\text{Occ}=0.5$  would correspond to a random B-site cation distribution, and an  $\text{Occ}=1$  describes a fully ordered Fe/Cu structure). Therefore, the polycrystalline powder sample is much more disordered than the single crystal. Next, we will present a comparison of the magnetic properties in both samples.

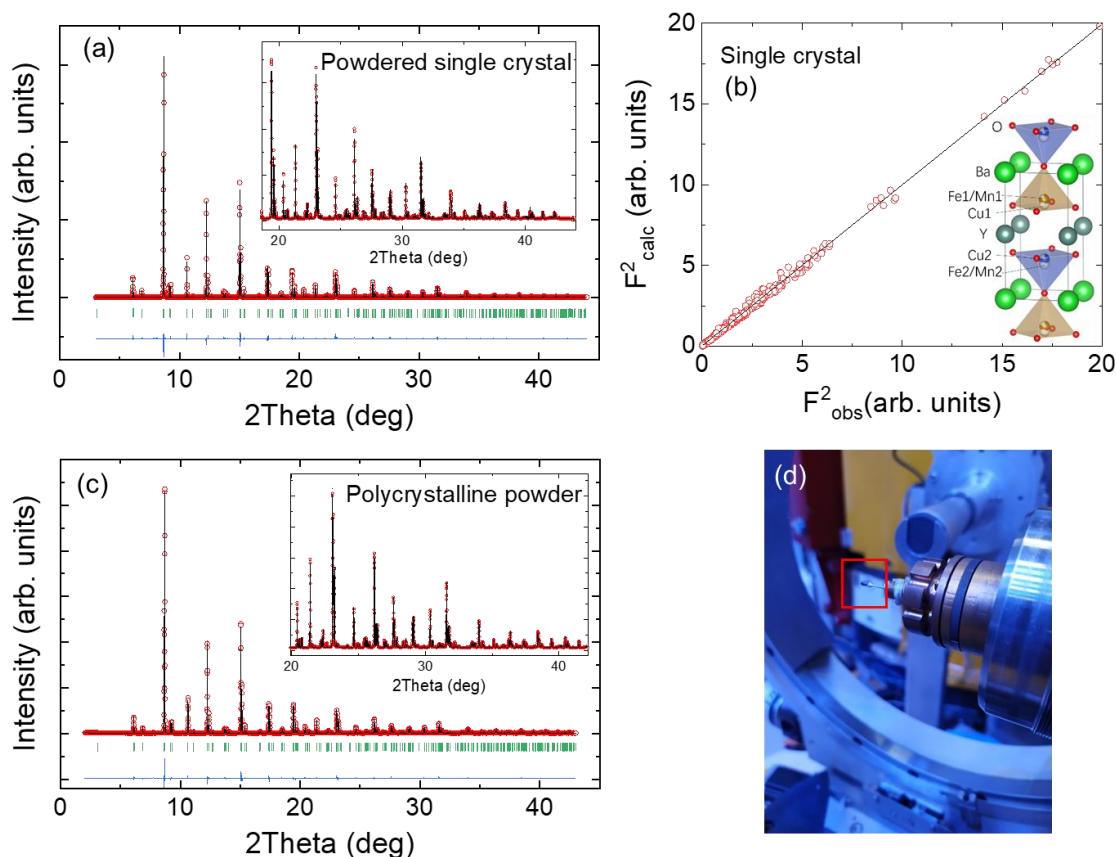


Figure 7.4. Rietveld refinement (black curve) of the synchrotron X-ray intensities (red circles) at 300 K for the (a) Powdered single crystal and (c) Polycrystalline powder sample, respectively. Bottom blue line is the observed-calculated difference. Inset: expanded region at high-angles; (b) [single-crystal neutron diffraction] Agreement plot of the refinement of nuclear reflections collected from the single crystal at 50 K ( $\lambda=0.836$  Å). The calculated structure factor is plotted against the experimental ones. Inset: *P4mm* structure showing the corner-sharing square bipyramidal layers. The color of each pyramid corresponds to the color of the dominant cation in it (blue: Cu; brown: Fe); (d) The mounted small piece of single crystal (in the red rectangle) for the neutron diffraction at the D9 four-circle neutron diffractometer in ILL.

Furthermore, according to the study we performed in the Chapter 4 for the polycrystalline samples, there is certain amount of extra oxygen which accommodates at the Y layers [the *1b*: (1/2, 1/2, *z*) position]. For this single crystal, we also carried out refinements to detect the extra oxygen in the crystal structure using the large set of structural reflections collected at D9, a value of  $\delta = 0.010$  (9) was obtained. It indicates that, within the error, we did not detect the extra oxygen in the single crystal, meanwhile, it means the oxidation state of Mn was well preserved.

**Table 7.1.** Structural parameters obtained by Rietveld refinement of the SXRPD data for the powdered single crystal (first row) and polycrystalline powder sample (third row) (MSPD@Alba, 300 K) and single-crystal neutron diffraction data (second row) (D9@ILL, 50 K) respectively. The “Occ” refers to the chemical occupation of the dominant cation in its square pyramid. The dominant cation in upper pyramid (brown) and lower pyramid (blue) being Fe and Cu, respectively.

Sample		$z(Y)$	$z(Fe1)$	$z(Cu2)$	$z(O_1)$	$z(O_2)$	$z(O_3)$	Occ
		(0 0 z)	(1/2 1/2 z)		(0 1/2 z)			
Single crystal	a=3.8747(3) Å	0.5108(3)	0.7515(8)	0.2849(8)	0.013(5)	0.329 (4)	0.694(4)	0.811(30)
	c=7.6645(3) Å							
Powder	a=3.8699(3) Å	0.4979(3)	0.7343(8)	0.2674(8)	-0.002(5)	0.312 (4)	0.682(4)	0.891(26)
	c=7.6359(3) Å							
	a=3.8735(3) Å	0.5116(4)	0.7551(6)	0.2850(3)	0.011(3)	0.327(1)	0.697(1)	0.704(22)
	c=7.6648(3) Å							

### 7.3.2 Magnetic characterization and neutron magnetic diffraction

The magnetic susceptibility of the powder and single crystal samples was measured using a VSM magnetometer in a Physical Properties Measurement System (PPMS, Quantum Design Inc) under a magnetic field of 2 kOe. In the case of the single-crystal, the field was applied parallel to the *ab*-plane. Neutron diffraction experiments were performed on both samples at the high-flux reactor of the ILL (Grenoble, France). NPD patterns on the powder sample were collected using the high intensity diffractometer D1B ( $\lambda=2.52$  Å) between 10 and 500 K. The homogeneity and orientation of the crystal was assessed using Orient Express. Further temperature dependent reciprocal space maps were recorded using the Cyclops neutron Laue diffractometer between 50 and 300 K. Finally, additional measurements were carried out at the D9 four-circle neutron diffractometer ( $\lambda=0.836$  Å). *q*-scans were previously collected along specific directions to assess the presence of the different magnetic propagation vectors. Several magnetic reflections associated to them were monitored between 50 K and RT using a displax cryostat. Finally, in addition to the above mentioned large set of nuclear Bragg reflections, two sets of 408 and 260 magnetic Bragg reflections were collected at 50 K respectively for the two magnetic propagation vectors  $\mathbf{k}_1=(1/2, 1/2, 1/2)$  and  $\mathbf{k}_3=(1/2, 1/2, 0)$  applied to the *P4mm* crystal cell.

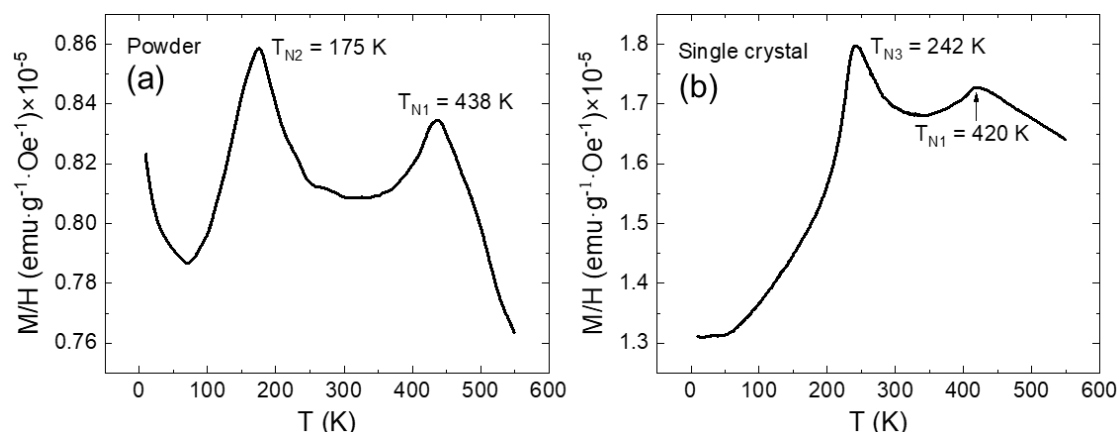


Figure 7.5.  $\text{YBaCuFe}_{0.95}\text{Mn}_{0.05}\text{O}_5$ : magnetic susceptibility curves (2 kOe, FC) for (a) the polycrystalline powder and (b) the single crystal samples. Transition temperatures are indicated in the curves.

Figure 7.5 displays the magnetic susceptibility for the two samples (under FC condition) from 10 to 550 K. Two antiferromagnetic transitions can be observed in both samples. The highest transition, corresponding to the collinear  $\mathbf{k}_1=(1/2, 1/2, 1/2)$  phase is peaked at  $T_{N1}=438$  K (polycrystalline powder) and 420 K (single-crystal). The lowest transition temperature deviates around 70 K comparing both samples but, as we will show below, this low-temperature transition corresponds to different spin configurations in our polycrystalline powder and single-crystal samples ( $T_{N2}$  and  $T_{N3}$  indicated in the figure).

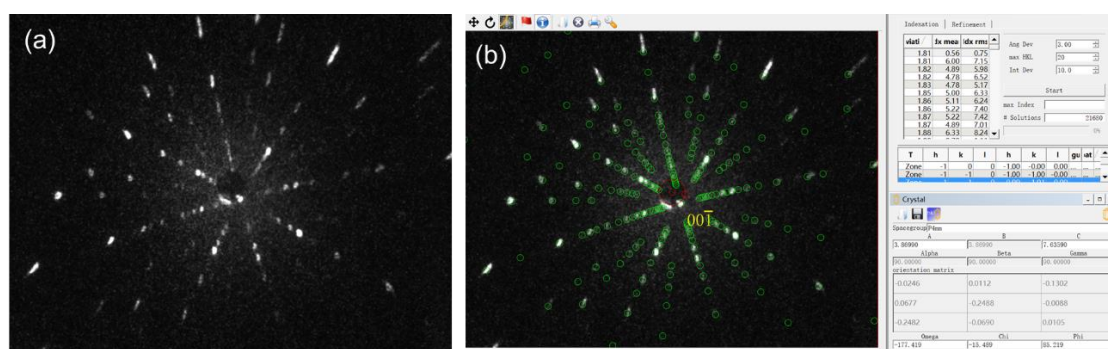


Figure 7.6. (a) Laue diffraction pattern collected on the Orient Express (ILL); (b) The simulation of the pattern (a) showing the  $c$  axis of the  $\text{YBaCuFe}_{0.95}\text{Mn}_{0.05}\text{O}_5$  single-crystal perpendicular to the detector.

Figure 7.6 shows the Laue diffraction pattern collected on the Orient Express (ILL), corresponding to the  $c$  axis of the crystal perpendicular to the detector. Furthermore, the

crystal was measured using the Cyclops Laue diffractometer between 50 and 300 K (using a displax cryostat) as shown in the Figure 7.7. These measurements enabled us to dynamically monitor the changes basically in the magnetic reflections.

In Figure 7.7(a) we present a section of the neutron Laue diffraction pattern collected on Cyclops at 50 K. In the Laue image the nuclear reflections are shown in white. The magnetic ones are shown in red (those corresponding to  $\mathbf{k}_1=(1/2, 1/2, 1/2)$  translation symmetry) and yellow (for  $\mathbf{k}_3=(1/2, 1/2, 0)$  propagation vector). The magnetic reflections indexed in the Figure 7.7(a) were integrated in order to obtain integrated neutron profiles along the curve shown in the Figure 7.7(a) across the lowest phase transition in the crystal ( $T_{N3}=242$  K). Figure 7.7(b) compares the neutron profiles from the crystal obtained from Cyclops at three temperatures (300, 200 and 50 K), showing a non-conventional magnetic behavior. Interestingly, the ICM satellites

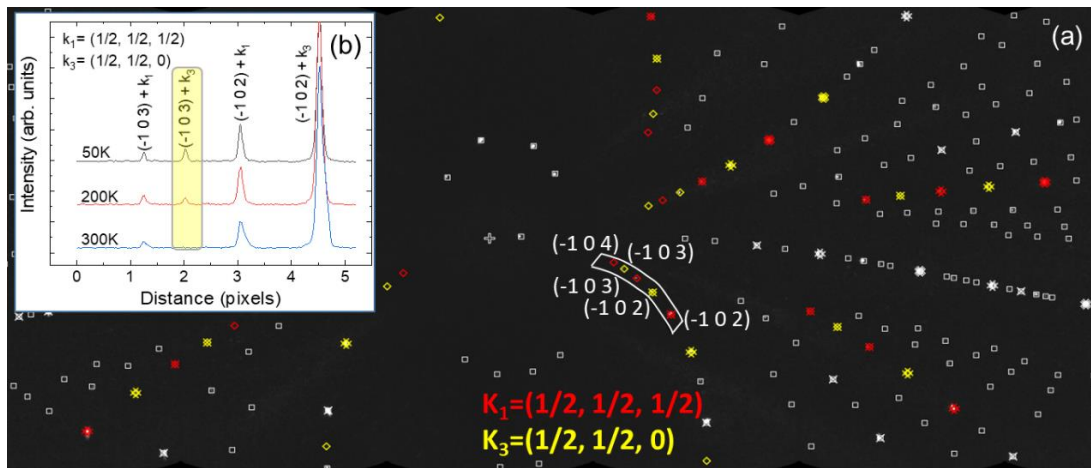


Figure 7.7. The  $\text{YBaCuFe}_{0.95}\text{Mn}_{0.05}\text{O}_5$  single crystal. (a) Section of Laue diffraction pattern collected on Cyclops at 50 K showing the indexation of the nuclear reflections (in white) and the magnetic ones with  $\mathbf{k}_1=(1/2, 1/2, 1/2)$  and  $\mathbf{k}_3=(1/2, 1/2, 0)$  propagation vectors (in red and yellow, respectively). (b) Comparison of the integrated profiles (along the curve indicated in the Laue picture) at three different temperatures.

characteristic of the spiral phase have been suppressed and are not observed. Instead, the new translational symmetry appearing upon cooling below  $T_{N3}$  is the CM wave-vector  $\mathbf{k}_3=(1/2, 1/2, 0)$ . Therefore, our preliminary magnetic characterization of the crystal revealed a behavior qualitatively different to the analogous powder sample

(same composition) prepared in polycrystalline form, which was previously studied using the neutron powder diffractometer D1B. In the next paragraphs we present a comparison of the different magnetic behavior found in the single crystal and polycrystalline samples and our conclusions to explain the origin of the unexpected differences.

A comparison of the main magnetic features revealed by neutron experiments is shown in Figure 7.8. The *left* panel in the figure (7.8a, b and c) corresponds to the polycrystalline powder sample and the *right* panel (7.7d and e) to the single crystal.

***Magnetic transitions in the polycrystalline sample:***

Temperature-dependent neutron diffraction measurements were carried out on the polycrystalline powder sample in the range 10 to 500 K. Figure 7.8(a) plots a Q-T projection of neutron diffracted intensities around the main  $(1/2, 1/2, 1/2)$  magnetic reflection. In agreement with the susceptibility, the two transitions correspond to (i) the CM phase which appears at the onset temperature  $T_{N1}$ , with propagation vector  $\mathbf{k}_1=(1/2, 1/2, 1/2)$ , and (ii) the ICM phase, showing up at  $T_{N2}$  ( $=T_S$ , the spiral transition) with characteristic split satellite reflections and propagation vector  $\mathbf{k}_2=(1/2, 1/2, 1/2\pm q)$ . An ICM magnetic modulation  $q=0.102$  r.l.u. was found at the lowest temperature. Figure 7.8(b) illustrates the neutron powder diffraction pattern collected at 50 K on D1B that shows the dominant ICM magnetic reflections from the spiral order appearing in the low-angle region. A small residual amount of the high-temperature CM collinear phase is also observed, indicating that the CM-ICM transformation was not complete. The evolution of the average ordered magnetic moments for the CM and ICM phases against temperature is depicted in Figure 7.8(c). The magnetic moments here were refined imposing  $m(\text{Fe})=m(\text{Cu})$ , and referred to the full amount of sample.

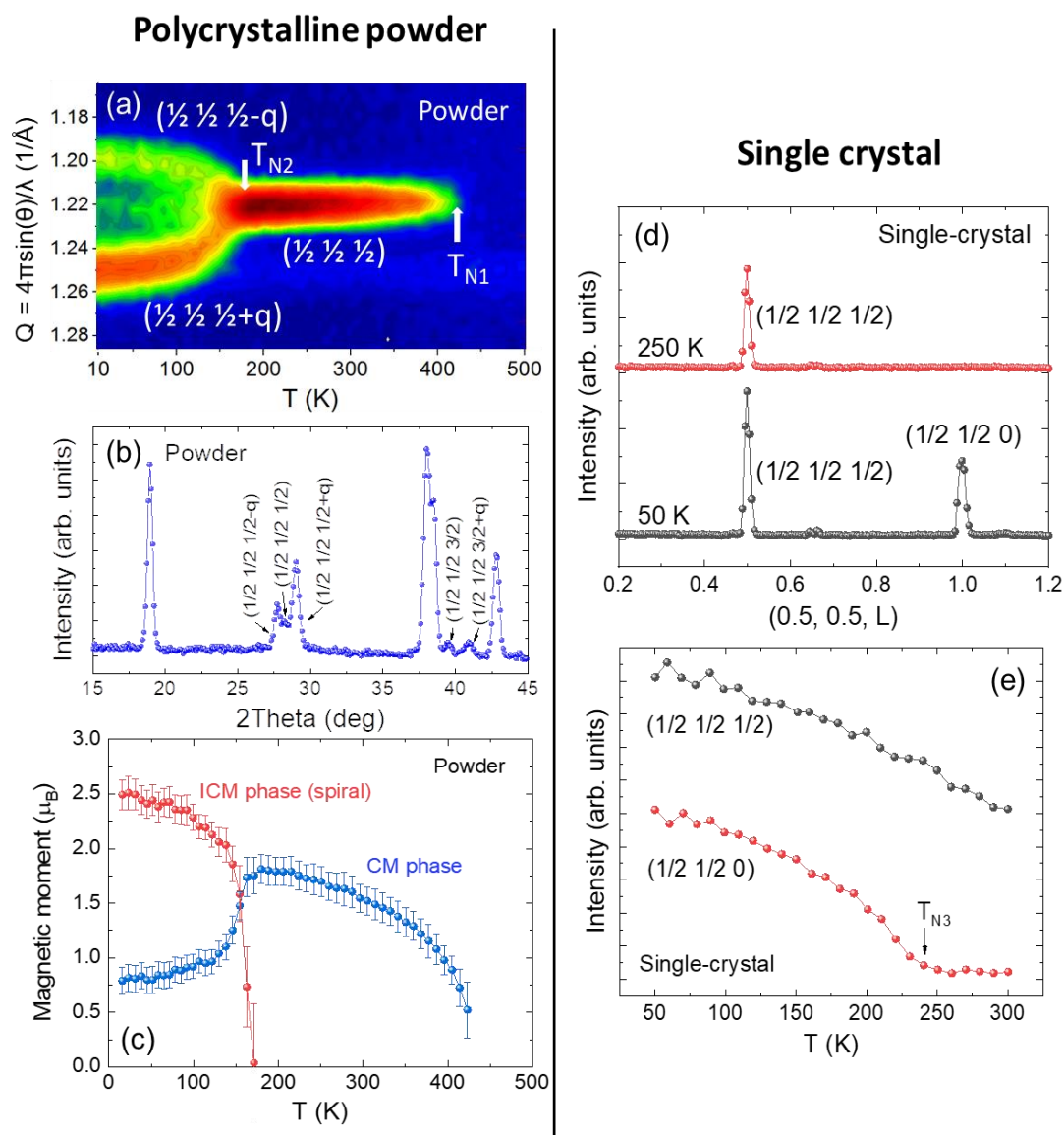


Figure 7.8.  $\text{YBaCuFe}_{0.95}\text{Mn}_{0.05}\text{O}_5$ . [Left panel] *Polycrystalline sample*: (a) Q-T projection of the temperature dependence for the neutron-diffracted intensities around  $(\frac{1}{2} \frac{1}{2} \frac{1}{2})$  reflection for the powder sample; (b) Low-angle region of the neutron diffraction pattern recorded at 50 K for the powder sample; (c) T-dependence of the (average) ordered magnetic moments associated to the CM and ICM phases for the powder sample. [Right panel] *single crystal*: (d)  $Q_L$ -scans in the single crystal performed along the  $(0.5, 0.5, L)$  line ( $0.2 < L < 1.2$ ). Comparison of the scans recorded at 50 K and 250 K (D9); (e) Temperature dependence of the neutron integrated intensities for the  $(\frac{1}{2} \frac{1}{2} \frac{1}{2})$  [ $\mathbf{k}_1$ ] and  $(\frac{1}{2} \frac{1}{2} 0)$  [ $\mathbf{k}_3$ ] magnetic reflections.

### ***Magnetic transitions in the single crystal:***

As mentioned above, the magnetic behavior is however remarkably different for the single crystal. Two  $Q_L$ -scans were performed at 50 K and 250 K on D9 along the line  $(0.5, 0.5, L)$  (in the range  $0.2 < L < 1.2$ ) with the purpose of tracing the possible

magnetic reflections, as shown in Figure 7.8(d). In the low temperature scan, two types of CM reflections from dissimilar collinear magnetic phases were detected, indexed according to the wave-vectors  $\mathbf{k}_1=(1/2, 1/2, 1/2)$  and  $\mathbf{k}_3=(1/2, 1/2, 0)$ . Warming the crystal, at 250 K, only  $\mathbf{k}_1$  reflections could be detected, indicating that the ordering temperature for the second collinear phase ( $\mathbf{k}_3$ ) occurs below 250 K. This was also confirmed by the T-evolution of the neutron-diffracted intensities for the two magnetic reflections as shown in Figure 7.8(e). Upon warming from 50 to 300 K, both reflections decrease, but the reflection coming from  $\mathbf{k}_3$  vanishes before 250 K, around the transition unveiled in the susceptibility at  $T_{N3}\approx 242$  K. In Figure 7.8(d) a tiny apophysis was observed around (0.5 0.5 0.65) which probably comes from a tiny misaligned domain. A main result of the neutron study was the lack of the ICM (spiral) magnetic phase in the single crystal sample. Furthermore, the anisotropy of the two CM collinear spin configurations observed in the crystal was carefully investigated and the details of the two magnetic orders were unveiled.

(G-point of the Brillouin zone)

The neutron magnetic data collections made on the crystal at 50 K enabled us to fully determine the spin configurations but also the orientation of the spins respect to the tetragonal unit cell for the two CM collinear phases. No previous reports were found in the literature concerning the orientation of the moments in the tetragonal  $\mathbf{ab}$  plane for this family of multiferroics, due to the inherent limitations to the *neutron powder diffraction*. Fortunately, most of these intrinsic limitations can be overcome disposing of crystals and performing single-crystal neutron magnetic diffraction. In this way, the large set of magnetic reflections on the single crystal enables us to refine the orientation of the spins in the two successive collinear phases appearing at  $T_{N1}=420$  K and  $T_{N3}=242$  K. The spin orientation can be defined by the polar angles  $\theta$  and  $\varphi$ . The former measures the angular distance of the spin to the  $c$  axis ( $\theta$ ), and  $\varphi$  measures the distance of the spin component in the  $\mathbf{ab}$  plane respect to the  $a$  axis. In addition, the amplitudes of the ordered magnetic moments at the nominally Fe and Cu sites were refined independently,



without constraints, but referred to the total volume of the crystal. The magnetic refinements unambiguously converged to the same solution, independently of the proposed initial values. The best agreements were found for the collinear spin configurations summarized in the Table 7.2, referred to the propagation vectors  $\mathbf{k}_1 = (1/2, 1/2, 1/2)$  and  $\mathbf{k}_3 = (1/2, 1/2, 0)$ . Ordered moments in Table 7.2 are referred to the total volume of the crystal. However, the magnetic evolution exposed in Figure 7.8(e) indicates that very likely the two magnetic phases develop in distinct regions of the crystal. There are no signs of a partial transformation of the AF1 regions ( $\mathbf{k}_1$ ) into the AF3 ( $\mathbf{k}_3$ ) across  $T_{N3}$ .

**Table 7.2.** Refined spin configurations, magnetic moments and orientation (in polar coordinates) for the two magnetic collinear phases  $\mathbf{k}_1$  and  $\mathbf{k}_3$  observed in the single crystal at 50 K.

50 K	m(Fe) ( $\mu_B$ )	m(Cu) ( $\mu_B$ )	$\theta$ (deg)	$\varphi$ (deg)	$R_F$	$R_{F^2W}$	$\chi^2$
$\mathbf{k}_1 = (1/2, 1/2, 1/2)$	2.23 (3)	-0.70 (4)	70 (2)	-89 (2)	10.8	18.7	13.0
$\mathbf{k}_3 = (1/2, 1/2, 0)$	0.74 (25)	-1.10 (23)	68 (3)	-26 (3)	13.7	22.0	15.5

**AF1 collinear phase:** For the AF1 collinear phase ( $\mathbf{k}_1$ ), the observed and calculated squared structure factors are plotted in Figure 7.9(a), and the spin arrangement is depicted in Figure 7.9(b) and (c). It is noteworthy that:

(i) We got a very different average magnetic moment at the upper and lower pyramids of the chemical unit cell. 2.23 (3)  $\mu_B$  at the nominal Fe site versus 0.70 (4)  $\mu_B$  at the nominal Cu pyramid. The m(Fe)/m(Cu) ratio found is 3.19. Notice that these are ordered moments averaged over the total crystal volume but we don't know the specific volume proportion occupied by the AF1 phase ( $\mathbf{k}_1$ ).

(ii) Orientation of the moments. As for the polar angles describing the spin orientation, the refined  $\theta$  angle is 70° (2) (see Figure 7.9(b)), a value very similar to the one determined by powder neutron diffraction in the analogous  $YBaCuFe_{0.95}Mn_{0.05}O_5$  polycrystalline sample (with the same composition, see Chapter 4). Interestingly, with regard to the spin orientation within the  $\mathbf{ab}$  plane, the refinements unambiguously lead

to  $\varphi \approx -89^\circ$  (2) (see Figure 7.9(c)), indicating that magnetic moments order parallel to the  $b$  axis. Solutions along the diagonal direction or parallel to  $a$  in the  $\mathbf{ab}$  plane lead to clearly worse agreement factors. Remind that determining the spin orientation in a tetragonal chemical cell is not possible from neutron powder diffraction. Schematic projections of the magnetic configuration in the CM  $\mathbf{k}_1$  phase are shown in Figure 7.10.

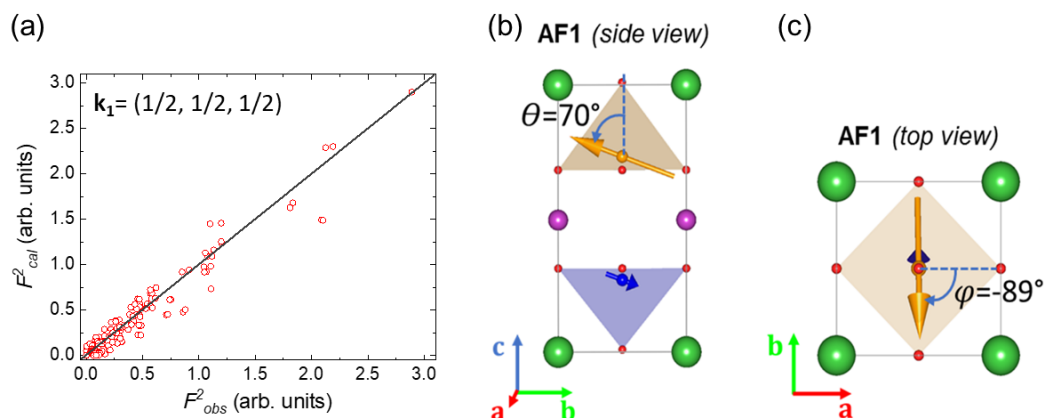


Figure 7.9. (a) [Single-crystal] Agreement plot of the refinement on magnetic reflections of the AF1 collinear phase  $\mathbf{k}_1$  collected at 50 K ( $\lambda=0.836$  Å). The calculated squared structure factor is plotted against the experimental ones; (b) The refined angle between the magnetic moment and the  $c$  axis; (c) Top view of the unit cell showing the refined angle of the magnetic moment in the  $\mathbf{ab}$  plane. In the unit cell, only the majority atoms are shown in the respective pyramid (Brown: Fe; Blue: Cu).

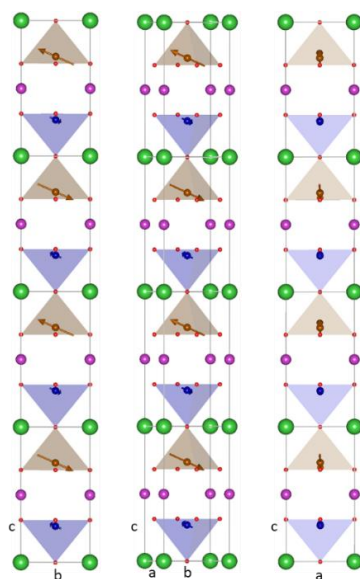


Figure 7.10. Three projections of the refined  $\mathbf{k}_1$  CM magnetic order at 50 K (AF1 phase). The projections show that in the  $\mathbf{ab}$  plane, the magnetic moment is parallel to the  $b$  axis.

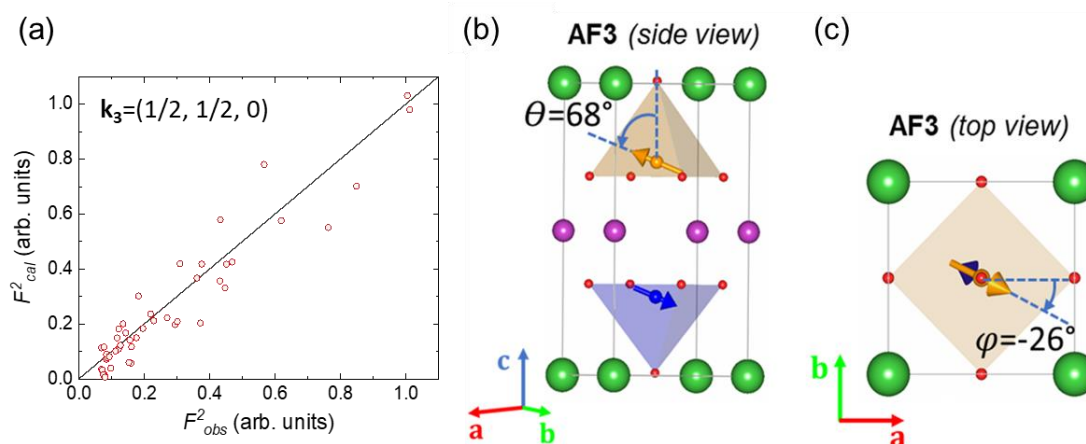


Figure 7.11. (a) [Single-crystal] Agreement plot of the refinement on magnetic reflections of the AF3 collinear phase  $\mathbf{k}_3$  collected at 50 K ( $\lambda=0.836$  Å). The calculated structure factor is plotted against the experimental ones; (b) Side view of the unit cell showing the refined angle between the magnetic moment and the  $c$  axis; (c) Top view of the unit cell showing the refined angle of the magnetic moment in the  $ab$  plane. In the unit cell, only the majority atoms are shown in the respective pyramid (Brown: Fe; Blue: Cu)

**AF3 collinear phase:** For the second collinear phase, with  $\mathbf{k}_3=(1/2, 1/2, 0)$ , the magnetic anti-translation for successive cells along  $c$  is suppressed ( $k_z=0$ ). The agreement plot of the experimental against the calculated intensities is shown in the Figure 7.11(a). The details for this spin configuration were summarized in Table 7.2. It is worth underlining the following points:

(i) Notice that the values obtained for the average ordered magnetic moments are low but, most interesting, the values at the two pyramids are much more similar between them than for the  $\mathbf{k}_1$  phase. For the AF3 phase we obtain  $m(\text{Fe})=0.74$  (25)  $\mu_B$  and  $m(\text{Cu})=-1.10$  (23)  $\mu_B$ , and hence the ratio  $m(\text{Fe})/m(\text{Cu})\approx 0.67$  is markedly lower than the AF1 phase. This result provides a strong evidence that this secondary phase appears in regions of the crystal presenting very large chemical disorder. Namely, it comes from regions where the distribution of Fe and Cu is quite disordered. At this point, remind that we proved in chapter 4 that the addition of Mn atoms to Fe sites favors the chemical disorder in the system [47]. Given the high level of Fe/Cu cationic order found in this crystal, we are led to the conclusion that the AF3 phase comes from the regions with a higher presence of Mn atoms.

(ii) Orientation of the moments. According to Table 7.3, the orientation of the moments respect to the  $c$  axis is within errors identical to the AF1 phase ( $\theta \approx 68^\circ$  (3)). Hence, the inclination of the easy-axis is not modified when comparing the two collinear phases. However, the conclusion is different regarding the orientation of the moments in the  $\mathbf{ab}$  plane. A  $\varphi$  angle of  $-26(3)^\circ$  indicates that the magnetic moments in the  $\mathbf{ab}$  plane are not aligned along the  $b$  nor the  $a$  axis or the diagonal. Several views showing the tilting of the magnetic moments respect to the  $c$  axis and their orientation within the  $\mathbf{ab}$  plane are shown in the Figure 7.11(b) and (c).

(iii) In addition, Figure 7.12 shows three projections of the refined AF3 magnetic phase including four unit cells to illustrate the translational symmetry along the  $c$ -direction. Notice that in the AF3 phase the coupling between the spins of a bipyramid is antiferromagnetic. This is in contrast to the AF1 order, where the spins sharing a bipyramid are ferromagnetically coupled in virtue of the ferromagnetic  $\text{Fe}^{3+}\text{-O-Cu}^{2+}$  exchange interaction along- $c$ . The presence of chemical disorder substitutes the weak ferromagnetic Fe-O-Cu bond by the strong AFM Fe-O-Fe pair. Much weaker are the  $\text{Fe}^{3+}\text{-O-Mn}^{3+}$  (or  $\text{Mn}^{3+}\text{-O-Mn}^{3+}$ ) AFM coupling within the bipyramids.

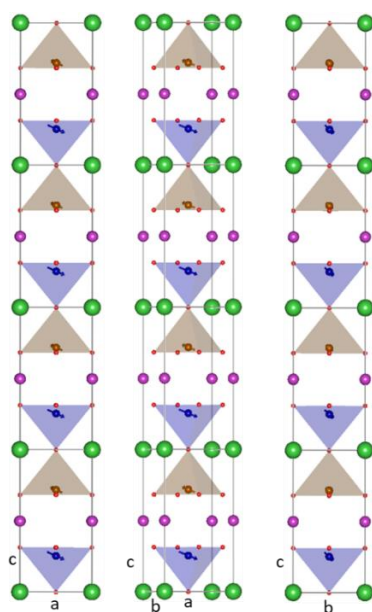


Figure 7.12. Three projections of the refined  $\mathbf{k}_3$  CM magnetic order at 50 K. The projections show that in the  $\mathbf{ab}$  plane, the magnetic moment deviates from  $a$  or  $b$  axis.

## 7.4 Summary and conclusions

In this work we have prepared and characterized the candidate chiral multiferroic compound  $\text{YBaCuFe}_{0.95}\text{Mn}_{0.05}\text{O}_5$  in two different forms: (i) as a polycrystalline solid synthesized by solid-state reaction (last cooling rate of 300 K/h) and (ii) as a high-quality single crystal grown by a modified TSFZ technique. A comparative study has been performed that included neutron diffraction measurements in both specimens. We have revealed very different magnetic properties in both samples. Neutron diffraction results disclosed the onset of the CM collinear and ICM spiral phases at, respectively 438 K ( $\mathbf{k}_1=(1/2, 1/2, 1/2)$ , AF1) and 175 K ( $\mathbf{k}_2=(1/2, 1/2, 1/2\pm q)$  with  $q=0.102$  r.l.u. for the polycrystalline sample. In contrast to the absence of the incommensurate chiral phase in the crystal, where the collinear phase (AF1) persisted down to the lowest temperature. Moreover, a second collinear phase (AF3) with  $\mathbf{k}_3=(1/2, 1/2, 0)$  develops in the crystal below  $T_{N3}\approx 242$  K.

Additionally, the B-site disorder was quantified, obtaining that the Fe/Cu chemical disorder is  $\sim 30\%$  for the powder sample and only  $\sim 11\%$  for the single crystal. Therefore, the TSFZ method used to grow the crystal produced a layered perovskite with a much lower level of Fe/Cu cationic order at the B/B' sites, compared to the powder sample. Thus, the qualitatively different magnetic properties should be attributed to the marked differences in the level of chemical disorder, strongly influenced by the preparation method, confirming its extraordinary relevance for the chiral and multiferroic potential properties of this family of perovskites. These results give thus strong support to the “*order by disorder*” theoretical models intended to justify the high-temperature stability of the non-collinear (spiral) incommensurate phase in these compounds.

Additional conclusions were also extracted from the study of the two coexisting magnetic collinear phases with  $\mathbf{k}_1=(1/2, 1/2, 1/2)$  and  $\mathbf{k}_3=(1/2, 1/2, 0)$ . In the first, the coupling of the spins sharing a bipyramid is ferromagnetic, while in the second spins are coupled antiferromagnetically. The average ordered moments at the Fe and Cu sites in AF3 are quite similar, in contrast to AF1. Therefore, the AF3 phase comes from

regions of the crystal presenting very high chemical disorder, favored by the presence of Mn. The regions of the crystal presenting AF1 order exhibit low levels of chemical disorder. In both magnetic phases of the crystal the orientation of the moments out of the **ab** plane is the same ( $\theta \approx 70^\circ$ , as in the sample prepared in polycrystalline form). This single crystal neutron diffraction study has enabled identify the orientation of the moments within the **ab** plane. For the **k<sub>1</sub>** phase, the magnetic moment is parallel to the **b** axis, the tetragonal symmetry being broken by the magnetic order. The diagonal direction is discarded. In the **k<sub>3</sub>** phase, the moment orientation in the plane adopts an angle  $\varphi \approx -26^\circ$  respect to the **a** axis. These results provide one of the first complete description of the structural (including the characterization of the level of chemical disorder) and magnetic structures on a single crystal of the YBCFO family of potential high-Tc multiferroics.

More work is needed in the future considering the lack of ICM phase in this Mn doped YBCFO single crystal. On one hand, the single crystal growth conditions should be properly modified to obtain a crystal sample with higher chemical disorder and a magnetic spiral phase as well; on the other hand, a tilted (not parallel to the **ab** plane) magnetic spin configuration is expected in the spiral phase, which favors the generation of spontaneous polarization according to the DM interaction.



# Chapter 8

## Conclusions and outlook

### 8.1 Conclusions

Apart from CuO (spiral and ferroelectric in a very narrow range), YBaCuFeO<sub>5</sub> is likely the only known potential spiral multiferroic (at zero field) with chiral magnetic order above 200 K. In this Thesis work, we have explored and investigated different strategies to tune and optimize the high-temperature chiral magnetic properties of this family of layered perovskites, structurally simple in appearance but very complex due to the presence of cation disorder. In fact, the exceptional stability of the chiral magnetic order in the YBaCuFeO<sub>5</sub> layered structure requires a non-conventional mechanism of the type “*spiral order by disorder*”. In this candidate chiral multiferroic compound we have studied the impact of selected cationic substitutions in materials prepared in polycrystalline and single crystal forms. Our strategy to upgrade the chiral magnetic properties of this AA'BB'O<sub>5</sub> oxygen deficient perovskite has been based on modifications of both, structural and physical elements in the system (such as the magnetic moment or the magnetic coupling, the spin-orbit coupling or the single-ion magnetic anisotropy) through cationic substitutions at the trivalent Fe and divalent Cu sites, selectively. Many compounds of the families YBa(Cu,B)FeO<sub>5</sub> (B: Co and Mg) and YBaCu(Fe,B')O<sub>5</sub> (B': Cr and Mn) were prepared in powder form or as single crystal. They were thoroughly analyzed and characterized combining a variety of



complementary experimental techniques: magnetometry, X-ray spectroscopies, synchrotron X-ray and neutron diffraction. Investigating their structural, electronic and magnetic properties. The corresponding conclusions obtained have been listed in the last section of each chapter. However, we have considered convenient to provide an overall view of the major findings, as summarized below, in this brief chapter.

- For the  $\text{YBaCuFe}_{1-x}\text{Cr}_x\text{O}_5$  family, it was not possible to stabilize trivalent  $\text{Cr}^{3+}$  in pyramidal  $\text{Cr}^{3+}\text{O}_5$  coordination. The XAS measurements indicate that all the Cr atoms were oxidized to  $\text{Cr}^{6+}$  under the sample preparation route employed. This is the valence of Cr in one of the detected secondary phases,  $\text{BaCrO}_4$ , confirming the conclusions from XAS. Nearly all Cr atoms are incorporated to the  $\text{BaCrO}_4$  rather than going to the trivalent Fe site in the  $\text{YBaCuFeO}_5$  structure.
- The previously known procedure to tune the level of Fe/Cu disorder in the structure was the cooling rate. We demonstrated an alternative way for increasing Fe/Cu disorder (that controls the level of frustration) without varying the cooling rate. Of particular importance for getting disordered single-crystals. In  $\text{YBaCuFe}_{1-x}\text{Mn}_x\text{O}_5$ , the Fe/Cu disorder was increased by Mn doping from  $n_d \sim 23\%$  in non-doped samples up to  $n_d \sim 33\%$  applying identical preparation conditions and cooling rates.
- Isovalent cationic substitutions (Co, Mg) of the divalent B-site in the  $\text{YBaCu}_{1-x}\text{B}_x\text{FeO}_5$  layered perovskite did not produce modifications in the Fe/Cu level of disorder in samples obtained keeping fix the cooling rate.
- The T-x magnetic phase diagrams of  $\text{YBaCu}_{1-x}\text{B}_x\text{FeO}_5$  for the B site substitutions Co/Mg have been built up to the paramagnetic state from NPD data and magnetometry. Co and Mg were found to be isovalent substitutions. A huge increase of the stability of the spiral order ( $T_S$ ) was obtained with small Co doping. Both Co and Mg dopings preserve a linear  $T_S$ - $q_S$  relationship but coefficients have been tuned. A triple point was achieved with a maximum spiral transition temperature  $T_S \approx 360$  K, well above RT. We have demonstrated the possibility to effectively tune the spiral stability (by B-site divalent doping) through the

contraction of the bipyramidal thickness  $d_2$ . The strategy was based on acting on the  $\text{Cu}^{2+}$  J-T splitting and the long apical Cu-Oa distance. The strong J-T splitting between basal and apical distances at  $\text{Cu}^{2+}$  sites was severely reduced by Co and Mg doping, increasing frustration effects.

- On another hand, the impact of introducing divalent Co and Mg at Cu sites strongly differs when considering magnetic phase competition and magnetic anisotropy. Co doping favors the formation of the new commensurate  $\mathbf{k}_3$  phase due to the AFM  $\text{Co}^{2+}/\text{Fe}^{3+}$  and  $\text{Co}^{2+}/\text{Cu}^{2+}$  pairs in the bipyramids. Beyond the multi-critical point, AF3 and AF1 orders compete and the second progressively gives way to the first. On the contrary, the AF3 collinear order is not favored by non-magnetic  $\text{Mg}^{2+}$  ions. No signs of the AF3 order were detected in the phase diagram for Mg family, including the critical phase separation region after the triple point.
- The evolution of the easy axis and the magnetic anisotropy was investigated in detail as a function of temperature and doping. The spiral orientation may critically determine the ferroelectric and magnetoelectric behavior in these systems. The T-dependence of the collinear ( $\theta_{col}$ ) and the chiral easy axis ( $\theta_s$ ) remains, respectively, practically constant for a given composition. Inserting divalent Co or Mg at the Cu site does not modify the collinear easy axis. Interestingly, concerning the spiral orientation, the impact is different for both. No changes on  $\theta_s$  occur with non-magnetic  $\text{Mg}^{2+}$ . Remarkably, the tilting of the magnetic spiral plane decreases strongly with  $\text{Co}^{2+}$  presenting anisotropic orbital occupation and an appreciable orbital component. We showed a systematic reorientation of the magnetic spiral plane increasing Co, changing from a more helical spin order ( $\mathbf{k} // \mathbf{Q}$ ) into a more cycloidal spin order ( $\mathbf{k} \perp \mathbf{Q}$ ). The most cycloidal spiral found is as well the most thermally stable ( $T_S \approx 360$  K) (in contrast to the behavior shown for B'-doped Mn-YBCFO samples).
- The largest incommensurability of the cycloidal spiral reported in these layered perovskites ( $q_s \approx 0.1918$  (2) r.l.u.) was obtained at the triple point of the Mg-doped

YBCFO family. We disclosed the possibility of tuning the modulation of the cycloidal order by doping, keeping the transition temperature  $T_S$  around its maximum value ( $\approx 360$  K).

- As for the  $\text{YBaCuFe}_{1-x}\text{Mn}_x\text{O}_5$  family, the trivalent substitution (Fe site) with  $\text{B}'=\text{Mn}$  was found to be non-isovalent. The phase diagram totally differs to the previous divalent B substitutions. The stability of the spiral order decreases with this doping, and the linear correspondence between  $T_S$  and the spiral modulation ( $q_S$ ) is lost. We have disclosed the absence of a triple point in the corresponding phase diagram. As for the  $\text{YBaCuFe}_{1-x}\text{Mn}_x\text{O}_5$  family, the tendency to a tetravalent state of Mn was unveiled and explained. The system tends to preserve the J-T deformation around  $\text{Cu}^{2+}$  sites by avoiding the presence of J-T distorted  $\text{Mn}^{3+}\text{O}_5$  pyramids, in order to compensate the high-energy penalty caused by the lattice deformation in the  $\text{CuMnO}_9$  units. The presence of extra oxygen was quantitatively evidenced.
- A quality  $\text{YBaCuFe}_{0.95}\text{Mn}_{0.05}\text{O}_5$  single crystal was grown by TSFZ. In contrast to a powder sample of the same composition, the ICM chiral phase is absent in the crystal, and substituted by AF3 order, due to a minor level of Fe/Cu chemical disorder (only  $\sim 11\%$ ).
- Collinear AF1 and AF3 phases persist down to the base temperature, with identical orientation of the moments out of the **ab** plane ( $\theta \approx 70^\circ$ ). The in-plane component, however, was found parallel to the **b** axis for the AF1 phase, and it adopted an angle  $\varphi \approx -26^\circ$  with respect to the **a** axis in the AF3 phase

## 8.2 Outlook and future work

Magnetoelectric multiferroic materials and spiral frustrated magnets have attracted considerable attention in the scientific community over the decades, by virtue of its exotic and fascinating properties and the potential coupling between the ferroelectricity and magnetism, which hold engaging promise for exploration in both fundamental

physics and applications perspectives. A bottleneck being the low transition temperatures of practically all known chiral (spiral) magnetoelectric multiferroics. This Thesis work has focused on the upgrade of the cycloidal magnetic properties of the high-temperature multiferroic candidate YBaCuFeO<sub>5</sub>. The author expects this work will help to define and inspire new design strategies in these and other anisotropic functional magnets able to adopt chiral and cycloidal magnetic phases at high temperatures.

Further studies are required to assess the impact of B/B'-site disorder on the phase diagrams revealed in present work, as they were built here keeping fix the level of disorder. More precise and systematic studies are necessary to better understand the role of disorder and of the layered structure of YBaCuFeO<sub>5</sub> on the so-called "*spiral order by disorder*" mechanism. A possible model for this non-conventional mechanism has been developed by Scaramucci and co-workers, but the interplay between disorder, structural geometry, stability and features of the competing chiral (cycloidal versus helicoidal) and non-chiral magnetic orders needs to be better explored and compared to the predictions of the models. One of the most critical issues are the intrinsic limitations of neutron powder diffraction to fully capture the details of these complex magnetic phases. The fabrication and investigation of single crystals is imperative, and it will allow studying the magnetoelectric response of this family under a variety of conditions. Very little is known yet about the response of the spiral to magnetic and electrical fields. From our understanding of the present experimental results, a huge impact on the properties is anticipated by the application of pressure or by the dimensions of the substrates in epitaxial thin films and heterostructures.

Our results open the door to engineering the anisotropy of the cycloidal spiral and of the chirality of the material, both having a great impact on the magnetoelectric coupling. It also opens the door to the combination of selected A- and B-site substitutions. Some could help to bring about a depression of the conductivity. Some of these research lines are already being developed in our group CMEOS during last years, in parallel to the work presented in this Thesis.



# Publications

- Tuning the tilting of the spiral plane by Mn doping in YBaCuFeO<sub>5</sub> multiferroic.  
Xiaodong Zhang, Arnau Romaguera, Oscar Fabelo, Francois Fauth, Javier Herrero-Martín and José Luis García-Muñoz.  
**Acta Materialia**, 206, 2021. doi: 10.1016/j.actamat.2020.116608.
- Magnetic properties of a highly ordered single crystal of the layered perovskite YBaCuFe<sub>0.95</sub>Mn<sub>0.05</sub>O<sub>5</sub>.  
Xiaodong Zhang, Arnau Romaguera, Felip Sandiumenge, Oscar Fabelo, Javier Blasco, Javier Herrero-Martín and José Luis García-Muñoz.  
**Journal of Magnetism and Magnetic Materials**, 551, 2022. doi: 10.1016/j.jmmm.2022.169165.
- Huge stabilization of a cycloidal order in Co-doped YBaCuFeO<sub>5</sub>.  
Xiaodong Zhang, Arnau Romaguera, Oscar Fabelo, Javier Herrero-Martín and José Luis García-Muñoz. (manuscript in preparation)
- Frustrated Jahn-Teller competition in Mn-doped YBaCuFeO<sub>5</sub> investigated by x-ray absorption spectroscopy and neutron diffraction.  
Xiaodong Zhang, Javier Herrero-Martín, Arnau Romaguera, Felip Sandiumenge, Oscar Fabelo and José Luis García-Muñoz. (manuscript in preparation)
- Phase diagram and stability of the chiral magnetic phase in Mg-doped YBaCuFeO<sub>5</sub>.  
Xiaodong Zhang, Arnau Romaguera, Oscar Fabelo, Javier Herrero-Martín and José Luis García-Muñoz. (manuscript in preparation)
- Chiral magnets by disorder: its role on the high-temperature magnetic spiral in the YBaCuFeO<sub>5</sub> perovskite.  
Arnau Romaguera, Xiaodong Zhang, Oscar Fabelo, Francois Fauth, Javier Blasco and José Luis García-Muñoz.  
**Physical review research**, 2022. (submitted)
- Is there a magnetic spiral in YBaCuFeO<sub>5</sub>?  
Arnau Romaguera, Xiaodong Zhang, Oscar Fabelo, Javier Herrero-Martín and José

Luis García-Muñoz. (manuscript in preparation)

- Magnetic inversion symmetry breaking and spin reorientation in  $\text{Tb}_2\text{MnNiO}_6$ : A polar strong ferromagnet.

José Luis García-Muñoz, Javier Blasco, Xiaodong Zhang, Oscar Fabelo.

**Physical review B**, 99, 2019. doi: 10.1103/PhysRevB.99.184444.

- Ferromagnetic metallic Sr-rich  $\text{Ln}_{1/2}\text{A}_{1/2}\text{CoO}_3$  cobaltites with spontaneous spin rotation.

Jessica Padilla-Pantoja, Arnau Romaguera, Xiaodong Zhang, Javier Herrero-Martín, Francois Fauth, Javier Blasco and José Luis García-Muñoz.

**Physical review B**, 104, 2021. doi: 10.1103/PhysRevB.104.054411.

# Bibliography

- [1] M. Fiebig, “Revival of the magnetoelectric effect,” *J. Phys. D. Appl. Phys.*, vol. 38, no. 8, 2005, doi: 10.1088/0022-3727/38/8/R01.
- [2] H. A., “On the Electric Effect of Rotating a Dielectric in a Magnetic Field,” *Phil. Trans.R.Soc*, vol. 2004, p. 129, 1905.
- [3] P. Curie, “On symmetry in physical phenomena, symmetry of an electric field and a magnetic field,” *J.Phys.Theor.Appl.*, vol. 3, pp. 393–415, 1894, doi: 10.1051 / jphystap: 018940030039300.
- [4] P. Debye, “Bemerkung zu einigen neuen Versuchen über einen magneto-elektrischen Richteffekt,” *Z.Physik*, vol. 36, pp. 300–301, 1926, doi: <https://doi.org/10.1007/BF01557844>.
- [5] D. N. Astrov, “Linear magnetolectric effect in Cr<sub>2</sub>O<sub>3</sub> in strong magnetic field,” *Sov.Phys.JETP*, vol. 11, p. 708, 1960.
- [6] I. E. Dzyaloshinslii, “On the magneto-electrical effects in antiferromagnets,” *Sov.Phys.JETP*, vol. 10, p. 628, 1960.
- [7] E. Dagotto, “Correlated electrons in high-temperature superconductors,” *Rev. Mod. Phys.*, vol. 66, no. 3, pp. 763–833, 1994.
- [8] Y. Tokura, *Colossal Magnetoresistive Oxides*. London: Gordon and Breach Science Publishers, 2000.
- [9] H. Schmid, “Multi-ferroic magnetoelectrics,” *Ferroelectric*, vol. 162, no. 1, pp. 317–338, 1994, doi: [doi.org/10.1080/00150199408245120](https://doi.org/10.1080/00150199408245120).
- [10] J. Wang *et al.*, “Epitaxial BiFeO<sub>3</sub> Multiferroic Thin Film Heterostructures,” *Science (80-. )*, vol. 299, no. 5613, pp. 1719–1722, 2003, doi: 10.1126/science.1080615.
- [11] T. Kimura, T. Goto, H. Shintani, K. Ishizaka, T. Arima, and Y. Tokura, “Magnetic control of ferroelectric polarization,” *Nature*, vol. 426, pp. 55–58, 2003, doi:



- <https://doi.org/10.1038/nature02018>.
- [12] W. Eerenstein, Morrison.F.D., Dho.J, Blamire.M.G., Scott.J.F., and N. D. Mathur, “Comment on ‘Epitaxial BiFeO<sub>3</sub> Multiferroic Thin Film Heterostructures,’” *Science* (80-.), vol. 307, no. 5713, p. 1203, 2005, doi: 10.1126/science.1105422.
- [13] Hur.N, Park.S, P. A. Sharma, Ahn.J.S., Guha.S., and S. W. Cheong, “Electric polarization reversal and memory in a multiferroic material induced by magnetic fields,” *Nature*, vol. 429, pp. 392–395, 2004, doi: <https://doi.org/10.1038/nature02572>.
- [14] T. Lottermoser, L. Thomas, Amann.Uwe, Hohlwein.Dietmar, Lhringer.Jorg, and M. Fiebig, “Magnetic phase control by an electric field,” *Nature*, vol. 430, pp. 541–544, 2004, doi: <https://doi.org/10.1038/nature02728>.
- [15] N. A. Spaldin, “Multiferroics beyond electric-field control of magnetism,” *Proc. R. Soc. A Math. Phys. Eng. Sci.*, vol. 476, no. 2233, 2020, doi: 10.1098/rspa.2019.0542.
- [16] S. W. Cheong and M. Mostovoy, “Multiferroics: a magnetic twist for ferroelectricity,” *Nat. Mater.*, vol. 6, pp. 13–20, 2007, doi: doi:10.1038/nmat1804.
- [17] T. H. Arima, “Spin-driven ferroelectricity and magneto-electric effects in frustrated magnetic systems,” *J. Phys. Soc. Japan*, vol. 80, no. 5, pp. 1–14, 2011, doi: 10.1143/JPSJ.80.052001.
- [18] K. F. Wang, J. M. Liu, and Z. F. Ren, “Multiferroicity: The coupling between magnetic and polarization orders,” *Adv. Phys.*, vol. 58, no. 4, pp. 321–448, 2009, doi: 10.1080/00018730902920554.
- [19] S. Dong, J. M. Liu, S. W. Cheong, and Z. Ren, “Multiferroic materials and magnetoelectric physics: Symmetry, entanglement, excitation, and topology,” *Adv. Phys.*, vol. 64, no. 5–6, pp. 519–626, 2015, doi: 10.1080/00018732.2015.1114338.
- [20] W. Eerenstein, N. D. Mathur, and J. F. Scott, “Multiferroic and magnetoelectric materials,” *Nature*, vol. 442, no. 7104, pp. 759–765, 2006, doi: 10.1038/nature05023.

- [21] B. Kundys, A. Maignan, and C. Simon, “Multiferroicity with high-TC in ceramics of the YBaCuFeO<sub>5</sub> ordered perovskite,” *Appl. Phys. Lett.*, vol. 94, no. 7, pp. 9–12, 2009, doi: 10.1063/1.3086309.
- [22] M. Mostovoy, “Ferroelectricity in spiral magnets,” *Phys. Rev. Lett.*, vol. 96, no. 6, pp. 10–13, 2006, doi: 10.1103/PhysRevLett.96.067601.
- [23] H. Katsura, N. Nagaosa, and A. V. Balatsky, “Spin current and magnetoelectric effect in noncollinear magnets,” *Phys. Rev. Lett.*, vol. 95, no. 5, pp. 1–5, 2005, doi: 10.1103/PhysRevLett.95.057205.
- [24] S. Ishihara, “Electronic ferroelectricity and frustration,” *J. Phys. Soc. Japan*, vol. 79, no. 1, pp. 1–11, 2010, doi: 10.1143/JPSJ.79.011010.
- [25] M. Fiebig, T. Lottermoser, D. Meier, and M. Trassin, “The evolution of multiferroics,” *Nat. Rev. Mater.*, vol. 1, no. 8, 2016, doi: 10.1038/natrevmats.2016.46.
- [26] D. Khomskii, “Classifying multiferroics: Mechanisms and effects,” *Physics (College Park, Md.)*, vol. 2, 2009, doi: 10.1103/physics.2.20.
- [27] A. G. Gavriliuk, S. A. Kharlamova, I. S. Lyubutin, I. Troyan, S. Ovchinnikov, and A. Postseluiko, “Structural and electronic transitions in gadolinium iron borate GdFe<sub>3</sub>(BO<sub>3</sub>)<sub>4</sub> at high pressures,” *J. Exp. Theor. Phys. Lett.*, vol. 80, no. 6, pp. 426–432, 2004, doi: 10.1134/1.1830662.
- [28] E. Ascher, H. Schmid, and D. Tar, “Dielectric properties of boracites and evidence for ferroelectricity,” *Solid State Commun.*, vol. 2, no. 2, pp. 45–49, 1964, doi: [http://dx.doi.org/10.1016/0038-1098\(64\)90571-X](http://dx.doi.org/10.1016/0038-1098(64)90571-X).
- [29] G. Smolenskii and I. Chupis, “Ferroelectromagnets,” *Sov. Phys. Uspekhi*, vol. 25, no. 7, p. 475, 1982, [Online]. Available: <http://stacks.iop.org/0038-5670/25/i=7/a=R02>.
- [30] T. Kimura, T. Goto, H. Shintani, K. Ishizaka, T. Arima, and Y. Tokura, “Magnetic control of ferroelectric polarization,” *Nature*, vol. 426, no. 6962, pp. 55–58, 2003, doi: 10.1038/nature02018.

- [31] J. Wang *et al.*, “Epitaxial BiFeO<sub>3</sub> Multiferroic Thin Film Heterostructures,” *Science* (80-.), vol. 299, no. 5613, pp. 1719–1722, 2003, doi: 10.1126/science.1080615.
- [32] I. E. Dzyaloshinskii, “A Thermodynamic Theory of Weak Ferromagnetism of Antiferromagnetics,” *J. Phys. Chem. Solids*, vol. 4, pp. 241–255, 1958.
- [33] T. Moriya, “New mechanism of anisotropic superexchange interaction,” *Phys. Rev. Lett.*, vol. 4, no. 5, pp. 228–230, 1960, doi: 10.1103/PhysRevLett.4.228.
- [34] J. B. Goodenough, A. Wold, R. J. Arnott, and N. Menyuk, “Relationship between crystal symmetry and magnetic properties of ionic compounds containing Mn<sup>3+</sup>,” *Phys. Rev.*, vol. 124, no. 2, pp. 373–384, 1961.
- [35] I. Tsukada, X. F. Sun, S. Komiya, A. Lavrov, and Y. Ando, “Significant suppression of weak ferromagnetism in (La<sub>1.8</sub>Eu<sub>0.2</sub>)CuO<sub>4</sub>,” *Phys. Rev. B*, vol. 67, 2003.
- [36] Y. Tokura and S. Seki, “Multiferroics with spiral spin orders,” *Adv. Mater.*, vol. 22, no. 14, pp. 1554–1565, 2010, doi: 10.1002/adma.200901961.
- [37] H. Katsura, N. Nagaosa, and A. V. Balatsky, “Spin Current and Magnetoelectric Effect in Noncollinear Magnets,” *Phys. Rev. Lett.*, vol. 95, no. 057205, pp. 5–29, 2005, doi: <https://doi.org/10.1103/PhysRevLett.95.057205>.
- [38] I. A. Sergienko and E. Dagotto, “Role of the Dzyaloshinskii-Moriya interaction in multiferroic perovskites,” *Phys. Rev. B*, vol. 73, no. 094434, 2006, doi: <https://doi.org/10.1103/PhysRevB.73.094434>.
- [39] M. Mostovoy, “Ferroelectricity in Spiral Magnets,” *Phys. Rev. Lett.*, vol. 96, no. 6, 2006, [Online]. Available: <https://doi.org/10.1103/PhysRevLett.96.067601>.
- [40] A. B. Harris, “Landau analysis of the symmetry of the magnetic structure and magnetoelectric interaction in multiferroics,” *Phys. Rev. B*, vol. 76, no. 054447, 2007, doi: <https://doi.org/10.1103/PhysRevB.76.054447>.
- [41] T. Kimura, G. Lawes, T. Goto, Y. Tokura, and A. P. Ramirez, “Magnetoelectric phase diagrams of orthorhombic RMnO<sub>3</sub> (R=Gd, Tb, and Dy),” *Phys. Rev. B*, vol.

- 71, no. 224425, 2005, doi: <https://doi.org/10.1103/PhysRevB.71.224425>.
- [42] T. Goto, T. Kimura, Lawes.G., A. P. Ramirez, and Y. Tokura, "Ferroelectricity and Giant Magnetocapacitance in Perovskite Rare-Earth Manganites," *Phys. Rev. Lett.*, vol. 92, no. 25, 2004, doi: <https://doi.org/10.1103/PhysRevLett.92.257201>.
- [43] L. Er-Rakho, C. Michel, P. Lacorre, and B. Raveau, "YBaCuFeO<sub>5+δ</sub>: A novel oxygen-deficient perovskite with a layer structure," *J. Solid State Chem.*, vol. 73, no. 2, pp. 531–535, 1988, doi: 10.1016/0022-4596(88)90141-7.
- [44] M. Morin *et al.*, "Incommensurate magnetic structure, Fe/Cu chemical disorder, and magnetic interactions in the high-temperature multiferroic YBaCuFeO<sub>5</sub>," *Phys. Rev. B - Condens. Matter Mater. Phys.*, vol. 91, no. 6, pp. 1–16, 2015, doi: 10.1103/PhysRevB.91.064408.
- [45] M. Morin *et al.*, "Tuning magnetic spirals beyond room temperature with chemical disorder," *Nat. Commun.*, vol. 7, no. 1, pp. 1–7, 2016, doi: 10.1038/ncomms13758.
- [46] T. Shang *et al.*, "Design of magnetic spirals in layered perovskites: Extending the stability range far beyond room temperature," *Sci. Adv.*, vol. 4, no. October, 2018.
- [47] X. Zhang, A. Romaguera, O. Fabelo, F. Fauth, J. Herrero-Martín, and J. L. García-Muñoz, "Tuning the tilting of the spiral plane by Mn doping in YBaCuFeO<sub>5</sub> multiferroic," *Acta Mater.*, vol. 206, p. 116608, 2021, doi: 10.1016/j.actamat.2020.116608.
- [48] R. D. Shannon, "Revised effective ionic radii and systematic studies of interatomic distances in halides and chalcogenides," *Acta Crystallogr. Sect. A*, vol. 32, no. 5, pp. 751–767, 1976, doi: 10.1107/S0567739476001551.
- [49] V. Caignaert *et al.*, "Crystal and Magnetic Structure of YBaCuFeO<sub>5</sub>," *J. Solid State Chem.*, vol. 114, no. 1, pp. 24–35, 1995, [Online]. Available: <https://doi.org/10.1006/jssc.1995.1004>.
- [50] E. Lesley and A. Elaine, *Solid state chemistry: An introduction*, 3rd editio. New York: Taylor and Francis CRC press, 2012.
- [51] H. A. Dabkowska and A. B. Dabkowski, *Crystal Growth of Oxides by Optical*

- Floating Zone Technique*. In: Dhanaraj G., Byrappa K., Prasad V., Dudley M. (eds) *Springer Handbook of Crystal Growth*. Berlin: Springer, Berlin, Heidelberg, 2010.
- [52] S. M. Koochpayeh, D. Fort, and J. S. Abell, "The optical floating zone technique: A review of experimental procedures with special reference to oxides," *Prog. Cryst. Growth Charact. Mater.*, vol. 54, no. 3–4, pp. 121–137, 2008, doi: 10.1016/j.pcrysgrow.2008.06.001.
- [53] Y. C. Lai, G. J. Shu, W. T. Chen, C. H. Du, and F. C. Chou, "Self-adjusted flux for the traveling solvent floating zone growth of YBaCuFeO<sub>5</sub> crystal," *J. Cryst. Growth*, vol. 413, pp. 100–104, 2015, doi: 10.1016/j.jcrysgro.2014.12.020.
- [54] Y. Nishimura *et al.*, "Growth of Y<sub>2</sub>Cu<sub>2</sub>O<sub>5</sub> single crystals by the traveling solvent floating zone method," *J. Cryst. Growth*, vol. 207, no. 3, pp. 206–213, 1999, doi: 10.1016/S0022-0248(99)00383-8.
- [55] Y. Ma, Y. Zeng, D. Perrodin, E. Bourret, and Y. Jiang, "Single-Crystal Growth of ZnO:Ga by the Traveling-Solvent Floating-Zone Method," *Cryst. Growth Des.*, vol. 17, no. 3, pp. 1008–1015, 2017, doi: 10.1021/acs.cgd.6b01232.
- [56] P. W. Anderson and J. M. Rowell, "Probable observation of the Josephson superconducting tunneling effect," *Phys. Rev. Lett.*, vol. 10, no. 6, pp. 230–232, 1963, doi: 10.1103/PhysRevLett.10.230.
- [57] A. O. Adeyeye and G. Shimon, "Growth and Characterization of Magnetic Thin Film and Nanostructures," in *Handbook of Surface Science*, 2015, pp. 1–41.
- [58] T. Thomson, "Magnetic properties of metallic thin films," in *Metallic Films for Electronic, Optical and Magnetic Applications*, 2014, pp. 454–546.
- [59] M. Eckert, "Max von Laue and the discovery of X-ray diffraction in 1912," *Ann. Phys.*, vol. 524, no. 5, pp. 83–85, 2012, doi: 10.1002/andp.201200724.
- [60] C. Fan and Z. Zhao, *Synchrotron Radiation in Material Science: Light Source, Techniques, and Applications*. WILEY-VCH, 2018.
- [61] J. Baruchel, J.-L. Hodeau, M. S. Lehmann, J.-R. Regnard, and C. Schlenker, *Neutron and Synchrotron Radiation for Condensed Matter Studies: Application to*

- Solid State Physics and Chemistry*. Springer-Verlag Berlin Heidelberg New York, 1994.
- [62] “ALBA Web Page.” <https://www.cells.es/en/beamlines/bl04-mspd>.
- [63] C. Giavovazzo *et al.*, *Fundamentals of Crystallography (2nd Edition)*. Oxford University Press, 2002.
- [64] V. Scagnoli *et al.*, “EuTiO<sub>3</sub> magnetic structure studied by neutron powder diffraction and resonant x-ray scattering,” *Phys. Rev. B - Condens. Matter Mater. Phys.*, vol. 86, no. 9, pp. 1–7, 2012, doi: 10.1103/PhysRevB.86.094432.
- [65] M. Garganourakis *et al.*, “Magnetic and electronic orderings in orthorhombic RMnO<sub>3</sub> (R=Tm, Lu) studied by resonant soft x-ray powder diffraction,” *Phys. Rev. B - Condens. Matter Mater. Phys.*, vol. 86, no. 5, pp. 1–5, 2012, doi: 10.1103/PhysRevB.86.054425.
- [66] G. E. Johnstone, R. A. Ewings, R. D. Johnson, C. Mazzoli, H. C. Walker, and A. T. Boothroyd, “Magnetic structure of DyMn<sub>2</sub>O<sub>5</sub> determined by resonant x-ray scattering,” *Phys. Rev. B - Condens. Matter Mater. Phys.*, vol. 85, no. 22, pp. 1–7, 2012, doi: 10.1103/PhysRevB.85.224403.
- [67] T. Chatterji, *Neutron Scattering from Magnetic Materials (1st Edition)*. Elsevier Science, 2007.
- [68] O. Halpern and M. H. Johnson, “On the magnetic scattering of neutrons,” *Phys. Rev.*, vol. 55, no. 10, pp. 898–923, 1939, doi: 10.1103/PhysRev.55.898.
- [69] “ILL web page.” <https://www.ill.eu/>.
- [70] A. Hewat, W. I. F. David, and L. van Eijck, “Hugo Rietveld (1932-2016),” *J. Appl. Crystallogr.*, vol. 49, pp. 1394–1395, 2016, doi: 10.1107/S1600576716012061.
- [71] H. M. Rietveld, “A profile refinement method for nuclear and magnetic structures,” *J. Appl. Crystallogr.*, vol. 2, pp. 65–71, 1969, doi: 10.1107/S0021889869006558.
- [72] G. Will, *Powder Diffraction: The Rietveld Method and the Two Stage Method to Determine and Refine Crystal Structures from Powder Diffraction Data*. Springer-Verlag Berlin Heidelberg, 2006.

- [73] J. Rodrıguiz-Carvajal, *An Introduction of the Program Fullprof 2000 (Version 2001)*. 2001.
- [74] F. de Groot and A. Kotani, *Core level spectroscopy of solids*, 1st editio. CRC Press, 2008.
- [75] “ALBA web Page.” <https://www.cells.es/en/beamlines/bl29-boreas>.
- [76] J. Kanamori, “Superexchange interaction and symmetry properties of electron orbitals,” *J. Phys. Chem. Solids*, vol. 10, no. 2–3, pp. 87–98, 1959, doi: 10.1016/0022-3697(59)90061-7.
- [77] D. E. Cox, W. J. Takei, and G. Shirane, “A Magnetic and neutron diffraction study of the Cr<sub>2</sub>O<sub>3</sub>-Fe<sub>2</sub>O<sub>3</sub> system,” *J. Phys. Chem. Solids*, vol. 24, pp. 405–423, 1963.
- [78] L. A. J. Garvie, A. J. Craven, and R. Brydson, “Use of electron-energy loss near-edge fine structure in the study of minerals,” *Am. Mineral.*, vol. 79, no. 5–6, pp. 411–425, 1994.
- [79] S. Yang *et al.*, “Robust Ferromagnetism of Chromium Nanoparticles Formed in Superfluid Helium,” *Adv. Mater.*, vol. 29, no. 1, pp. 1–6, 2017, doi: 10.1002/adma.201604277.
- [80] M. Asa *et al.*, “Interdiffusion-driven synthesis of tetragonal chromium (III) oxide on BaTiO<sub>3</sub>,” *Phys. Rev. Mater.*, vol. 2, no. 3, pp. 1–10, 2018, doi: 10.1103/PhysRevMaterials.2.033401.
- [81] D. Chen *et al.*, “A Strain-Driven Antiferroelectric-to-Ferroelectric Phase Transition in La-Doped BiFeO<sub>3</sub> Thin Films on Si,” *Nano Lett.*, vol. 17, no. 9, pp. 5823–5829, 2017, doi: 10.1021/acs.nanolett.7b03030.
- [82] N. Daffé *et al.*, “Magnetic anisotropies and cationic distribution in CoFe<sub>2</sub>O<sub>4</sub> nanoparticles prepared by co-precipitation route: Influence of particle size and stoichiometry,” *J. Magn. Magn. Mater.*, vol. 460, pp. 243–252, 2018, doi: 10.1016/j.jmmm.2018.03.041.
- [83] W. Frientrupd, C. T. Chene, A. Erbr, F. U. Berlin, and D. Berlin, “Site specific and doping dependent electronic structure of YBa<sub>2</sub>Cu<sub>3</sub>O<sub>x</sub> probed by O1s and Cu2p

- x-ray absorption spectroscopy,” vol. 71, pp. 1563–1566, 1995.
- [84] A. Scaramucci *et al.*, “Multiferroic Magnetic Spirals Induced by Random Magnetic Exchanges,” *Phys. Rev. X*, vol. 8, no. 1, p. 11005, 2018, doi: 10.1103/PhysRevX.8.011005.
- [85] A. Scaramucci, H. Shinaoka, M. V. Mostovoy, R. Lin, C. Mudry, and M. Müller, “Spiral order from orientationally correlated random bonds in classical X Y models,” *Phys. Rev. Res.*, vol. 2, no. 1, pp. 1–26, 2020, doi: 10.1103/physrevresearch.2.013273.
- [86] Y. C. Lai *et al.*, “Magnetic ordering and dielectric relaxation in the double perovskite YBaCuFeO<sub>5</sub>,” *J. Phys. Condens. Matter*, vol. 29, no. 14, 2017, doi: 10.1088/1361-648X/aa5708.
- [87] R. D. Shannon, “Revised Effective Ionic Radii and Systematic Studies of Interatomic Distances in Halides and Chalcogenides,” *Acta Crystallogr.*, vol. 32, no. 5, pp. 751–767, 1976, doi: 10.1107/S0567739476001551.
- [88] W.-C. Liu, Y.-Z. Zheng, Y.-C. Chih, Y.-C. Lai, and Y.-W. Tsai, “X-ray multi-beam resonant diffraction analysis of crystal symmetry for layered perovskite YBaCuFeO<sub>5</sub>,” *J. Appl. Crystallogr.*, vol. 49, no. 5, pp. 1721–1725, 2016, doi: 10.1107/S1600576716013248.
- [89] F. Millange, E. Suard, V. Caignaert, and B. Raveau, “YBaMn<sub>2</sub>O<sub>5</sub>: Crystal and magnetic structure reinvestigation,” *Mater. Res. Bull.*, vol. 34, no. 1, pp. 1–9, 1999, doi: 10.1016/S0025-5408(98)00214-1.
- [90] J. B. Goodenough, “An interpretation of the magnetic properties of the perovskite-type mixed crystals La<sub>1-x</sub>Sr<sub>x</sub>CoO<sub>3-λ</sub>,” *J. Phys. Chem. Solids*, vol. 6, no. 2–3, pp. 287–297, 1958, doi: 10.1016/0022-3697(58)90107-0.
- [91] P. W. Anderson, “New approach to the theory of superexchange interactions,” *Phys. Rev.*, vol. 115, no. 1, pp. 2–13, 1959, doi: 10.1103/PhysRev.115.2.
- [92] S. Nemrava *et al.*, “Three Oxidation States of Manganese in the Barium Hexaferrite BaFe<sub>12-x</sub>Mn<sub>x</sub>O<sub>19</sub>,” *Inorg. Chem.*, vol. 56, no. 7, pp. 3861–3866, 2017,



- doi: 10.1021/acs.inorgchem.6b02688.
- [93] K. O. Kvashnina *et al.*, “Electronic structure of complex copper systems probed by resonant inelastic X-ray scattering at Cu L<sub>3</sub> edge,” *Phys. B Condens. Matter*, vol. 404, no. 20, pp. 3559–3566, 2009, doi: 10.1016/j.physb.2009.05.058.
- [94] D. P. Shoemaker, J. Li, and R. Seshadri, “Unraveling atomic positions in an oxide spinel with two Jahn-Teller ions: Local structure investigation of CuMn<sub>2</sub>O<sub>4</sub>,” *J. Am. Chem. Soc.*, vol. 131, no. 32, pp. 11450–11457, 2009, doi: 10.1021/ja902096h.
- [95] A. Waskowska, L. Gerward, J. S. Olsen, S. Steenstrup, and E. Talik, “CuMn<sub>2</sub>O<sub>4</sub>: Properties and the high-pressure induced Jahn-Teller phase transition,” *J. Phys. Condens. Matter*, vol. 13, no. 11, pp. 2549–2562, 2001, doi: 10.1088/0953-8984/13/11/311.
- [96] P. Wei, M. Bieringer, L. M. D. Cranswick, and A. Petric, “In situ high-temperature X-ray and neutron diffraction of Cu-Mn oxide phases,” *J. Mater. Sci.*, vol. 45, no. 4, pp. 1056–1064, 2010, doi: 10.1007/s10853-009-4042-2.
- [97] S. Mohanta, S. D. Kaushik, and I. Naik, “Coexistence of spin-canting and metamagnetism in tetragonal distorted spinel CuMn<sub>2</sub>O<sub>4</sub>,” *Solid State Commun.*, vol. 287, no. October 2018, pp. 94–98, 2019, doi: 10.1016/j.ssc.2018.10.014.
- [98] B. I. Shraiman and E. D. Siggia, “Spiral phase of a doped quantum antiferromagnet,” *Phys. Rev. Lett.*, vol. 62, pp. 1564–1567, 1989, doi: 10.1103/PhysRevLett.62.1564.
- [99] N. Ivanov, S. Kruger, and J. Richter, “Square-lattice Heisenberg antiferromagnet with two kinds of nearest-neighbour bonds,” *Phys. Riview B*, vol. 53, no. 2633, 1996, doi: 10.1103/physrevb.53.2633.
- [100] D. Dey, S. Nandy, T. Maitra, C. S. Yadav, and A. Taraphder, “Nature of spiral state and absence of electric polarisation in Sr-doped YBaCuFeO<sub>5</sub> revealed by first-principle study,” *Sci. Rep.*, vol. 8, no. 1, pp. 1–9, 2018, doi: 10.1038/s41598-018-20774-7.
- [101] N. Hollmann *et al.*, “Local symmetry and magnetic anisotropy in multiferroic

- MnWO<sub>4</sub> and antiferromagnetic CoWO<sub>4</sub> studied by soft x-ray absorption spectroscopy,” *Phys. Rev. B - Condens. Matter Mater. Phys.*, vol. 82, no. 18, pp. 1–6, 2010, doi: 10.1103/PhysRevB.82.184429.
- [102] T. Burnus *et al.*, “Local electronic structure and magnetic properties of La Mn<sub>0.5</sub>Co<sub>0.5</sub>O<sub>3</sub> studied by x-ray absorption and magnetic circular dichroism spectroscopy,” *Phys. Rev. B - Condens. Matter Mater. Phys.*, vol. 77, no. 12, pp. 1–7, 2008, doi: 10.1103/PhysRevB.77.125124.
- [103] M. E. Dos Santos, R. Aparecido Ferreira, P. Noronha Lisboa-Filho, and O. Peña, “Cation distribution and magnetic characterization of the multiferroic cobalt manganese Co<sub>2</sub>MnO<sub>4</sub> spinel doped with bismuth,” *J. Magn. Magn. Mater.*, vol. 329, pp. 53–58, 2013, doi: 10.1016/j.jmmm.2012.09.070.
- [104] I. Urcelay-Olabarria *et al.*, “Neutron diffraction, magnetic, and magnetoelectric studies of phase transitions in multiferroic Mn<sub>0.90</sub>Co<sub>0.10</sub>WO<sub>4</sub>,” *Phys. Rev. B - Condens. Matter Mater. Phys.*, vol. 85, no. 9, pp. 1–10, 2012, doi: 10.1103/PhysRevB.85.094436.
- [105] J. Blasco *et al.*, “Magnetoelectric and structural properties of Y<sub>2</sub>CoMnO<sub>6</sub>: The role of antisite defects,” *Phys. Rev. B*, vol. 93, no. 21, pp. 1–12, 2016, doi: 10.1103/PhysRevB.93.214401.
- [106] S. Guillemet-Fritsch, C. Tenailleau, H. Bordeneuve, and A. Rousset, “Magnetic properties of cobalt and manganese oxide spinel ceramics,” *Advances Sci. Technol.*, vol. 67, pp. 143–148, 2010, doi: <https://doi.org/10.4028/www.scientific.net/AST.67.143>.
- [107] J. Herrero-Martín *et al.*, “Direct observation of noncollinear order of Co and Mn moments in multiferroic Mn<sub>0.85</sub>Co<sub>0.15</sub>WO<sub>4</sub>,” *Phys. Rev. B - Condens. Matter Mater. Phys.*, vol. 91, no. 22, pp. 3–7, 2015, doi: 10.1103/PhysRevB.91.220403.
- [108] J. Y. P. Ko, Y. M. Yiu, H. Liang, and T. K. Sham, “X-ray absorption and luminescence studies of Ba<sub>2</sub>Ca(BO<sub>3</sub>)<sub>2</sub>: Ce<sup>3+</sup> / Na<sup>+</sup> phosphors,” *J. Chem. Phys.*, vol. 132, no. 23, pp. 1–6, 2010, doi: 10.1063/1.3437612.

- [109] S. M. Stishov and A. E. Petrova, “Critical Points and Phase Transitions,” *J. Exp. Theor. Phys.*, vol. 131, no. 6, pp. 1056–1063, 2020, doi: 10.1134/S106377612011014X.
- [110] A. Romaguera, X. Zhang, O. Fabelo, F. Fauth, J. Blasco, and J. L. García-Muñoz, “Chiral magnets by disorder: its role on the high-temperature magnetic spiral in the YBaCuFeO<sub>5</sub> perovskite,” *Phys. Rev. Res.*
- [111] T. Kimura, Y. Sekio, H. Nakamura, T. Siegrist, and A. P. Ramirez, “Cupric oxide as an induced-multiferroic with high-TC,” *Nat. Mater.*, vol. 7, no. 4, pp. 291–294, 2008, doi: 10.1038/nmat2125.
- [112] Y. Kawamura, T. Kai, E. Satomi, Y. Yasui, and Y. Kobayashi, “High-Temperature Multiferroic State of RBaCuFeO<sub>5</sub> (R=Y, Lu and Tm),” *J. Phys. Soc. Japan*, vol. 79, pp. 073705–073709, 2010, [Online]. Available: <https://doi.org/10.1143/JPSJ.79.073705>.
- [113] P. A. Stadelmann, “EMS - a software package for electron diffraction analysis and HREM image simulation in materials science,” *Ultramicroscopy*, vol. 21, no. 2, pp. 131–145, 1987, doi: 10.1016/0304-3991(87)90080-5.